Surface acoustic wave microfluidic pumps for on-chip diagnostics

Roberts Rimsa

Submitted in accordance with the requirements for the degree of

Doctor of Philosophy

University of Leeds

School of Electronic and Electrical Engineering

Bioelectronics Group

August 2018

The candidate confirms that the work submitted is their own, except where work which has formed part of jointly authored publications has been included. The contribution of the candidate and the other authors to this work has been explicitly indicated below. The candidate confirms that appropriate credit has been given within the thesis where reference has been made to the work of others.

The work in Chapter 5 and 6 of the thesis has appeared in publication as follows:

Publication (Journal article): R. Rimsa, A. J. Smith, C. Wälti, and C. D. Wood. A planar surface acoustic wave micropump for closed-loop microfluidics. *Applied Physics Letters*, **111**, 234102 (2017).

I was responsible for conducting experimental work, analysing the experimental results, discussions of results and writing the publication. The contribution of the other authors was discussions of results and writing of the publication.

Abstract

Most of point-of-care diagnostics and lab-on-chip devices that do on-chip sample preparation require active fluid actuation. In a laboratory setting, this is done via bulky benchtop equipment such as syringe pumps, peristaltic pumps and pressure systems. However, integration of a pumping unit onto the device allows for increased portability and decreased footprint of the device. Although there are multiple examples of realised micropumps based on different technologies, no one solution offers a combination of small footprint, low costs, scalable manufacturing and high performance required for point-of-care devices.

Surface acoustic wave (SAW)-based micropumps are an exciting alternative to the current micropump systems due their small footprint and simplicity of manufacturing, yet many of the SAW micropumps presented to date suffer from poor performance and/or utilisation of open channels, which can be a problem regarding contamination. The SAW micropump demonstrated here uses a novel planar design and SAW scattering effects to significantly improve the pump performance and maintain closed channels, which is a pre-requisite for point-of-care applications.

This thesis evaluates the fabrication of SAW devices and microfluidic channels using soft lithography. After evaluating the SAW device design concerning electrical characteristics both experimentally and theoretically, the first iteration of SAW micropumps utilising SAW momentum along the piezoelectric substrate is presented and characterised in terms of fluid flow velocity profiles and volume flow rates produced. Subsequently, a concept of a more efficient SAW micropump is presented based on out of the plane interaction between SAW and liquid. To fully utilise this interaction a protocol on the development of 3D microfluidic channels is introduced followed by a discussion on SAW-liquid coupling setting the scene for a demonstration of efficient and closed-loop SAW micropump that delivers pressure gradients up to an order of magnitude higher than the best to-date reported values at a similar input power levels.

Finally, the newly developed pump is utilised in an on-chip flow cytometer to showcase the advanced flow manipulations, showing the potential applications of the SAW micropump beyond simple fluid actuation.

Abbreviations

ABS (plastic)	Acrylonitrile butadiene styrene
AC	Alternating current
DC	Direct current
DNA	Deoxyribonucleic acid
dNTP	Nucleoside triphosphate
EO (flow)	electroosmotic
ESCARGOT	Embedded SCAffold RemovinG Open Technology
FACS	Fluorescence-activated cell sorting
FDA	Food and Drug Administration (of the United States)
FFF	Fused Filament Fabrication
IDT	Interdigitated transducer
LHS	Left-hand side
$LiNbO_3$	Lithium niobate
LOC	Lab-on-chip
MEMS	Microelectromechanical system
PC	Polycarbonate
PCB	Printed circuit board
PDMS	Polydimethylsiloxane
PIV	Particle image velocimetry
PMMA	Poly(methyl methacrylate)
POC	Point-of-care
PZT	Lead zirconate titanate
RHS	Right-hand side
RMS	Root-mean square
RPM	Revolutions per minute
RSAW	Rayleigh surface acoustic wave

SAW	Surface acoustic wave
SH-SAW	Shear-horizontal surface acoustic wave
SMA	Subminiature version A connector
SPUDT	Single phase unidirectional transducer
TSMC	Taiwan Semiconductor Manufacturing Company
μTAS	Micro-total analysis system
UVO (cleaner)	ultraviolet ozone

This page is intentionally left blank.

This thesis is dedicated to my mum, dad and sister. Thank you

for your endless love and support.

This page is intentionally left blank.

Acknowledgements

First of all, I would like to say a big thank-you to my supervisors Dr Chris Wood and Professor Christoph Wälti. I am grateful for your guidance and help during the joyous meetings on Thursdays and life lessons you have taught me along the way. Many thanks for dedicating your time to me during my PhD and this write-up period, it truly has been a life-changing experience. Also, thank you to the EPSRC, the Molecular-Scale Engineering CDT, University of Leeds and Sheffield for providing me with a chance to do this PhD.

Thanks to all of my colleagues in the Bioelectronics group for those countless coffee shop trips, engaging lunch break conversations and, generally, for making the day to day lab work fun. A special thank you to Dr Andrew Lee, Dr Michal Szymonik and Dr Rajan Sharma for your invaluable advice and help during the PhD, and for the many times, you have read this thesis.

On a more personal note, a big thanks to another Bioelectronics member almost-Dr Alban Smith for being my chess nemesis, personal advisor and a friend; and for being a general style icon in Bioelectronics.

Finally, this work and thesis would not have been possible without the advice, support and love from my wife, Juta. Thank you for being there at all times.

This page is intentionally left blank.

Contents

List of figures

This page is intentionally left blank.

List of tables

Chapter 1

Introduction

1.1 Introduction

The microchip industry has shaped the world for the past 40 years thanks to the invention of the transistor earlier in the 20th century.[1] Indeed, the ability to crunch numbers at unprecedented speeds has given humankind abilities such as sending a man to the moon, making air travel ubiquitous and the sharing of the information without the need to be in the vicinity of the source. The latter is an example of how other fields have built success on the fact that millions of simple number operations can be performed in an instant. The smartphone revolution is the pinnacle of the microchip industry which, again, has allowed many other fields to exploit the immense computing power available at our fingertips. Take, for example, mobile banking which has revolutionised the way people handle money[2]; at first glance the banking and microchip industry has but a few things in common.

Right now we are seeing a microelectronics industry slow-down due to the challenges of scaling transistor sizes, which have now reached 12 nm. Moore's law, an empirical law, which stated that the transistor count on a die will double every 12 months, has been

revised by the Semiconductor Industry association multiple times now.[3]

As growth in the microelectronics industry slows, microfabrication companies, such as TSMC (Taiwan Semiconductor Manufacturing Company) are seeking new avenues of development, which coincides with advancements in the scaling of biosensor and point of care diagnostics (POC) devices.[4, 5, 6] Microchip companies like TSMC are investing in these technologies with the idea that the next world-shaping trend will be in personalised medicine (sometimes referred to precision medicine), which will disrupt the existing, one-size-fits-all approach of the current patient system, and POC devices are one of the enablers for this.[7, 8, 9]

Microfluidics is one of the facilitating technologies for enabling the POC devices, which rely on reduced sample sizes and on-chip sample preparation systems. There are many examples of proof of principle microfluidic devices (often regarded as Lab on Chip (LOC) devices) in applications ranging from chemistry to biosensors to polymerase chain reactions.[10, 11, 12, 13, 14, 15, 16] However, in a similar fashion that vast amount of transistors on a single chip allow to perform billions of calculations per second thus creating a computer chip, there is a need for large scale integration to truly unleash the potential of microfluidic devices. For example, being able to perform laboratory grade experiments onto a single, portable chip could see large scale parallelisation of experiments, such as enzyme-linked immunosorbent assay (ELISA) tests, currently done by robotic pipetting machines, done on a single chip, thus helping the development of diagnostic tests.[17, 18]

Despite the clear advantages of the technology, microfluidics as a field has struggled to see large scale device use in industry (besides examples like Illumina).[19] Drawing parallels to the now matured microelectronics industry, microfluidics currently is where microelectronics technology was before the invention of the integrated circuit and complementary metal oxide semiconductor (CMOS) technology.[18] The missing piece is the integration of the proof of principle microfluidic technologies into a single device.

To achieve this integration there is an inherent need to move the liquid sample between the various parts of the system without adding bulk or taking up large area of the device, thus setting the scene for this thesis.

1.1.1 Basic concepts

Although there is a dedicated theory section in this thesis, it is important to introduce a few basic concepts used in the literature review to aid the reader in understanding the context of micropump development. Some of the key concepts utilised here are *polymerase chain reaction (PCR)*, *Reynolds number* and *laminar flow*, and *microfluidic flow resistance*.

PCR is a molecular biology technique used to exponentially amplify DNA (or part of it) with a known sequence.[20] The amplification of DNA molecules from the starting sample aids efficient detection and helps to improve the limit of detection of the system due to an increased number of molecules present. The PCR process has three key steps:

- Denaturation - this step heats the liquid containing DNA to temperatures where double-stranded DNA (target DNA) splits into two single-stranded DNA sequences due to the breaking of hydrogen bonds (typical temperatures $94 - 98°C$).

- Annealing - a lower-temperature step, in which short single-stranded DNA fragments, called primers, bind to the target DNA ends in the solution. Primers are designed to be complementary to the sequence of target DNA ends.

- Extension - this is the final step of a PCR cycle where an enzyme called polymerase searches for the double stranded DNA, binds to the end of the primer, and builds a complementary strand to the target sequence by using deoxynucleoside triphosphates (dNTPs), which are the building blocks of DNA.

These three steps are repeated sequentially for 30 - 60 times, although depending on the

polymerase and the target DNA it is possible to combine steps 2 and 3 for a 2-step PCR protocol.[20, 21]

Reynolds number is a dimensionless number used to describe the regime of fluid flow.[22] There are two main regimes of fluid flow - *laminar* and *turbulent* which are defined by having a Reynolds number below 2300 or above 2600, respectively. Laminar fluid flow is a flow where fluid flows in parallel layers with no lateral mixing, vortices or eddies in the flow, and fluid velocity within the same layer is constant. A turbulent flow regime is completely opposite to laminar flow, in that it is chaotic and fluid velocity can change across the width of the channel, as well as the in the same layer. There is an intermediate flow regime between laminar and turbulent fluid flows, where laminar flow starts to develop local turbulence, yet the flow is not fully developed.[23] The Reynolds number can be calculated using:

$$R_e = \frac{vL}{\nu} \tag{1.1}$$

where v is the fluid velocity, L is a characteristic dimension such as channel radius and ν is the kinematic viscosity of the fluid. In microfluidics, the Reynolds number is almost always in the laminar flow regime.

Microfluidic resistance is a term that links the pressure drop across a microfluidic channel to the volume flow rate of the liquid, in the same way that electrical resistance links voltage drop and current. A particularly important feature of microfluidic resistance is that the hydraulic radius of the channel (i.e. the channel area to double perimeter ratio) dominates the microfluidic resistance equation. This means that even small changes in channel dimensions can lead to significant changes in microfluidic resistance.[24] Microfluidic resistance is given by:

$$R_H = \frac{8\mu L}{\pi r^4} \tag{1.2}$$

where μ is the fluid viscosity, L is the channel length, and r is the channel radius.

1.2   Lab-on-Chip (LOC)

As discussed in Section 1.1, a reduction in the size of diagnostic tools could enable their use to become more widespread, thus fully unleashing the potential of personalised medicine. Before delving into the details of LOC devices, it is important to identify the key components that make up a typical LOC device. These are the components of a standalone LOC device, which is often integrated onto a single cartridge that is complimented by a sophisticated instrument. The instrument operates the LOC device and converts the read-out data into meaningful information. By having a separate cartridge and instrument systems, this ensures there is no cross-contamination between samples and allows for simple operation of the instrument.[25] Lee *et al.* asserts that a typical LOC device will have most of the following[26]:

- **Sample preparation system** - typically, a pre-concentration or filtering step. Depending on the analyte and the LOC system this step might be unnecessary, but for some of the assays this will require rare cell capture, concentration of cells/biomolecules and cell lysis.

- **Reactor and/or mixing system** - this would be a PCR step for any DNA based LOC devices, or an incubation step (requiring mixing) in the case of more sophisticated biosensors.

- **Separation system** - this can either be a wash system in the case of DNA/other target molecule hybridisation device or dielectrophoretic separation of DNA/protein in other cases.

- **Detection/Readout system** - this is dictated by the analyte of interest, and the environment within the fluid. Examples include fluorescence, electrochemical signal readout, mass spectroscopy, colourimetry, etc.[26]

- **Fluid handling system** - unless it is a lateral flow device[1], there will be an active fluid handling system. It is important to minimise the size of the pumps if it is integrated into the LOC itself rather than the readout system. Fluid handling is an integral part of the LOC device, because it interconnects all the different modules listed here. It must provide efficient and non-harmful means of transporting biological sample from module to module; without this capability it is impossible to develop a functional LOC device. Commercial LOC systems therefore put strong emphasis on the development of liquid handling systems.[27, 28]

An active fluid handling system is an integral component for all but the most trivial LOC devices. However, despite its significance there is still no single 'gold standard' means of pumping liquid that combines small footprint, high performance, scalable manufacturing and low cost.

Significant effort has went into scaling down both diagnostic and analysis systems, typically named LOC or Total Micro Analysis systems (µTAS).[29] The name LOC comes from the idea of scaling analysis systems onto a small chip which would be able to perform the same tests as a large, laboratory-scale system. The research into miniaturised analysis systems has been active since the late 1970s, but significant advancement only came with the development of microfluidics in 1990s.[30, 31] One of the first examples of a modern LOC device was presented by the Manz group, which demonstrates an example of chip-based capillary electrophoresis.[32, 33]

Further work in the field has seen the integration of additional components as microfabrication techniques have advanced. For example, heaters for on-chip DNA amplification through PCR[34, 35] and integrated valves for more advanced PCR processes[36]. Notably, each chip design is driven by the application, thus the key parameters in these studies were the time from sample injection to test result. This is

---

[1]A LOC device that utilises capillary driven flow of liquid in porous media, such as, paper. Most notable example of lateral flow devices is pregnancy tests.

a crucial factor for any POC diagnostic application - quicker tests allow for a higher number of patients to be tested in a given time unit or higher number of tests on a single patient.[37]

The aforementioned LOC examples are currently largely reliant on microfabrication techniques developed by the microchip and microelectromechanical system (MEMS) industries. Micromachining, which is the overarching name for techniques utilised by MEMS industries, allows for accurate feature fabrication at a resolution down to a few μm; however, this comes at a significant fabrication cost because the processes rely on cleanroom environments for fabrication.[33, 38] Micromachining remained the primary means of fabricating LOC devices until the advent of cheap soft lithography methods and materials.

Alternative means of fabricating LOC devices employs master-mould replication via soft lithography. Soft lithography is a family of techniques that rely on the repeated casting of a certain design via the use of a template, usually called a master mould. This is a negative of the desired design, just as a stencil is in screen printing.[38] Figure 1.1 shows the schematic of microfluidic channel replication through the use of soft lithography. The channel material can either be an elastomer, such as polydimethylsiloxane (PDMS) or plastic such as polymethylmethacrylate (PMMA), polycarbonate (PC) or others.[39, 40, 41, 42]

The microfluidic channel material choice is important. PDMS is well suited for rapid prototyping channel designs due to the ease and speed of channel production, as well as the generally low cost of the material.[39, 43, 44] On the other hand, plastics such as PMMA, PC and others can be mass manufactured through the use of injection moulding; consequently, this option is more appealing for the commercialisation of such devices.[45, 46] PDMS, however, has more recently emerged as a material of choice for any work involving live cells and more complex microfluidic cellular structures (named the "organ-on-chip"), in which the live cells of a particular organ are cultivated

(a) Silicon wafer

(b) Photoresist / Silicon wafer

Deposit photoresist

Add a photomask

(c) Photomask

(d) 500nm - 500μm / 500nm - 500μm / Master

UV light exposure
Remove photomask
Dissolve photoresist

Pour PDMS
Cure, and peel off PDMS

(e) PDMS

(f) PDMS / Embossed microstructures
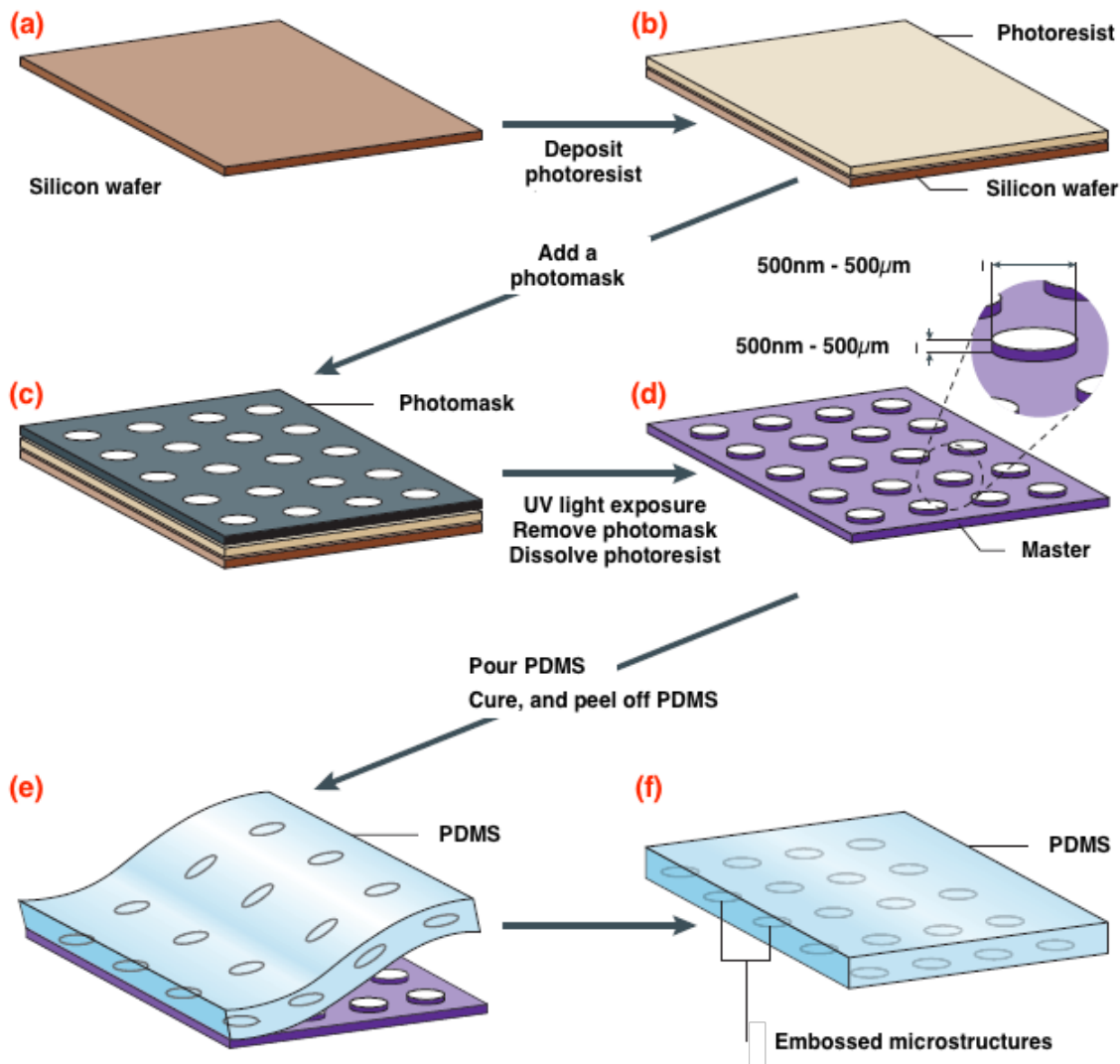
Figure 1.1: A schematic diagram depicting the replication of features using a master mould. (a) A flat and clean substrate is required; typically, silicon wafers are used due to their flatness; (b) A photoresist is spin-coated onto the substrate material to the desired thickness, which is dependent on the desired feature size (typically few µm thick); (c) The light-sensitive photoresist is selectively exposed to light through the use of a dedicated photomask; (d) The photoresist is immersed in a solution that removes either exposed or unexposed areas of the resist (areas removed are dependent the type of resist); (e) The soft-lithography material (in this case, PDMS) is poured over the master mould (template); (f) the PDMS is hardened at elevated temperature. Figure reproduced from [43] with permission from Springer Nature.

in microfluidic channels and are subjected to characterised, intentional perturbations intended to replicate those typically experienced by cells in a real organ.[47, 29, 48, 49] Contrary to its plastic counterparts, PDMS is gas and vapour permeable, meaning that cells can obtain more oxygen and exchange carbon dioxide produced during metabolism; therefore PDMS is the preferred material of choice when working with live cells in microfluidics.[50, 51] To date, liver[49], lung and gut[52], heart[53], as well as various diseases of these organs[54] have been successfully demonstrated in PDMS based organ-on-chip devices. Furthermore, there are examples of rare cell cytometers built on-chip.[55, 56, 57]

In conclusion, soft lithography allows for quick and cheap replication of microfluidic channels following the production of master moulds, which are still produced using conventional micromachining techniques[58] (albeit, more recently 3D printing has been employed to reduce the costs of the master moulds[59]), thus reducing the cost of the devices.

The previous sections have showed the context of LOC devices within the expanding field of personalised medicine, and have showed that LOC devices have historically evolved as a result of advancements in microfabrication industry. However, to fully take advantage of LOC technology, there is a need for an inherently better way of actuating liquid around the miniaturised modules of the device.[29, 60, 61] This was the key premise that defined the need to develop a microfluidic pump that fits the previous requirements of small footprint, high performance, low cost and scalable for manufacturing, thus resulting in this PhD work.

1.3   The structure of this thesis

The first chapter of this thesis examines the background of personalised medicine and the need for better liquid handling systems as a part of the LOC device.

In the second chapter the existing literature on various types of microfluidic pumps is explored, and a literature review focusing on SAW micropumps is done.

The third chapter describes the theoretical background that underpins physics covered in this thesis - the basic physics of microfluidics, the surface acoustic waves and the interaction of surface acoustic wave with liquid.

Chapter 4 includes the materials and the device preparation methods used in the three following experimental chapters.

Chapter 5 reviews the device fabrication and characterisation methods, the pump characterisation technique and finally discusses the initial approach employed in this work.

Chapter 6 then discusses an improved version of surface acoustic wave micropump, which has also formed a base of a publication[62].

In Chapter 7 the previously described pump is utilised for more advanced fluid manipulations required for an on-chip flow cytometer.

Chapter 8 summarises and concludes the work done in this thesis, along with providing a future outlook.

1.4   Statement of originality

This thesis has 4 key contributions to the field. First of all, is a thorough analysis of SAW wavelength choice and IDT design principles described in Chapter 5. None of the SAW micropump papers to date have thoroughly explained the principle of choice for wavelength used in the paper. Throughout this PhD I have studied 10 different wavelengths, how they couple to the piezoelectric substrate, and how the IDT design choice affect parameters such as aperture width and finger pair count, and finally how the

wavelength affects the performance of a SAW pump.

Second contribution is the development of a simple protocol for high resolution 3D microfluidic channel fabrication in a single PDMS cast described in Chapters 4 and 5. Previous processes were evaluated and in the desired design of channels produced low yields. While stacking of PDMS blocks allows 3D channel fabrication, due to the diffraction of the light between the layers, particle image velocimetry is severely complicated.

Since SAW couples to the liquid at 22° with respect to the normal, 3D microfluidic channels allows to harness most of the SAW energy. Combining this with the selection of the most efficient SAW wavelength for the given substrate and geometry, allowed me to develop a fully enclosed SAW micropump, which at low input powers (i.e. up to 0.5 W), delivers an order of magnitude higher output powers than to date best SAW micropumps. This work is described in Chapters 5 and Chapter 6.

Final contribution to the field is a particle sorting system described in Chapter 7. Having shown an efficient SAW pump, the next step was to utilise it in a more complex network. Thus, I have shown fluid flow focusing and shifting using SAW micropump network, which is capable of sorting up to 10 particles per second, which is comparable to other particle sorting systems that are utilising the hydrodynamic flow shifting as the mechanism for shifting.

This page is intentionally left blank.

Chapter 2

Literature review

2.1 Literature review of microfluidic pumping systems

There are two principal types of microfluidic systems: droplet microfluidics, which is concerned with manipulating small amounts of liquid in the form of, for example, droplets in air[63, 64, 65] (referred to as digital microfluidics) or droplets of aqueous liquid in immiscible oil or *vica versa* used for small sample studies [66, 67, 68, 69, 70, 71]. In contrast, continuous flow microfluidics uses liquid of a single phase (oil or water), which is continuously introduced into the reaction chamber.[61, 29, 72, 73, 47] Of these approaches, droplet microfluidics is considered useful for single entity studies, enabling use of small sample volumes.[66] On the other hand, continuous flow microfluidics are typically utilised in systems requiring higher sample throughput and in which simpler channel geometries are required/can be tolerated.[61] The work in this thesis focuses on the development of a liquid handling system suited for continuous flow microfluidics with applications in POC diagnostics field. As such, the literature discussed in the following section is limited to a review of continuous flow microfluidic systems. For more information on droplet microfluidics, some excellent reviews can be found in the references.[74, 75, 76]

2.2 Commercially available liquid pumping systems

It is important to begin by discussing commercially available bench-top technologies used for achieving fluid pumping in microfluidic systems. There are three main categories of liquid pumps: syringe pumps, peristaltic pumps and pressure-based pumps, these are explored in the subsequent sections.

2.2.1 Syringe pumps

A syringe pump is the most common way of moving liquid within microfluidic systems. These pumps are based on a precise linear actuator system, such as a stepper motor and a lead screw, which controllably compress a syringe containing the fluid to be introduced into the microfluidic system. Example of a syringe pump is given in Figure 2.1. Such
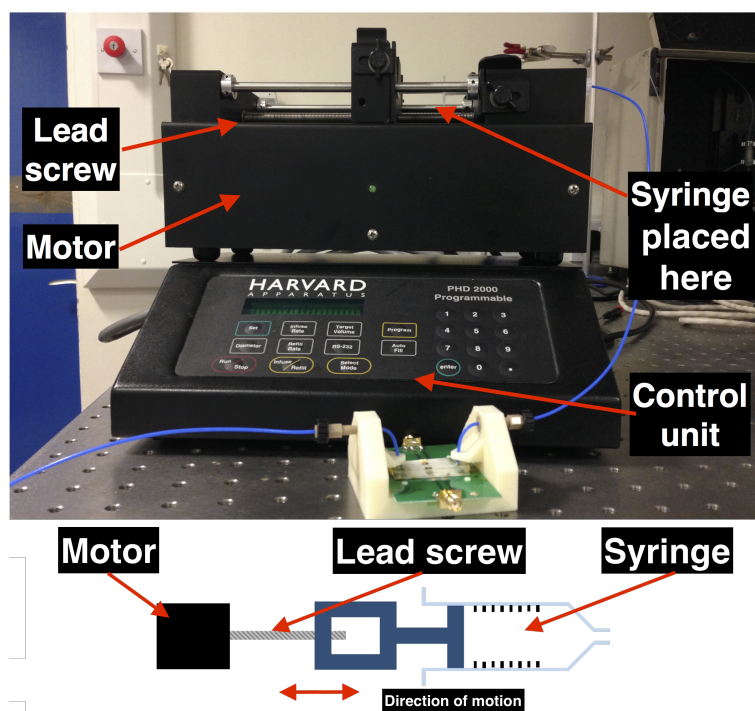
Figure 2.1: The schematic and example of a commercial syringe pump.

systems vary in price from few hundred pounds to thousands of pounds, with high-precision motors and linear motion systems used in the high-end models forming a substantial part of the cost. Due to the simplicity of the system and advancements in affordable 3D printing, there are multiple open-source designs for syringe pumps, which utilise commercially available linear motion parts and 3D printed parts.[77] The key advantages of syringe pumps are their simple and robust design, which ensures system longevity, and their ability to pump large range of volumes (this, effectively, depends on the volume of syringe used). The simplicity of this setup is contrasted by the limited portability of such systems, which means it cannot be placed onto a POC diagnostics cartridge, and the slow response times of the pump, which makes it impossible to create sudden increases of pressure in the system. Consequently, syringe pumps are suited for the infusion of large volumes at constant flow rates, as required in cell separating technologies, for example.

2.2.2 Peristaltic pumps

Peristaltic pumps offer an alternative continuous flow setup. A peristaltic pump consists of a flexible tube that is sequentially compressed by a set of rollers moving the zone of compression radially. Where the tube volume is restricted by the rollers a local pressure drop is caused, which sucks the liquid into the tube, and transits it along with the motion of the rollers as shown in Figure 2.2. Miniaturised peristaltic pumps have been demonstrated by Unger *et al.*[78] for inclusion on chip, which typically adopt a linear design in contrast to the radial designs of their larger counterparts. This is described in more detail in Section 2.6.

Peristaltic pumps are inherently scalable and can therefore produce volume flow rates ranging between nl/min[79] to more than 1000 l/min[80]. Furthermore, since the actuator never comes into contact with the pumped fluid, peristaltic pumps can be used in harsh chemical conditions, where pumping of aggressive liquids such as hydrochloric acid

and sodium hydroxide is necessary, for example, in industrial plastic manufacturing.[80] Another inherent advantage is reduction of cross-contamination since fluid is only in contact with tubing and not open to atmosphere at any point.

The main disadvantage of the peristaltic pump is the degradation of the tubing due to constant friction between the rollers and the tubing; therefore the tubing will require regular replacement. The second disadvantage of the peristaltic pump arrises from sequential compress-release cycle, which creates a pulsating flow. This can be a disadvantage for applications that rely on constant volume flow rate, such as continuous flow PCR.
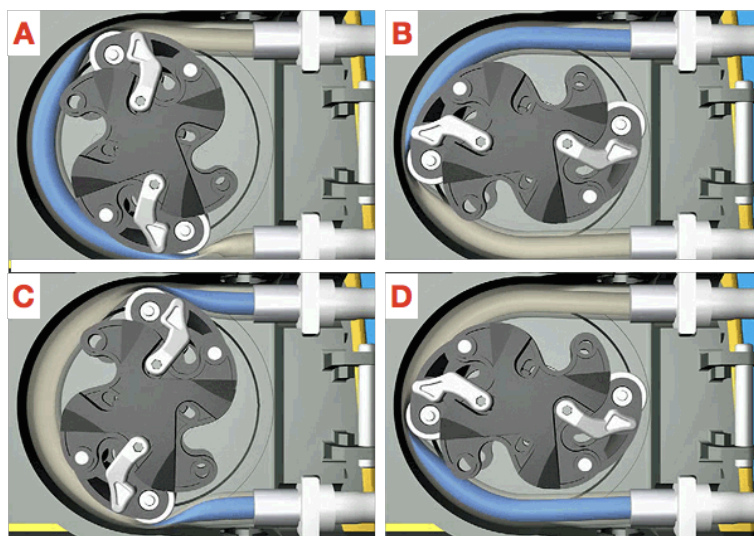
Figure 2.2: The sequential peristaltic pump action as the liquid is sucked into the lower pressure region (A) and is moved towards the exit of the pump (D). Image adapted from [81].

2.2.3 Precision pressure systems

Precision pressure systems such as those made by Fluigent, Elveflow and others rely on pre-pressurising a liquid storage chamber, liquid is flown into the microfluidic channels by opening a set of valves that are controlled by a feedback loop, allowing for stable volume

flow rates.[82] The principle of operation is reliant on fast-working pumps which regulate the pressure in the closed liquid storage chamber. Pressure controlled microfluidic pumps are by far the most expensive external pumping solution, often costing at around £10,000 for a multi-channel control system. The key advantages of the pressure-driven systems are the typically quick response times (on the order of 100 ms), but these are dependent on the air to liquid ratio in the pressurised chamber. Secondly, since this is a pressure driven system, the volume flow rate of is often very stable, which is important for activities like flow cytometry.

As with the previously described methods, portability is an issue due to the necessity of a pressure generating unit, which cannot be scaled down and integrated onto the POC device itself. The second disadvantage is the cost of the system, which can only be justified if the response time and the volume flow rate stability is paramount to the work carried out.

2.3   Summary of commercial devices

Three main commercial liquid pumping systems have been reviewed here. Syringe pumps are the most common microfluidic pumping systems due to their simplicity and ease of use; however, these systems suffer from long lag times between changes in flow rate, and the fixed volume that can be passed through the device. Peristaltic pumps are cheap continuous pumps with no volume limit; however, they are restricted by the wear of the tubing, compatibility between the liquid and the tubing, and the pulsed nature of the fluid flow. Finally, precision pressure driving systems have excellent response times and generally have no compatibility issues between pumping fluid and the system; however, these systems are costly, and the controlling units are typically large.

Having reviewed the commercially available external microfluidic pumping solutions, the current research into microfluidic pumping solutions will next be examined.

2.4   Electroosmotic micropumps

Electroosmotic (EO) flow of liquid is induced by application of an electric field across a liquid containing electric charges. Liquid flow is induced by the applied electric field imposing a Coulomb force on an electrical double layer of ions next to the channel walls.[83] Typically, the electrodes generating the electric field are placed in the inlet and the outlet of the microfluidic channels. Since the fluidic channel walls are usually fabricated from a dielectric material, the flow profile of EO flow is not parabolic.[24] The flow velocity is found to be almost uniform along the width of the channel, and it becomes non-uniform at distance of less than 200 nm from the channel wall, as shown in the Figure 2.3.
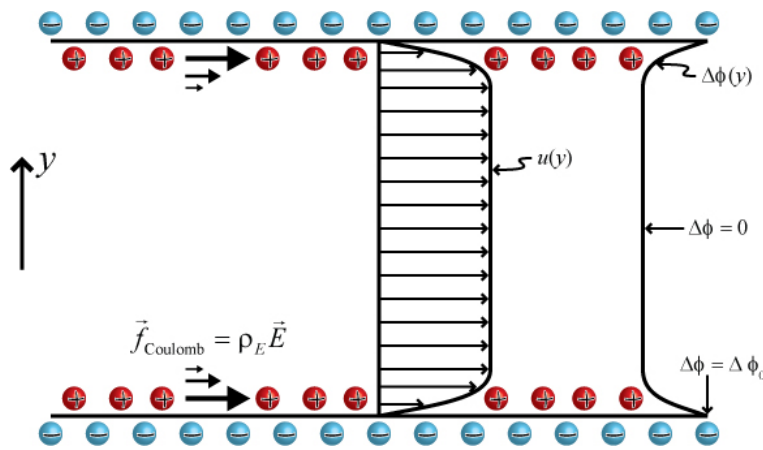
Figure 2.3: The flow profile of EO flow, adapted from [24].

2.5   DC EO pumps

Considering that the operating principle of the EO is based on a surface confined effect, the channel dimensions are thus critical; the channel depth is typically on the order of tens of μm to enhance the EO flow. The linear velocity of the liquid in EO flow can be

defined by the Equation 2.1

$$v_{eo} = \frac{\epsilon \zeta V}{4\pi \mu L} \tag{2.1}$$

Where ϵ is the dielectric constant of the buffer solution, ζ is the zeta potential, V is the applied voltage, μ is the liquid viscosity, and L is the channel length across which the voltage is applied. It can be seen that the fluid velocity and the volume flow rate are directly proportional to the voltage.[84] Therefore, DC EO flow pumps typically have operating voltages in the kV region. Early reports by Pretorius *et al.* reported the first use of the EO effect for pumping liquid, and achieved a fluid flow velocity of 200 µm/s at an applied electric field of 2000 V/cm. [85, 86] To enhance the EO effect and increase the flow velocity, porous capillaries were used with pore sizes ranging between 1 and 20 µm. These were further refined to reduce the pore size of the capillaries to 0.1 µm, which enhanced the performance of the pump. As a result, the volume flow rate of the pump was reported to be 83 nl/min at the applied electric field of 160 V/cm.[87] Early application of EO pumps was for high-performance liquid chromatography, where volume flow rate is not the key performance factor. However, to use an EO pump in a POC diagnostics tool, it would be necessary to achieve flow rates on the order of 100 µl/min.[88] Such flow rates were reported by Paul *et al.* but at an extremely high applied voltage of 10 kV.[89, 85] the high electric field necessary to operate this pump cannot be utilised in a POC device due to potential harm to the end user, and also because the high electric fields cause excessive bubble formation and pH changes within microfluidic channels.[84] Consequently the remainder of this discussion focusses on low-voltage EO pumps only.

2.5.1 Membrane-porosity based EO pumps

One approach to reduce the operating voltage is achieved by reducing the distance across which the voltage is applied, thereby maintaining a high electric field. One such technique utilises a porous membrane material in which a high electric field is established in the

membrane pores. Figure 2.4 shows the schematic of the experimental setup utilised by Snyder *et al.*[90]
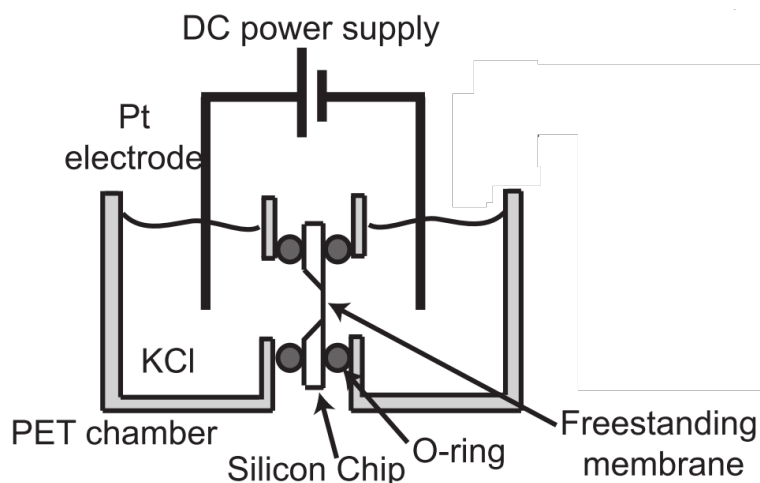
Figure 2.4: The experimental setup of a porous membrane EO pump. Figure adapted from [90], ©2013 National Academy of Sciences.

This EO pump consisted of a porous 15 nm-thick silicon membrane, which had multiple active windows (with different surface areas) across which the liquid was pumped. The pump was capable of delivering up to 10 µl/min flow rate at an applied voltage of 20 V (equivalent electric field 1.3 MV/cm), although the operational voltage could be as low as 0.25 V for the pump to work. This demonstrates that it is possible to lower the operating voltage of EO pump by scaling down the length across which voltage is applied.

In addition, a porous silicon membrane for EO pumps was also demonstrated by Yao *et al.*[91] Whereas Snyder *et al.* used a porous nanocrystalline Si membrane, Yao *et al.* employed uniformly spaced micrometre-sized pores in silicon wafer with a thermally grown porous silica on top for EO pumping, as seen in Figure 2.5.[91] Yao *et al.* show that the that the pore diameter decreases with increasing thickness of the silica membrane. This acts to decrease the volume flow rate at a given applied voltage while simultaneously increasing the maximum pressure generated by the device. The maximum volume flow rate achieved across membranes comprised of only the native silicon dioxide (which is
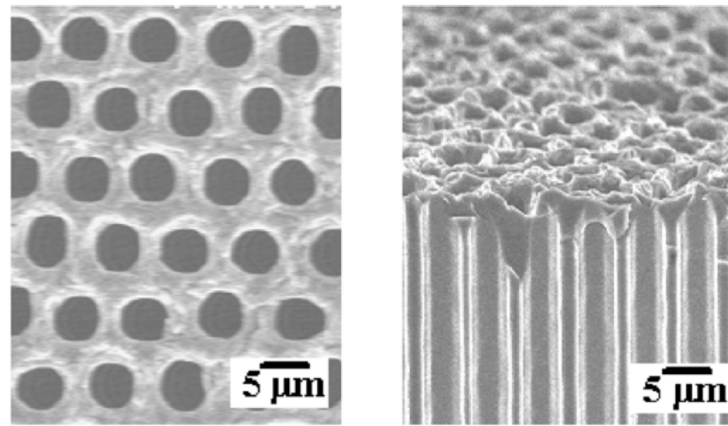
Figure 2.5: The experimental setup of a porous membrane of the EO pump. Figure adapted from [91], ©2006 IEEE .

on the order of 1 nm thick) was 14 μl/min at an applied voltage of 25 V.[91, 92] In contrast, devices formed from a 0.25 μm thick thermally grown oxide achieved flow rates of 12.5 μl/min at 35 V (1.4 MV/cm) applied voltage. The fact that native oxide devices perform better is to be expected, as the native oxide films are significantly thinner than the grown oxide films, which results in a higher electric field. On the other hand - controllably grown oxide devices should have much more stable and repeatable characteristics as it has been shown that native oxide swells after being submerged in water for prolonged times, which is a potential concern for devices intended to pump liquid.[92]

This work was expanded beyond silicon membranes by Vajandar *et al.* who used alumina oxide as the porous material achieving up to 0.6 ml/min volume flow rate at an applied electric field of 1 kV/cm.[93] Electroosmotic liquid pumping through nanometer-sized pores have also been shown in polycarbonate[94] and also carbon nanotube substrates[95] with operating principles similar to those as outlined by Snyder, Yao and Vajandar *et al.*[90, 91, 93]

2.5.2 AC EO pumps

An alternative strategy to scaling down the distance between the electrodes is to use an AC electric field to induce fluid flow. The initial theoretical and experimental work on AC-EO pumps was done by Ajdari[96] who demonstrated a local, unidirectional fluid flow could be achieved by applying an AC electric field to planar and symmetric electrodes.[84] Although there was an apparent EO flow, it was only local and did not result in a net fluid flow. Ajdari showed theoretically that it is possible to induce a net positive EO fluid flow using AC fields by utilising non-symmetric electrodes, a schematic of which can be seen in Figure 2.6.[96]
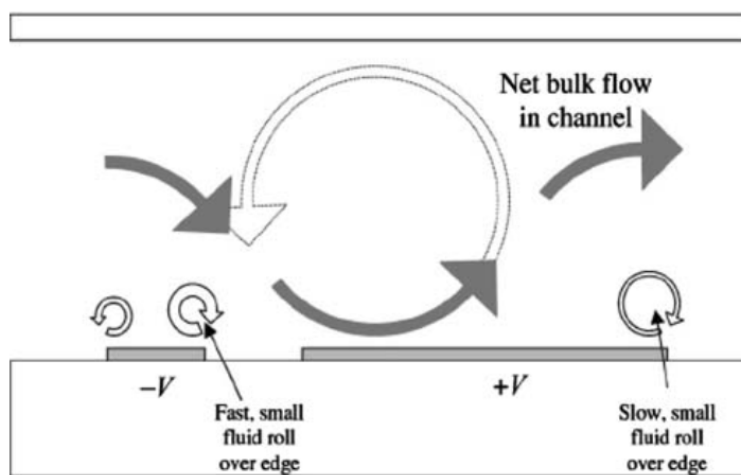
Figure 2.6: A schematic of the electrode design for AC-EO as proposed by Ajdari, where a net EO flow is generated by applying an AC electric field to non-equal sized electrodes. Figure reproduced from [84] with permission from Springer Nature.

An experimental proof of principle was done by Brown *et al.*, in a system consisting of 4.2 and 25.7 μm wide electrodes separated by a 4.5 μm gap with a repeated pitch of 50 μm.[97] Due to the small spacing between the electrodes, small applied voltages (up to 1.2 V, RMS) resulted in electric fields of up to 250 V/cm and were shown to propel the liquid at a linear velocity of up to 75 μm/s. When this is compared to DC

EO, the electric fields necessary are significantly lower, thus expanding the applications of EO flow pumps. Similar results were also reported by Studer *et al.*, where arrays of asymmetric interdigitated electrodes (IDTs) were utilised to generate a fluid velocity on the order of 300 µm/s with an applied RMS voltage below 6 V, see Figure 2.7.[98] Importantly, Studer *et al.* demonstrated that the EO pump direction is dependent on the frequency of the applied AC signal, and that the flow direction was observed to reverse as the applied AC frequency was increased above few tens of kHz.
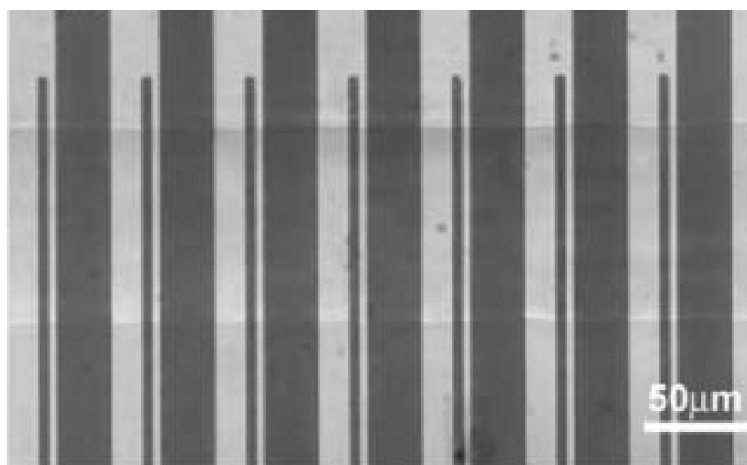
Figure 2.7: The EO pump design used by Studer *et al.* Figure reproduced from [98] with permission from The Royal Society of Chemistry.

It is important to note that the non-uniform electric field in asymmetric IDT systems will also generate a dielectrophoretic particle movement, which explains as to why often EO pumps are the preferred means of manipulating liquid in dielectrophoresis systems.[99, 100, 101]

An alternative electrode geometry was demonstrated by Lastochkin *et al.* who proposed that using a strip and a T-shaped electrode pair will generate a net fluid flow in a pump by exploiting oxidisation/reduction reactions at the electrodes as seen in Figure 2.8.[102] This yields in an EO pump capable of delivering volume flow rates of 0.7 µl/min with an applied electric field of 1.3 kV/cm. Utilisation of high-frequency oxidisation/reduction

enabled the authors to generate a local electric charge which drove the EO flow. They were able to avoid bubble generation by choosing the electrode material and buffer contents to avoid reactions that would yield gas generation.[102]
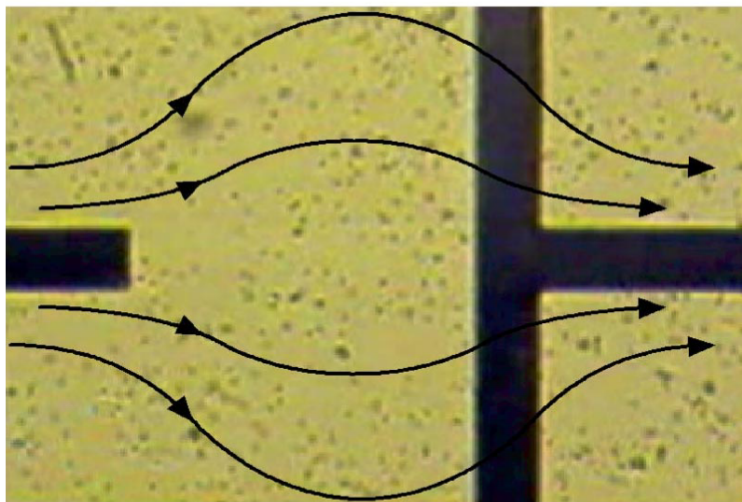
Figure 2.8: An EO pump design based on high-frequency electrochemical reactions. Due to the asymmetry in the electrode geometry, there is a net volume flow rate of the liquid. The black lines show the net electroosmostic flow streamlines. Figure reprinted from [102] with the permission of AIP Publishing.

2.5.3 Summary of EO micropumps

Two types of EO pumps were discussed herein based on the use of DC and AC electric fields. DC-based electroosmotic pumps typically have a simple electrode setup, where the cathode and anode are immersed in the inlet and the outlet of the channels, respectively, and EO flow is produced by the charge generated along the dielectric walls of the microfluidic channel. However, this kind of setup requires high voltage sources to make it operate at the volume flow rates required for POC applications. Not only the high voltage is a risk to the end-user, but also such high electric fields cause radical pH changes of the aqueous media, as well as excessive bubble generation and Joule heating.

Small voltages can be used in a DC-based EO pumps, that utilise porous membranes across which the electric field is applied, which then causes liquid pumping through the membrane. These membranes usually have thicknesses of tens of nanometers to few micrometres. Consequently, a small voltage applied across the membrane will result in a high-electric field, which will in turn generate EO flow. However, these pumps are not capable of delivering the required volume flow rate of tens of μl/min, required in POC devices.

Another way of decreasing the operating voltage is to use AC electric fields for EO pumping. The operating principle of such pumps relies on non-uniform electrode geometry, which causes a net EO flow from the smaller to the bigger electrodes. This method was first proposed by Ajdari, and later confirmed experimentally by multiple other groups. However, although the operating voltage of the pumps is decreased, so is the volume flow rate achieved by the pumps.

EO pumps can therefore only be used in a POC device where low sample volume flow rates are acceptable, such as biosensors, or in instances where the POC device does not have to be battery operated, and therefore high driving voltages can be achieved using mains supply. This however, limits POC device use in, for example, the developing world. Finally, EO pump operation is dependent on the conductivity of the liquid, as the EO is dependent on the liquid ion interaction with the electric double layer on the surface of an insulator. Consequently this limits the EO pump operation to high conductivity liquids.

2.6   Membrane pumps

The principle of a membrane pump is based on the use of a membrane (or a system of membranes), which is externally actuated, thus creating a local volume change within a microchannel. The local volume change results in a local pressure change, which drives the liquid motion.[88]

2.6.1   Pneumatic membrane pumps

PDMS is a typical material that is used in membrane pumps due to its low cost, ease of preparation, relatively good adhesion to different materials, as well as suitability for spin-coating.[58, 50, 61, 29, 103, 104] Consequently, there are multiple examples of using PDMS as a membrane material. The actuation of the elastomer membrane can be achieved through the use of actuation chambers, which deflect the membrane, either pneumatically[78] or thermopneumatically[105]. Both of these techniques rely on pressure increase of a gas (air in most cases) in the channel actuating chambers.[105, 78, 88]

Pneumatically driven membrane pumps were first reported by the Quake group in their seminal paper in 2000.[78] The operating principle of pneumatically actuated PDMS pumps can be seen in the Figure 2.9. Considering that the pump is based on a small valve that opens or closes the channel, the resultant fluid displacement per valve is minuscule. A set of valves are therefore required to obtain constant fluid flow, as shown in Figure 2.9. This article started the research of PDMS-based membrane pumps and, at the time of writing this thesis, has been cited more than 2400 times making it one of the most influential papers in the field of microfluidic pumps. The valves at the heart of these micropumps, are now referred to as Quake valves.

Keeping the same operating principle, there are a few variables that can be changed to
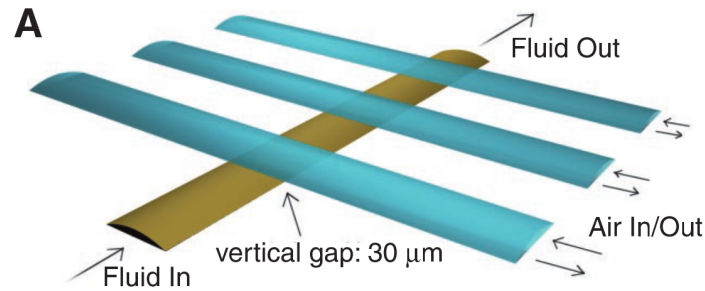
Figure 2.9: The operating principles of a pneumatically actuated membrane pumps, first reported by Unger *et al.* Figure from [78], reprinted with permission from AAAS.

improve the design of the Quake-valve based micropumps. By differing the placement of the actuating channels, it is possible to increase the height of the channel from 10 μm to 56 μm, without comprising the pump characteristics as shown by Studer *et al.*[106] However, even with increased channel height, the cross-section of the channel still has to resemble a half-circle to aid the actuation.

Further, to reduce the footprint of the equipment, it is important to reduce the pressure required for channel actuation, which can be achieved by altering the membrane characteristics. For example, Studer *et al.* found that the actuation pressure decreases linearly with respect to decreasing membrane thickness, with the lowest actuation pressure of 2 kPa achieved for a membrane thickness of 3.8 μm.[106] However, thin membranes do not close the channels completely, thus there is a tradeoff between successful channel actuation and the actuation pressure. Furthermore, handling of such thin PDMS membranes can be problematic and decrease the device fabrication yield. Alternatively Pandolfi and Ortiz showed that, by inducing controlled swelling in the PDMS membrane, it is possible to reduce the actuation pressure required to 3 kPa for 15 μm thick PDMS membranes. The controlled swelling decreases the stress in the membrane, consequently decreasing the actuation pressure.[107]

The relatively large footprint of the pneumatic actuation devices is countered by the scalability of the pumps. Thorsen *et al.* have shown that it is possible to fabricate more than 3500 individually addressable micro-valves in one square inch area (625 mm^2), which can act as valves or local micropumps.[18] Figure 2.10 shows an example of the valve integration achieved by Thorsen *et al.*
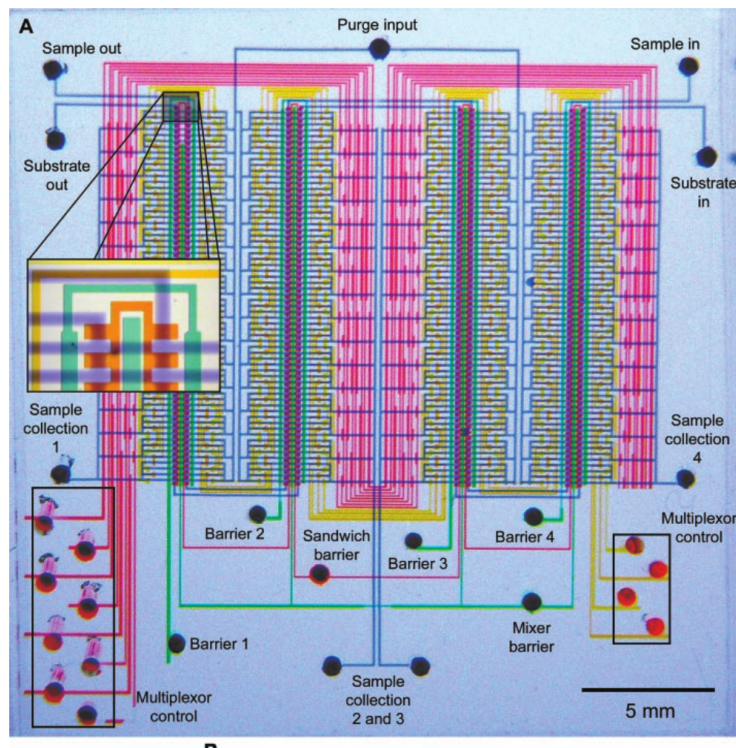
Figure 2.10: Large-scale integration of Quake valves achieved using standard PDMS microfluidic chip fabrication methods. Figure from [18], reprinted with permission from AAAS.

Unger *et al.* showed that at 50 kPa actuation pressure, it is possible to obtain 0.12 µl/min flow rate. A follow-up publication by Studder *et al.* showed that it is possible to obtain the same volume flow rate at ¼ of the actuation pressure. By adjusting the actuation chamber placement and volume, Sundararajan *et al.* have demonstrated a single-layer membrane micropump with a volume flow rate of 0.4 µl/min.[108] By adjustment of the pumping chamber volume and utilisation of normally-closed doormat style microvalves, Grover *et al.* were able to show PDMS micropumps exhibiting volume flow rates of up to

14.4 μl/min.[109] By utilisation of three actuation chambers connected in series, Lien *et al.* demonstrated peristaltic membrane pumping using a single pneumatic source with a maximum volume flowrate of 100 μl/min at 173 kPa actuation pressure.[15] At a similar pressure of 137 kPa, Huan *et al.* were able to obtain only 6 μl/min pumping rate using a single chamber device, although the channel resistance of their devices was higher, and furthermore the bottom substrate of their devices was PMMA, rather than glass, which might have adversely affected the volume flow rate.[110, 88]

The volume of the microvalves affects the response time of the valve, defined as the time it takes for the valve to completely close from being fully open. This effect was used by Lai and Folch, where a series of different volume pumps were actuated in a 'single-stroke' as shown in Figure 2.11.[111] Due to response time differences between adjacent valves, a single stroke produced a peristaltic liquid movement of up to 6 μl/min.

2.6.2 Thermopneumatic membrane pumps

Pneumatic actuation of the previously described elastomer membrane pumps is achieved through the use of an external, pressure-generating equipment. An alternative to a pneumatic membrane pump is a thermopneumatic micropump, in which the membrane motion is induced by heating a gas (usually air) in the actuating channel. The operational principle of these pumps is based on the Charles law.[112] Since heat is generated through resistive heating of an element such as a circuit track on a printed circuit board (PCB) or electrodes deposited on a chip, the footprint of these pumps is smaller than that of classic pneumatic micropumps.

The first thermopneumatic pump was reported by Pol *et al.*, in a paper where the flexible membrane was formed from a 19 μm thick silicon membrane, and which achieved volume flow rates of up to 34 μl/min.[113] The use of a thermopneumatic system allows reduction of the applied voltage in comparison to comparable piezoelectric membrane pumps,
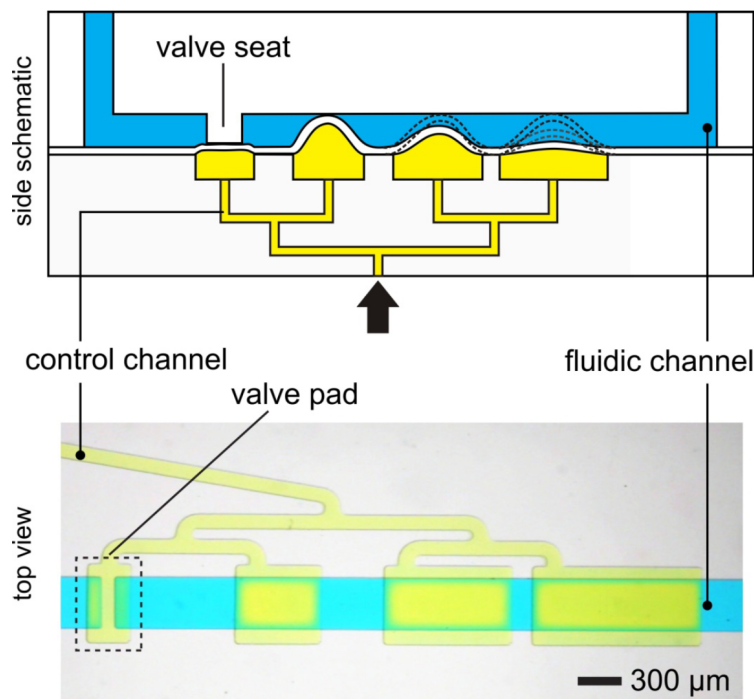
Figure 2.11: The operating principles of a pneumatically actuated membrane pumps, with working principles based on the response time differences of different volume valves. Figure reproduced from [111] with permission from The Royal Society of Chemistry.

which typically require DC voltages in excess of 100 V. The fabrication of these pumps in a cleanroom allows the pumps to be manufactured on a large scale, as described in [113]. However, reliance on cleanroom fabrication makes solid membrane pumps expensive in comparison to cheaper membrane materials, such as PDMS. With the advent of soft-lithography tools kick-started by Whitesides' group in the late 1990s, elastic silicone materials became the main membrane material used in thermopneumatic pumps (and pneumatic pumps).[58, 114, 88] The key reasons for this transition were the low cost of PDMS (and the like) materials, as well as the ease of replication of the design, which is achieved by casting the material over pre-made moulds, allowing large numbers of devices to be formed from a single mould. The associated cost reduction also allows ordering moulds with higher resolution from more reputable manufacturers.

Ou *et al.* demonstrated a PDMS-membrane based thermopneumatic pump with a 50 μm thick membrane.[115] By utilising an asymmetric valve system, the group were able to obtain 0.1 μl/min volume flow rate with 1.75 W energy drawn on the device. Song and Lichtenberg used the principle of thermopneumatic pumps in a single chamber system, where the heater element is connected to the same chamber the liquid injected. By cooling the resistive element at a constant rate, a continuous fluid flow of 0.34 μl/min was obtained at a given cooling rate of 10 K/min.[116] The principle of operation of the pump described in [116] is shown in Figure 2.12.
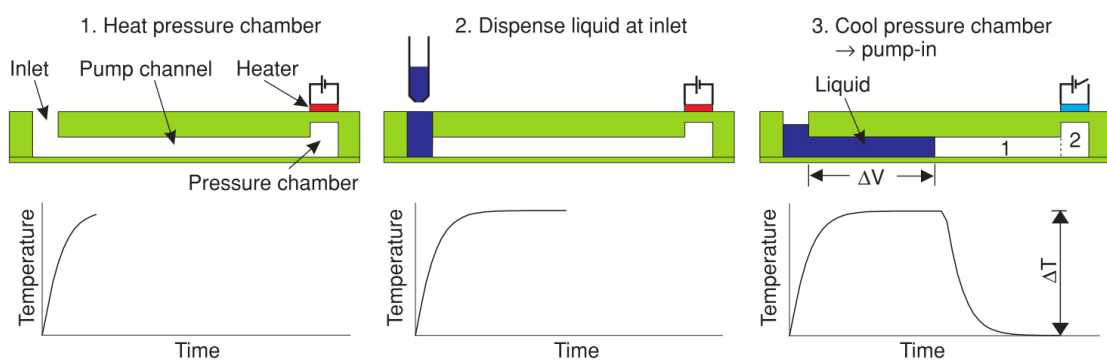
Figure 2.12: The operating principle of the thermopneumatic pump. Figure from [116], ©IOP Publishing.

2.6.3 Piezoelectric membrane pumps

Another type of pneumatic membrane pumps utilises a piezoelectric membrane which has electrodes patterned on it's surface. By applying a voltage to the electrodes, the membrane deflects due to the piezoelectric effect. Application of AC voltage stimulates oscillation of the membrane, which consequently produces liquid movement. Piezoelectric membrane pumps typically use materials with large piezoelectric coefficients to generate maximum membrane deflection and therefore which produces the biggest volume change per cycle.[60]

Bu *et al.* reported a system of three lead zirconate titanate (PZT) membranes capable of producing 200 μl/min volume flow rate, with a maximum membrane deflection of 7 μm and applied voltage of 100 V.[117]. The volume flow rate was sufficient to perform on-chip PCR with single heating cycles below 2 s.
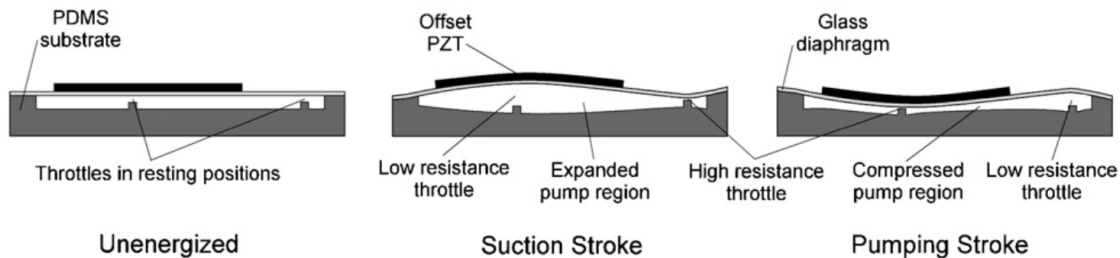
Figure 2.13: The operating principles of a microthrottle based centre-offset micropump reported by Tracey *et al.* Figure from [118], ©IOP Publishing.

Piezoelectric membrane pumps were developed thanks to advances in the microfabrication industry. However, material costs still remain the same, therefore for large-scale production research has shifted towards low-cost materials such as PDMS and PMMA as the base material.[60] To reduce material costs and increase the portability of piezoelectric membrane pumps, there is on-going research into single-stroke piezoelectric pumps as a replacement technology for the valve-based micropumps. One approach is to use flow-rectification as a means to improve the piezoelectric pump performance. Due to the channel resistance scaling with the fourth power of the channel radius, even small changes in channel dimensions can lead to significant changes in the flow resistance, which, effectively, rectifies the flow direction. Tracey *et al.* show an example of flow a rectification based micropump that utilises microthrottles in the channel. By having a centre-offset piezoelectric membrane, flow rectification is achieved as shown in the Figure 2.13.[118] The pump reported in [118] can produce volume flow rates of up to 1.6 ml/min at 1.6 kHz actuation frequency and 360 V (peak to peak) applied voltage. Notably, two channels in parallel can be actuated with a single piezoelectric disc, consequently reducing the price of the pump.

Similarly, Johnston *et al.* utilise microthrottles to open and close the inlet or outlet of the chamber, consequently improving the volume flow rate of a single actuator micropump[119] up to 130 μl/min at 360 V peak to peak applied voltage.

In 1996 Stehr *et al.* reported a piezoelectric membrane-based pump, which utilised a lagging deflection rate of a silicon membrane induced by oscillations of the piezoelectric membrane, to achieve volume flow rates in excess of 2 ml/min at 200 V drive voltage.[120] The operating principle of this pump is shown in Figure 2.14. Stehr *et al.* achieved these flow rates in a hybrid system where the piezoelectric pumping unit was combined with thermoplastic microfluidic channel system, thus showing the early trends of switching towards lower cost systems.
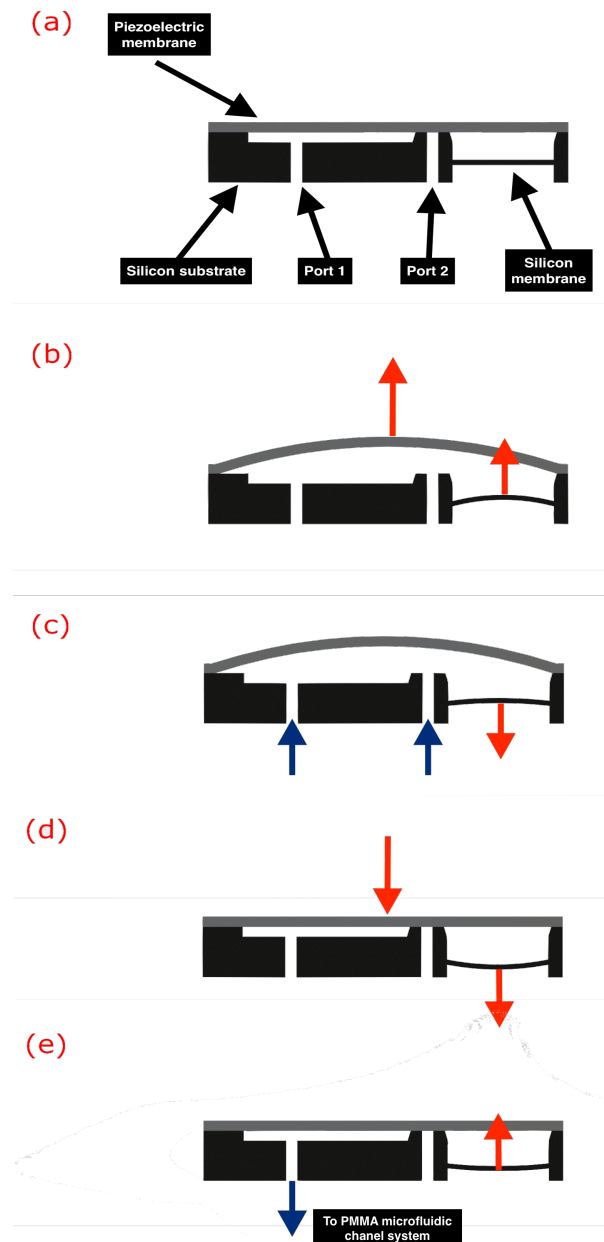
Figure 2.14: The operating principles of a piezoelectric membrane pump reported by Stehr *et al.* consists of 5 steps: (a) Stand-by state; (b) The piezoelectric membrane is rapidly actuated, which causes the buffer membrane(made from silicon) to deflect; (c) The fluid is sucked in both ports driven by the relaxation of the silicon membrane; (d) Port 2 is rapidly blocked by the piezoelectric membrane consequently deforming the silicon membrane; (e) As the silicon membrane relaxes all the fluid is pushed through the Port 1. Figure adapted from [120]. Red arrows show the direction of membrane deflection, and blue arrows show the fluid flow direction.

2.6.4   Summary of membrane pumps

Two types of membrane-based pumps were discussed herein - pneumatic membrane pumps and thermopneumatic pumps. Generally, there are two different pneumatic pumps depending on the material of the membrane used. Piezoelectric pumps were the first pneumatic pumps described in the literature, stemming from the MEMS industry and advances in the microfabrication industry. Typically, materials with high piezoelectric coefficient, such as PZT, are used to ensure high membrane displacement, therefore increasing the displaced volume per actuation cycle. Due to the piezoelectric material used, the membrane can be actuated at high frequencies (often tens of kHz), consequently significantly increasing the volume flow rate of piezoelectric membrane pumps, which is on the order of few ml/min. Due to microfabication of the piezoelectric membrane pumps, these pumps can be fabricated in large quantities. However, the cost per unit is still relatively high, which limits the applications of piezoelectric membrane pumps in POC diagnostic devices. Along with the relatively high cost, these pumps require high DC voltages (usually in excess of 100 V amplitude) to induce sufficient deflection of the membrane. A cheaper alternative to piezoelectric pumps are Quake-valve pumps. These pumps use an external pneumatic source, which cycles applied pressure to an actuating channel. By using a peristaltic pumping pattern in which a series of valves are opened and closed sequentially, it is possible to obtain directed fluid flow. Although cheap, these pumps require an external pressure actuation source (often requiring applied pressures of more than 100 kPa), which increases the footprint of the devices. Furthermore, elastomer-based membrane pumps typically produce volume flow rates one to two orders of magnitude lower than their piezoelectric membrane pumps.

The second type of membrane pumps discussed were thermopneumatic pumps, which utilise thermal expansion of gas to deflect a membrane in the actuation chamber. Since the heating element can be scaled down (in the form of electrodes deposited on the substrate, or a PCB for example), these devices have a small footprint compared with those based on

Quake-valves (or piezoelectric membrane pumps). However, the achievable volume flow rates are on the order of 0.1 to 0.34 µl/min, smaller than pneumatic micropumps using the same membrane material, and significantly lower than piezoelectric membrane-based micropumps.[115, 116, 88, 60, 118] Consequently, the application of thermopneumatic pumps can be somewhat limited, however, the principle of the thermopneumatic actuation can be used for microfluidic valves, which do not require short response times.

2.7   Acoustic force micropumps

Another means of achieving fluid flow in microfluidic channels is through the use of surface acoustic waves (SAWs). For the purposes of this work a SAW is a mechanical wave that propagates along the surface of a piezoelectric substrate, with its energy confined to few (<5) wavelengths depth in the substrate.[121, 122] The concept of SAWs was first introduced by Lord Rayleigh in his seminal paper, and subsequently the most common form of SAW is named after him - the Rayleigh SAW.[123] Rayleigh SAWs are those whose mechanical displacement lies perpendicular to the surface of the substrate. This is the most common mode of SAW propagation, and they can be generated in a wide variety of materials including lithium niobate[124, 125, 126, 127], GaAs[128, 129], quartz[130, 131, 132] and others. A more detailed discussion of SAW generation and the solid state material theory of the SAWs can be found in the Chapter 3. An image of a Rayleigh SAW can be seen in Figure 2.15
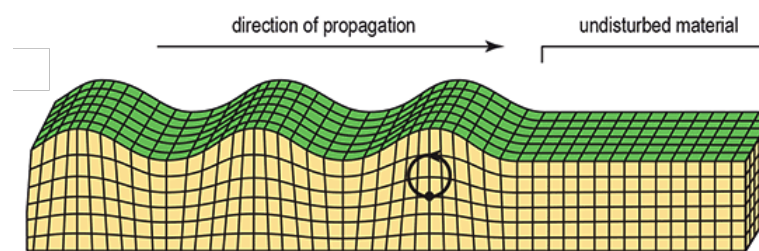
Figure 2.15: An image of a Rayleigh SAW. Figure adapted from [133], ©University of Kansas 2014.

SAWs are used most commonly in telecommunication devices operating at radio frequencies[121], including as filters and delay lines. Most surface acoustic wave devices consist of interdigitated electrodes (IDTs, see Figure 2.16) formed on the piezoelectric material surface aligned with the SAW wave propagation axis.

In the telecommunications industry, one of the IDT is connected to an input source, and the other IDT is connected to the rest of the electronic circuit. Since the IDTs are designed
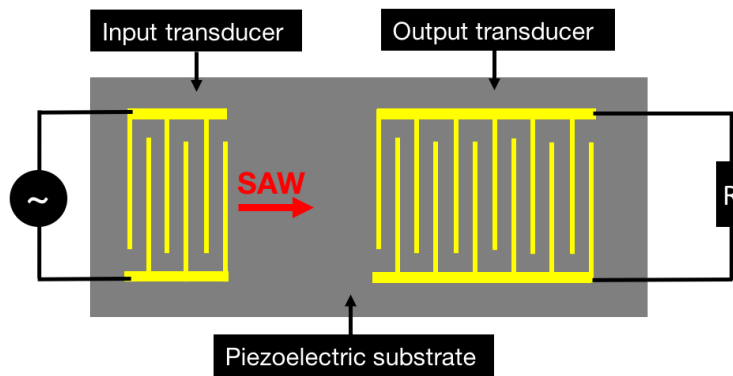
Figure 2.16: A schematic of a IDT setup used in the telecommunications industry.

to generate a SAW only at the fundamental frequency (along with a small bandwidth around the fundamental frequency), the applied signal can be filtered from the unwanted noise, which does not generate a SAW; this is the principle of the SAW filter.[121]

In the recent years, more focus has been given to utilising SAWs as sensors and tools for liquid manipulations. The use of surface acoustic waves as biosensors and particle/droplet manipulation devices is beyond the scope of this thesis. The reader can find more information in the overview reviews by Länge *et al.*[134], Fu *et al.*[135] and Jakubik[136]. There is more information on specific devices the reader can refer to:

- fluid mixing[137, 138],

- 1D particle alignment[139],

- 2D particle alignment[140],

- cell trapping and separation[141, 142, 55, 143, 144, 145, 57],

- liquid nebulisation[146, 147].

This work, however, focuses on the fluid pumping using SAWs, therefore the following sections will be devoted to review of work in this area.[148, 149, 124, 150].

The earliest work on SAW induced liquid pumping was performed by Girardo *et al.*, who utilised SAW induced fluid atomisation to advance the fluid front into a microfluidic channel, as seen in Figure 2.17.[150] The work performed was utilising lithium niobate (LiNbO$_3$) substrate using PDMS microfluidic channels, and the SAW frequency utilised in this work was 160 MHz with the S_{12} insertion loss of -40 dB. The operating principle of this pump is based on atomisation of the fluid front: once a sufficient amount of droplets land on the LiNbO$_3$ surface, they coalesce, and form the new, advanced fluid front.
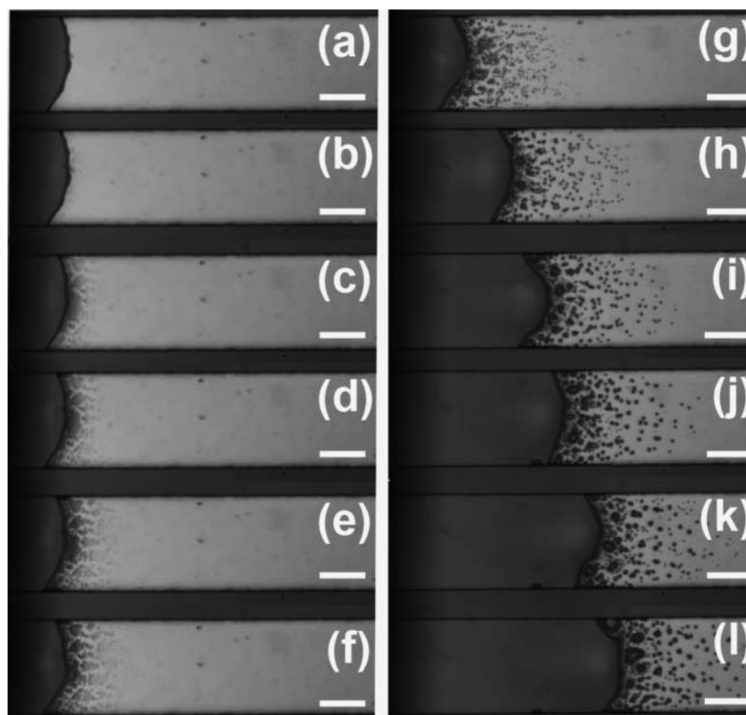
Figure 2.17: Advance of the liquid front in the presence of a SAW. The principle of operation of the pump described by Girardo *et al.* is based on the atomisation of the fluid front by the SAW. Time between (a) and (l) is 5.5s. Figure reproduced from [150] with permission from The Royal Society of Chemistry.

The subsequent work of the Pisignano group has been focused on multiplexing of the previously described pump. In a publication by Masini *et al.*, the group reports the use of the pump in a 6 x 6 matrix of microfluidic channels, showing the ability to direct the fluid

flow as necessary. An image of the multiplexed pump can be seen in Figure 2.18.[151]
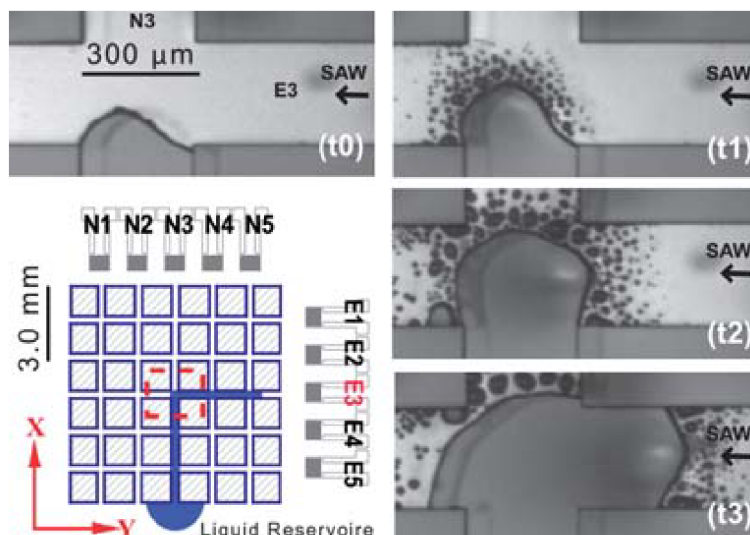
Figure 2.18: A multiplexed microfluidic pump system based on the pump by Girardo *et al.* Figure reproduced from [151] with permission from The Royal Society of Chemistry.

The main advantages of the pump described in publications [150] and [151] are the ability to operate the pump in a completely closed system (although the [150] had open-ended channels) and the independence of pump operation on the fluid composition, which means that fluids with different conductivities can be used (one of the fundamental limitations of the EO pump). On the other hand, each of the IDTs requires applied power of 27 - 33 dBm, which means high power consumption for volume flow rates limited to approximately 500 nl/min, which is relatively low compared to the membrane-based micropumps.

A publication by Tan *et al.* showed a continuous fluid flow induced by a SAW in a microfluidic channel.[152] The experimental setup consisted of an open-top channel which was directly engraved in the $LiNbO_3$ substrate, and the experimental setup can be seen in Figure 2.19. Tan *et al.* were studying the effect of the channel width to SAW wavelength ratio on the fluid velocity induced by the SAW, which was fixed at 200 µm wavelength.
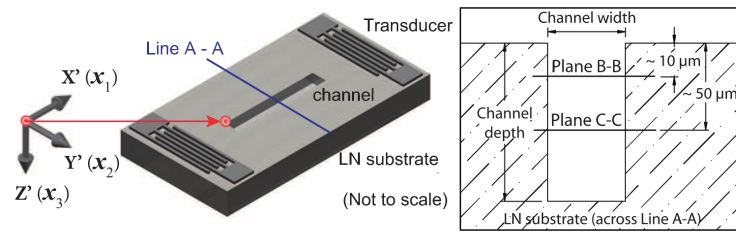
Figure 2.19: The experimental setup utilised by Tan *et al.* Figure reproduced from [152], ©2009 Europhysics Letters.

This work focuses on the fluid flow in two planes of the channel - the top plane, B-B, which is the one expected to interact most strongly with the SAW, and the C-C plane, in which the bulk flow effects could be studied. In the B-B plane Tan *et al.* demonstrated, that as long as the width of the channel is smaller than the wavelength of the SAW, the fluid flow is uniform, with speeds up to 10 mm/s, see Figure 2.20
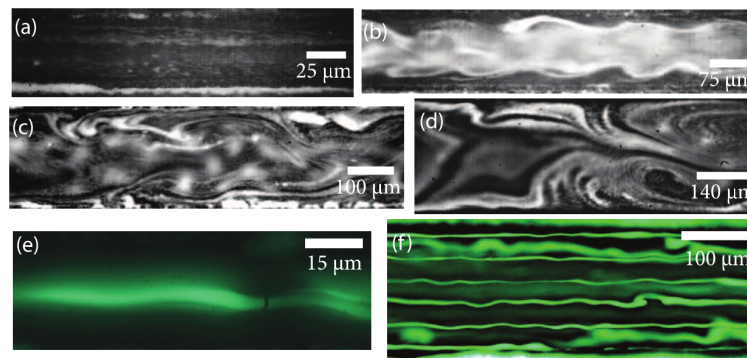
Figure 2.20: Images (a) - (d) show the fluid stream lines imaged with fluorescent particles for channel widths of 50, 150, 200 and 280 μm, respectively. SAW wavelength is fixed at 200 μm. Images (e) and (f) show the bulk fluid movement along C-C plane, as expected, the SAW is reflected into the main bulk volume of the fluid, where it causes standing waves, which causes particle alignments. Figure reproduced from [152], ©2009 Europhysics Letters.

However, as the width of the channel becomes larger than the SAW wavelength, the fluid flow becomes more chaotic. This is most likely because wider channels would support more SAW reflection positons, which then mix the flow. The authors confirm this using

simulations showing that with increasing time, more SAW energy is wasted as reflections which slow down the flow due to SAW-SAW interactions, and standing wave formation in the channel.[152, 145] A similar effect can be observed along C-C plane, where the fluid experiences SAW reflections that create standing waves resulting in particle capture.

An enclosed (i.e. the liquid is sealed in the channels) SAW pump has been demonstrated by Langelier *et al.*[124] Since PDMS is an elastic material with a low Young's modulus[153, 154], it will dampen SAW, which propagates underneath it as seen in Figure 2.21a.
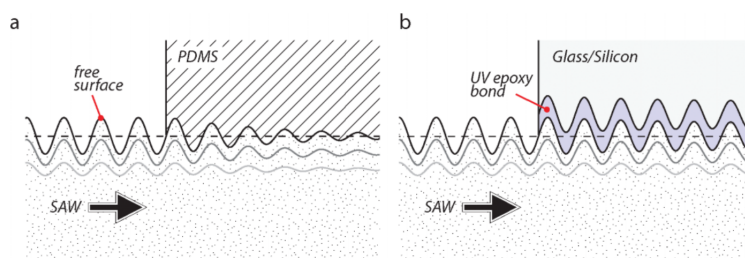
Figure 2.21: The schematic of SAW damping by materials like PDMS (a) and harder materials such as glass or silicon (b). Figure reproduced from [124] with permission from The Royal Society of Chemistry.

However, the piezoelectric and pyroelectric properties of $LiNbO_3$ complicate the fabrication process of microfluidic channels made from materials other than PDMS. Thus, at the heart of the publication by Langelier is a technique that allows bonding $LiNbO_3$ to glass substrates.[124] Materials with a higher Young's modulus will have a complex wave attenuation mechanism which combines attenuation and reflection, see Figure 2.21b for a schematic. The attenuation component for rigid materials is certainly lower than that of elastic materials (such as PDMS) coefficient thus increasing the transmitted energy. Langelier *et al.* have shown that the total attenuation of SAW is smaller in a glass block than that of equivalent length PDMS block, thus it must be concluded that the reflection losses of SAW are not as significant. As a consequence of using a more SAW-reflective material, the authors were able to improve the transmitted SAW energy by 20 dB

(comparing to the same channel geometry made using PDMS), which corresponds to 100 times higher transmitted energy. The authors assessed transmitted energy by measuring the S_{12} characteristics of different device designs using a network analyser.[124]

The SAW pump consisted of a loop-like channel design with a serpentine feature (see Figure 2.22a for a full schematic of the design and the subsequent sub-Figures for various microscope images of channels during SAW operation) connected to the main SAW interaction region seen in Figure 2.22e and 2.22f.
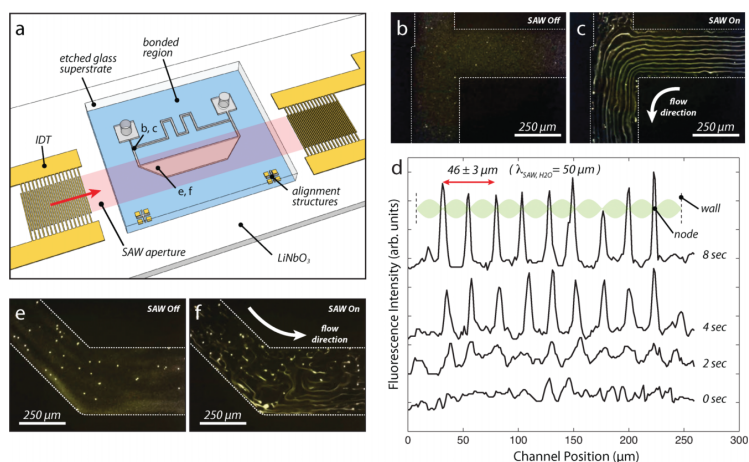
Figure 2.22: The experimental setup (a), particle aggregation regions (b,c) and observed flow (e,f) induced by the pump described by Langelier *et al.* Figure reproduced from [124] with permission from The Royal Society of Chemistry.

The channel width was increased directly in front of the SAW aperture for a larger volume of interaction with the SAW. The pump generates 46 Pa across the contour at applied power of 0.4 W. The pressure difference was calculated using the method described in Chapter 5. Figure 2.22c shows particle alignment away from the SAW aperture similarly to that observed by Tan *et al.* This can be attributed to the use of more rigid materials, which scatter and reflect the SAW leading to standing waves and therefore creating local higher and lower pressure regions where the tracer particles aggregate.

One of the key problems facing POC devices is requirement for any sample-handling

cartridges to be disposable to minimise cross-contamination between samples.[155, 156, 12] The price of any disposable unit must therefore be kept as low as possible. Consequently, a SAW micropump that is integrated into the disposable cartridge must be small and low cost, or the SAW micropump itself must be separate to the disposable cartridge, and therefore the fluid flow must be induced remotely. Schmid *et al.* have taken the latter approach and demonstrate a SAW pump that can produce fluid flow in a remote chip through the use of a thin water layer that couples the SAW from the LiNbO$_3$ to the glass superstrate, as shown in Figure 2.23.[148] As it can be seen, the
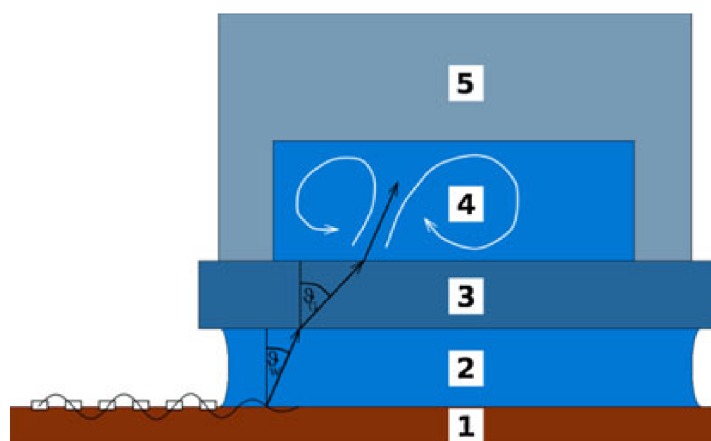
Figure 2.23: The experimental setup of the SAW pump described by Schmid *et al.* 1 - LiNbO$_3$ chip, 2 - water layer, 3 - glass chip, 4 - water in the microfluidic channel network, 5 - PDMS microfluidic channels. Figure reproduced from [148] with permission from Springer Nature.

microfluidic channels are made from PDMS and are bonded to a glass superstrate, forming a potentially disposable cartridge. The authors were able to produce pressure differences of up to 4.8 Pa and volume flow rates of up to 150 µl/min at an applied power of 0.8 W. The pressures generated by the pump are significantly lower than those reported by Langelier *et al.* due to the large channels used in the publication.[148] However, the volume flow rate is appropriate for POC device applications, which is more important in applications such as shuttle-flow PCR[157], in which the contour geometry is circular,

and the flow therefore does not experience high back-pressures.

The key issue with the SAW micropump described by Schmid *et al.* stems from the use of an intermediate medium, in this case water, to couple the SAW into the remote microfluidic channel. This introduces two key limitations: firstly the efficiency of the device is reduced as the SAW is damped both by the coupling water layer and when coupling through the glass layer. Secondly, such thin layer of water is prone to evaporate, thus severely limiting the operation time of such SAW device.[158] The authors also note that the presence of the water layer limits the operating power to 0.8 W. At higher powers, the vibrations of the water layer induced by the SAW are too strong, which prevents imaging of the microfluidic channels.[148]

Finally, using a similar approach to Schmid *et al.*[148], Dentry *et al.*[159] avoid using an intermediate glass layer and instead couple a SAW directly into an adjacent microfluidic channel via a water layer which is connected to an open aperture, as seen in Figure 2.24a.

The work described in [159] studies the effect of the SAW wavelength on the pressure and volume flow rate attained by the pumps by utilising a closed-loop (yet open channel) design seen in Figure 2.24b, as well as the created pressure difference in the setup seen in Figure 2.24c. The wavelengths used in the study are 16 and 32 µm, and the beam chamber length seen in Figure 2.25 is designed to attenuate the SAW amplitude to 1% of the initial value (i.e. ensuring that 99% is coupled into the overlaid fluid), which in turns changes the length of the racetrack (closed-loop) length. The maximum pressure attained between inlet and outlet ports was 15 Pa (measured by the setup seen in Figure 2.24c), and a maximum measured volume flow rate of 100 µl/min, both of these characteristics compare very well to the previously reviewed publications on SAW micropumps. However, it is important to note that the device is not capable of delivering 15 Pa pressure at 100 µl/min volume flow rate and *vica versa*. The highest delivered power shown by the authors is 8.8 Pa at 76 µl/min, implying that the efficiency of the device does not increase linearly with
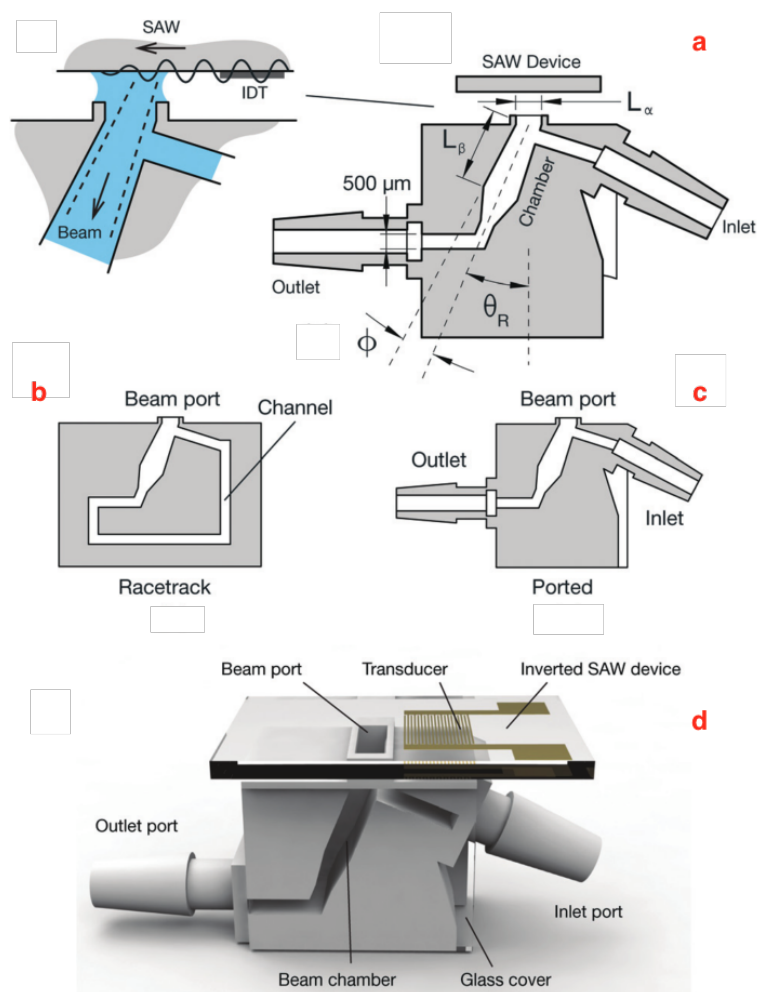
Figure 2.24: The experimental setup of the SAW pump described by Dentry *et al.* The setup (a) involves coupling the SAW from the substrate into the microfluidic channels through a droplet of water and open channel aperture. Authors have also explored various different pump designs, (b) a closed-loop device for measuring the pressure gradients generated by the SAW pump, (c) a ported device design directly connected to open atmosphere pressure. Figure 2.24d shows a 3D schematic of the setup seen in (a). Figure reproduced from [159] with permission from The Royal Society of Chemistry.
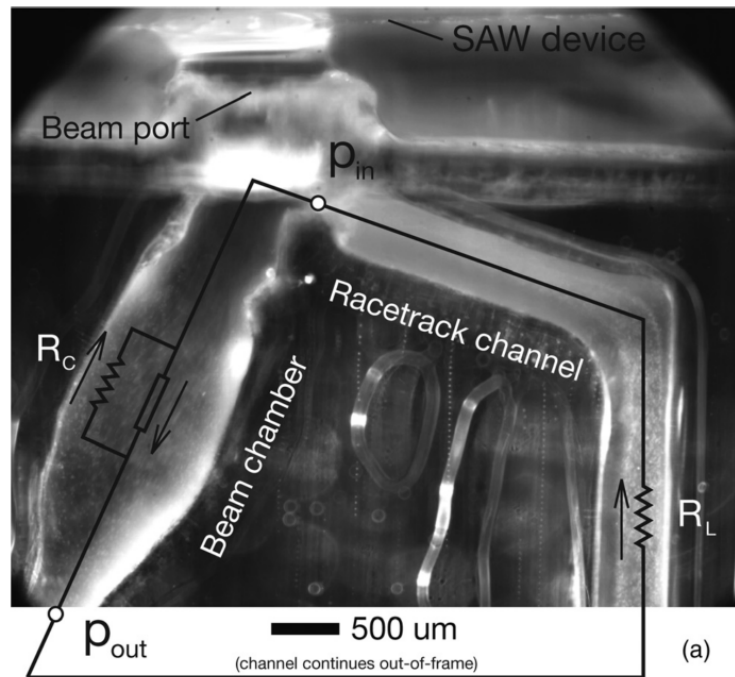
Figure 2.25: The image of the racetrack channel setup used to determine the volume flow rate of the devices, with the design features such as the beam port outlined. Figure reproduced from [159] with permission from The Royal Society of Chemistry.

applied power. The delivered power of the pump (calculated by the product of the pressure and volume flow rate) clearly shows that this is the best performing SAW micropump to date.

Dentry *et al.* stated that longer wavelength devices perform better than short wavelength devices. However, this result could be affected by the fact that beam port length was identical for both wavelength devices, meaning that the shorter wavelength devices would experience relatively higher SAW losses within the beam port, which do not contribute to liquid streaming.[159]

Notably, there are two main limitations inherent to the SAW micropump described by Dentry *et al.* Firstly, due to the channel design used by the authors, the delivered pressure by the pump increases exponentially with applied power. Therefore for peak performance

authors applied 2.2 W of RF power to the devices, which is very high for a POC device, while applying lower power to devices leads to poor performance. Secondly, the open droplet required to couple the SAW into the chamber presents a route for contamination. [160] Conversely, if the SAW micropump could be contained in a sealed device allowing re-use of the substrate, then the use of harsh chemicals (such as concentrated sodium hypochlorite solution) required to clean such a device for medical use, would be damaging the IDTs.[160]

2.7.1 Summary of acoustic force micropumps

Surface acoustic waves offer an excellent solution for POC micropumps. The surface acoustic wave micropumps have low operating voltage. They can be produced using standard microfabrication techniques and exhibit long lifetimes due to the small strains induced in the system. Surface acoustic wave micropump research was started by Pisignano group in the University of Salento, where the group has been focusing on atomisation of a fluid front, induced by surface acoustic waves, to transfer fluid along a channel. The atomisation process is used to pull a droplet towards the surface acoustic wave source by continuous coalescence of atomised droplets which have been expelled from the fluid front. The group showed the concept of such a pump in 2008 followed by a more complicated 2D channel system in 2010.

Another group heavily invested in the surface acoustic wave micropumps is run by Professor Yeo from Monash University. This group has published multiple papers on devices formed on lithium niobate substrates, ranging from simple straight channel geometries, to fully enclosed glass channel system, and finally to highly efficient 3D printed microfluidic channel networks. Yeo's group have shown the principle of the surface acoustic wave with the highest delivered power to date.

Finally, investigations into potentially disposable, microfluidic cartridge systems has been

performed by Professor Franke's group, now at the University of Glasgow. The group has shown that it is possible to couple surface acoustic waves into a remote set of microfluidic channels thus inducing fluid flow.

2.8   Motivation for SAW micropumps

Although the progress on SAW-driven microfluidic pumps has been considerable, the current work leaves a lot to be desired. On the one hand there are systems such as those described by Dentry *et al.*[159] and Girardo *et al.*[150], which use an open channel geometry to produce high-performance SAW micropumps capable of delivering the volume flow rates and associated high pressures required for use in POC devices, which may often contain low Reynolds number environments. However, the key issue with such systems is their open nature, which provides access points for contamination and which therefore makes such devices less likely to gain the approval of Health and Safety governing bodies, such as the Food and Drug Administration (FDA), as is required for any medical application.

On the other hand, fluid flow can be remotely induced by the SAW such as that by Schmid *et al.*[148] Such systems pass the criterion of the completely closed system (in terms of sample containment); however, these suffer from a need of coupling medium which transmits the SAW into the remote channels. The extra medium limits the delivered power of the device due associated dampening of the SAW, and furthermore, the operating time of such devices is limited by the evaporation rate of the coupling layer, which usually is on the order of few minutes. This constraint can rarely be met by the relatively slow PCR processes, which typically require tens of minutes in the quickest cases, thus such devices would be limited to simple and quick biosensor tests only.[157, 63, 88]

A shared limitation of the previously described SAW micropumps is the relatively high cost of the starting material. A 6" $LiNbO_3$ wafer currently costs on the order of 200, therefore even the smallest SAW-pumps will be too costly to be incorporated in the cheapest of applications. However, these pumps could still be used in more expensive POC tests that would benefit from scaling down the sample volume (and consequently the necessary reagent costs, which account for large part of the total unit cost) and

performing multiple tests on the same cartridge.[161] It is therefore important to put emphasis on integration that microfluidics, and SAW pumps in particular, offer to the various applications (such as multiplexed POC tests), and for some of these applications integration will indeed outweigh larger associated costs, thus paving the way for use of SAW micropumps.

Finally, limitation of the previously described SAW micropumps is their relatively high power consumption for a given pump output power. It is important to put the power consumption in perspective, Belgrader *et al.* report a typical portable PCR and readout unit, can operate continuously for 4 h, using a standard laptop battery.[162] This equates to about 15 W of continuous power draw given the standard battery operation voltage. In perspective, an actuator used in a syringe pump has a continuous power draw of about 10 W during operation.[77] This means that any actuator driven micropump, will have a significant effect on the battery-life of the instrument. Therefore, because of the high power consumption for the currently used micropumps, there still exists a need for a fully enclosed, high-performing SAW micropump with low power consumption, setting the scene for this thesis.

This concludes the literature review chapter, however, in order to summarise all the publications reviewed in this chapter, Table 2.1 has been made in the following page.

Table 2.1: A summary of micropumps presented in this Chapter.

Authors	Type of micropump	Applied electric field, kV/cm	Applied power, W	Fluid velocity, mm/s	Pressure gradient, kPa/m	Volume flow rate, μl/min	Relative substrate cost	Relative footprint
Pretorius et al. [86]	DC EO	2	-	0.2	~ 0.2[1]	9.4	High	Low
Theeuwes [87]	DC EO	0.16	-	-	~ 1.4[1]	0.083	High	Low
Paul et al. [89]	DC EO	12	-	-	~ 2.9[1]	100	High	Low
Snyder et al. [90]	DC EO	1300	-	-	~ $1 * 10^{-6}$[1]	10	High	Low
Yao et al. [91]	DC EO	1400	-	-	~ $6 * 10^{-6}$[1]	14	High	Low
Vajandar et al. [93]	DC EO	1	-	-	-	600	High	Low
Wang et al. [94]	DC EO	500	-	-	~ 0.0014[1]	300	High	Low
Brown et al. [97]	AC EO	0.25	-	0.075	-	0.039	High	Low
Studer et al. [98]	AC EO	0.12	-	0.5	-	0.06	High	Low
Lastochkin et al. [102]	AC EO	1.3	-	1	-	1.3	High	Low
Unger et al. [78]	Elastic Membrane	-	-	-	-	0.12	Low	High
Studer et al. [106]	Elastic Membrane	-	-	-	-	0.12	Low	High
Sundararajan et al. [108]	Elastic Membrane	-	-	-	-	0.4	Low	High
Grover et al. [109]	Elastic Membrane	-	-	-	-	14.4	Low	High
Lien et al. [15]	Elastic Membrane	-	-	-	-	100	Low	High
Lai et al. [111]	Elastic Membrane	-	-	-	-	6	Low	High
Bu et al. [117]	Piezoelectric Membrane	10	-	-	~ 3000	200	High	Low
Tracey et al. [118]	Piezoelectric Membrane	8.78	-	-	~ 1000	1600	High	Low
Johnston et al. [119]	Piezoelectric Membrane	8.78	-	-	~ 300	130	High	Low
Stehr et al. [120]	Piezoelectric Membrane	111	-	-	~ 2400	2000	High	Low
Pol et al. [113]	Elastic Membrane[2]	25	-	-	~ 200	34	Low	Low
Ou et al. [115]	Elastic Membrane[2]	-	1.75	-	-	0.1	Low	Low
Song et al. [116]	Elastic Membrane[2]	-	0.05	-	-	0.34	Low	Low
Girardo et al. [150]	SAW	-	1	2.6	-	0.01	High	Low
Langelier et al. [124]	SAW	-	0.4	-	~ 1.5	2.44	High	Low
Schmid et al. [148]	SAW	-	1	4.9	~ 0.11	150	High	Low
Dentry et al. [159]	SAW	-	2.2	-	~ 0.47	100	High	Low

[1]per 1 V/cm applied field
[2]thermopneumatic

Chapter 3

Theory of Microfluidics and Surface Acoustic Waves

At the heart of this thesis are two underlying technologies, which are combined to develop a micropump, these are - microfluidics and surface acoustic waves. This chapter will explain what each of these technologies are, giving a brief background and the underlying principles. Finally, the last section will describe how these two technologies interface with each other to allow the development of SAW micropump devices.

3.1 Microfluidics

Microfluidics is a field of engineering and physics that deals with precise control of fluid confined within a small volume, such as small droplet (pl to µl volume) or in fluidic channels with a small cross-section area (typically at least one dimension is below 1 mm). Recently, there has been a particular interest in using microfluidic devices for applications in biology and diagnostics due to a need to scale down sample volumes, which allows observing small populations of sample, such as cells for example.[29]

Microfluidics also exhibits interesting physical properties as a result of being confined within a small volume, for example, surface effects become dominant.[163]

For example, viscosity, diffusion, and surface tension become increasingly more important. Mixing occurs on slower timescales, whilst surface tension dominates at any interfaces due to a higher proportion of the material being at the interface (due to increased surface to volume ratios). Another example, is low momentum diffusion times defined as the time it takes for a system dissipate a disturbance, this timescale in microfluidic systems typically is on the order of few microseconds.

In terms of fluid flow, almost all microfluidic systems operate in either the creeping regime or the laminar flow regime. The quantification of flow regime is performed by assessing Reynolds number, which is a dimensionless quantity given by:

$$R_e = \frac{\rho v L}{\mu} \tag{3.1}$$

where ρ is the liquid density, v is the velocity of the liquid, L is a typical dimension, e.g. the diameter of the tube, the microfluidic channel height or hydraulic radius of the channels and μ is the viscosity of the liquid.[23] The Reynolds effectively describes the ratio of inertial forces to viscous forces. Typically, if the Reynolds number is below 2300 then the flow is most likely to be laminar, whereas if the Reynolds number is higher than 2600 the flow will most likely be completely turbulent. Values between these two limits describe situations in which the flow is transitioning from laminar to turbulent.[164] An example for a transitioning flow can be seen in Figure 3.1

A special case exists for Reynolds numbers which are less than unity. Such regime is regarded as creeping flow, also known as Stokes flow.[24] Stokes flow is a special case of laminar flow because of the very low contribution of inertial forces to the flow dynamics, physically a system operating under creeping flow conditions either has very small fluid velocities or high fluid viscosities. One of the most prominent physical implications of creeping regime is that the flows are reversible in direction and time. An example of

Figure 3.1: An example of a transitioning flow. The image shows the hot air rising (also called thermal plume in fluid dynamics) from a conventional candle captured using Schlieren photography. Figure from [165] ©2011 Taylor & Francis.

the time and direction reversibility in creeping flow regime is injection of dye solution in highly viscous liquid (such as glycerol or corn syrup) that is contained in a cylinder shaped vessel with another rotating rod in the middle, see Figure 3.2. Upon rotation of the middle rod, the dye will start to move due to shear movement. However, if the rod is rotated in the opposite direction, it is possible to "unmix" the dye. This shows the time and direction reversibility, which is a prominent characteristic of systems operating at creeping flow regime.[166]

Since inertial forces can effectively be ignored in creeping flow systems, the fluid motion equations governed by Navier-Stokes equation can be linearised and solved using differential equations.[24] The following section will be devoted to derivation of the Navier-Stokes equations, which govern the fluid flow in microfluidics, based on work by Professor Brian Kirby[24] and Professor Patrick Tabeling[22] in their respective books.

3.1.1 Navier-Stokes equations

Derivation of the Navier-Stokes equations relies on conservation of mass and momentum in steady-state fluid flow, along with a few key assumptions. The first assumption is that the liquid is incompressible and uniformly dense, this is a valid assumption for most Newtonian liquids.[22] The incompressible fluid assumption allows us to neglect any transformation of kinetic energy into internal energy (e.g. any increase in temperature).[24] This derivation considers a small sample volume in liquid (with volume V and surface S), so the following equations relate to this sample volume.

Conservation of mass is given by the surface integral of the mass flux across a control area:

$$\frac{\delta}{\delta t} \int_V \rho \, dV = - \int_S (\rho \vec{u}) \cdot \vec{n} \, dA \tag{3.2}$$

In Equation 3.2 $\vec{n}$ is the unit outward normal from surface S with a sample volume V and t is time, ρ is the fluid density and $\vec{u}$ is the fluid velocity. Since it was assumed that the

Figure 3.2: An example of a system with $R_e \ll 1$, where two injected dyes experience time reversibility. Image obtained from [167].

fluid is incompressible, the left hand side (LHS) of the Equation 3.2 is zero, and therefore becomes:

$$\nabla \cdot (\rho \vec{u}) = 0 \tag{3.3}$$

However, we know that $\nabla \rho = 0$ due to the assumption that the density of the fluid is uniform, therefore the conservation of mass can be simplified to:

$$\nabla \cdot \vec{u} = 0 \tag{3.4}$$

To incorporate conservation of momentum, Cauchy momentum equation is used[1]:

$$\rho \frac{\delta \vec{u}}{\delta t} + \rho \vec{u} \cdot \nabla \vec{u} = \nabla \vec{\sigma} + \sum f_i \tag{3.5}$$

The Cauchy momentum equation states that any changes in momentum $\rho \frac{\delta \vec{u}}{\delta t}$ can be calculated by taking into account the net momentum convection - $\rho \vec{u} \cdot \nabla \vec{u}$, the net force produced by stress applied to control surface area, $\nabla \vec{\sigma}$, and the sum of all the external forces per unit volume applied onto the control volume of sample - f_i. In Equation 3.5 $\vec{\sigma}$ is a general stress tensor and the f_i are the external forces acting on the liquid, e.g. gravitational forces or Coulomb forces. The Cauchy momentum equation is a general momentum conservation equation in a continuum. To obtain the Navier-Stokes equation, the general stress tensor has to be written in terms of fluid velocity and viscosity.[24] Therefore, by utilising the divergence of the general stress tensor[23] for an incompressible Newtonian fluid can be written as:

$$\nabla \cdot \sigma = -\nabla p + \nabla \tau \tag{3.6}$$

---

[1] N.B! Cauchy momentum equation is a derivation from the momentum conservation for a continuum. However, this requires utilisation of dyadic tensors and divergence theorem, which is beyond the scope of this thesis. For a full Cauchy momentum equation derivation see [24], along with the previously derived mass conservation equation.

As can be seen, Equation 3.6 introduces two new terms - p is a pressure term which arises from the stress perpendicular to the sample surface, and which is independent of the velocity of the fluid. The final term, τ, represents the viscous forces acting on the fluid. τ contains both tangental and normal components, and is therefore dependent on the velocity of the fluid.

In one dimension, the viscous forces can be related to the fluid velocity using:

$$\vec{\tau} = \mu \frac{\delta \vec{u}}{\delta y} \tag{3.7}$$

which, in a three dimensions, for an incompressible Newtonian fluid can be written as:

$$\vec{\tau} = \nabla \cdot \mu \nabla \vec{u} \tag{3.8}$$

In Equation 3.8 it was important to assume an incompressible Newtonian fluid, as the general term for stress is a 3x3 tensor relating to the strain via constant with value 2μ, where μ is the viscosity of liquid.

Assuming that the viscosity of the fluid is uniform and by combining of Equations 3.5, 3.6 and 3.8, we obtain:

$$\rho \frac{\delta \vec{u}}{\delta t} + \rho \vec{u} \cdot \nabla \vec{u} = -\nabla p + \mu \nabla^2 \vec{u} + f_i \tag{3.9}$$

In Equation 3.9 Equation 3.9 can be simplified even further, since in a unidirectional incompressible flow $u.\nabla u = 0$, the Equation 3.9 becomes:

$$\rho \frac{\delta \vec{u}}{\delta t} = -\nabla p + \mu \nabla^2 \vec{u} + f_i \tag{3.10}$$

3.1.2 Poiseuille flow

In order to derive a flow profile, we will begin by considering the simplest case of a microfluidic chip: a straight channel of a circular cross-section (see Figure 3.3).

The key assumptions for derivation of the flow profiles are:
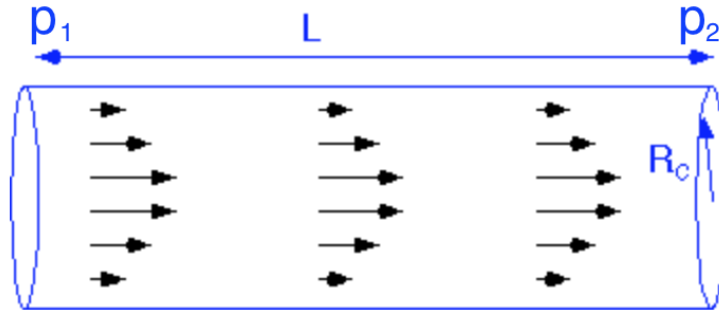
Figure 3.3: The schematic for fluid flow profile derivation in a straight channel of circular cross-section.

- The liquid in the system is a non-compressible Newtonian liquid, such that Equation 3.9 can be used.

- The fluid flow is unidirectional, thus the convective term can be ignored allowing use of Equation 3.10.

- There are no body forces acting on the liquid, e.g. no gravity, or the mass of the fluid is negligible.

- Only the steady state case is considered, so the fluid has no acceleration, i.e. $\frac{\delta u}{\delta t} = 0$.

- Only the two-dimensional case is considered, because of radial symmetry.

- Polar coordinate system is used with the zero point located in the middle of the cylinder.

Considering these assumptions, Equation 3.10, reduces to:

$$\nabla p = \mu \nabla^2 u \qquad (3.11)$$

Furthermore, since the only direction in which the velocity will change is radially from the channel centre. Equation 3.11 can be re-written as:

$$\frac{p_2 - p_1}{L} = \mu \frac{\delta^2 u}{\delta r^2} \qquad (3.12)$$

To solve Equation 3.12 and therefore to find the velocity profile, we must define our boundary conditions:

- We assume that there is a "no-slip" condition at the walls, meaning that the velocity at the walls is 0 and $u(r = R_c) = 0$.

- We also assume symmetry conditions: the velocity at given r value will always be the same, thus $\frac{\delta u}{\delta r}(r = 0) = 0$.

These two boundary conditions can be used to find the two integration constants required to solve Equation 3.12, resulting in a velocity profile given by:

$$u(r) = \frac{\Delta p}{4\mu L}(R_c^2 - r^2) \tag{3.13}$$

As it can be seen, the velocity of the fluid across the diameter of the channel will change parabolically. This is regarded as the Poiseuille flow profile. Previous publications show that the theory of fluid flow profile indeed matches with the experimental results, see Reference [168] as an example.

3.2 Surface Acoustic Waves

Surface acoustic waves (SAW) are mechanical waves that propagate along the surface of an elastic substrate and whose energy is confined to a region close to the substrate surface, usually no more than five wavelengths deep. The SAW propagates at a speed equal to its acoustic velocity within the material, and its amplitude decays exponentially into the substrate.[121] Table 3.1 shows acoustic velocities in air for common SAW device materials.

Table 3.1: Acoustic velocities for common SAW materials and their respective cuts.

Material	Cut	Propagation direction	Acoustic velocity (v_{SAW}), m/s
Lithium niobate	128° Y-cut	X	3982[169]
Lithium tantalate	42° Y-cut	X	4022[57]
Quartz	ST	X	3158[121]
Gallium arsenide	[100]	[011]	2864[121]

There are two main types of SAW:

- Shear-horizontal SAW (SH-SAW) - SH-SAWs exhibit a mechanical displacement within the plane of the substrate and normal to the wave propagation direction, i.e. they are a transverse wave. See Figure 3.4 for a schematic.

- Rayleigh SAW (RSAW) - RSAWs are a combination of transverse and longitudinal waves, meaning that the mechanical displacement of a RSAW occurs both perpendicular and parallel to the propagation direction of the wave. See Figure 3.5 for a schematic.

The following sections will, firstly, describe how to excite a SAW on a piezoelectric substrate and, secondly, derive the SAW propagation equation.
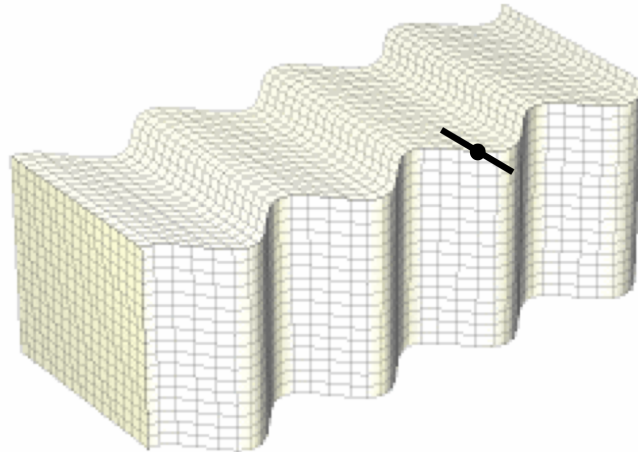
Figure 3.4: A schematic of the SH-SAW, the black line shows the in-plane movement of a fixed particle (black dot) in a SH-SAW. Image reprinted from [170] with permission from Elsevier.
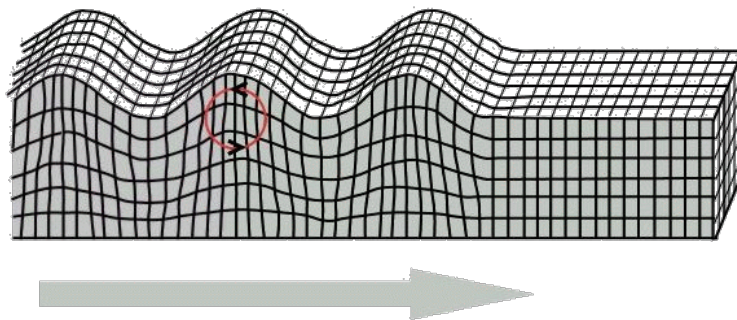
Figure 3.5: A schematic of a RSAW, note the red circle showing a region of both transversal and longitudinal nature of the wave. Image from [171], ©2015 Purdue University.

3.2.1 SAW excitation

This section focuses on the means of producing an electrically driven SAW within a piezoelectric material. On a piezoelectric material, SAWs are generated by applying an AC electric field to interdigitated electrodes (IDTs) formed on the substrate surface, see Figure 3.6. If the frequency of the AC field and the spacing between the IDTs is matched,

a SAW is generated.
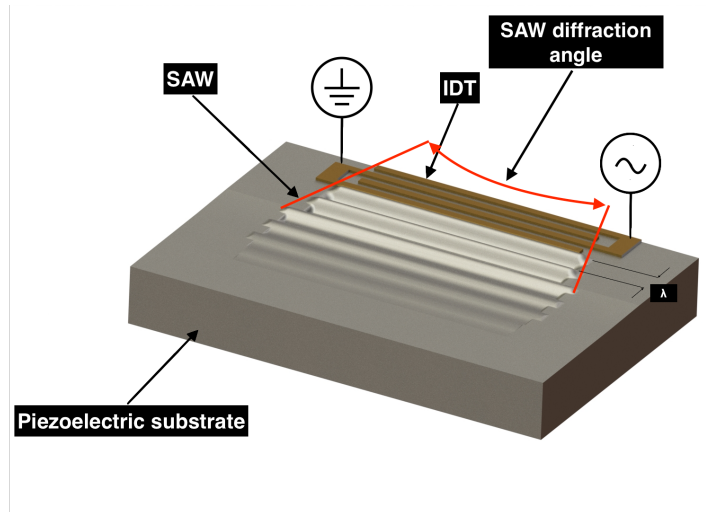
Figure 3.6: A schematic of IDTs in a typical setup, where one of the electrodes is grounded and an oscillating signal is applied to the other, thus generating a SAW.

The relationship between the acoustic velocity (v_{saw}) in the material, the AC electric field frequency (f) and the SAW wavelength (λ) is given by Equation 3.14:

$$v_{SAW} = f \cdot \lambda \tag{3.14}$$

Typically, the mark to space ratio (the ratio of the gap width to the electrode width) of the IDTs will be 1:1, thus the SAW wavelength would be four times the electrode width. However, there are alternative designs to the electrodes, some of which are made to produce unidirectional SAW devices, since a symmetric 1:1 electrode design (seen in Figure 3.6) produces equal amplitude SAWs propagating in both directions.[121, 145, 172] Although the insertion loss of a 1:1 mark to space ratio electrode design usually is slightly lower, it was utilised in this work due to simplicity of electrode fabrication process. Since the smallest SAW wavelength used in this work was 20 µm, the smallest electrode width was 5 µm. For designs that use alternative mark to space ratio (such as split electrode or single phase unidirectional transducer (SPUDT)), the minimum feature size can be as little as 1/8 of wavelength, which significantly complicates the

fabrication protocol.[173] Also, Oh *et al.* mention that the utilisation of piezoelectric with high coupling coefficient (such as LiNbO$_3$), can reduce some of the insertion losses experienced by IDTs with 1:1 mark to space ratio.[173]

3.2.2 SAW propagation description

In order to describe a SAW propagating along a piezoelectric substrate, we need to derive a wave equation that contains information about the mechanical stress and electrical displacement of the crystal caused by this wave. To do this, the basic equations for elastic compressional and shear waves will be combined with equations describing piezoelectricity. Derivations are obtained by following the methods in [174] and [121].

Description of elastic waves

To make notation of subscripts easier, the Einstein summation will be used, and all diagrams and equations are described for an orthogonal Cartesian coordinate system. **Stress** (T) is defined as the force exerted per unit area of material.[121] Stress is described by the direction of the force and the normal of the area onto which the force is exerted.

$$T_{xy} = \frac{F_x}{A_y} \tag{3.15}$$

For a simple compressional wave, force and area are in the same direction as the wave propagation. If the direction of force does lie along the area normal, a shear stress is induced. **Strain** (S) is defined as the fractional change of length, i.e. the change of length over original length (L). Strain also can be described in terms of physical particle displacement (u) due to the wave, as the rate-of-change of displacement in the direction of wave propagation.

$$S = \frac{\Delta L}{L} = \frac{\partial u}{\partial z} \tag{3.16}$$

Label	subscripts
1	xx
2	yy
3	zz
4	yz,zy
5	xz,zx
6	xy,yx

Table 3.2: Subscript abbreviation

For small strains, the stress and strain can be related using Hooke's law $F = -kx$.

$$T_{zz} = c_{zzzz}S_{zz} \tag{3.17}$$

Since both stress and strain have two subscripts for every direction, the elasticity tensor c_{zzzz} (i.e. the Young's modulus, a constant that relates stress to strain) has four subscripts. To simplify the notation, we can replace double subscripts with a single subscript, according to Table 1:

Since each of the subscripts can have a value between 1 and 6, the elasticity tensor consists of 36 components. Subscripts 1-3 relate to compressional effects, while 4 to 6 relate to shear effects; thus the elasticity tensor can be reduced to two 3x3 matrices, one relating to compressional effects and another for shearing effects.[121] Therefore, stress and strain can be related by:

$$
\begin{vmatrix} T_1 \\ T_2 \\ T_3 \\ T_4 \\ T_5 \\ T_6 \end{vmatrix}
=
\begin{vmatrix}
c_{11} & c_{12} & c_{13} & c_{14} & c_{15} & c_{16} \\
c_{12} & c_{22} & c_{23} & c_{24} & c_{25} & c_{26} \\
c_{13} & c_{23} & c_{33} & c_{34} & c_{35} & c_{36} \\
c_{14} & c_{24} & c_{34} & c_{44} & c_{45} & c_{46} \\
c_{15} & c_{25} & c_{35} & c_{45} & c_{55} & c_{56} \\
c_{16} & c_{26} & c_{36} & c_{46} & c_{56} & c_{66}
\end{vmatrix}
\cdot
\begin{vmatrix} S_1 \\ S_2 \\ S_3 \\ S_4 \\ S_5 \\ S_6 \end{vmatrix}
\tag{3.18}
$$

Finally, it is possible to describe the propagation of the wave in terms of Newton's second law ($F = ma$). Equation 3.16 showed that strain can be related to the particle displacement direction; similarly stress can be related to particle displacement, u, via:

$$\nabla T = \rho_s \frac{\partial^2 u}{\partial t^2}$$

(3.19)

where ρ_s is the density of solid, and t is the time. Consequently, the force can be obtained from:

$$F = \frac{\partial T}{\partial x}$$

(3.20)

Therefore the particle displacement in terms of time and distance can be written as:

$$\frac{\partial T_{xy}}{\partial x} = \rho_s \frac{\partial^2 U_x}{\partial t^2}$$

(3.21)

Which is the full wave equation for an elastic wave.

Propagation of waves in piezoelectric materials

To describe the propagation of acoustic wave in piezoelectric material, we will use unit vectors i, j, k in the direction of x, y and z axes of Cartesian coordinate system, respectively. The three unit vectors therefores can be expressed as:

$$i = \begin{bmatrix} 1 \\ 0 \\ 0 \end{bmatrix}, j = \begin{bmatrix} 0 \\ 1 \\ 0 \end{bmatrix}, k = \begin{bmatrix} 0 \\ 0 \\ 1 \end{bmatrix}$$

(3.22)

A piezoelectric material has a crystal structure in which the positive and negative charge centres are not in the same place. The unit cell is therefore said to lack inversion symmetry (Figure 3.7). Therefore, application of a mechanical stress to the crystal structure will induce a dipole within that structure. Equivalently, an application of electric field to the unit cell will cause a mechanical deformation.[121] Consequently, applying a voltage to alternating fingers of an IDT produces an alternating pattern of mechanical expansion and

compression due to the piezoelectric effect. These regions oscillate in time due to the alternating direction of electric field, and this gets converted into a wave. To derive a full
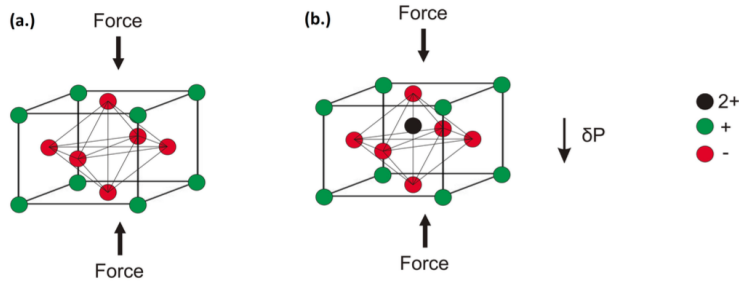
Figure 3.7: (a) A unit cell with inversion symmetry and (b) a unit cell without inversion symmetry. Image from [175] ©University of Leeds.

wave expression for a travelling wave in a piezoelectric medium, we need to define the electric displacement (D) in terms of the dielectric constant (ϵ) and electric field (E).

$$D_i = \epsilon_{ij} E_j \tag{3.23}$$

Earlier it was shown that strain can be written in terms of the particle displacement, therefore the stress-strain relationship can be written as:

$$T_{ij} = C_{ijkl} \frac{\partial U_l}{\partial k} \tag{3.24}$$

Which allows the wave equation to be rewritten as:

$$C_{ijkl} \frac{\partial U_l}{\partial k \partial j} = \rho \frac{\partial^2 U_i}{\partial t^2} \tag{3.25}$$

However, within a piezoelectric medium, some of the mechanical energy of the travelling wave is converted back into electrical energy and correspondingly, some of the electric field developed in the piezoelectric material will be converted back into mechanical energy, thus the stress-strain relationship can be written in terms of piezoelectric tensor(e_{ikl}):

$$T_{ij} = C_{ijkl} S_{kl} - e_{ikl} E_j \tag{3.26}$$

And the electric displacement with respect to the electric field becomes:

$$D_i = e_{ikl}S_{kl} + \epsilon_{ik}E_k \tag{3.27}$$

The electric field can be written in terms of the potential[176]:

$$E = -\nabla\phi \tag{3.28}$$

Finally, substituting Equation 3.28 for E in Equations 3.27 and 3.26 and combining it with Equation 3.25, a system of full coupled wave equations are obtained:

$$\rho\frac{\partial^2 U_i}{\partial t^2} - C_{ijkl}\frac{\partial U_l}{\partial k\partial j} - e_{ikl}\frac{\partial^2 \phi}{\partial k\partial l} = 0 \tag{3.29}$$

$$e_{ikl}\frac{\partial^2 U_l}{\partial i\partial k} - \epsilon_{ik}\frac{\partial^2 \phi}{\partial k\partial i} = 0 \tag{3.30}$$

3.3   SAW device intergration with microfluidics

When a travelling SAW interacts with liquid it is mechanically dampened by the liquid through a leaky-SAW mechanism. Considering the simplest case of a liquid droplet positioned on a piezoelectric surface in air, a SAW will be diffracted as it enters the liquid because the velocity of sound in the liquid is different to that of air[177], as shown in Figure 3.8. The SAW within the droplet is attenuated by the liquid through viscous dissipation which, consequently, creates an internal fluid flow within the droplet. An in-depth theoretical treatment of SAW coupling mechanism and a description of fluid flow generated in the liquid has been studied by Vanneste and Buhler.[179] Thorough mathematical derivation of the fluid flow contributions and stream function derivations (both in an open droplet and in a channel) can be found in [179] and are beyond the scope of this work, therefore only the main concepts and results found by authors will be presented here. Briefly, the "stream function" is a parameter that describes how the liquid velocity changes along x and y axes in a 2D system. The stream function can be related to streamlines, which are a family of curves representing fluid velocity in the liquid.
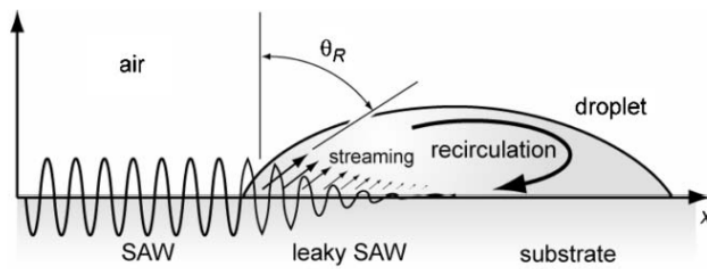
Figure 3.8: Schematic of travelling SAW coupling to liquid droplet through leaky SAW. Image reproduced from [178] with permission from The Royal Society of Chemistry.

As the SAW couples into the liquid, it transfers energy into the liquid and generates multiple types of fluid flow: this process is known as acoustic streaming.[180, 181]

Acoustic streaming consists of two main components - *interior streaming* and *boundary streaming*. Interior streaming is associated with vortices generated by the SAW in the bulk of the liquid, while boundary streaming describes the vortices generated within thin boundary layers. Navier-Stokes equations describe the mean flow of the liquid bulk, whereas Eulerian and Lagrangian models are used to describe vortices generated within the thin boundary layers. Figure 3.9 shows the 2D damping of a 53- μm-wavelength SAW as it couples into the water at $x = 0$. The y-axis shows the normal velocity of solid-liquid interface. In order to evaluate the flow induced in the liquid, the authors evaluate the stream function of the flow in 2D by calculating the volume flux through series of curves with respect to x,y coordinates and t.[179] As mentioned earlier, there are two main contributions to the acoustic flow. Figure 3.10 shows a comparison between stream functions calculated by considering only the mean flow (interior streaming, Figure 3.10a) within a 1 mm thick water layer, and those calculated by considering both interior and boundary streaming (Figure 3.10b). From Figure 3.10 predicts that the SAW generates an internal vortex within the liquid, which was subsequently observed experimentally by several groups.[178, 182, 183] When the applied SAW power is sufficiently high, whole droplets can be actuated using this method.[64, 184] Despite the applications of droplet
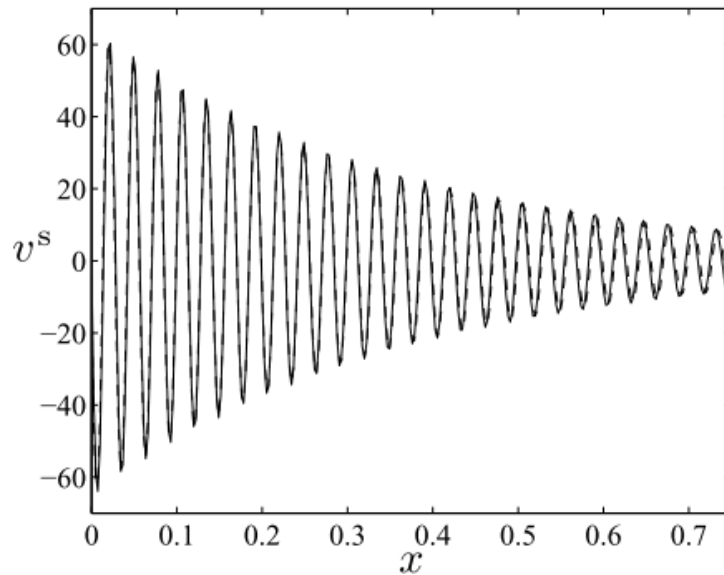
Figure 3.9: Normal velocity of surface (in mm/s) plotted versus distance in the liquid, at $x = 0$ SAW enters the liquid. Image reproduced from [179] with permission from The Royal Society.
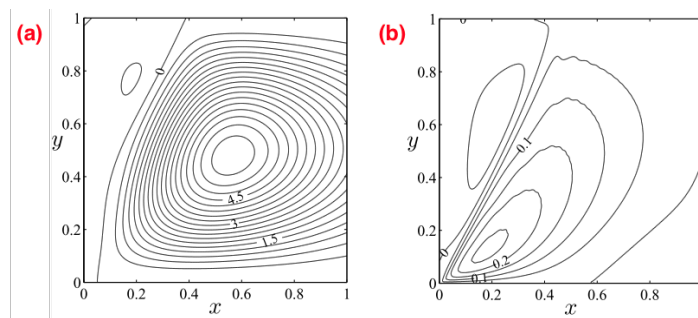
Figure 3.10: Calculations of the stream functions within a fluid with respect to position in channel (y is the height, x is the length, both in mm) in water performed by considering (a) only interior streaming, and (b)both interior and boundary acoustic streaming. Contour labels have units of (a) mm^2/s and (b)$10^{-3}mm^2/s$ for RHS. Figure reproduced from [179] with permission from The Royal Society.

actuation in the field of digital microfluidics, there remains a need for actuating liquid within microfluidic channels with height on the order of 100s of μm. Because of this, Vanneste and Buhler have evaluated the stream function in a 100 μm high fluid layer as

shown in Figure 3.11, which shows that, as the liquid is confined to a thinner region (for example, within a microfluidic channel), the formation of vortices within the liquid is somewhat suppressed in favour of generating a flow in the direction of SAW propagation. This can be explained as follows: since the height of the fluid is now comparable to the wavelength of the SAW, the boundary layer fluid flow (governed by Eulerian and Lagrangian flows) is as large as the interior flow. The SAW generates a flow in the boundary layers, which causes the interior of the liquid (which takes up less volume now, since the fluid is confined) to move as well. Therefore, the stream function has smaller vertical components and a bigger flow component.[179]
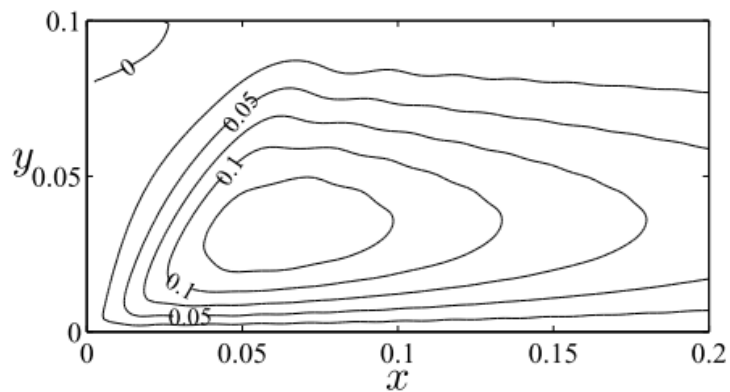
Figure 3.11: Stream function of water with respect to position in channel (y - height, x - length, both in mm). Calculations were performed by considering both internal and boundary streaming. Figure reproduced from [179] with permission from The Royal Society.

Chapter 4

Materials and Methods

This Chapter discusses the fabrication of the SAW devices and the microfluidic channels and explains the device assembly procedure. Further, the electrical assemblies used to drive devices and to characterise device performance will be discussed. Finally, a section is devoted to the protocols used to prepare tracer particles for fluid flow measurements and the associated particle image velocimetry protocols developed in this thesis.

4.1 SAW device fabrication

SAW devices were fabricated using 3" 128° Y-cut, x-propagating "black" $LiNbO_3$ wafers supplied by *PM Optics, MA*. In this sense, "black" refers to the fact that dopants were added to the $LiNbO_3$ during growth, in order to decrease the pyroelectric effect which otherwise can complicate fabrication. S1813 (*Shipley, MA*) photoresist was spun at 5000 RPM on the wafers before cutting them into chips using a 0.4 mm thick resin blade on a *LoadPoint Micrace 66* wafer saw. The chip dimensions varied according to each individual experiments.

IDTs were fabricated using a sacrificial layer photoresist process, also known as lift-off

resist (LOR) process. Before spinning on LOR (*Shipley, MA*), chips were cleaned by leaving them in "piranha solution" consisting of sulphuric acid (H_2SO_4) and hydrogen peroxide (H_2O_2) in a 7:3 ratio for 10 min, followed by a rinse with DI water, and blow-drying using N_2 gas. Following this, chips were cleaned in an O_2 asher at 50W power for 5 min. Finally, a dehydration bake was performed at 185°C (the temperature was ramped from 50°C to 185°C for a total of 3 min to avoid electrostatic discharge) for 10 min. Ramping was performed for all resist coating steps as it was noticed that there is some observable pyroelectric effect even in the "black" lithium niobate ($LiNbO_3$) chips, which causes an electric discharge if the chips are put on a high-temperature surface without appropriate precautions. Although, not all electrical discharge resulted in observable degradation of the material surface, subsequent device characterisation (described in Section 4.4) revealed significantly worse performance, which suggests some structural damage occurs within the material during such electric discharge.

LOR resist was spun onto the chips at 4000 RPM for 45 s, resulting in a 400 nm thick LOR film. The LOR was baked at 185°C for 3 min; the temperature was ramped in the same manner as described earlier. After baking, the chips were allowed to cool down for 3 min before spin coating S1813(*Shipley, MA*) photoresist at 4500 RPM for 45 s. The photoresist was soft-baked at 115°C for 3 min, again ramping the temperature from 50°C to 115°C, over a minute. The measured S1813 film thickness was 1.3 µm.

The photoresist was exposed through a Soda Lime glass mask (*Delta Mask, Netherlands*), at an exposure dose between 70 - 90 mJ/cm^2. The exposed resist was then developed in MF-319 solution for 60 - 70 s depending on the feature size. Typically, it is sufficient to develop S1813 for about 40 - 45 s, however, extra time was taken to create an undercut in the underlying LOR. The LOR is not photosensitive, but it is isotropically etched when exposed to MF-319, allowing an undercut to be achieved after pro-longed development times. After development, devices were rinsed in DI water and blow-dried using N_2 gas. Figure 4.1 shows an example of 100 µm wavelength device imaged using a 50x

objective after resist development, but prior to metal deposition. It can be seen that the line roughness is negligible in comparison to the feature size.
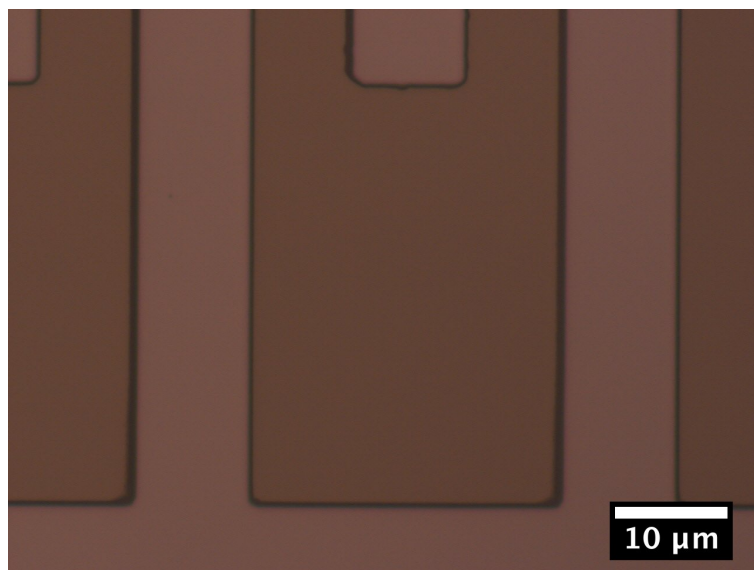
Figure 4.1: A microscope image of a 100 μm wavelength device after resist exposure and development, taken through a 50x objective.

Finally, before loading chips into the evaporator, they were cleaned in an O_2 asher at 50 W power for 1 min to remove any residual resist from the exposed features. A 5 nm Ti layer followed by 50 nm Au layer was deposited using electron beam evaporation, at a typical pressure of 4 x 10^{-7} mbar, ensuring low defect-density in the deposited film.

Metal lift-off was performed in 1165 developer that was heated to 80°C, and the samples were left in the developer for 1 h. Once the metal film had lifted off, chips were rinsed in IPA, blow-dried with N_2, spun-coat with S1813 photoresist (coated and baked using the same parameters as previously described) to protect the IDTs and stored until required. Note that no sonication was used to ensure that the deposited electrodes were not lifted-off from the surface.

4.2   Microfluidic channel fabrication

Master moulds for PDMS fluidic channels were fabricated using a stereolithographic 3D printer (*Miicraft, Taiwan*). The 3D printer resin used was HT Miicraft, supplied by *Spot-A materials, Spain*. The channel width and height in the planar sections was 500 μm and 100 μm, respectively.

Since 3D printer resin is based on acrylic chemistry, PDMS will not cure when in direct contact with master mould. The moulds were therefore coated with a thin fluorocarbon layer by CHF_3 deposition in an RIE chamber for 2 min at 50 W power. This fluorocarbon coating makes the surface highly hydrophobic[185] which has two main effects: firstly, the surface of the master moulds is passivated, allowing cast PDMS to cure completely; secondly, the hydrophobic surface aids peeling off the PDMS from the moulds, once set. [185, 186]

PDMS itself was made using SYLGARD-184 silicone elastomer kit supplied by *Dow Corning, USA*, by mixing base and curing agent in a 10:1 weight to weight ratio. PDMS was de-gassed for 20 min at 5 mbar pressure before pouring it over the moulds and baking on a hot-plate for 1 h at 70ºC. Once cured, the PDMS was peeled from the moulds, trimmed into the required dimensions, sonicated in IPA for 5 min and blow-dried using N_2 gas before storing until required.

Three-dimensional microfluidic channels were fabricated by combining the protocol named ESCARGOT (term coined by Saggiomo and Velders[187]) with the previously described use of stereolithography 3D printer for master mould fabrication.[186] Resin-based 3D printers are capable of printing suspended features with sub-500 μm dimensions. However, after PDMS casting and curing around such a 3D strucuture, the difficulty lies with removal of the mould.[186] Chan *et al.* describes a protocol of direct-one step moulding of three-dimensional microfluidic channels.[185] This protocol relies on ripping out the three-dimensional master mould from partially-cured PDMS block,

which will self-repair upon further curing without the master mould. Although the paper states yield of more than 80%, replication of the protocol was unsuccessful during this work, with a yield below 10% (N=15).

Consequently, there was a need for a protocol that allowed three-dimensional microfluidic channel fabrication in a single PDMS cast. A single-cast process was necessary because, in order to characterise microfluidic pumps, fluorescent particle image velocimetry (PIV) was required. However, two-layer multi-layer PDMS structures have been shown to result in poor imaging because of diffraction at the layer interface.[60, 78] The protocol developed here consisted of 3D printing the planar microfluidic channel master mould along with a vertical pillar (grey areas in the Figure 4.2), followed by temporarily adhering an acrylonitrile butadiene styrene rod (ABS, common fused deposition modelling printing plastic) to the top of the pillars using a few drops of acetone.
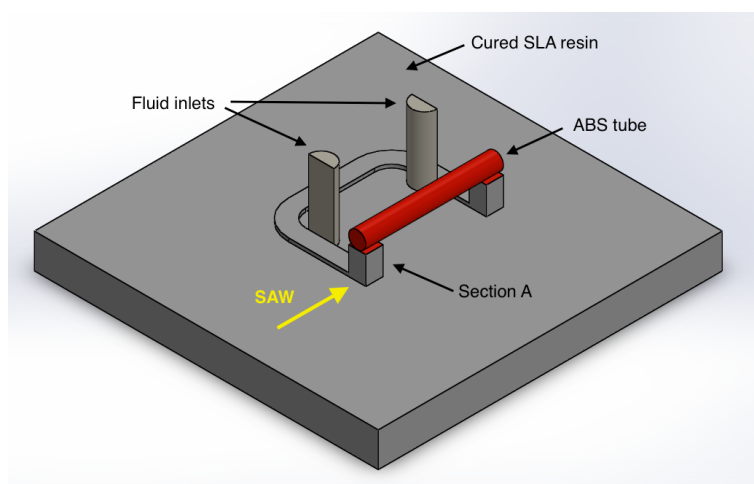
Figure 4.2: A schematic of a three dimensional microfluidic channel mould, suitable for fabrication of a closed microfluidic channel a single PDMS cast.

The master moulds were then baked for 30 minutes at 65°C in an oven to evaporate any residual acetone from the ABS rods. The degassed PDMS was next poured over the moulds, taking care to ensure that no air bubbles were introduced, particularly at the overhanging ABS structures. PDMS was then cured as described previously. Once

cured, the PDMS blocks were carefully peeled out of the master moulds. Since ABS does not adhere well to the acrylic resin the ABS will easily broke away from the acrylic master mould and remained embedded within the PDMS. The PDMS block complete with embedded ABS rod was sonicated in acetone for 30 minutes dissolving the ABS. Residual acetone was then removed from the PDMS by baking in the oven at 65°C for 30 min to prevent solvent-induced swelling of the PDMS.[188]

4.3   Chip assembly

The fabricated PDMS channels were bonded to the IDT-containing chips using an oxygen plasma bonding process.[78, 144, 189] Firstly, the $LiNbO_3$ chips were placed in acetone beaker for 5 min to strip the photoresist that was protecting the IDTs. Then both the PDMS block and $LiNbO_3$ substrates were rinsed with IPA and dried with N_2. Upon drying, both PDMS and $LiNbO_3$ chips were placed in UVO cleaner (Jelight Company, Model 42) for 5 min, which creates dangling -OH groups on the material surfaces. The process bonding using an oxygen treatment of the surfaces followed by immediate contact between the surfaces is referred as the plasma bonding, made popular by Whitesides group.[114, 39] After UVO exposure, the samples were pressed together for 1 min and then placed on a hot plate for 20 min at 70°C with a light weight (< 50 g) on top of the PDMS in order to finalise the plasma bonding process.[190]

Once the $LiNbO_3$ and PDMS were bonded, the sample was glued onto an in-house made printed circuit board (PCB) using a thermal epoxy glue (Electrolube TBS20S). The electrical connections between the PCB and the SAW device were made using a gold wire-bonder. Finally, an SMA connector was soldered onto the PCB to allow electrical connections between the operating equipment and the electrical chips.

During experiments, the devices were mounted onto a 40 x 40 x 10 mm^3 brass block, which was used as a heatsink. The Figure 4.3 shows a fully assembled chip glued onto the

PCB. The middle section of the PCB consists of multiple, plated vias, which are connected to the ground plane and provide a better thermal conductivity to the PCB. This setup was designed to keep the chip below 300 K when driven using 3 W electrical input, which is the load required for experiments described in Chapter 7 which utilise three individual IDTs per device, each powered by 1 W electrical power. The absolute maximum heat load therefore corresponds to the unlikely scenario of all of the input electrical power being converted directly into heat.
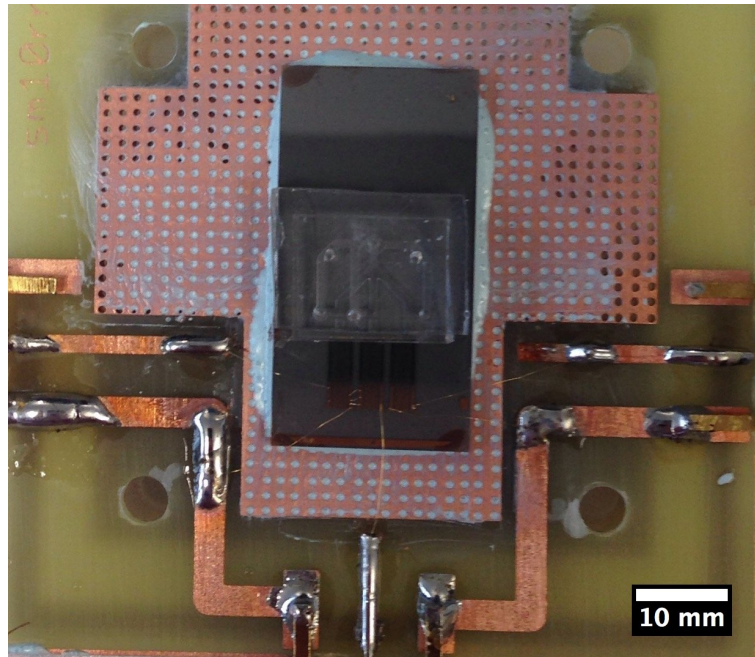
Figure 4.3: A fully assembled chip with the LiNbO$_3$ substrate and PDMS channels glued onto the PCB.

4.4 Electrical characterisation

In order to understand the following discussion, a brief introduction to scattering parameters (S-parameters) is necessary. Scattering parameters describe the steady state behaviour of an electrical system under a small, continuous electrical signal input. The

system is assumed to be a black box (i.e. the internal features are unknown) and has multiple ports, typically either one or two. The scattering parameters describe the relationship between the incident and reflected waves. An incident wave is a wave that passes through the system via inlet and outlet ports, and a reflected wave is a wave that is reflected back to the inlet port. Figure 4.4 shows the incident (a) and reflected (b) waves in a two port system.

Figure 4.4: A schematic of incident (a) and reflected (b) waves in a two port system.

The relationship between incident and reflected waves therefore can be written:

$$\begin{pmatrix} b_1 \\ b_2 \end{pmatrix} = \begin{pmatrix} S_{11} & S_{12} \\ S_{21} & S_{22} \end{pmatrix} \begin{pmatrix} a_1 \\ a_2 \end{pmatrix} \tag{4.1}$$

Parameters S_{11} and S_{22} describe the reflected signal from the black box system, called voltage reflection coefficient. The amplitude of S_{12} and S_{21} parameters describe the insertion loss of the device, i.e. the loss of signal induced by the black box between two ports with the same reference. Insertion loss allows to characterise the efficiency of the device, and is a crucial parameter for SAW device quantification as it gives the fundamental frequency of the device as well allows to calculate the SAW power produced by the SAW device.

All the devices were characterised using an Agilent 8753E S-parameter Network Analyser in a single port setup, using RF coaxial cables rated up to 3 GHz. The measured scattering parameter data were analysed using Microwave office and Origin Pro 9.0 software packages. Prior the S-parameter analysis the solder joints of the devices were

tested with a multimeter to ensure a good connection between the network analyser and the LiNbO$_3$ chip.

To measure the S_{12} parameters, the devices were measured on the Network Analyser in a two-port setup, which combines the magnitude and phase readings into a single output readout.

4.5 Electronic experimental setup

Chapters 5 and 6 utilise a setup with a single power input. The signal, generated using a signal generator (2022E, *Marconi Instruments, UK*), was fed into *Minicircuits (NY, USA)* ZHL-1-2W+ amplifier capable of producing up to 2 W output power. The amplifier was biased at 24 V using a DC source (E3620A, *Agilent Technologies, CA, USA*)

Chapter 7 requires the capability to individually address each of three channels used for fluidic pumping. This was not possible with the setup utilised in Chapters 5 and 6, and therefore a customised setup was built, which is as follows. The signal generation was based on *Analog Devices (MA, USA)* AD9959 evaluation board. The AD9959 is a chip consisting of four direct digital synthesiser cores, capable of producing up to four different frequency signals. Each core can be individually addressed using the evaluation board and a custom Python script (courtesy of *Mr Dominic Platt*) powered by a Raspberry Pi 3 computer.

Each signal generated by the AD9959 board was amplified using a custom-made RF amplifier, which consisted of two sequential RF gain blocks, each providing fixed signal amplification. Figure in Appendix A(a) shows a schematic of the custom RF amplifiers, and the resultant PCB design is shown in Appendix A (b). Briefly, initial signal amplification was performed by a *Hittite Microwave Corporation (MA, USA)* HMC481ST89 chip, which produces 19 dBm (P1dB) output (P1dB compression point

indicates the power level that causes the gain to drop by 1 dB from its small signal value, where the amplifier is in the linear gain mode). The final amplification (up to 30 dBm) was performed using a *Macom Technology solutions (MA, USA)* MAAM-010617 chip, capable of 31 dBm output (P1dB) point. Both of the gain blocks were connected in series to provide sequential signal amplification. The remaining of the circuit elements seen in Figure A.2 are used to provide impedance matching for the input signal, except for the capacitors on the signal line which filter any DC noise. Figure 4.5 shows the input signal versus the measured output signal of each of the three amplifiers made for this purpose. The output signal was measured by using an oscilloscope protected using 20 dB attenuator.
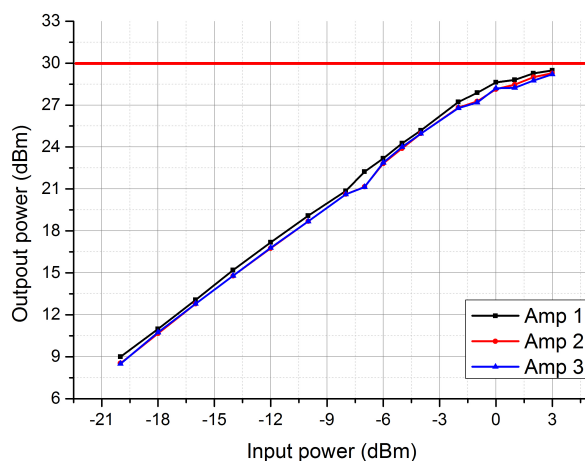
Figure 4.5: A plot of the output signal as a function of the input signal for the custom amplifiers at 100 MHz input frequency. The red line shows the desired output level of 30 dBm.

4.6 Tracer particles

In this work 2 µm (L3030, *Sigma-Aldrich, UK*) and 5 µm (G0500B, *Thermo Fischer Scientific, UK*) diameter carboxylate-modified polystyrene particles were used to image

fluid flow in the devices. Unless otherwise stated, the particles were used in 0.125% (v/v) dilution of the original concentration in DI water (> 13.6 MΩ) with 0.1% (v/v) Triton X-100 (*Sigma-Aldrich, UK*) added to ensure that the polystyrene beads would not stick to the PDMS.

For the characterisation of the microfluidic pumps described in Chapter 6, the particles were not diluted in DI water, but in a DI water-ethylene glycol mix (*324558, Sigma-Aldrich, UK, molecular weight: 62.07 g/mol*), with a molar ratio of 3:1. The ratio was used to raise the viscosity of the mixture was 3.69 times higher than that of DI water, in order to slow down particles for easier tracking.[191]

4.7 Particle tracking

To characterise the microfluidic pumps described in Chapters 5 and 6, particle image velocimetry (PIV) was performed. The particle motion was recorded using a Rolera EM-C2 CCD camera at 62.5 frames per second. In order to analyse the PIV data the channel was divided into 25 equal width sections within which the average particle velocities could be measured. The particles were tracked using ImageJ software[192] with the *Trackmate*[193] plugin, which allows frame to frame particle identification, coordinates and corresponding velocities to be extracted. This data was exported into MS Excel, where a custom macro command sorted the particles according to their coordinates along the width of the channel. The macro then counted how many particles had velocities 0 - 10 µm/s, 10 - 20 µm/s, etc., until there were no more particles to be counted. A Gaussian profile was fitted to a plot of particle count versus velocity, giving the average velocity value of all particles present along one of the 25 specified channel positions across the width of the channel. Using this technique, velocity profiles were produced for each device at a range of applied powers. No fewer than 10,000 (typically 15,000) particles were tracked to produce each velocity profile.

Finally, ProFit 7.0 software was used to fit Equation 5.7 to each of the velocity profiles using a custom Python script.

Chapter 5

Device characterisation and early work on SAW-micropumps

5.1   Introduction and chapter summary

As described in Chapter 2 there are a number techniques for producing liquid flow within a microfluidic channel. However, none of those have the combined characteristics of low cost, small footprint, low power consumption and high performance. Therefore, the work in this thesis has been dedicated to utilising SAWs to build a micropump that satisfies all of the previously mentioned characteristics. This chapter provides a review of the protocols utilised for device fabrication, and an evaluation of the key steps to device fabrication, i.e. the cleanroom fabrication of $LiNbO_3$ chips and microfluidic channel fabrication, and the importance of 3D printing for microfluidic channel fabrication.

Although there are previous reports of different methodologies for achieving liquid pumping using SAWs, there is no thorough analysis as to why certain wavelengths of SAWs are used, how to design the IDTs and how the choice of materials affect the electrical performance of each device. This chapter and part of the next chapter

sets out to perform a thorough electrical characterisation of different wavelength SAW devices, with the intention of maximising the efficiency of SAWs on $LiNbO_3$ substrates for pumping liquid within PDMS microfluidic channels. Although this thesis focuses on the aforementioned materials, the principles can be applied to any set of piezoelectric substrates and microfluidic channel materials. The chapter begins with a discussion of the design principles of IDTs whose impedance is matched to the driving electronics. This is followed by a discussion of how SAWs are transmitted through PDMS material, alongside an investigation of pump efficiency versus SAW wavelength.

Finally, the chapter concludes with the early work on SAW-micropumps, in particular the early design of fluidic channels. A thorough analysis of the flow profiles and achieved pressure gradients is presented alongside a discussion of the key limitations of this generation of device, which are used to inform improvements to the SAW micropumps, presented in subsequent Chapters.

5.2 Device fabrication and fabrication process evaluation

5.2.1 Active SAW devices

All SAW devices were fabricated in a cleanroom environment following the protocols described in the Chapter 4. Figure 5.1 shows a 10x magnification image of a successfully fabricated $LiNbO_3$ chip with gold IDTs.

The mark to space ratio of the metallised (yellow colour) to open (grey) areas is close to unity; this is achieved through an appropriate selection of the exposure time during the photolithography process. For example, over exposure (when using 'positive' photoresist, such as S1813 used here) is characterised by higher than unity mark to space ratio. Conversely, under exposure usually leads to poorly defined features, which do not resemble the pattern on the photomask.
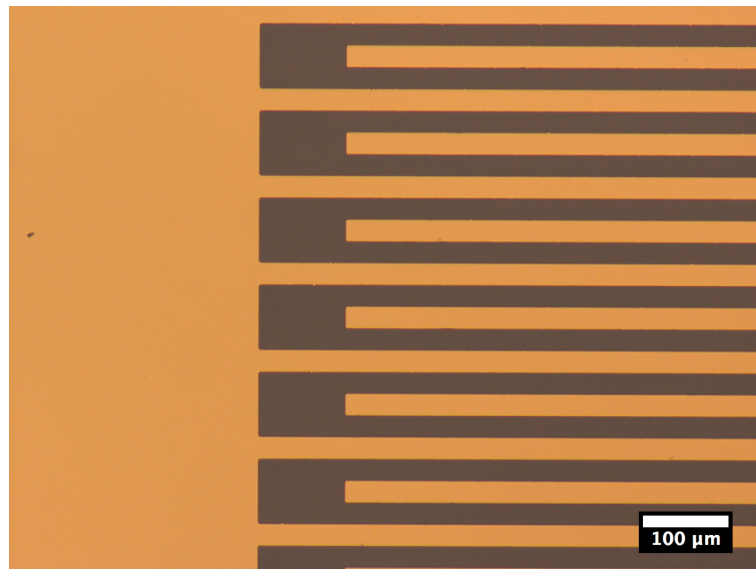
Figure 5.1: A 10X magnification image of a successfully fabricated IDT for a 100 μm wavelength SAW device.

The next step in the fabrication process is thin film metal deposition followed by lift-off. Considering a two-layer lithography process is used here, an appropriate undercut ensures a high yield of devices during the lift-off stage. It also decreases the 'lily padding' effect, which is characterised by the presence of a residual material at the edges of the electrodes. This effect is a common source of failure in single-layer lithography protocols, as shown in Figure 5.2. After fine-tuning the protocol, the fabrication yield of the devices was 83% ($N = 102$).

In order to image an undercut formed in photoresist a high magnification lens with a small focal depth must be used, which allows focusing on the top and bottom of the S1813 resist layer. By subtracting both images, it is then possible to obtain the profile of the undercut and consequently, image it. Figure 5.3 shows a picture of 100 μm wavelength device before the Ti/Au metallisation. The measured undercut was approximately 2 μm.
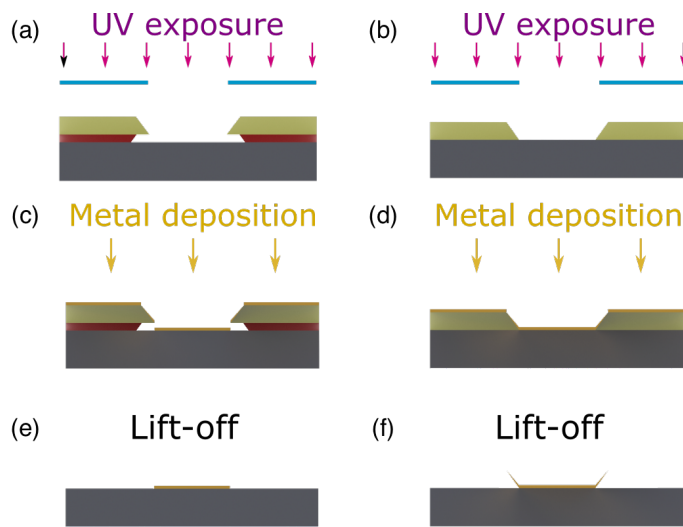
Figure 5.2: LHS: A schematic of an undercut formed in a two-resist process where the bottom resist is a sacrificial layer formed from lift-off resist, and the top resist is a positive resist. Use of two-resist process reduces metal linkage between the required features and the waste material, thus decreasing failure rate during the lift-off process. RHS: A single layer photoresist protocol that produces pronounced 'lily-padding' after lift-off. If a single resist protocol is used, an undercut profile still can be achieved by treating the top layer of the resist with a chemical that reduces its etch rate in the developer. *Note: The reason why the sidewalls of the positive resist are slanted is due the nature of contact-photolithography, where the edges of the top resist layer are slightly over-exposed due to diffraction of UV light.[38]*

5.2.2 Microfluidic channel fabrication and the importance of 3D printing in this process

Arguably, microfluidics as a field has been evolving side-by-side with the developments of the MEMS and general silicon devices, all of which heavily rely on cleanroom fabrication. Consequently, the most common way of fabricating microfluidic channels is through the use of photolithography processing, either to build enclosed microfluidic channels in a substrate material [46] or to prepare master moulds for soft-lithography as discussed
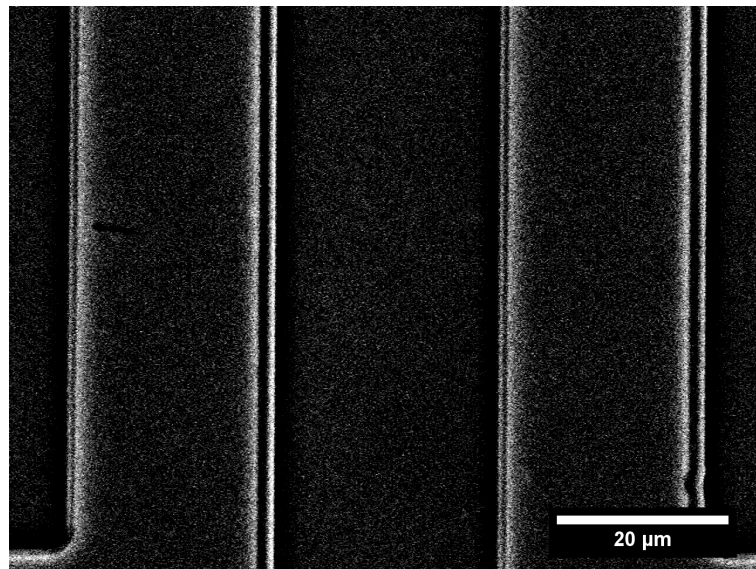
Figure 5.3: An image of an undercut formed in the photoresist pattern for a 100 μm wavelength SAW device. The image was generated by capturing separate images at focal points on the top and bottom of S1813 resist, and then subtracting the images to highlight the non-overlapping regions.

in the Chapter 2. [194, 61] The latter approach was taken at the start of this work. However, it quickly became apparent that master mould fabrication in a cleanroom is time-consuming and cost-effective only if the design of the microfluidic channels does not change. Thus, cleanroom fabrication of microfluidic channel master moulds is prohibitively expensive, and consequently is ill suited for rapid prototyping and multiple design iterations of microfluidic channels. Furthermore, as discussed in Chapter 2 this method is limited to the formation of planar structures only unless expensive two-photon lithography systems[195] or complicated multi-layer channel structures[104] are used.

All of the microfluidic channels reported in this work were made from PDMS using soft-lithography. PDMS is particularly suited to LOC applications owing to its low cost, which enables single-use platforms where fouling and/or cross-contamination is a concern; its rapid prototyping capabilities, for development of complex channel networks; and finally, its gas permeability, which is particularly advantageous for biological applications such as the organ-on-chip.[196, 197, 49] For this work, the ability to rapidly prototype different

designs of PDMS microfluidic channels was of significant importance, along with the capacity for future integration of SAW pump with organ-on-chip systems.
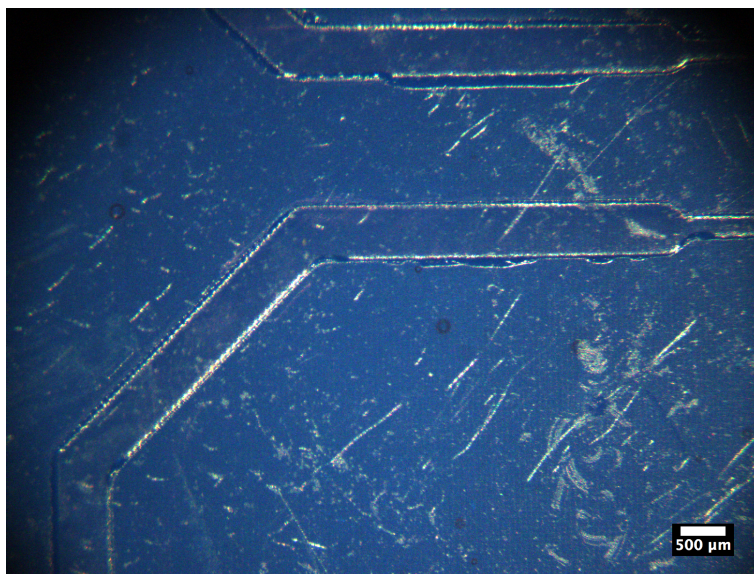
Figure 5.4: Surface of a 3D printed master moulds before the RIE.

The protocol of preparing a master mould through the use of stereolithography 3D printing is detailed in Chapter 4. As such, only the results and analysis steps of the process will be discussed here. After the 3D printer has finished producing the mould, it cannot be used for soft lithography straight-away, as the resin consists of acrylic-based chemistry (the exact content of the resin is proprietary), and the PDMS just above the printed surface does not set. Therefore, to passivate the surface and aid peeling off the PDMS, the surfaces were treated in an RIE chamber. Figure 5.4 and Figure 5.5 show the master moulds before and after RIE treatment of the master moulds respectively. Prior to RIE passivation, the material surface is glossy, however, after RIE, the surface appears to have a more matte finish, presumably due to increased surface roughness owing to partial surface etching during the RIE process.

The aforementioned surface roughness of the master moulds has no adverse effects on plasma bonding the PDMS to the $LiNbO_3$ substrate. Figure 5.6 shows a PDMS channel

Figure 5.5: Surface of a 3D printed master mould after the RIE passivation step, with a characteristic matte finish. Note for this particular sample a red-coloured base resin was used, instead of the blue base seen in Figure 5.4.

plasma-bonded to a $LiNbO_3$ chip. The few scattered defects observable within the plasma bond are also present on the master moulds themselves, and that most likely is due to contamination of the resin bath utilised by the 3D printer (which is not housed within a cleanroom).

Once the $PDMS-LiNbO_3$ plasma bonding procedure has completed, the plasma bond is strong and stays over extended periods of time (>2 years). In fact, none of the PDMS channels that were bonded during the course of this work have delaminated to date. No strict quantification of the plasma bond strength was done, but Figure 5.7 shows a chip, where the PDMS block has been ripped off from the chip. The $PDMS-LiNbO_3$ bond is clearly stronger than the PDMS-PDMS bond within bulk of the block. Thus it can be concluded that the bonding strength is higher than 180 kPa according to a study done by Tang and Lee.[198] The bond was also found to survive flow rates of 5 ml/min (channel cross section was: 500 μm width and 100 μm height) without signs of deterioration.
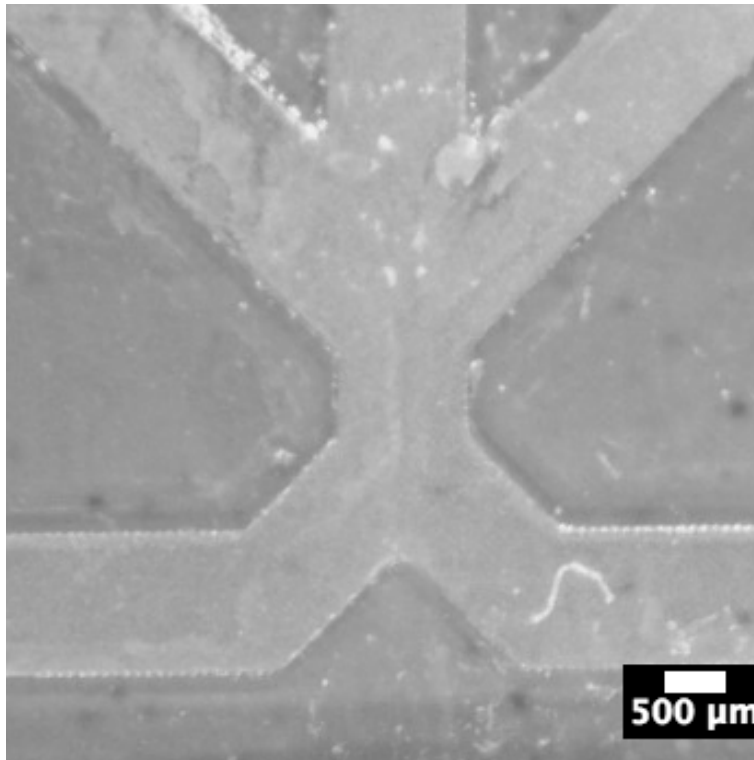
Figure 5.6: Micrograph of a successfully bonded PDMS fluidic channel onto $LiNbO_3$, using plasma bonding process. Although the master moulds have increased surface roughness due to the RIE process, this does not result in poor plasma bonding of the PDMS to $LiNbO_3$.

5.3 Electrical characterisation of the devices and SAW transmission through PDMS

The SAW devices were characterised using a Network Analyser to obtain the S_{11} scattering parameter. As discussed in Section 4.4 S_{11} gives information about what fraction of the applied power is reflected back to the signal source as a function of applied frequency. A trough is expected at the fundamental frequency of the SAW device, which corresponds to the frequency at which the transfer of applied signal into an acoustic wave is a maximum. If the applied power to the device is not reflected back into the network analyser, it can be assumed that the majority of the applied signal is used either to generate
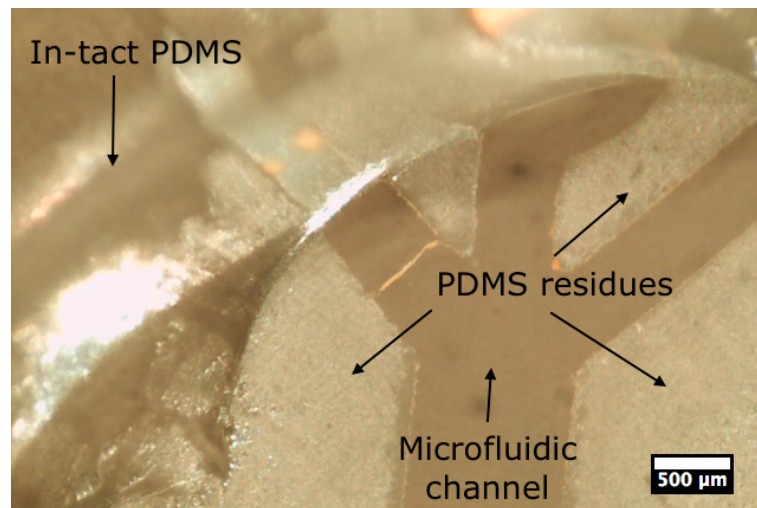
Figure 5.7: A chip with part of the PDMS block ripped off. The plasma bond between PDMS and LiNbO$_3$ is stronger than the PDMS-PDMS bond.

a SAW, or is lost in phonon generation or through radiative losses, for example.[199] Although in a single-port device it is impossible to know precisely what fraction of energy is used to produce a SAW, the numerical value of the resonant S_{11} scattering parameter can give a good approximation, which aids in characterising the device efficiency. In this work, a minimum required S_{11} value was chosen as -15 dB, which, assuming no losses, corresponds to more than 97% of energy coupled into the launched acoustic wave.

Initially, devices were fabricated with an arbitrary impedance and then impedance matched to the 50 Ω impedance using a surface-mount, lumped element circuit. Since this method relies on simulating the device parameters after matching using a 'black box' approach, the actual impedance is rarely actually 50 Ω. Therefore an alternative approach was introduced in which the IDTs were designed to have 50 Ω impedance (at the operating frequency). This relies on modelling the IDTs as a delay line consisting of multiple capacitors and inductors, as described in [200]. This approach allows the IDT impedance to be controlled through four variables, namely H_w, R_{in}, f_0 and N_p. These correspond respectively to the acoustic aperture width (the overlap length of signal and ground IDT fingers), the IDT input resistance, the SAW centre frequency and the finger

pair count. These variables are related through the following equation:

$$H_w = \frac{1}{R_{in}}\left(\frac{1}{2f_0 C_s N_p}\right)\frac{4k^2 N_p}{(4k^2 N_p)^2 + \pi^2} \tag{5.1}$$

C_s and k^2 are the material dependent constants of static capacitance and piezoelectric coupling coefficient, respectively.[121] R_{in} was fixed at close to 50 Ω, to match RF equipment used. As a result, the relationship between N_a, the number of finger pairs, and acoustic aperture width (H_w) could be plotted for a given SAW wavelength/frequency as shown in Figure 5.8 for a 100 μm wavelength SAW device.
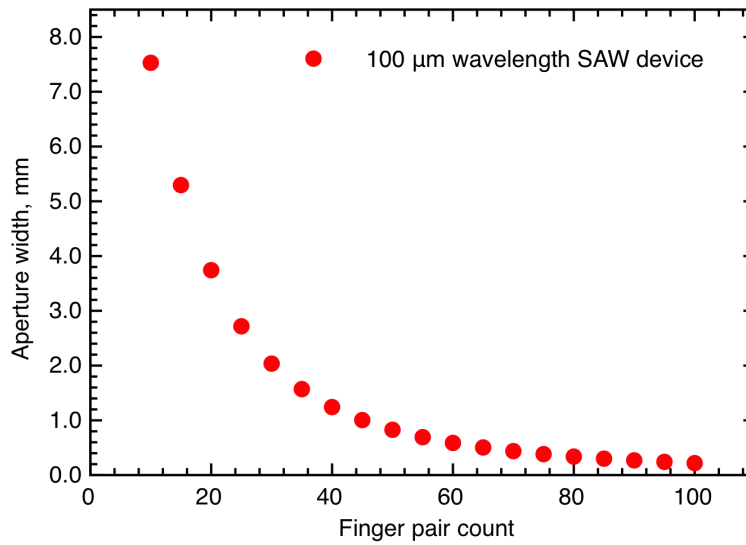
Figure 5.8: A graph depicting how the acoustic aperture varies with finger pair count for 100 μm wavelength SAW device.

Equation 5.1 and Figure 5.8 can be further used in determining the design constraints of a SAW device. A design rule of thumb for SAW devices described by Professor S. Datta in [121] states the aperture width must be at least five wavelengths wide in order to keep the SAW device efficiency high. Thus a 100 μm wavelength device with more than 65 finger pairs will have higher losses due to signal scattering according to this rule, as a result device design should be constrained to no more than 65 finger pairs.
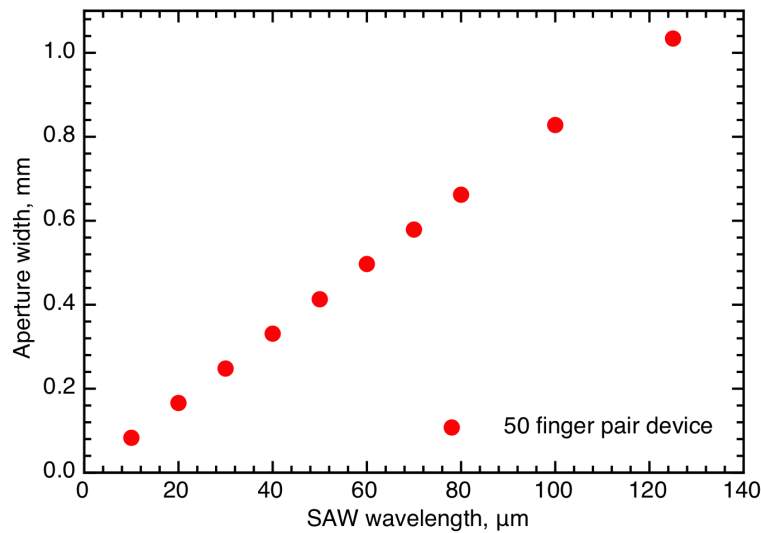
Figure 5.9: A graph of how the aperture width varies with respect to the finger pair count for 100 μm wavelength SAW device.

On the other hand, if the finger pair count and the input impedance are fixed, the aperture width changes linearly with the SAW wavelength, and the gradient of this function will be dependent on the material constants C_s and k^2.

Figure 5.10 shows the difference in S_{11} for a lumped element matched 100 μm wavelength device (blue line) and a device designed to have an intrinsic impedance of 50 Ω (red line), both at the same SAW wavelength. Although S_{11} has a higher value for the lumped element, matched device still qualifies for the minimum -15 dB trough value. The difference between the reflected signal amplitudes is only 1.2%: with the values being 0.4% for the lumped-element matched device and 1.6% for the intrinsically 50 Ω device. It is quite important to note that the lumped element matching circuit seems to produce a resonator-like S_{11} response at the 25 - 35 MHz region, this response also was one of the reasons for moving towards intrinsically matched devices. The resonator-like response might be due to the resonant response of the LiNbO$_3$ chip, but Ogi *et al.* studied LiNbO$_3$ crystals and found various resonant frequencies at around 1 MHz value for a single crystal with all dimensions of 5 mm.[201] However, the chips used here are
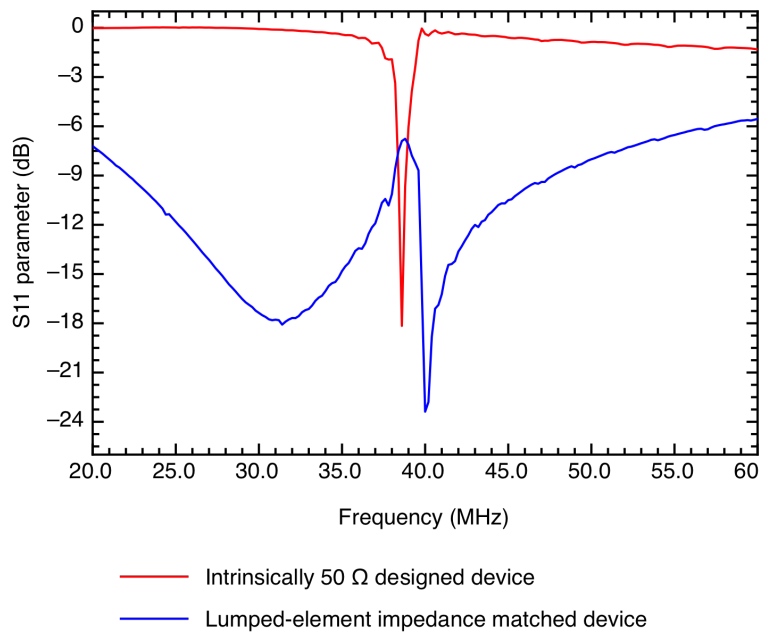
Figure 5.10: A comparison between a device designed with an intrinsic impedance of 50 Ω (red curve) and one which has been matched to 50 Ω impedance using a lumped-element matching circuit.

significantly thinner (0.5 mm thick substrates were used), thus potentially inducing a shift towards higher frequencies. The impedances and fundamental SAW frequencies of all intrinsically matched devices fabricated in this work can be found in Appendix B, where it can be seen that upon fabrication protocol optimisation most of the SAW devices have impedance between 45 and 55 Ω in the device wavelength range that was used in Chapter 6.

5.3.1   SAW transmission through PDMS

In order to isolate the SAW IDTs from the liquid within the microfluidic channel, the IDTs must be located externally to the channel and the SAW must therefore propagate beneath the PDMS wall before interacting with the liquid. It is therefore important to understand how the SAW interacts with the overlaid PDMS, and how this interaction depends on the wavelength of the SAW. Since PDMS is a material with low Young's modulus [202], it is expected to elastically dampen the SAW.[148] The 3D printer used here to fabricate the moulds limits the resolution of the thinnest possible channel wall that can be made in front of the IDT aperture to 156 ± 9 µm (N = 8 test pieces used to average the channel wall thickness). In order to assess the PDMS-induced losses, two-port devices were fabricated to allow measurement of the full scattering parameters (S_{11}, S_{12}, S_{21} and S_{22}) of SAWs at different wavelengths both with and without a 156 µm PDMS wall positioned between opposing IDTs. A typical device used in the transmission study can be seen in the Figure 5.11.
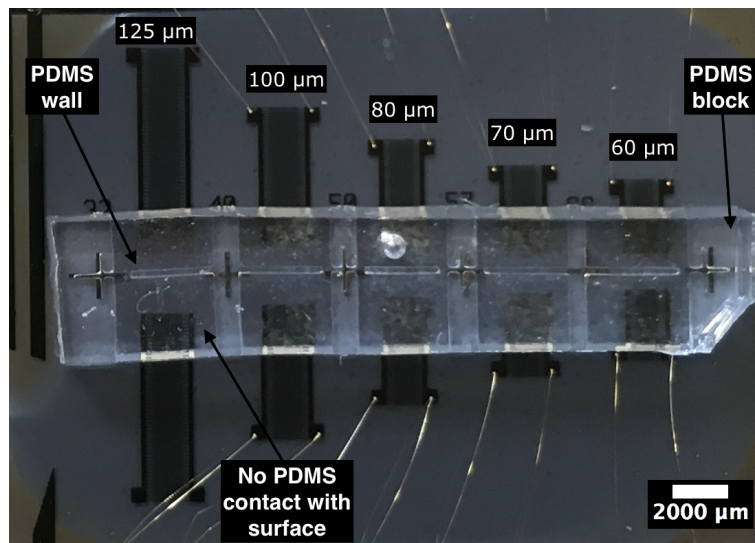
Figure 5.11: Image of SAW devices with wavelengths from 60 µm to 125 µm, each with a 156 µm thick PDMS block plasma bonded between opposing IDTs.

All devices were designed to have 50 Ω impedance and acoustic aperture width between

0.8 - 1.0 mm to aid the alignment process during the plasma bonding (see Table 5.1).

Table 5.1: Acoustic aperture widths and finger pair count for SAW devices operating at different wavelengths, with a design impedance of 50 Ω and acoustic aperture between 0.8 and 1.0 mm. These values were calculated using Equation 5.1.

Device wavelength, µm	Aperture width, µm	Finger pair count
20	748	20
25	936	20
30	815	25
40	814	30
50	785	35
60	745	40
70	869	40
80	803	45
100	1000	45
125	1030	50

By restricting these two design parameters the characteristic impedance was determined only by number of finger pairs used in different wavelength devices. Without a PDMS wall present between the two sets of IDTs, the insertion loss of each device as function of frequency could be measured. The subsequent introduction of a PDMS wall in between opposing IDTs, allows assessment of how much of the applied energy is lost within the PDMS wall. The delay line length between the opposing IDTs was maintained to 20 wavelengths for all devices to reduce the SAW dampening in air to minimum. These losses were determined to be $\alpha_{loss} = 2.1 * 10^{-4} \, dB/wavelength$ (less than 1% of the total losses in the system) due to transmitting a SAW as calculated using Equation 5.2[121]:

$$\frac{\alpha_{loss}}{\tilde{\nu}} = 1.69 * 10^6 (\frac{k^2}{2C_s})|C_y|^2 \tag{5.2}$$

where $\tilde{\nu} = 2\pi\lambda$ is the wavenumber, and k^2, C_s, C_y are piezoelectric coupling constant, equivalent dielectric constant and ratio describing particle displacement at the surface given an applied potential, respectively. These are material dependent constants that can be found in reference [121].

Figure 5.12a shows the S_{12} characteristics of devices in air (dashed line) and with a PDMS wall of 156 ± 9 μm plasma bonded in between opposing IDTs (solid line). The Table 5.2 summarises the peak transmission values and corresponding centre frequency for each device. The S_{12} parameters of unloaded, impedance matched devices are consistent to previously published literature values, e.g. for 125 μm operating wavelength[203, 124] and for 40 μm operating wavelength[139]. Devices without any impedance matching tend to report significantly lower S_{12} values at frequencies similar to the ones used here. [204, 205, 206]
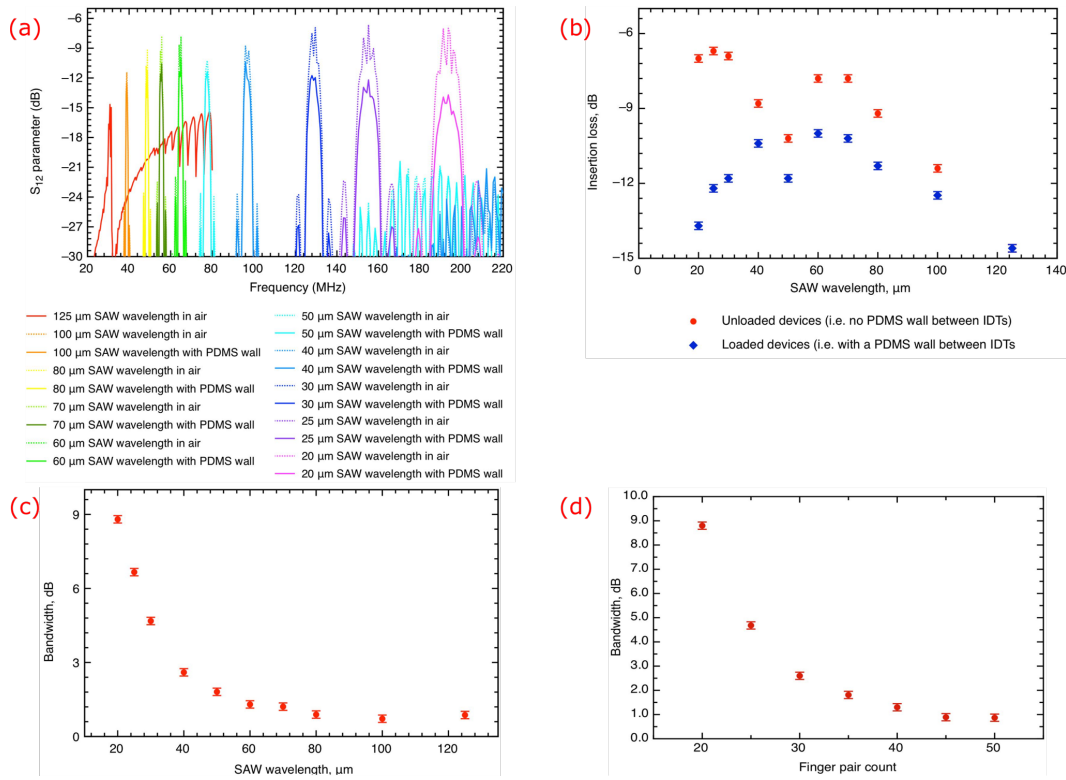
Figure 5.12: A Figure showing: (a) S_{12} characteristics of different wavelength devices in air, and with a PDMS block between the IDTs, (b) Insertion loss dependence to SAW wavelength for unloaded (red dots) and loaded devices (blue squares), (c) 3dB bandwidth dependence on SAW wavelength, and (d) 3dB bandwidth dependence on finger pair count in IDT.

Table 5.2: S_{12} characteristics of different wavelength devices in air and with a PDMS wall between the IDTs.

SAW wavelength, μm	S_{12} value in air, dB	S_{12} with PDMS wall, dB	PDMS absorption (ζ), dB
20	-7	-13.7	-6.7
25	-6.7	-12.2	-5.5
30	-6.9	-11.8	-4.9
40	-8.8	-10.4	-1.6
50	-10.2	-11.8	-1.2
60	-7.8	-10	-2.2
70	-7.8	-10.2	-2.7
80	-9.2	-11.3	-2.1
100	-11.4	-12.48	-1.08
125	-14.6	-14.6	-0.7

Figure 5.12b shows three important trends that have previously been described in the literature, and are essential in order to understand the results from Chapter 6.

The first trend is that longer wavelength devices are observed to have a lower SAW coupling efficiency. This is especially apparent as the wavelength reaches 80 μm. SAW device design guidelines state that the substrate thickness should be at least five times the wavelength of the SAW, which is approximately the distance into the substrate the SAW is coupled into, to ensure low back-scattering losses from the underside of the substrate.[121] A device with a substrate thickness less than five times the wavelength of the SAW will suffer from significant back-scattering of the wave from the bottom surface of the substrate, which in this case is fixed to a PCB and therefore cannot move freely.

The measured S_{12} parameters quantify the efficiency of each respective set of transducers (η_t) as defined by the Coquin and Tiersten[130]. Here the efficiency is defined as the electric power extracted from the SAW divided by the acoustic power of the wave[130,

199, 121] and is defined by Equation 5.3

$$\eta_t = GQ_m\eta_m \tag{5.3}$$

In Equation 5.3 G, Q, η_m are dimensionless factors corresponding to the electrode efficiency, the electric quality of the transducers and the material efficiency, respectively and which are each discussed in more detail below.

The electrode efficiency factor is related to the location of the electrodes (top surface only, or top surface IDTs with metallised bottom of the chip acting as ground IDTs) with respect to the substrate, and to their metallisation ratio (for mark to space ratio of 1, the metallisation ratio is 0.5). There are two types of electrode arrangements: the alternate phase array (used in this work owing to its higher efficiency) in which electrodes are spaced a half-wavelength apart from each other and are connected to signal and ground; and the single phase array, in which electrodes are spaced a full wavelength apart, and all of them are connected to the signal line. In this case, the ground connection is provided by the rear surface of piezoelectric material. Such an arrangement allows for the application of higher maximum power to the chip.[130] The electrode efficiency in alternate phase array is given by (see Reference [130] for a full derivation):

$$G = \frac{\pi^2}{K_2 K_2' \epsilon_{11}} \tag{5.4}$$

where ϵ_{11} is the dielectric constant of the piezoelectric material in the direction of SAW propagation, K_2 and K_2' are elliptic integrals of the first kind that are used to solve Jacobian elliptic functions to determine the surface potential on the electrodes. In this case, $K_2, K_2' \sim \lambda_{SAW}$, and therefore $G \sim \frac{1}{\lambda_{SAW}^2}$.

Electric quality of the transducers can be obtained from the first principles, and the equation for the transducer electric quality Q is given by:

$$Q = \frac{1}{\omega_0 C_{eq} R_t} \tag{5.5}$$

In Equation 5.5 the ω_0 is resonant angular frequency ($\omega_0 = 2\pi f_0$ where f_0 is the fundamental SAW frequency), C_{eq} is the equivalent circuit capacitance of the transducers and R_{in} is the impedance of the transducers, which here we fix cat 50 Ω. The equivalent circuit capacitance, C_{eq}, can be calculated by using the electromechanical coupling coefficient, k and the static capacitance, C_s of the piezoelectric material, and is dependent on the bandwidth of the device.

Finally, the material efficiency, η_m is dependent on the cut of the piezoelectric crystal and the piezoelectric coefficients of the material, and is therefore independent of the wavelength of the SAW.

By combining Equations 5.3 to 5.5, it can be seen that the transducer efficiency should be dependent on the SAW wavelength according to: $\eta_t = G Q_m \eta_m \sim \frac{1}{\lambda_{SAW}}$. Considering we can only measure S_{12}, it is not possible to calculate the absolute transducer efficiencies, thus only relative transducer efficiency comparisons between different wavelength transducers can be performed. Note that the S_{12} peak values should be expressed as fractions not in dB here. Figure 5.13 shows a first-degree polynomial fit to the first four data points of the S_{12} plot.
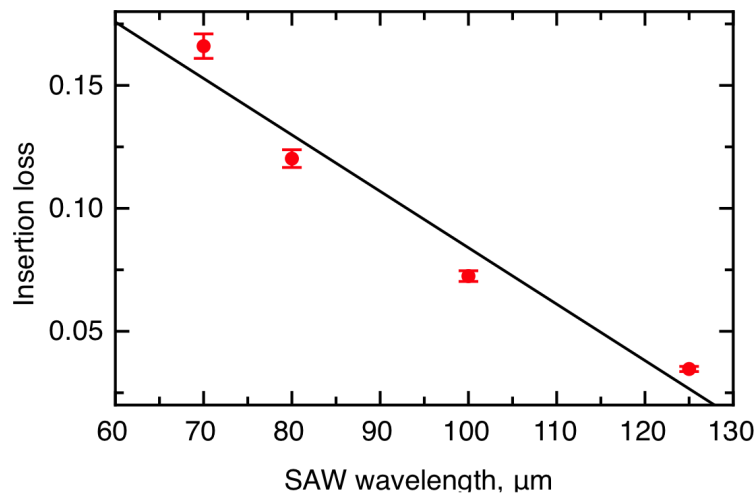
Figure 5.13: S_{12} data as a function of SAW wavelength with a linear fit (black line). $R^2 = 95.2\%$ for the linear fit.

The second trend observed in Figure 5.12b relates to shorter wavelength devices for the PDMS wall tends to dampen more energy from the SAW. This can be explained by the attenuation length of the SAW defined as the distance into an overlaid material over which the wave amplitude decreases by a factor of e with respect to its initial amplitude.[199] The attenuation length of the SAW is described by [148]:

$$l_{SAW} = \frac{\rho_{sub}v_{sub}}{\rho_{med}v_{med}}\lambda_{SAW} \tag{5.6}$$

In Equation 5.6 the ρ and v terms correspond to density and velocity of sound in the substrate (subscript sub) and medium (subscript med) respectively, while λ_{SAW} is the SAW wavelength.

The third trend shown in Figure 5.12c and Figure 5.12d is that, with increasing number of finger pairs, the SAW transmission bandwidth becomes smaller and therefore supports a reduced range of frequencies around the fundamental frequency. Figure 5.12d shows the bandwidth dependence on the finger pair count in the bare, 'in air' devices illustrated in Figure 5.12a.

In summary, although the shorter wavelength devices exhibit a higher SAW coupling efficiency between the applied power and the SAW mechanical energy, they exhibit increasing attenuation in the PDMS, which dominates their response. On the other hand, longer wavelength devices have significantly longer attenuation lengths and therefore experience significantly reduced dampening as a result of interaction with the PDMS, but these devices suffer from increased back-scattering from the rear surface of the substrate. As a consequence, devices operating at wavelengths between 40 and 70 μm tend to offer the best compromise, and are likely to produce the most efficient micropumps.

5.4   Early work on the SAW-micropumps

The initial work on the SAW-micropumps was based solely on SAW devices operating at 100 µm. The channel design can be seen in Figure 5.14, which utilises circular channel (later referred to as a "racetrack" layout), similar to that described by Langelier *et al.*[124]. As the SAW passes beneath the liquid, it will transfer some of its mechanical energy to liquis as described in Figure 5.14b. To characterise the performance of the microfluidic
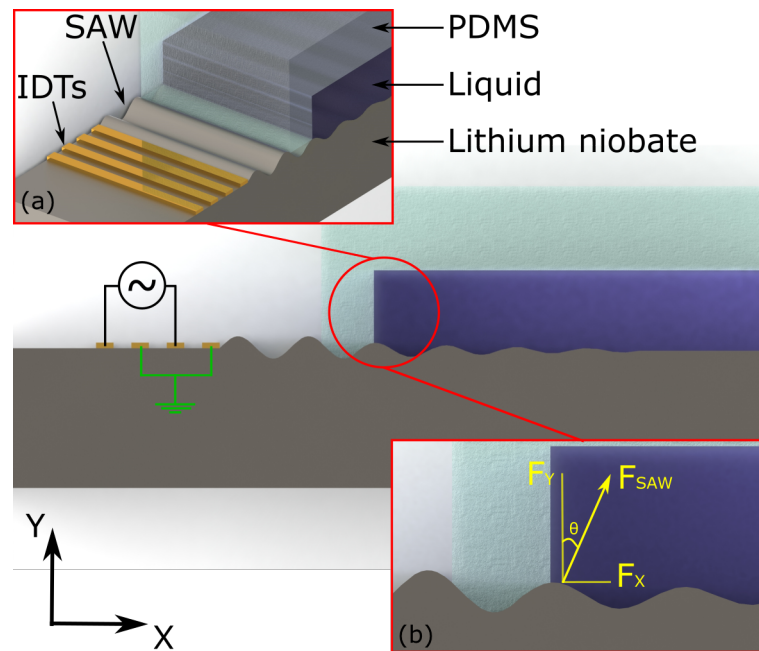
Figure 5.14: Schematic of the initial concept of the SAW-micropump, and the proposed working mechanism. The SAW is generated by the IDTs, transmitted through the PDMS (where it is dampened, and reduced in amplitude), and finally coupled into the liquid, where the liquid absorbs the SAW energy. See the inset. *N.B. Not to scale, a typical amplitude of a SAW is around 2 nm.*

pump, the velocity and the position of fluorescent tracer particles were recorded as they pass through the microfluidic channels, as described in Chapter 4.

From the tracked particle positions, it is possible to obtain a velocity profile for the flow across the width of each channel, which in turn allows the pressure gradient and

the volume flow rates to be indirectly calculated and compared for each microfluidic pump.[22] From the shape of the velocity profile, it is also possible to determine whether the flow is pressure-driven, as described by Schmid *et al.*[148] The velocity profile is given by:

$$u(y,z) = \frac{4G}{\mu w} \sum_{n=1}^{\infty} \frac{(-1)^{n+1}}{\beta_n^3} \left(1 - \frac{cosh(\beta_n z)}{cosh(\beta_n 0.5h)} \right) cos(\beta_n z) \tag{5.7}$$

Here, μ is the viscosity of the liquid, w is the width of the channel, z is the height within the channel at which the measurements were taken, h is the total height of the channel and β is given by $\beta = (2n-1)\pi/w$. The final term, G, is the pressure gradient, which can be determined by fitting Equation 5.7 to the experimental data, using G as a variable. For example, Figure 5.15 shows G (black line) fitted to experimental data (red dots) for a 100 µm wavelength SAW device powered at 0.5 W. The observed parabolic velocity profile is confirmation that we are observing a pressure driven flow. This result is expected considering that the acoustic force is inducing a pressure difference in the channel.[22]

Figure 5.16 shows the pressure gradient dependence on applied power for a 100 µm wavelength SAW device within the same channel. The data (red line) is fitted to a linear line (black line).

The linear relationship observed in Figure 5.16 is consistent with previously reported data[148] in which the applied power was varied across a similar range. However, owing to the small hydrodynamic radius the pressure gradients are an order of magnitude higher than those reported by [148], although at an order of magnitude smaller observed flow velocity.

The volume flow rate, Q, can be derived from Equation 5.7[22], and is given by:

$$Q = \frac{8Gh}{\mu w} \sum_{n=1}^{\infty} \frac{1}{\beta_n^4} \left(1 - \frac{2}{\beta_n h} tanh(\frac{\beta_n h}{2}) \right) \tag{5.8}$$

The fits of pressure gradient, such as that shown in Figure 5.16 allow the volume flow rate
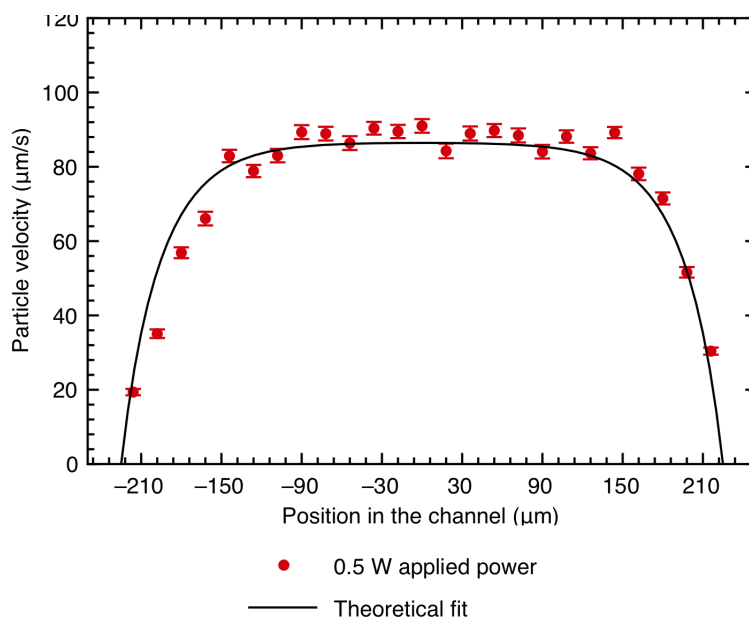
Figure 5.15: The average velocities of tracer particles (red dots) measured as a function of position across a fluidic channel of cross-sectional dimensions $h = 100 \ \mu m, w = 500 \ \mu m$ when pumped by a 100 μm wavelength SAW device at 0.5 W applied power fitted to the pressure gradient, G (black line). $R^2 = 91\%$ for the fit.

generated by the 100 μm wavelength SAW devices to be calculated for different applied powers, as shown in Figure 5.17.

As a consequence of the small microfluidic channels used here, the volume flow rate is small and compares poorly to previously published values, e.g. 150 μl/min at applied pressure of 4.8 Pa[148]. Therefore, the micropump described in this chapter can only be applied to situations in which it is advantageous to have small microfluidic channel dimensions, but in which there is no need for high volume flow rates such as infusion with microneedles[207].

The main limitation of achieving higher flow velocities (and consequently higher pressure gradients) seems to be the relatively low component of diffracted acoustic wave energy which lies parallel to the fluid flow propagation direction (the x-component shown
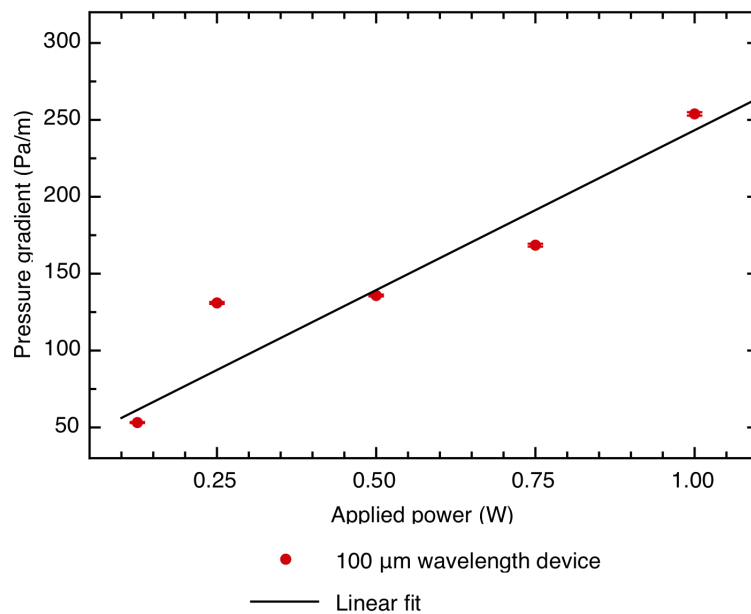
Figure 5.16: The pressure gradient dependence on applied power for 100 μm wavelength device. $R^2 = 87.6\%$ for the linear fit.

in Figure 5.14). This agrees with with the theoretical calculations of Vanneste and Buhler[179], who calculate that the streamlines in the vertical direction (corresponding to the z-axis in Figure 5.14) are an order of magnitude stronger than the streamlines lying parallel to the direction of SAW propagation (y-axis in Figure 5.14).

5.5 Conclusions

This chapter has examined the key aspects of cleanroom fabrication of lithium niobate devices highlighting the need for a good undercut to achieve an optimal fabrication yield. The stereolithography 3D printer was identified as a critical equipment for the fabrication of microfluidic channel master moulds, which allowed swift prototyping of multiple channel designs at a significantly lower cost than alternative SU-8 master mould fabrication process in the cleanroom. As a result, it was possible to conduct multiple
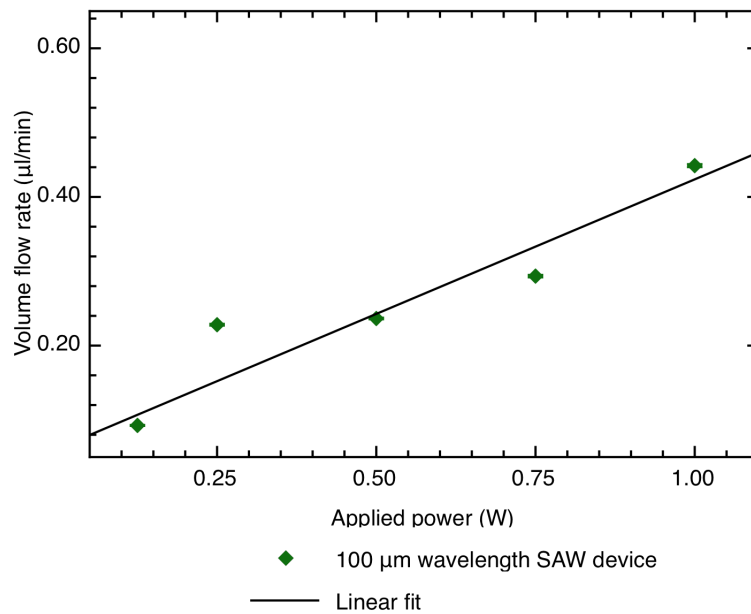
Figure 5.17: The volume flow rate dependence on applied power for 100 µm wavelength device. $R^2 = 87.6\%$ for the linear fit.

design iterations before settling on a racetrack-like design with which to investigate SAW pumping efficiency.

During the project, devices initially required lumped-element circuit impedance matching to 50 Ω, which corresponds to the impedance of the device driving electronics. Although this process significantly enhances the S_{11} scattering peak value, the peak form often tends to be distorted, because the impedance matching is done for a small range of frequencies around the resonance value. Therefore, the next iteration of SAW devices were designed to have intrinsic 50 Ω impedance.

The effect on SAW losses of introducing a PDMS wall in front of the IDTs was then investigated, in an arrangement, which mimicked the design of subsequent PDMS microfluidic channels, in order to identify an optimal SAW wavelength to produce the maximum pressure gradient and volume flow rate by the SAW microfluidic pump. A compromise between SAW-fluid interaction length, and increased losses within the PDMS

suggest an optimal SAW wavelength will lie in the range of 40 - 60 μm.

Finally, the operating principles of a SAW-micropump were discussed using a theoretical model outlined by Tabeling [22] that allows calculation of the pressure gradient and flow rate for a given micropump, from measurements of the flow profile taken across the channel.

Although a working concept of SAW-micropump has been demonstrated, due to relatively low achieved flow velocity and volume flow rates, it was not feasible to integrate the SAW-micropump into a more complex system, such as an on-chip sorting device. As a result, a different approach to harnessing SAW power by utilising three-dimensional microfluidic channels will be explored in Chapter 6.

Chapter 6

A more efficient SAW micropump

6.1   Introduction

The previous Chapter explained the basic techniques used for characterising SAW devices, both electrically (by analysing the scattering parameters obtained from a Network Analyser) and mechanically (by measuring flow profiles across an integrated microfluidic channel). The SAW micropump performance presented in Chapter 5 was limited by the assumption that the majority of motion induced in an overlaid fluid by the SAW would lie in parallel to the SAW propagation direction. This Chapter sets out to improve significantly on this performance by exploiting the three-dimensional nature of SAW interaction with an overlaid fluid, through the introduction of 3D fluidic channels.

This three-dimensional interaction between SAW and an overlaid fluid is analysed theoretically and experimentally by using the previously performed electrical characterisation of the SAW devices to characterise the performance of different wavelength SAW-pumps for pumping fluid around three-dimensional microfluidic channels.

Finally, this generation of SAW pumps is compared to published SAW-based micropump

performance, and form the basis of a publication[62].

6.2 SAW-liquid scattering angle and its importance in designing a micropump

To increase the volume flow rate and linear flow velocity of a SAW-based micropump, it is important to maximise the energy coupled from the SAW into the overlaid liquid. When the SAW reaches a solid-liquid interface, it is elastically scattered according to Snell's law owing to acoustic velocity mismatch between the water and substrate.[148] The scattering angle of a SAW into water (also called Rayleigh angle) can be calculated
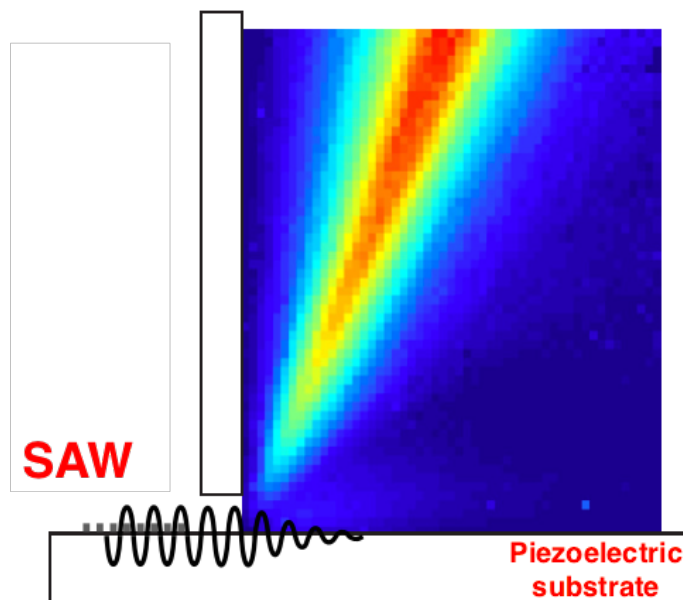
Figure 6.1: Measurements of a normalised velocity field in liquid, overlaid with a schematic of a SAW propagating along the surface of a $LiNbO_3$ substrate. As can be seen the SAW is scattered at an angle into the liquid, which can be obtained from the Snell's law. Reprinted with permission from [149] ©2014 American Physical Society.

using Equation 6.1, and is approximately 22° from the surface normal calculated using SAW velocity on $LiNbO_3$ substrate (v_{SAW} = 3989 m/s) and the sound velocity in water (v_{H_2O} = 1498 m/s).[148]

$$\theta = arcsin\frac{v_{H_2O}}{v_{SAW}} \tag{6.1}$$

The SAW scattering angle is confirmed experimentally by Dentry *et al.* who studied SAW-liquid (water) coupling at different frequencies.[149] Figure 6.1 shows a schematic of a SAW coupling to water. The colourmap region shows a normalised liquid velocity field measured experimentally and averaged over 500 frames, where blue represents regions with a low-velocity, and red represents the highest velocity field. The angle between the normal and the middle of the maximum area is 22.3° corresponding well with the expected values. From Figure 6.1 it can be seen that majority of the SAW energy in the liquid is in an upwards direction, which explains why the pump described in Chapter 5 produces such a low flow velocity. Figure 6.1 also shows the volume of interaction between the SAW and the liquid, i.e. the region in which the SAW is generating fluid flow (sometimes referred to as the "beam").[208, 209] This volume, and consequently the speed of the actuated liquid, are highly frequency dependent. The distance that the SAW propagates in to the liquid before being fully attenuated is inversely proportional to the frequency of the SAW, meaning that short wavelength SAWs have a higher power density.

To harness most of the SAW energy, the "launch region" of the microfluidic channels should be arranged normally with respect to the plane of the substrate as illustrated in Figure 6.2. This in itself is a technical challenge considering the inherently planar way in which microfluidic channels are commonly fabricated as discussed in Chapter 5. The next section is therefore dedicated to explaining the procedure for making three-dimensional microfluidic channels.
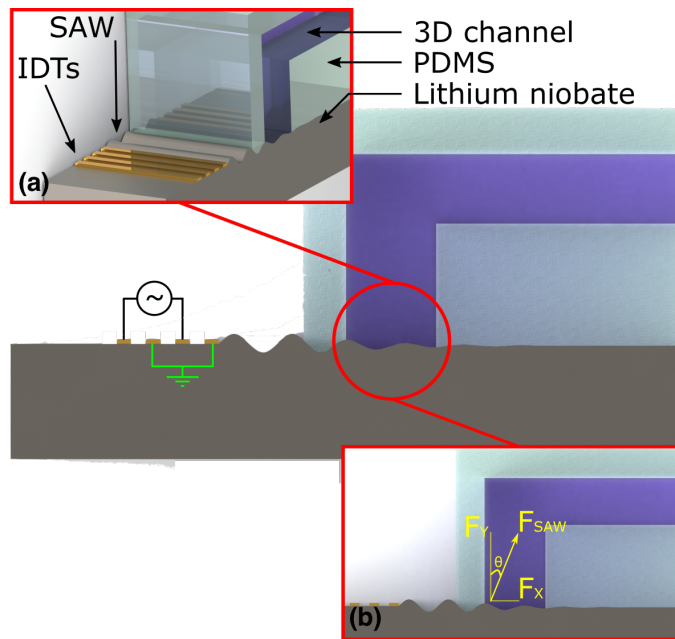
Figure 6.2: A schematic of the proposed SAW-pump designed to exploit the SAW scattering angle of 22°. Since the fluid path goes upwards, the SAW beam has enough room to generate a high-velocity stream of liquid. By utilising this design, it is possible to exploit both the vertical (F_y) and horizontal (F_x) components of the acoustic force, the former of which is larger by a factor of 2.5 almost.

6.3   Three-dimensional microfluidic channel fabrication

The conventional way to construct three-dimensional microstructures is by using multiphoton lithography (commonly referred to as two-photon lithography). This method can produce high resolution, three-dimensional patterns in photoresist, such as the ones shown in Figure 6.3. The resolution of the structures commonly reported is on the order of 1 μm.[210] However, these systems rely on very accurate mirror movements and, in particular, on mostly proprietary photoresists, thus making these systems expensive, and often custom built. [210, 211] It is possible to use multilayer PDMS structures to obtain three-dimensional microfluidic channels cheaply.[78, 212] However, most of the previously reported multi-layer PDMS structures use circular vias to connect to the top
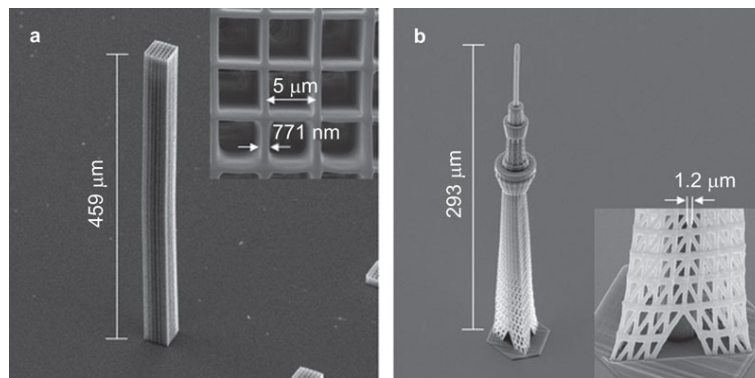
Figure 6.3: Images of high-aspect ratio structures produced by multi-photon lithography system. Figure reproduced from [210] with permission from Springer Nature.

layer(s) of the structure[78, 213], which are unfit for the use here as the effective thickness of the wall in front of the SAW aperture would not be constant due to the curvature of the via. Stereolithography 3D printing has been previously used to prepare two-[186] and three-dimensional[185] microfluidic channel master moulds. However, in this work, it was not possible to replicate the protocol described by Chan *et al.*[185] with a sufficient yield although the channel dimensions used were on the same order.

Instead, the method described by Chan *et al.*[185] was combined with another method called ESCARGOT introduced by Saggiomo and Velders[187]. The ESCARGOT method is based on immersing acrylonitrile butadiene styrene plastic (ABS, commonly used in fused filament fabrication (FFF) 3D printing) rods into PDMS, followed by curing the PDMS and finally dissolving the ABS plastic away leaving an enclosed, 3D microfluidic channel. The particular protocol developed here is thoroughly described in Chapter 4.

A schematic of the channel mould design is shown in Figure 6.4. Firstly, the grey areas in Figure 6.4 (labelled "Section A"), were 3D printed as a continuous one mould containing the lower section of the racetrack, alongside four vertical sections: two to serve as fluid inlets/outlets for loading the channel, and two to provide the raised return path for the fluidic channel. An ABS tube was then aligned manually to the two vertical square pins under a stereomicroscope, and temporarily glued using acetone, producing
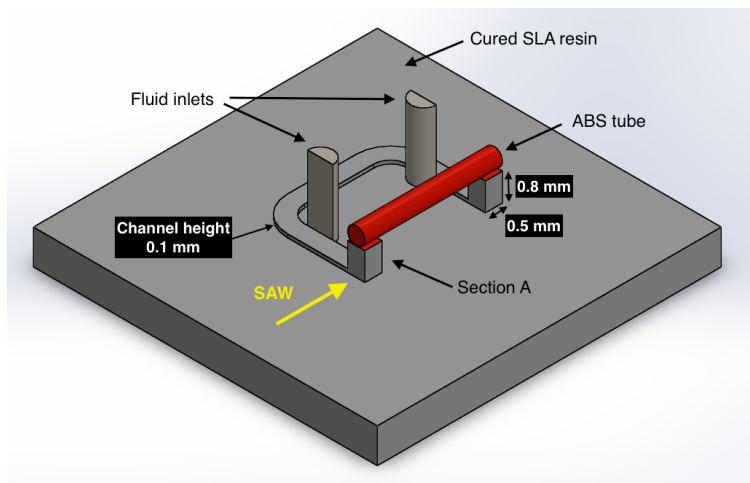
Figure 6.4: A schematic of the three-dimensional racetrack design mould used here to characterise the SAW pump. Channel dimensions in the planar regions are: 0.5 mm width and 0.1 mm height.

the three-dimensional moulds as shown in Figure 6.5. Once the PDMS had been degassed, cast, cured and peeled from the moulds, the ABS rods were dissolved in acetone whilst sonicated in an ultrasonic bath. Although PDMS is known to swell when exposed to acetone[188], no swelling during the sonication was observed experimentally and furthermore, this process is reversible. To evaporate any residual acetone from the PDMS block, the samples were incubated at $65°$ for 30 minutes. Figure 6.6 shows the final PDMS channel following dissolution of the ABS rods. The three-dimensional profile of the channel can be clearly seen in the picture. The cross-sectional area of the ABS rods was matched that of the rest of microfluidic channels in order to match the flow resistance of the channels, and therefore ensure that the particle velocity is uniform throughout the channel.

6.4 Micropump characterisation

To thoroughly understand and characterise the performance of each SAW-micropump, it is important to understand how much applied energy is converted into a SAW energy. The
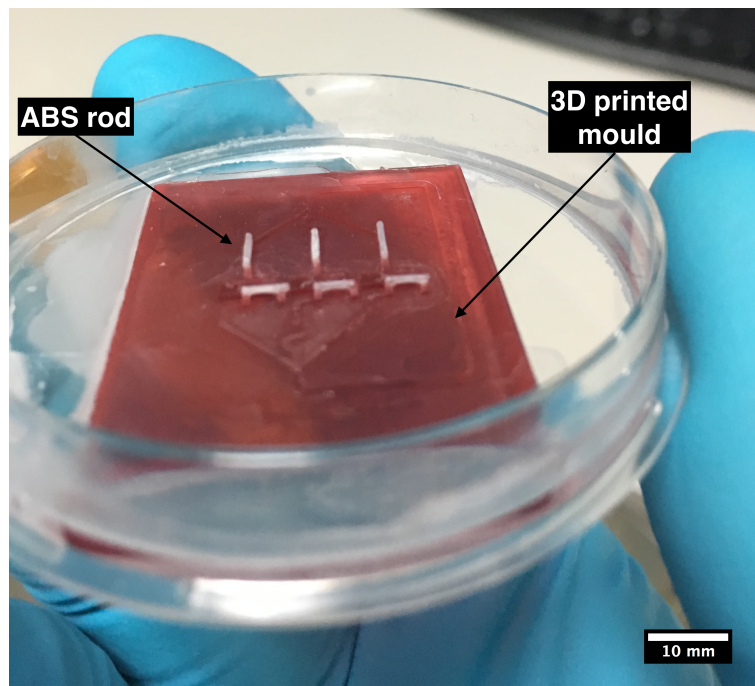
Figure 6.5: A photograph of a 3D printed mould prior to PDMS casting containing ABS tubes temporarily glued to the vertical square pins, the design of the channel was used in Chapter 7.

discussion in Chapter 5, Section 5.3 investigates losses associated with SAW absorption into PDMS microfluidic channel wall, by analysing the S_{12} parameters values for different wavelength devices, both in air and with a PDMS wall between the IDTs. However, the SAW-micropumps used here employ only a single SAW-generating IDT with a PDMS wall in front of the aperture. However, since the IDT design is identical to those discussed in Chapter 5, it is a reasonable assumption that the S_{12} and S_{21} parameter values are the same for devices of equivalent wavelength. The SAW power as a fraction of the applied power can be estimated to be half of the S_{12} value for a 2-port device, plus the additional damping introduced by the PDMS. Note, this calculation must be performed in dB to allow linear addition of the PDMS absorption. Therefore, following the discussion in Chapter 5, the relative transducer efficiency (including the PDMS wall in front of the
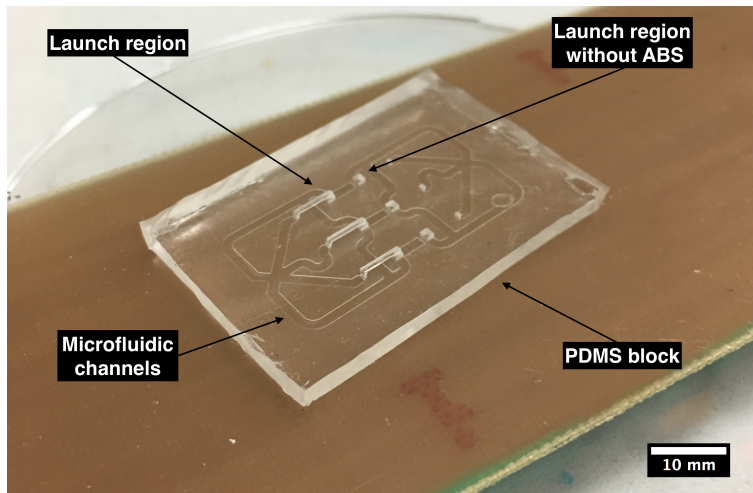
Figure 6.6: A picture of a PDMS block with ABS rods dissolved in PDMS, the design will be later used in Chapter 7.

acoustic aperture), η_{rt}, is given by [in dB]:

$$\eta_{rt} = \frac{1}{2} S_{12} + \zeta_{PDMS} \tag{6.2}$$

Figure 6.7a shows the relative transducer efficiency as a function of wavelength in dB (red dots) and Figure 6.7b - in a fraction (blue dots). The highest transducer efficiency occurs at a SAW wavelength of 40 µm, and corresponds to 25% of the applied energy being transmitted through the PDMS wall. Consequently, at 0.5 W applied electrical power, approximately 125 mW of power can be expected to be coupled into the liquid from the SAW.

The proportion of SAW energy absorbed by an overlaid liquid, α, can be estimated using Equation 6.3, which relates the ratio of the SAW amplitudes before coupling into the fluid and after penetrating a distance $L = 1.4mm$ (this distance is set by the height of the vertical launch region in the fluidic channel, section A in Figure 6.4):

$$\alpha = 1 - e^{\frac{-\beta * L}{\lambda_{SAW}}} \tag{6.3}$$

In Equation 6.3 L is the penetration distance of the SAW into the liquid after Rayleigh
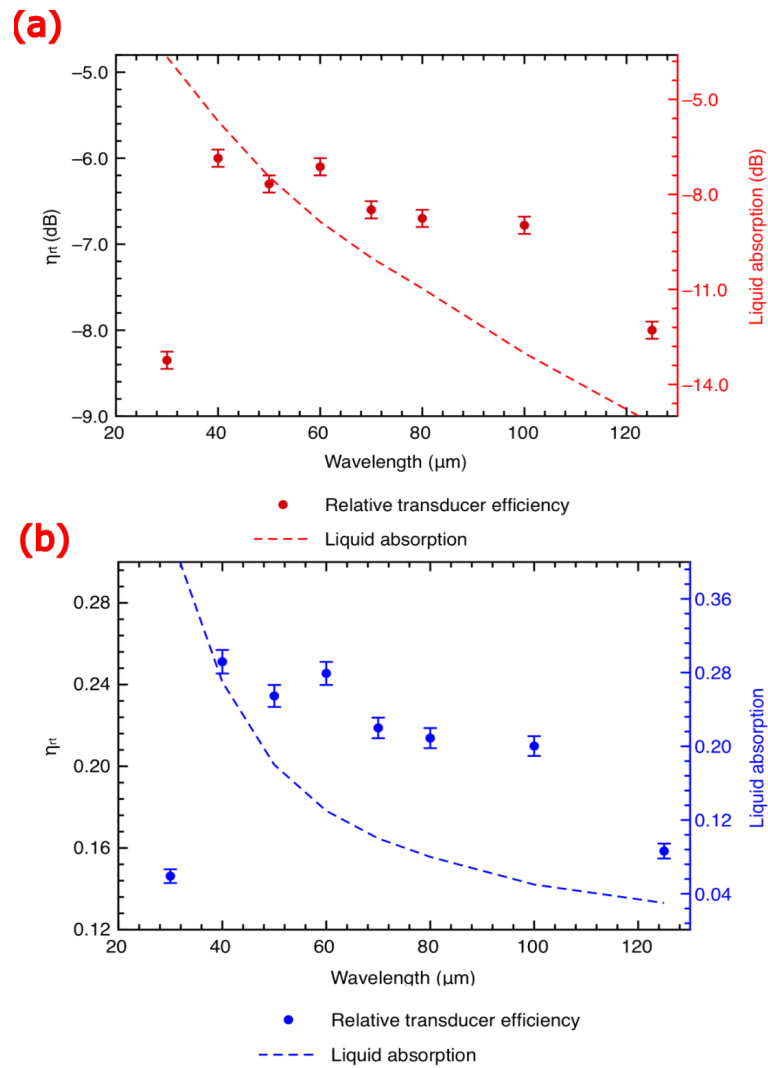
Figure 6.7: A plot of the relative transducer efficiency as function of the wavelength in (a) dB (red dots) and (b)in a fractional form (blue dots). The dashed lines show the fraction of SAW absorbed by the overlaid liquid within distance $L = 1.4\ mm$, as a function of the SAW wavelength, calculated using Equation 6.3

.

scattering, λ_{SAW} is the acoustic wavelength, and β is the wavelength-dependent attenuation coefficient of a sound wave in liquid, given by:

$$\beta = \frac{b\omega^2}{2\rho c^3} \tag{6.4}$$

where ρ is the density of the liquid, and $b = (\frac{4}{3}\mu + \mu^o)$, and μ and μ^o are the shear and bulk viscosities of the liquid, respectively.

It is important to note the exponential behaviour of the liquid absorption, as this implies that shorter wavelengths should have significantly higher pumping efficiency. From this it is possible to extract what fraction of SAW power is coupled into the liquid, and therefore how much of energy is converted into mechanical energy of the liquid in the system.

The more efficient SAW devices were characterised in the same fashion as the devices described in the Chapter 5. The velocity of tracer beads was measured as a function of position across the channel width to produce a flow profile for each device, such as that shown in Figure 6.8 for an operating wavelength of 40 μm. The flow profiles for the rest of devices can be found in Appendix C. The velocity profiles of all the different wavelength devices measured had the flow profile as seen in Figure 6.8, and the flow in all devices can therefore be said to be pressure-driven.[22] The velocity of particles in these devices was found to be over an order of magnitude higher those measured in Chapter 5. In fact, the speed of the beads in DI water was too high to be measured using the available camera, which was limited to recording at 62 frames per second. As a result, the particles were suspended in a DI water and ethylene glycol mix (3:1-mole fraction), to increase the liquid viscosity by 3.6 times and therefore to slow the particles velocities.[191] Addition of ethylene glycol also will slightly change the Rayleigh scattering angle, Hebert Jr reported that the acoustic velocity for a 4:1 mole fraction mix is 1590 m/s.[214] Therefore, using this value it can be estimated that the Rayleigh scattering angle will be about 23° (up from 22.3° for DI water). As can be seen from Equation 5.7, the velocity of the beads is inversely proportional to the viscosity of the fluid. This alteration to the flow solution had the additional benefit of decreasing the velocity measurement error. This is mainly
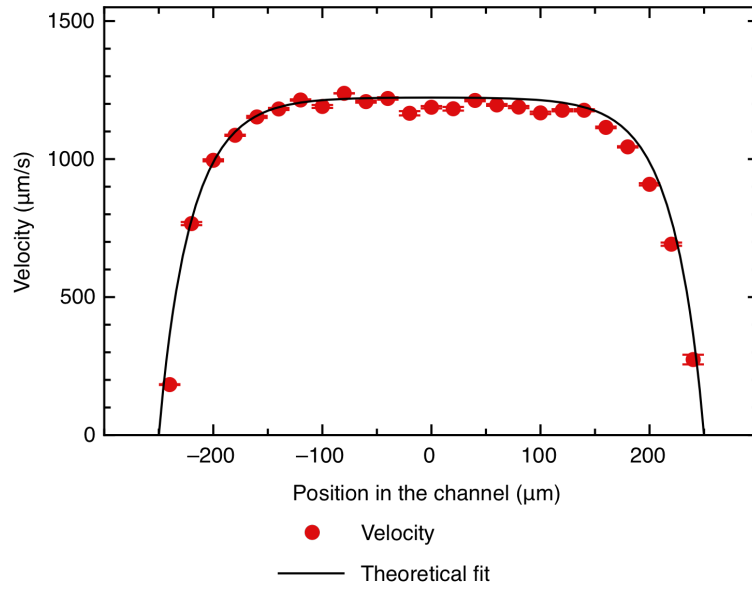
Figure 6.8: A velocity profile of a 40 μm wavelength SAW device with an input power of 0.25 W, and beads suspended in DI water ethylene glycol mix. $R^2 = 98.7\%$ for the fit.

due to reduced bead sedimentation rate, which resulted in fluorescent beads remaining at the same Z position throughout the measurement, which consequently decreased the variation in the speed of the beads arising from changes in height. This can be understood by considering the equilibrium forces acting on a bead suspended in liquid[215]:

$$F_g = F_{drag} = \frac{4}{3}\pi g r^3 (\rho_b - \rho_l) \tag{6.5}$$

where F_g is the gravitational force acting on a bead, F_d is the drag force, r is the particle radius, $g = 9.81 \ m/s^2$ is gravitational acceleration, ρ_b is the density of the bead and ρ_l is the density of the liquid. As the bead reaches its terminal velocity (v_t (which is almost instantaneous in a small-Reyonold's number system like the one described here), the drag force on the bead can be described by the Stokes drag force[216], and expressed for the terminal velocity:

$$v_t = \frac{2}{9}\frac{(\rho_p - \rho_l)}{\mu_d} g r^2 \tag{6.6}$$

where μ_d is the dynamic viscosity of the liquid.

The pressure gradient of different wavelength SAW devices was calculated as a function of applied power, as shown in Figure 6.9.

Theoretically it has been found that the maximum velocity of the fluid from SAW attenuation is readily achieved at low input powers, yet it does not result in high pressure gradient (and consequently volume flow rate) across the channel because the beam volume (volume of fluid in which the SAW interacts with the overlaid liquid) of SAW is little. Increased SAW power leads to increase in beam volume (yet the maximum fluid velocity in the beam stays the same), which results in higher pressure gradients.[149] Therefore, increase in applied power leads to higher pressure gradients generated, as seen in Figure 6.9.

The relationship between applied electrical power and pressure gradient is observed to be linear. This is expected, since the relationship between applied electrical power, and the resulting acoustic power is linear and the Stokes flow in turn varies linearly with acoustic power.[148] However, it is worth noting that the slope for each of these linear functions is different. This means that at a fixed input power, the delivered pressure gradient will be a non-linear function, thus there is a definite peak performance wavelength, which in the case of chosen channel geometry and substrate is at 40 μm. The non-linear nature of delivered pressure gradient function with respect to SAW wavelength could be attributed to the exponential function of liquid attenuation with respect to SAW wavelength.

It is important to note that devices operating at wavelengths of 40 and 60 μm were only measured up to 0.5 W since the application of higher powers was observed to cause excessive bubble formation in the liquid. This behaviour can be attributed to cavitation caused by high pressure gradients generated at these wavelengths.

Figure 6.10 shows the dependence of pressure gradient on SAW at a fixed applied power of 0.5 W. The total energy coupled into the fluid can be assessed by multiplying the calculated energy coupled from the SAW into the overlaid liquid (α, Equation 6.3) by the measured relative transducer efficiency (η_t), and is shown as blue crosses in Figure
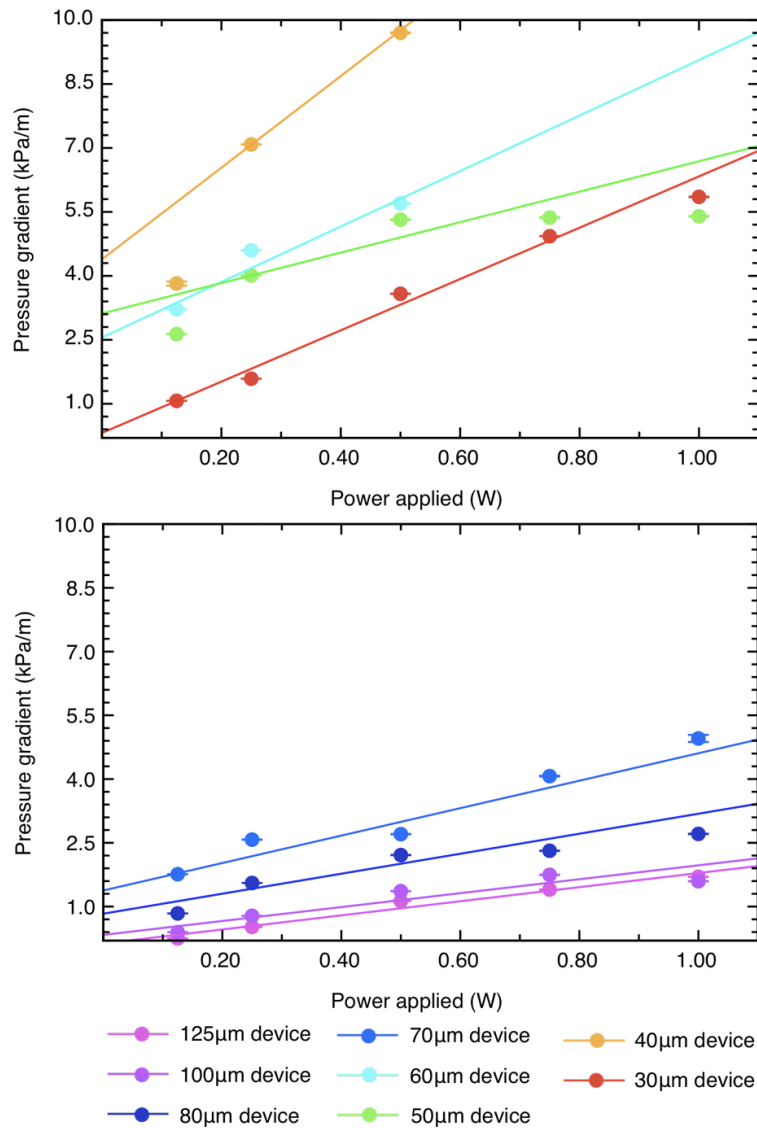
Figure 6.9: Pressure gradient plotted with respect to the input power for multiple devices. A linear function was fitted to each of the wavelengths, R^2 for the linear fits are as follows: $R^2_{125\mu m}$ = 96.9%, $R^2_{100\mu m}$ = 83.0%, $R^2_{80\mu m}$ = 88.2%, $R^2_{70\mu m}$ = 87.3%, $R^2_{60\mu m}$ = 86.9%, $R^2_{50\mu m}$ = 72.1%, $R^2_{40\mu m}$ = 93.7%, $R^2_{125\mu m}$ = 98.3%.
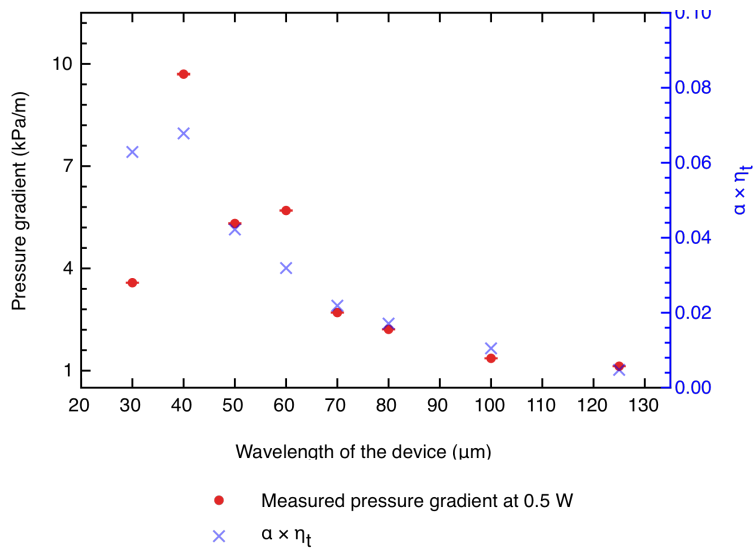
Figure 6.10: Pressure gradient at 0.5 W input power for different wavelength devices (red dots). The blue crosses show the product transducer efficiency and the liquid absorption coefficient; this product shows the fraction of the applied power coupled into the liquid.

6.10. Although the generated pressure gradient is expected to be proportional to the total energy coupled into the liquid, a large discrepancy is observed at a 30 µm SAW wavelength. This may be explained by considering that the interaction volume between the diffracted SAW is signficantly reduced, which results in reduced surface area over which viscous dissipation of the momentum occurs resulting in lower flow velocities. This is demonstrated in Figure 6.11 which shows the measured interaction volume between the SAW and the liquid as a function of SAW frequency.[149] The SAW interaction volume is observed to decrease significantly at frequencies above 200 MHz (corresponding to wavelengths below 40 µm), which correspondingly decreases the maximum fluid velocity.

It is also important to note the 60 µm device that performs better than expected. Considering that the impedance and S_{11} values of the 60 µm devices are similar to those of 50 and 70 µm, and that the relative transducer efficiency does not have an increase at 60 µm, most likely the increase of the increased pressure gradient is a geometrical effect of SAW scattering or resonance associated with the geometry of the three-dimensional
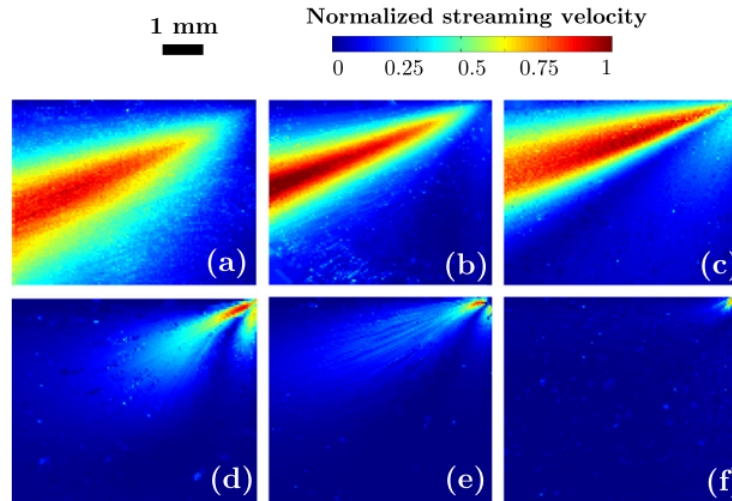
Figure 6.11: The SAW beam volume dependence on the frequency. (a) 19.7 MHz, (b) 54.2 MHz, (c) 122 MHz, (d) 240 MHz, (e) 490 MHz, and (f) 936 MHz. The power levels for frequencies were matched for comparison, and the velocity of the liquid was normalised with respect to the maximum velocity measured for the particular frequency. (a) U_S = 7 mm/s, P = 7.4 mW; (b) U_S = 23 mm/s, P = 5.8 mW; (c) U_S = 47 mm/s, P = 2.7 mW; (d) U_S = 27 mm/s, P = 3.2 mW; (e) U_S = 42 mm/s, P = 7.5 mW; and (f) U_S = 28 mm/s, P = 0.8 mW. Reprinted with permission from [149] ©2014 American Physical Society.

channels. This could potentially be tested by changing the width of the PDMS wall in front of the aperture, and checking wether the peak still persists.

To quantify the efficiency of the SAW pumps reported here and therefore to allow direct comparison with literature values, the delivered power, P_{pump}, defined as the energy imparted on the fluid to increase its velocity and pressure can be calculated using Equation 6.7:

$$P_{pump} = pQ \tag{6.7}$$

where Q is the volume flow rate given by Equation 5.8, Chapter 5, and p is the pressure drop across the fluidic channel:

$$p = Gl \tag{6.8}$$

where G is the pressure gradient derived by fitting Equation 5.7 to the measured flow profiles, and l is the contour length of the microfluidic channel, which for all channels used here is equal to 15 mm. The efficiency of the pump, η_{pump} is then determined by using Equation 6.9:

$$\eta_{pump} = \frac{P_{pump}}{P_e} \tag{6.9}$$

where the P_e is the applied electrical power. However, as discussed in Chapter 5, the applied electrical power is not the actual power coupled into the liquid. Instead the product of the transducer efficiency, η_t and the liquid absorption coefficient, α (as shown in Figure 6.10) is more appropriate quantity to use to calculate the SAW pump efficiency. The relative pump efficiency, $\eta_{p.rel}$ is therefore given by:

$$\eta_{p.rel} = \frac{P_{pump}}{\eta_t \alpha P_e} \tag{6.10}$$

Table 6.1 provides values for the transducer efficiency, the delivered power at 0.5 W input power, the pump efficiency with respect to the applied electrical power and the pump efficiency with respect to the power absorbed by the liquid, for devices operating at all design wavelengths.
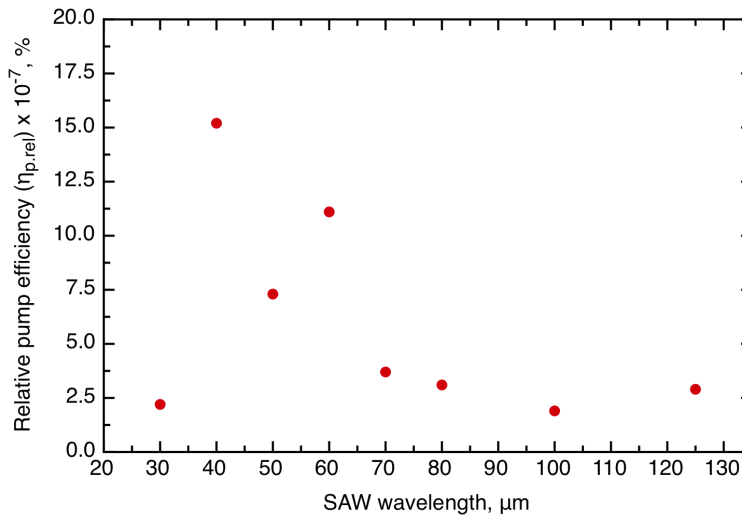
Figure 6.12: A plot of the relative pump efficiency with respect to SAW wavelength.

Table 6.1: Various characteristics of the more efficient SAW pumps.

SAW wavelength, µm	Transducer efficiency, %	Delivered power (P_i = 0.5 W), nW	η_{pump}, $*10^{-8}\%$	$\eta_{p.rel}$, $*10^{-7}\%$
30	14.6	7.00	1.4	2.2
40	25.1	51.39	10.3	15.2
50	23.4	15.45	3.1	7.3
60	24.5	17.74	3.5	11.1
70	21.9	3.99	0.8	3.7
80	21.4	2.67	0.5	3.1
100	21.0	1.01	0.2	1.9
125	15.8	0.70	0.1	2.9

The overall behaviour of the pumps shown in Figure 6.12 follows the relationship seen in Figure 6.10, as expected. The best performing pump is observed at an operating wavelength of 40 µm, which agrees with previous assessments of relative transducer efficiency and SAW-liquid coupling efficiency.

It may also be seen from Figure 6.12 and Table 6.1, that the liquid absorbs more than six orders of magnitude less power than the SAW-pump outputs, suggesting that the flow generation is still a highly inefficient process. The observed fluid flow velocity at the source of the SAW, i.e. within Section A in Figure 6.4 is at least an order of magnitude higher than the steady-state flow velocities measured at other locations within each channel, although the exact value cannot be measured as the liquid velocity is too high for the equipment used here. Measurements with very high frame rate cameras (more than 1000 frames per second) suggest the fluid velocity in the vortices is on the order of 100 mm/s.[149] Figure 6.13 shows that, within this launch region, flow are vortices

observed.
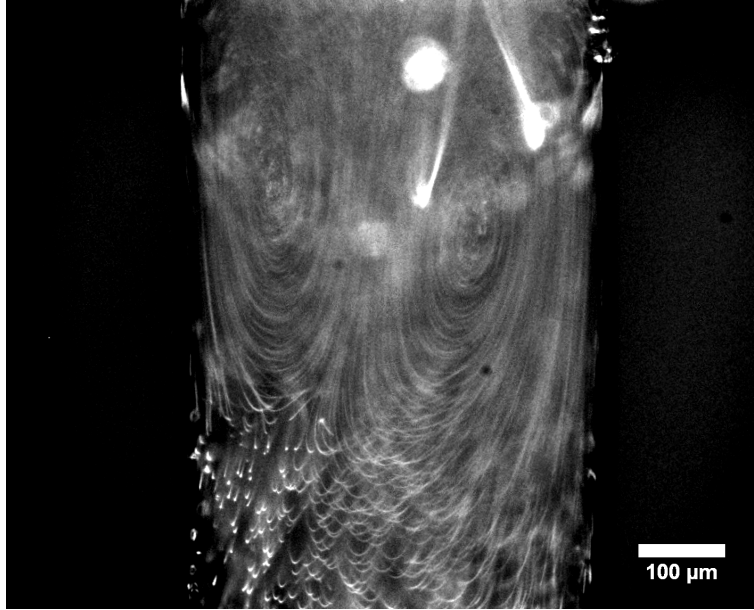
Figure 6.13: A captured image of vortices formed in the liquid at the point of entry (top of the image) into the microfluidic channel, i.e., at the top of Section A, Figure 6.4.

The velocity of particles within these vortices is significantly higher than the linear velocity measured around the channel, suggesting that the conversion of SAW power into linear flow remains highly inefficient.

The pressure difference driving the vortices generated by the SAW can be calculated by integrating the volume force generated by the SAW along the height of the channel. The volume force is caused by the damping of SAW which happens through a relaxational dissipation.[148] The integration is done along the SAW propagation axis, which is along the Y-axis as shown in Figure 6.2b:

$$F_y = \frac{2P_a}{cAl_a cos\theta} e^{-\frac{2x}{l_a}}$$ (6.11)

In Equation 6.11 c is the velocity of sound in liquid (water in this case), l_a is attenuation length of the SAW in the liquid (calculated using by Equation 5.6), P_a is the acoustic

power of the SAW, given by

$$P_a = \eta_t P_e \tag{6.12}$$

Finally, the pressure difference, Δp, is given by:

$$\Delta p = \int_0^{h/cos\theta} F_y \, dy \tag{6.13}$$

where h is the height of the channel at which point SAW interacts with liquid, in this case $h = 1.3 \ mm$, corresponding to the height of Section A in Figure 6.4.

For a 40 μm wavelength device driven at 0.5 W input power, the pressure difference generated by the SAW is: $\Delta p \sim 3200$ Pa. In comparison, pressure calculated using Equation 6.8 is approximately 145 Pa, again confirming that the mechanism of liquid momentum dissipation is not an efficient process. The values found here are in agreement with those measured by Schmid *et al.*, who also observed more than an order of magnitude difference between the vortex-driving pressure and the effective pump pressure measured around a fluidic channel.[148]

Considering the calculations done in Equation 6.13 and Table 6.1 it is clear that not all of applied energy to the IDTs is converted to fluid flow, which brings a discussion on the possible loss mechanisms. More importantly, seeing that there is excessive bubbling observed in 40 and 60 μm devices, a question might arise wether the key energy dissipation mechanism is not heating of liquid boiling the liquid after some time. The racetrack design hols approximately 1 μl of liquid, thus the energy required to boil such small amount of fluid indeed is small (comparable to the energy input per second of the device). However, there are two main aspects to the argument that shows that the liquid is not heated to boiling temperatures during micropump operation. First of all, is that 50 and 70 μm devices have similar transducer efficiencies (and therefore losses), yet these do not seem to produce the liquid boiling, and can be operated at even higher input powers than 40 μm devices without causing bubbles. Secondly, although the liquid mass is small, the system consists of more than just liquid, thus the lost power would also heat up other

parts of the system, for example: the PDMS block will absorb large part of SAW energy and consequently will heat up, but considering it has much larger volume than the liquid, the temperature increase will be small. More importantly, as discussed in Chapter 4 the LiNbO$_3$ chip is glued to plated-via PCB using thermally conductive epoxy, and the PCB is mounted onto a large brass block during the experiments. The brass block the acts as a heatsink, preventing the heating of the system. Therefore, the bubble generation in the 40 µm and 60 µm devices, most likely can be associate to cavitation rather than liquid boiling.

6.5   Comparison with literature values

Although the results described in this Chapter are promising and the pump characteristics demonstrate significantly improved performance with those described in Chapter 5, it is important to put the SAW pump described here in the context of the previously published work on SAW micropumps.[62] Figure 6.14 shows the delivered power gradient with respect to applied power for multiple of the devices investigated here, in comparison with the best performing literature values to date. A more thorough review of previously published work can be found in Chapter 3; here only the results are discussed. Note that instead of comparing the delivered power, instead the delivered power *gradient* is used as the basis for comparison. This is because the delivered power is a function of pressure (see Equation 6.7), which itself is dependent on the microfluidic channel geometry (specifically the total channel length, as seen in Equation 6.8); thus it is not an objective characteristic.

SAW micropumps which do not exploit the vertical component of the scattered SAW, including those presented in Chapter 5, alongside those published by Langelier *et al.*, are seen to perform significantly worse than the pumps detailed in this Chapter.

Furthermore, the system described by Schmid *et al.* also exhibits a low delivered power
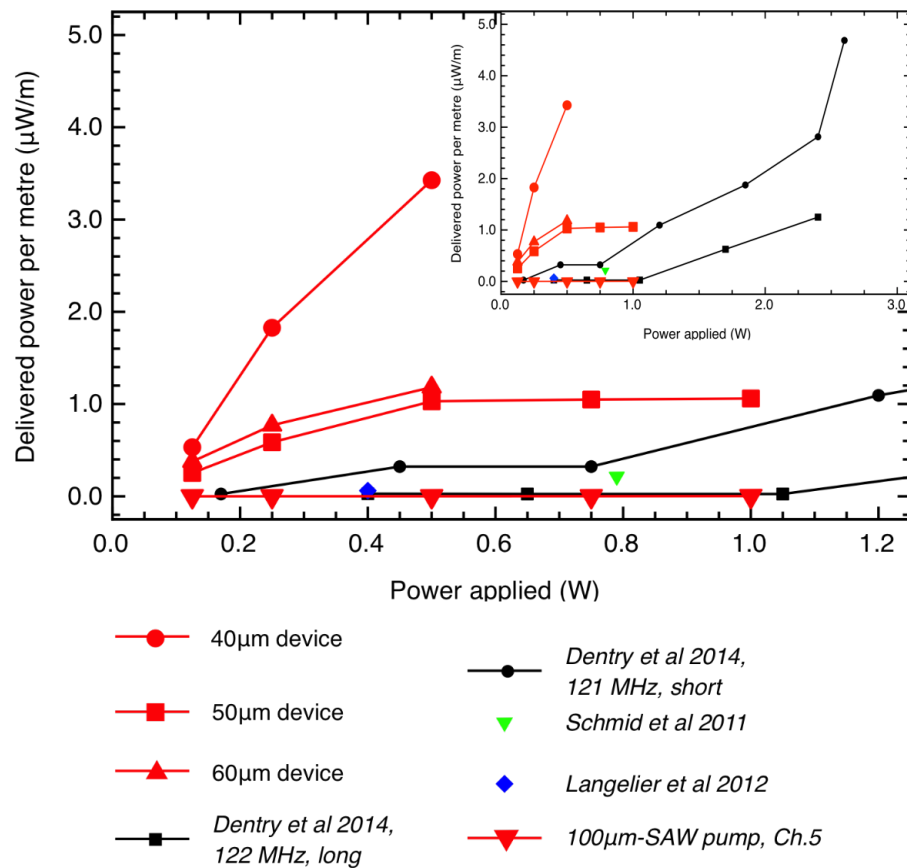
Figure 6.14: A comparison of previously published work with the results presented here. The output power of the pump has been converted to power per unit length to factor out the geometry of the channels and make an accurate comparison.

gradient in comparison with other results. This can be attributed to the reported low relative transducer efficiency $\eta_t = -11.1$ dB[148], which are thought to arise from high losses introduced at the water and glass interfaces through which the SAW must couple before finally interacting with the liquid to be pumped.

Similarly, the SAW pump described by Dentry *et al.* [159] was found to perform worse at low input powers, because the SAW has to be first coupled through an intermediate water droplet before interacting with the microfluidic channel. This layer of water is observed to dampen the SAW without contributing to the acoustic streaming (i.e. liquid pumping),

the loss for 122 MHz device due to the water layer can be estimated using Equation 6.3, $\alpha = -6.65$ dB. At higher powers, the system reported by Dentry *et al.* performs better than the system reported here, possibly through use of a high-power SAW effect not previously described.[159] One of the reasons for the non-linear performance of the pump at high input powers could be attributed to vibrations of the water droplet (or the piezoelectric substrate), which cause peristaltic motion of the droplet thus aiding the liquid pumping.

6.6 Conclusions

In this Chapter it has been shown that a SAW interacts with an overlaid liquid vertically from the surface. Consequently, the utilisation of planar microfluidic channels will produce inefficient micropumps such as those discussed in Chapter 5. To harness the majority of the SAW energy, a protocol to develop three-dimensional microfluidic channels has been described here. This protocol allows the preparation of three-dimensional microfluidic channels cheaply, and in a single PDMS cast, which allows diffraction-free imaging of tracer particles flowing around the channels.

Furthermore, different wavelength SAW pumps were studied with respect to their relative transducer efficiency, fluid absorption characteristics, generated pressure gradient and other pumping characteristics. The best performing devices by far were those operating at 40 μm wavelength, which could produce 10 kPa/m pressure gradients at low input powers of 0.5 W. The low power consumption of these devices is especially important when considering the integration of SAW micropumps into point-of-care devices, which should ideally be battery operated.

An analysis of SAW damping by an overlaid liquid was performed, which explained why shorter wavelength devices tend to perform unexpectedly poorly. It was confirmed that the mechanism of SAW acoustic streaming, i.e. viscous dissipation of the liquid momentum, is a highly inefficient process, a conclusion supported by the fact that the

pressure generated by the source of the SAW launch region is on the order of 3 kPa, whilst the measured effective pressure contributing to linear fluid flow is only 145 Pa (assessed for 40 μm wavelength devices).

Finally, the SAW pumps presented here were compared with previously published equivalent devices. The delivered power gradients achieved here are an order of magnitude higher than any previously reported SAW micropumps at low input powers (up to 0.5 W). As a result, it can be concluded that this pump design represents significant step forward in the use of SAWs as a means to generate liquid flow in real-world applications, and this was the primary goal for this thesis.

The following Chapter demonstrates applications of the developed SAW micropumps, including their use as an on-chip fluorescently activated cell sorting (FACS) system.

This page is intentionally left blank.

Chapter 7

Advanced manipulations of fluid flow on chip

7.1   Introduction

In the previous two chapters, the use of SAWs to provide fluid pumping within microfluidic channels was discussed from the perspective of electrical characterisation and fluid dynamics. Following improvements in IDT design, alongside appropriate selection of SAW operating wavelength (throughout this Chapter - 40 µm), and through utilisation of three-dimensional microfluidic channels, a SAW micropump was developed capable of producing delivered power gradients that exceed previously published values by an order of magnitude, whilst operating at low input powers.

The next step in this work is to demonstrate the versatility of these pumps at controlling more complex fluid flows, such as that required for an on-chip sorting device, by creating arrays of individually addressable IDTs.

The first step in this process was to characterise the chosen SAW pump design in terms of its response time, i.e. the time it takes for the pump to switch between different liquid

velocities.

This was next extended to demonstrate hydrodynamic fluid flow manipulations, including flow focusing and flow shifting. Flow focusing, for example, plays a vital role in on-chip particle sorting, as it is necessary to confine the material of interest to a small region of space before sorting to ensure high enrichment levels. In order to demonstrate the concept, fluorescent tracer particles are used throughout this Chapter to characterise fluid flow. Additionally, flow shifting is demonstrated in which the lateral position of a focused stream of fluorescent tracer particles is altered across the width of the channel.

The penultimate section of this chapter introduces two different pump array designs which are used to demonstrate the concept of on-chip particle sorting using SAW pumps, and to characterise the force exerted on the particles travelling down the centre of the channel. The Chapter culminates in a discussion of achieved fluid shifting rates (and consequently, the achievable particle sorting speeds) in comparison to theoretically predicted limits.

7.2 Fluid response time

To build an on-chip sorting system, it is important to understand how the fluid velocity can be altered and on what timescales this happens. These timescales are governed by the fluid response time, which defines the minimum transition time between fluid velocities in a given system. For example, when using a conventional syringe pump, the response time varies from a few seconds up to several minutes.[148] To measure the response time of the SAW micropumps discussed here, the applied electrical power was adjusted in time by amplitude modulation of the carrier frequency with a low-frequency square wave. Since the SAW pump pressure is input-power dependent, amplitude modulation of the carrier signal allows the applied power (and therefore resultant flow velocity) to be switched controllably at a defined frequency. This was achieved using an amplitude-modulation mixer circuit, in a combination with a signal generator.

In this set of experiments, instead of tracking every particle in every frame, a region of interest was defined, which encompassed the central 100 μm of the microfluidic channel. This was done since tracking and manipulating data for every particle frame by frame is computationally expensive, and yet does not give significantly more information.
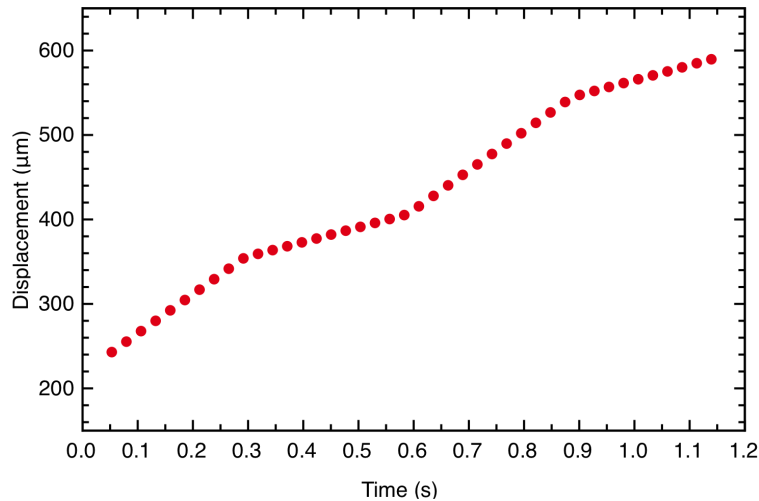
Figure 7.1: A plot of the frame by frame displacement of a test particle used to assess fluid response times, in which the particle velocity corresponds to the gradient of the plot. The plot consists of two linear regimes, and the time it takes to change the gradient in this plot corresponds to the pump response time.

The transient flow experiments were performed using an applied carrier signal power of -12 dBm modulated with a 2 Hz square wave which allowed control of the peak to peak voltage in the range between 150 and 350 mV. Particles within the region of interest were tracked individually using *Trackmate* plugin, as discussed previously. Figure 7.1 shows the coordinate change of a single particle when the SAW micropump was modulated at a frequency of 2 Hz.

The instantaneous particle velocity can be obtained by differentiating the particle position in Figure 7.1 with respect to the time as shown in Figure 7.2. It can be seen clearly that the particle experiences two distinct speed regimes corresponding to the two states of modulation.
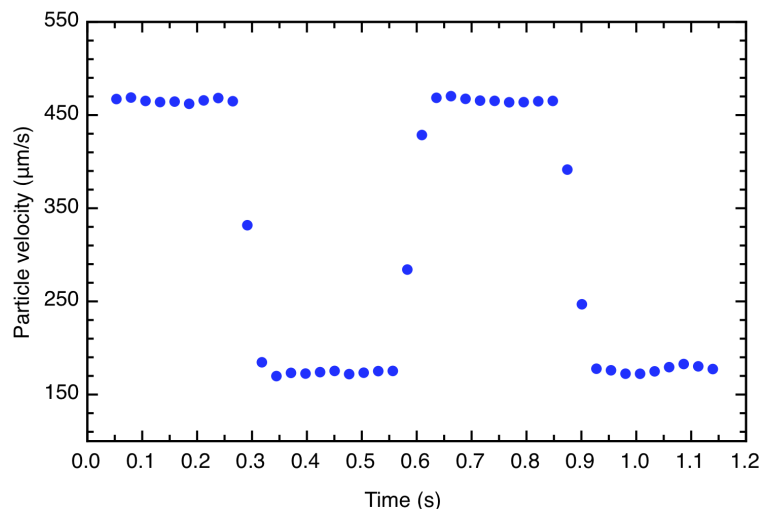
Figure 7.2: The velocity of a test particle, obtained by differentiating its position with respect to time.

The particle velocity was normalised to [0, 1] values and then fitted with a sigmoid, as shown in Figure 7.3.

The next step in the analysis fitted two linear functions to the upper and lower plateau values, the transition time between these two values then is the fluid response time.[217] The sigmoid function has been used here as to take into account not only the exponential rise or fall of the fluid velocity but also the saturating-like features of the curve as the speed approaches the plateau value. Table 7.1 shows the liquid response times calculated from particle velocities measured at several modulation amplitudes at 2 Hz modulation frequency, which are also plotted in Figure 7.4.

Both in Table 7.1 and Figure 7.4 data shows large error, which represents the standard deviation of the measurement. The source of error is likely associated to the fact that the time between two frames in the setup was limited to 26 ms, which means that the transition happens in three frames or less making it complex to reliably fit data. It is important to understand if the fluid response time is dependent on the magnitude of the pressure change required to step between the maximum and minimum measured
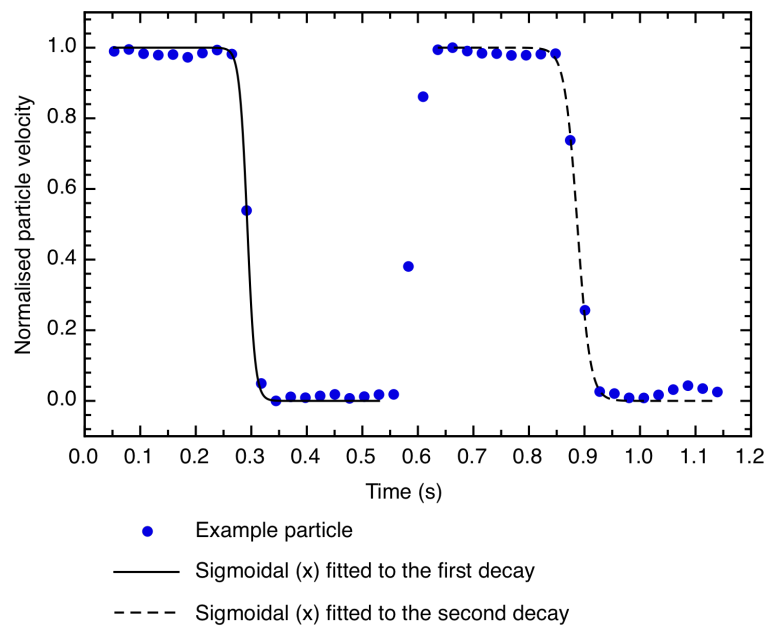
Figure 7.3: Normalised fluid response time fitted with two sigmoidal function (solid line for first decay and a dashed line for the second decay), which is determined as the fall (or rise) time between 1% and 99% of the lower and upper plateau values. $R^2 = 99.8\%$ for both of the sigmoidal fits.

particle velocities in Figure 7.3. If so, this would imply that a pressure build-up limits the switching time, rather than the response time of the fluid. Figure 7.4 shows the velocity switch time as a function of pressure difference required to switch between the two velocity states. Figure 7.4 shows that the fluid response time is almost independent of the pressure difference, which implies that the particle reaches terminal velocity instantly (as expected theoretically).[218] The modulating signal switching speed (less than 2 μs) is far faster than response times, which have an average value of 76.2 ± 16 ms; therefore the measured fluid response time is a characteristic of the SAW device, and potentially could be associated with the slow momentum dissipation discussed in Chapter 6. Another way to describe the relatively constant fluid response time is to analyse the microfluidic channel using hydraulic circuit analysis[24], in which the Hagen-Poiseuille law (Equation 7.1) states that the flow rate is linearly dependent on the pressure difference across the

Table 7.1: The response time of water measured at multiple modulation amplitudes at 2 Hz modulation frequency. The time between two frames was limited to 26 ms.

Input power difference, W	Pressure difference, Pa	Modulation frequency, Hz	Fluid response time, ms
0.12	30.1	2	72 ± 15
0.15	35.5	2	74 ± 20
0.17	43.2	2	76 ± 8
0.20	55.0	2	80 ± 19
0.26	64.5	2	79 ± 18

system. In the same fashion, Ohm's law (shown in Equation 7.2) states that the current flowing in a circuit is linearly dependent on the applied voltage difference.

$$Q = \frac{p}{R_h} \tag{7.1}$$

In the Equation 7.1 Q is the volume flow rate, p is the pressure difference between inlet and outlet, and R_h is the hydraulic resistance of the channels.

$$I = \frac{V}{R} \tag{7.2}$$

In Equation 7.2 I is the current flowing in the resistor with resistance, R, and the V is voltage difference across the resistor.

Similarly, the compliance of the system (which describes the ability of the channel-fluid system to store fluid under pressure) can be modelled as capacitance in electric circuit and should be considered here.[24] Considering that the liquid used here is water, it can be assumed to be incompressible and therefore the liquid does not contribute to the system compliance. However, the microfluidic channels themselves are fabricated from PDMS, which has a finite compliance, due to its low Young's modulus.[24, 202] Figure 7.5 shows a magnified view of section A (refer to Figure 6.4), in which the darker region is the
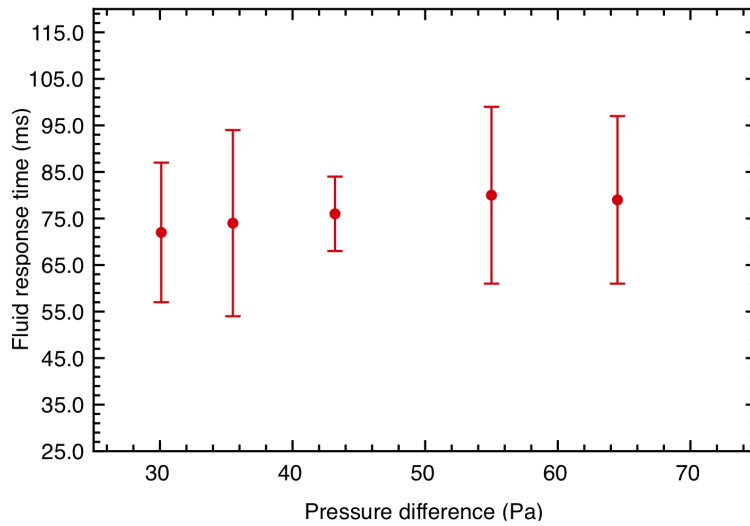
Figure 7.4: Graph showing the dependence of fluid response time on the change in pressure difference at 2 Hz modulation frequency. Error bars show the standard deviation in the fluid response time measurements. The high deviation is likely to be associated with the low frame rate of the setup used here.

vertical channel section protruding out of the picture. When the SAW is turned on, the PDMS side-wall separation decreases implying that some of the SAW energy is lost in deformation of the PDMS.

Having visually observed effect of PDMS compliance, it is important to understand how this effect contributes to the fluid response times. Sudden pressure changes produced by the SAW-pump (by switching the SAW-power) are smoothed out by the release (or absorbtion) of elastic energy by elastic expansion (or contraction) of the PDMS walls.[24] During this process, the effective volumetric flow rate, Q_c at which the fluid is stored or released by the system is given by:

$$Q_c = C_h \frac{dp}{dt} \tag{7.3}$$

where the C_h is the hydraulic capacitance of the PDMS system, p is the pressure, and t is the time. It can be seen that, if there is no change in pressure, there is no change in flow
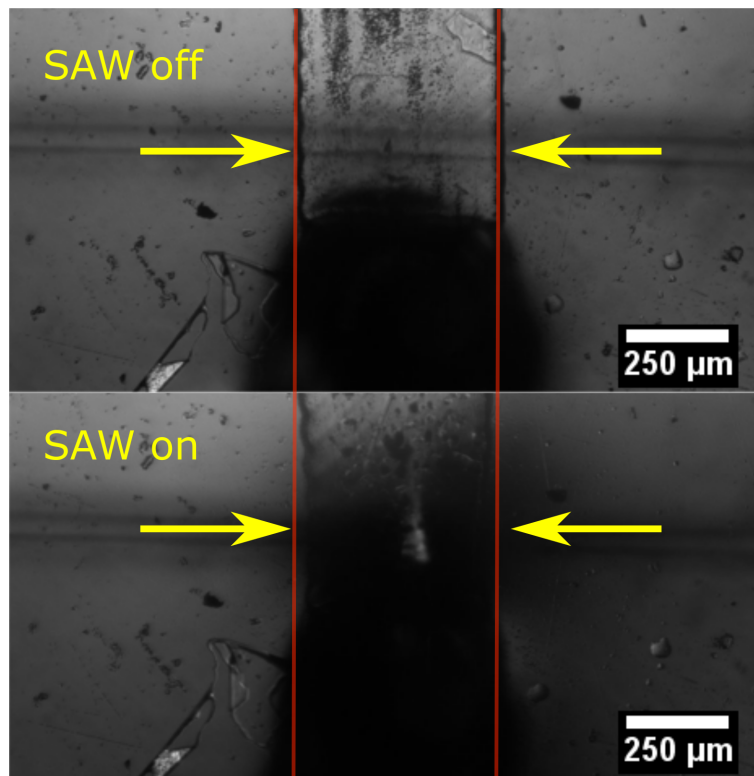
Figure 7.5: Micrographs of the PDMS channel (a) with the SAW switched off, and (b) undergoing compression after the SAW is turned on, an effect which illustrates the finite compliance of the PDMS microfluidic channel wall.

rate (Q_c = 0). However, if the pressure in the system is altered (e.g. during drive power modulation), there is a finite contribution to the flow rate arising from the PDMS, which effectively increases the fluid response time.

The compliance stemming from the low Young's modulus is one of the key contributors to high fluid response times. Another effect of the channel collapse seen in Figure 7.5 is that the hydraulic diameter of the channel is reduced during the collapse of the channel. Since the microfluidic resistance has the fourth power relationship to the hydraulic diameter, even small decrease in the hydraulic radius will lead to significant increase in the resistance. The increase of resistance during channel collapsing (degree of collapse, presumably is dependent on SAW power, as seen in Equation 7.3) will lead to longer

response time due to the fact that smaller effective pressure difference is accelerating the particles.

Schmid *et al.* showed previously that an alternative method of measuring the response time of a fluid is done by fitting an exponential decay function to the velocity profile (from Figure 7.2), this is shown in Figure 7.6 as this accurately represents the physics of the process. From this, the decay constant, τ, which corresponds to the fluid response time, can be determined. An average decay constant of $\tau = 29 \pm 3$ ms ($N = 36$) was
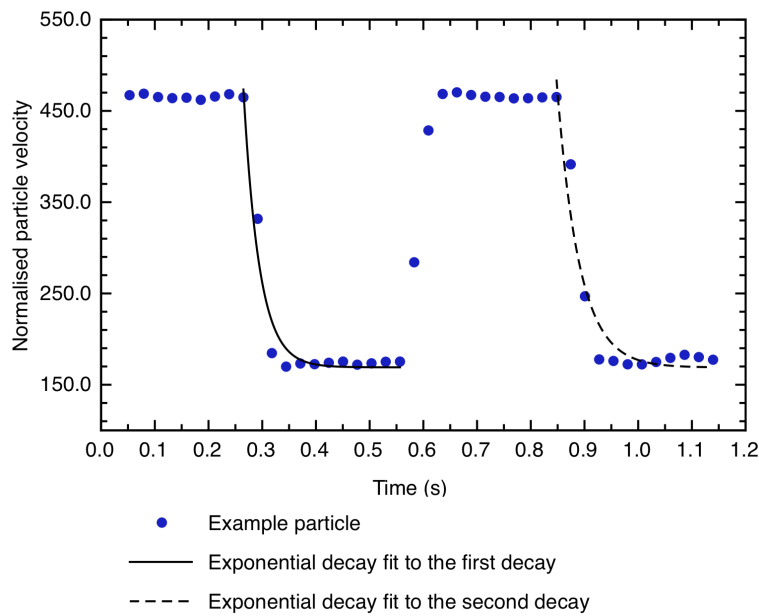
Figure 7.6: The blue dots in the plot show the particle as a function of time. The black lines are an exponential decay fitted to the velocity transition (solid line for the first decay, a dashed line for the second), that allows the decay constant of the velocity transition to be determined.

measured by averaging across all modulation frequencies given in Table 6.1. This value is significantly lower than the observed fluid response time of ~ 76.2 ms obtained previously because it estimates the pressure drop to only $1/e$ (36%) of the maximum value. Therefore, to accurately determine the particle sorting time, 3τ value could be used, which would represent the decay to within 5% of the initial value.

An important timescale in microfluidic systems is referred to as a momentum diffusion time, which characterises how quickly a given microfluidic system can dissipate a sudden disturbance. The momentum diffusion time can be approximated by conducting an order of magnitude analysis of the Navier-Stokes momentum equation:

$$\rho\left(\frac{\delta u}{\delta t} + u\nabla u\right) = -\nabla p + \mu\nabla^2 u + f \tag{7.4}$$

where ρ is the fluid density, u is the fluid velocity, t is time, ∇u is the three dimensional velocity operator, ∇p is the pressure operator, f is the volume force and μ is fluid viscosity. Since we are only considering small changes of velocity, and moreover we are not expecting the three-dimensional flow profile to change, the volume force and pressure terms on the RHS of Equation 7.4 have a value of 0. Hence, a sudden disturbance in the flow is governed by a balance between the instantaneous change in the fluid momentum and the viscous dissipation of the disturbance. Consequently, Equation 7.4 can be rewritten as:

$$\rho\frac{\delta u}{\delta t} \sim \mu\nabla^2 u \tag{7.5}$$

In Equation 7.5 the velocity, u, is dependent on the volume flow rate, Q, and the cross-sectional area of the channel, A, by $u \sim Q/A$. Furthermore, the timescale corresponds to the momentum diffusion time, so $\delta t \sim \Delta t_m$. Finally, the gradient, ∇, is dependent on the effective hydraulic diameter of the fluidic channel, therefore $\nabla = \frac{1}{D_h}$.[131] As a result, Equation 7.5 can be rewritten as:

$$\frac{\rho}{\Delta t_m}\frac{Q}{A} \sim \frac{\mu}{D_h^2}\frac{Q}{A} \tag{7.6}$$

Finally, Equation 7.6 can be rearranged to produce an expression for Δt_m:

$$\Delta t_m \sim D_h^2\frac{\rho}{\mu} \tag{7.7}$$

The ratio μ/ρ is referred to as the kinematic viscosity of the liquid. By factoring in the channel dimensions used here, and recalling that the experiments were performed in an

ethylene glycol - water mix (with a corresponding viscosity 3.6 times that of water), the momentum diffusion time can be approximated as $\Delta t_m \sim 10$ ms.

The momentum diffusion time therefore imposes a theoretical maximum sorting rate in a system that uses flow switching, to sort particles. The maximum sorting rate in such system is $\nu_{max} = 100$ particles/s, which can be obtained by:

$$\nu_{max} = \frac{1}{\Delta t_m} \qquad (7.8)$$

For example, Chen *et al.* show a µFACS system based on hydrodynamic gating where cells are sorted by closing two of three outputs in the system to divert the particles to open outlet. The reported sorting rate of such system is 1.4 cells per second.[219] Similarly, Sugino *et al.* who use heat-activated valves to selectively close outputs achieve cell sorting rates of 2.8 cells per second.[220]

To achieve higher sorting rates of similar size particles in on-chip sorting systems an external force on the system must be exerted, e.g. a dielectrophoretic force[221], acoustic force[222] or laser-based bubble generation[223].

The theoretical maximum sorting rate using the system described here can be obtained from the Figure 7.4. The fluid response time is nearly independent of the applied pressure difference, consequently the response time of the pump is estimated to be $\Delta t_{pump} = 76.1$ ms, which corresponds to the maximum sorting rate of approximately $\nu = 13$ particles per second.

7.3 Hydrodynamic fluid manipulations

7.3.1 Design considerations

Particle sorting consists of two main actions: sorting and flow focussing. Sorting, i.e. the ability to direct the particles towards different regions of the fluidic system, requires the

ability to hydrodynamically shift the liquid (and therefore, the particle) along the width of the microfluidic channel. In order to improve sorting efficiency and accuracy, focus of the fluid flow within the microfluidic channel is also desirable. Previous designs of hydrodynamic flow focusing are based upon only two distinct designs both of which have three input channels and one output.[224, 225, 226] The first design comprises side channels arranged at an acute angle with respect to the central channel (see Figure 7.7a)[227] whereas the side channels in the second design are arranged perpendicularly to the central channel (see Figure 7.7b) - typically this arrangement is used to generate microdroplets, for example.[228]

All microfluidic channels here were fabricated according to the same protocol as described in Chapter 4. Figure 7.8 shows an example of a microfluidic channel design based on the first arrangement, in which two side channels are arranged at a fixed angle with respect to the central inlet channel. A serpentine feature was added to the central channel to equalise the length of all the channels.

7.3.2 Flow focusing

As discussed previously, to enhance cell sorting rates it is important to pre-focus the fluid flow so as to confine the particles of interest to a narrow stream within the microfluidic channels. When focused sufficiently tightly, this results in particles entering the sorting region in a single file.[229] This is important for two reasons, the first of which is that for efficient sorting, it is important to be able to deflect each particle individually, and secondly any particle detection mechanism is usually restricted to processing a single particle at a time to reduce the time required for image processing and decision making during the sorting process.

Hydrodynamic flow focusing is achieved by adjusting the respective flow rates in each of the three inlet channels in order to create a "sheath" flow around a central stream
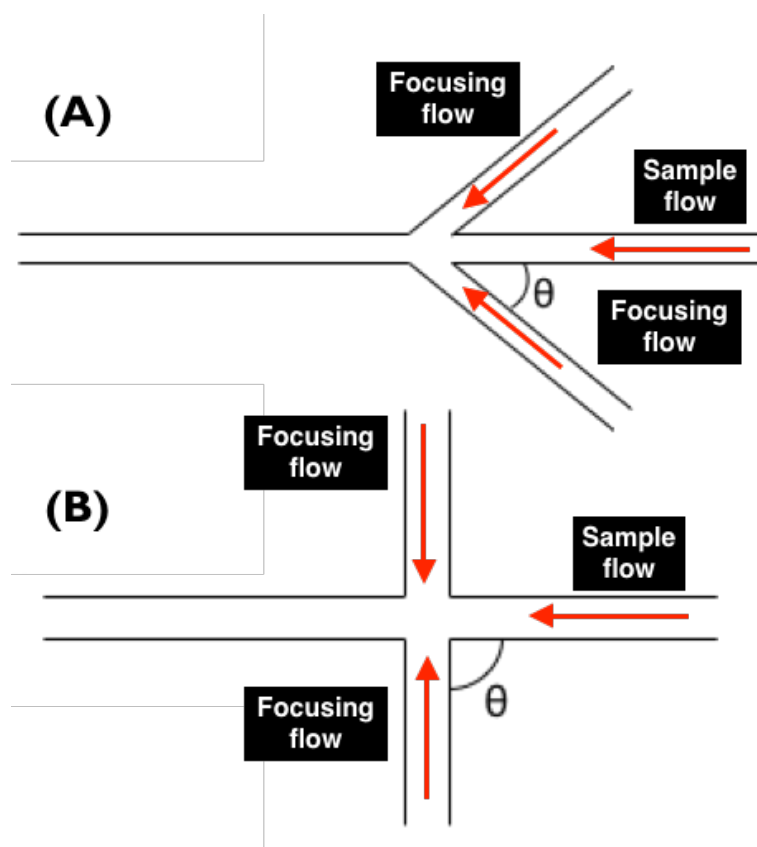
Figure 7.7: Two types of microfluidic channel designs that have been shown to achieve hydrodynamic fluid flow focusing: (a) an arrangement in which side channels are positioned at a defined angle (typically $22.5° - 45°$ with respect to the central stream, and (b) in which the side channels are perpendicular to the central channel, a design typically used for microdroplet generation.
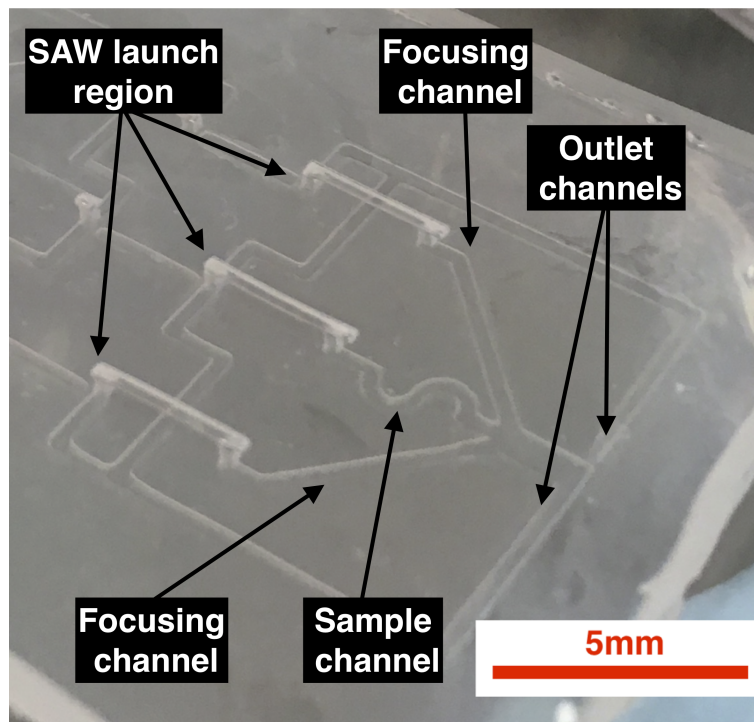
Figure 7.8: A microfluidic channel designed to allow cell sorting on chip, with side channel arrangement from Figure 7.7a.

containing the particles to be sorted. As described in Chapter 5, for a SAW-based micropump, the flow rate is directly proportional on the power applied to the IDTs. Consequently, by fixing the input power of the side channels that generate the sheath flow, and adjusting the power of the central SAW pump, it is possible to modulate the width of the central stream (as shown in Figure 7.9). The flow rate from the side channels was selected at 18.5 µl/min (achieved by fixing the applied power), whereas the central channel flow rate was set at 20.1, 18.5, 15.7 or 13.3 µl/min values (corresponding to Figures 7.9 (a), (b), (c) and (d) respectively). It can be seen that when the flow rates for all three inlet channels are equal (Figure 7.9b, the corresponding width of each flow-stream is similar.
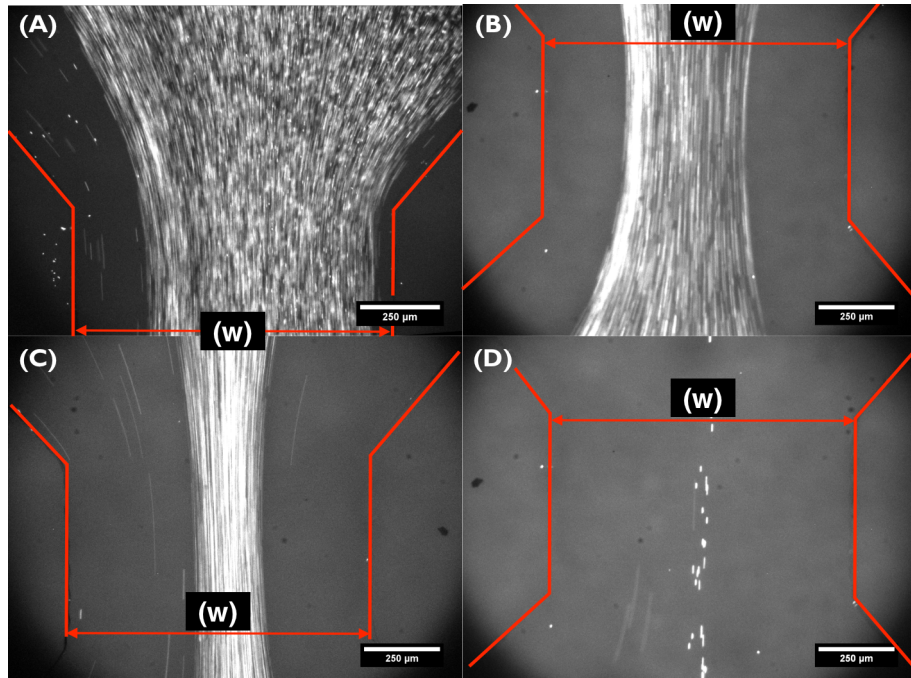
Figure 7.9: Hydrodynamic flow focusing using a three channel setup, in which fluorescent particles are flown through the central stream and flow focusing achieved by varying the ratio of the central to the side flow rates. Note that the slight shift to one side is due to the side IDTs not having identical transducer efficiency. w shows the width of the outlet channel. The central channel flow rate was fixed at 18.5 µl/min, and the side channel flow rates were varied between 20.1, 18.5, 15.7 or 13.3 µl/min values (corresponding to (a), (b), (c) and (d) respectively).

The theoretical width of the central stream, l_m, can be calculated using:

$$l_m = l_c * \frac{Q_m}{Q_{lhs} + Q_m + Q_{rhs}} \qquad (7.9)$$

where the Q_{lhs}, Q_m, Q_{rhs} are the flow rates of the LHS, central and RHS channels, and l_c is the total width of the channel after the three inlets have joined together in a single channel. A detailed discussion of this equation is given by Kirby[24]. Briefly, away from the junction the flow velocity is, across the width of the channel, parabolic as expected from Poiseuille flow (as opposed to when the three inlets join together, where the flow velocity across the width is dependent not only to the Poiseuille distribution, but also the respective inlet flow velocity), therefore applying the conservation of mass, it is possible

to calculate the cross-sectional area of each component of the flow, i.e. the LHS, central or the RHS stream. Considering all streams have the same height, then the cross-sectional area ratio will correspond to a width ratio. Figure 7.10 shows both the expected and measured values for the width of the central stream as a function of flow rate, when the side channel flow rates are fixed at 18.5 µl/min.
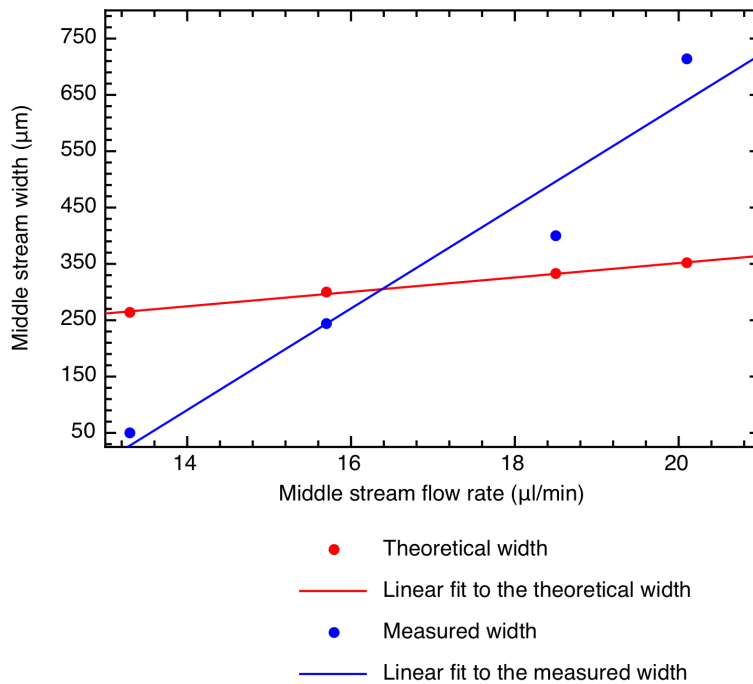
Figure 7.10: The theoretical and experimental widths of the central stream as a function of volume flow rate in the central stream. The R^2 values of linear fit for theoretical and experimental results were 99.6% and 93.6%.

It can be seen in Figure 7.10 that the measured width values do not follow the corresponding predicted widths. This could arise from the fact that the equation used to predict the stream width assumes that the channel walls are infinitely rigid and therefore that the channel volume does not change. However, as discussed in Section 7.2 the PDMS channels used here have a finite compliance, which is likely to affect the measured flow rates, making them deviate from predicted values.

7.3.3 Flow shifting

The most important part of on-chip particle sorting system is the ability to shift the position of individual particles across the width of the microfluidic channel, i.e. to deflect them into different channels or sorting chambers. It is possible to shift the central stream, by fixing the flow rate of corresponding micropump, and then to adjust independently the power applied to the side channel IDTs. An increase in flow rate from one of the side channels coupled with a simultaneous decrease in flow rate from the other, results in the shift of the central stream as demonstrated in Figure 7.11.
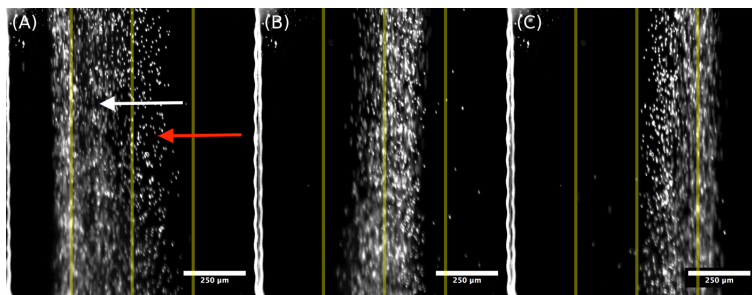
Figure 7.11: Micrographs of flow shifting of a central flow stream with a fixed flow rate of 8.1 μl/min, achieved by adjusting of the power applied to the side IDTs to produce corresponding flows from the LHS and RHS side channels of (a) 8.1 and 12 μl/min, (b) 9.7 and 10.1 μl/min and (c) 10.1 and 8.4 μl/min. Note the slower particles that are in focus and at the bottom of the channel lag behind the particles in the central stream, because of lower forces that are actuating the shift at the bottom of the channel. This is due to the nature of the flow in microfluidic channels, i.e. the Poiseuille flow.

Shifting of central stream is dependent on the fluid response time, which characterises the time it takes for the SAW pump to adjust the pressure (as discussed in Section 7.2). The flow rate in the central channel was fixed to 8.1 μl/min in Figure 7.11, whilst the flow rates from the LHS and RHS side channels were set to (a) 8.1 and 12 μl/min, (b) 9.7 and 10.1 μl/min, and (c) 10.1 and 8.4 μl/min.

During these experiments, a number of particles were observed to travel at a slower

velocity than the majority, as evidenced by the lack of motion blurring of some particles in Figure 7.11. This can be explained by considering the nature of flow in microfluidic channels, in which the fluid velocity close to the microfluidic channel walls (indicated by the white arrow in Figure 7.11a) is significantly slower than it is in the bulk of the liquid (red arrow, Figure 7.11a). This particle velocity distribution arises from the Poiseuille flow profile in three-dimensions, as shown in Figure 7.12.[230] As a result of Poiseuille
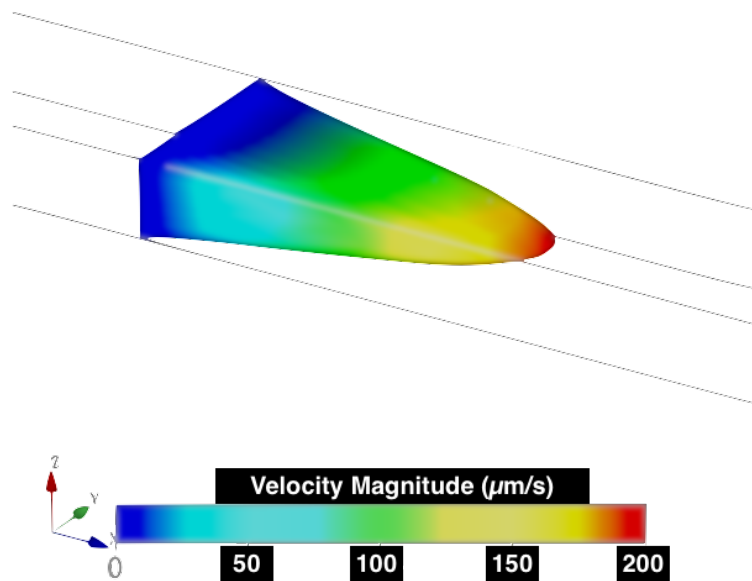
Figure 7.12: A COMSOL simulation of Poiseuille flow in a microfluidic channel in three-dimensions. Image adapted and processed from [231].

flow, particles present in the centre of the channel respond quicker to a change in pressure caused by adjusting the flow from either side channel, and are therefore shifted more quickly to one side than those positioned closer to the channel walls. This results in a broadening of the focussed flow stream, in which the slower particles lag the faster particles and are therefore located to one side of the focussed flow.

7.4 Proof-of-principle particle sorting using a SAW micropump

7.4.1 Design considerations

Two subsequent designs of microfluidic channel, type (a) and (b) were tested as proof-of-concept, on-chip cell sorting devices, as shown in Figure 7.13a and 7.13b, respectively. Each on-chip particle sorting system designed here consists of three-inlet channels, in which the sample of interest is injected into the central channel and the two side channels are used to generate a sheath flow to focus the central stream (as shown in Section 7.3.2). The side streams are also used to actuate the position of the sample within the central stream to allow it to be sorted into a chosen outlet channel, of which there are two. The proposed sorting system operates by directing the particles of interest down either the RHS or the LHS outlet channels, as seen in Figure 7.13.

Automated decision making and particle detection techniques are not discussed here, as the focus is to demonstrate proof-of-concept particle flow manipulation using SAW micropumps. Considering that the racetrack channels are designed to recirculate the material, once the particles of interest have been sorted into either outlet channel, they must be removed from the flow and collected in a manner that does not prevent liquid recirculation. One option is to introduce micropillars to capture the particles (or cells later on) whilst allowing fluid to pass through, but this will result in the fluidic channel resistance increase as more and more particles are captured thereby reducing the operating time of the device.[232, 233] Alternatively, it is possible to exploit the sedimentation of the particles (described by Equation 6.6) by building a well that is long enough to allow the particle to sediment sufficiently (dependent on the sedimentation velocity), but which will not increase the effective flow resistance as more particles are captured (see Figure 7.14 for an example).
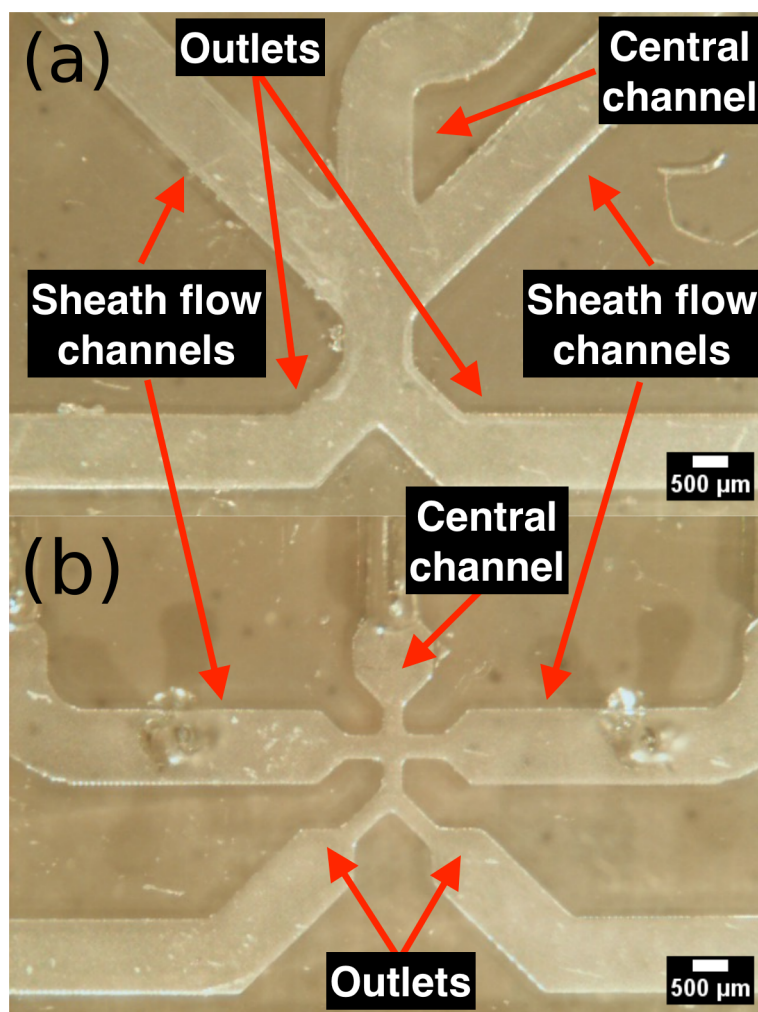
Figure 7.13: Two types of designs used for on-chip particle sorting in which the side channels are arranged (a) at 45° (type a) and (b) 90° (type b) with respect to the central channel. Each design contains two outlet channels into which particles of interest can be deflected.
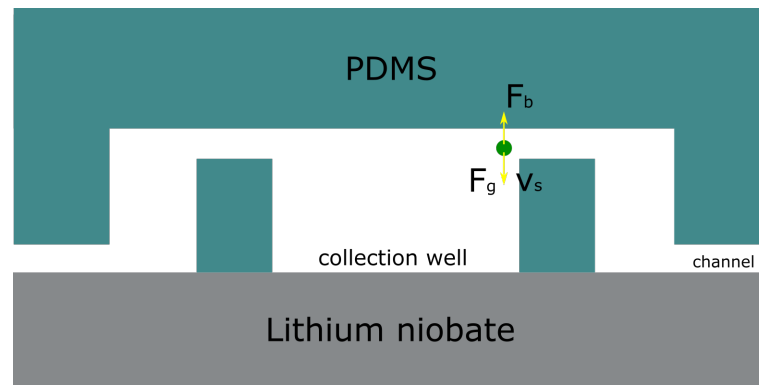
Figure 7.14: A schematic depicting the sedimentation-based mechanism of capturing the sorted cells into the sedimentation wells. An example particle with the gravitational and buoyancy forces depicted on the particle before the development of drag force which develops as the particle reaches the terminal sedimentation velocity.

The next step is to analyse the forces exerted on the particles during the sorting process using both designs, type(a) and type (b), seen in Figure 7.13.

7.4.2 Force calculations

In order to identify which design type (a) (angled side channels) or type (b) (perpendicular side channels) is expected to produce the best particle-sorting capabilities, an analysis of the forces exerted on a particle (Figure 7.15) was performed for each design by setting the angle between the central and the side channels as a variable, in which case type b corresponds to an angle $\alpha = 90°$.

Consider a single particle moving in the central channel with a coordinate value $x < {}^w/_2$, where w is the width of the channel and $x = 0$ is defined as the left hand edge of the central channel, as shown in Figure 7.15.

Figure 7.15a shows the forces acting on a particle when it has entered the sorting region. F is the force exerted on the particle due to the pressure difference in the sorting region channels, F_d with x and y suffixes, indicate the drag force acting along the x and y axis
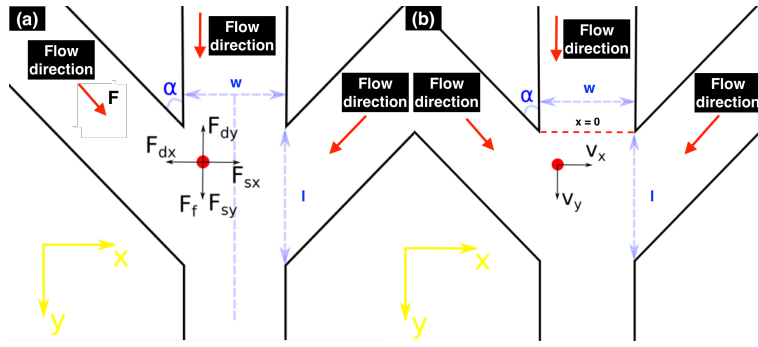
Figure 7.15: Analysis of the forces exerted on the particle by the sheath flow (a) and the consequent velocities developed by the particle during sorting from RHS to LHS of the channel (b).

respectively. F_f is the driving force exerted on the particle by the fluid flow, which acts along the y-axis, F_{sx} and F_{sy} are the x and y components of the sorting force, generated by the pressure difference across the channel.

The interaction time between the particle and the sorting force is determined by the particle velocity in the y-direction. This interaction time is used to determine the relationship between the velocity of the fluid, and the necessary lateral velocity that must be induced on the particle by the sorting force in order to adjust the particle trajectory sufficiently such that it enters the RHS sorting channel.

If we assume that the x-coordinate of the particle must be actuated by the time the particle has travelled half of the length of the sorting region, l (indicated in Figure 7.15), the distance travelled in the y-direction is therefore:

$$Y_{max} = \frac{l}{2} \tag{7.10}$$

The vertical coordinate $y = 0$ is set to coincide with the position of first interaction between the particle and the side stream flow, i.e. the point at which the central and side channels intersect. Thus interaction time between the force and the particle is given by:

$$\Delta t_{int} = \frac{l}{2v_y} \tag{7.11}$$

The main difference between type (a) and type (b) channel designs is the angle of the sorting force, F. In a type (a) device therefore, it can be seen that only x-component of the force contributes to a change in the x-coordinate of the particle. At the same time y-component acts to increase the velocity of the particle, which in turn reduces the interaction time between the force and particle. This therefore suggests that, for the same flow rates from the side channels, the type (a) channel designs will produce weaker sorting forces than the type (b) design, which in turn will result in reduced particle sorting rates in type (a) devices.

Since particles in low Reynolds numbers systems almost instantaneously reach their terminal velocity, the transient characteristics of the particles can be ignored and only the steady state is considered. Since velocity is an additive term, the velocity components can be summed along the y-axis (see Figure 7.15b):

$$v_y = v_f + v_s \tag{7.12}$$

where v_f is the velocity of the fluid flow, and v_s is the velocity induced along the y-axis by the sorting force. The width of the channel, w, and the interaction length, l, are related by $l = w * sin(\alpha)$, where α is the angle between the central and the side channel, it is therefore possible to rewrite Equation 7.11:

$$\Delta t_{int} = \frac{w}{2 * (v_f + v_s) * sin(\alpha)} \tag{7.13}$$

The interaction time is then used to determine the relationship between the fluid flow velocity and the required velocity in the x-direction which will ensure that the particle trajectory is altered sufficiently enough to allow sorting. The particle velocity along the x-axis can therefore be written as:

$$v_x = \frac{w}{2\Delta t_{int}} \tag{7.14}$$

Here we have assumed that the particle must travel the maximum possible distance, which corresponds to half of the channel width according to the streamlines seen in Figure 7.16.
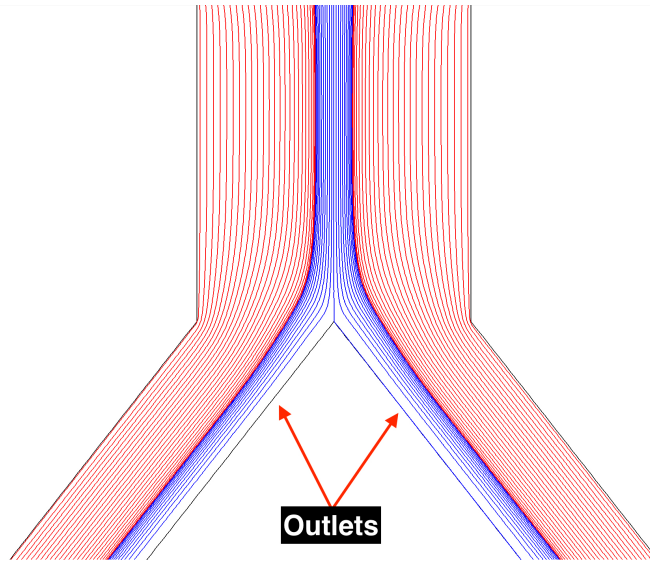
Figure 7.16: A finite element model of the fluid streamlines in a three-inlet setup, in which the fluid in the central channel (blue streamlines) is focused using equal volume flow rates from the side channels (red streamlines). The volume flow rate ratio between the sheath flows and the central was 4 to 1. It can be seen that the streamline exactly in the central of the channel stops where the channel divides in two outlets. Therefore if the particle is to be moved in from the LHS to RHS, in the worst case scenario, it must travel a distance equal to half of the width of the channel. This simulation was performed with help from *Dr Akshay Kale*.

The terms v_x and v_s are respectively the x- and y-components of velocity, v, induced on the particle by the force F generated by the difference in pressure between the side streams, as discussed. Therefore:

$$v_x = v * sin(\alpha) \tag{7.15}$$

where, for type b channels, $\alpha = 90°$ and $v_x = v$. Additionally:

$$v_s = v * cos(\alpha) \tag{7.16}$$

By combining Equation 7.13 with Equations 7.15 and 7.16, Equation 7.14 can be re-

written as:

$$v * sin(\alpha) = ((v_f + v * cos(\alpha)) * sin(\alpha) \tag{7.17}$$

It can be seen that the channel width does not affect the relationship between the sorting and flow velocities, though this solution is only expected to be valid for constant channel widths. By rearranging Equation 7.17, the sorting velocity, v, can be calculated:

$$v = \frac{sin(\alpha)}{sin(\alpha) - sin(\alpha)cos(\alpha)} * v_f \tag{7.18}$$

It can be seen that the sorting velocity is dependent only on the angle between the side and central channels, and the initial fluid velocity. Figure 7.17 shows a plot of the velocity ratio v/v_f as a function of angle α. As $\alpha \to 90°$, corresponding to a device in which the side channels are perpendicular to the central channel the ratio tends to unity. A ratio of greater than unity for all other cases, indicates that the sorting is becoming increasingly less effective as the angle between channels becomes smaller.
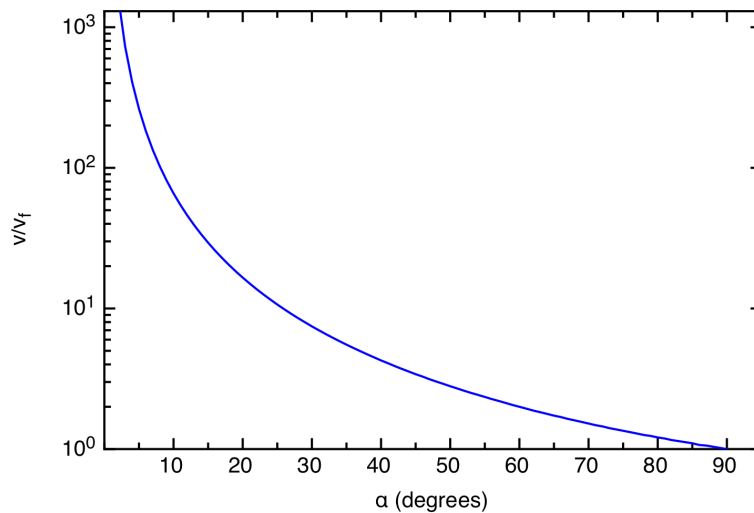
Figure 7.17: A plot of the ratio between the total fluid velocity in the y-direction as a function to the applied fluid velocity and the angle between the central and side channels. Note the logarithmical plot on the ordinate axis.

The minimum necessary pressure difference between both side channels required to

induce fluid a velocity, v, (i.e. to sort a particle from one side to another) can be obtained by considering the equilibrium drag forces along the x-axis, as shown in the Figure 7.15b:

$$\vec{F}_{sx} + \vec{F}_{dx} = 0 \tag{7.19}$$

Consequently:

$$F_{sx} = F_{dx} \tag{7.20}$$

The force exerted on a single particle with a radius, r in a liquid with viscosity, μ, therefore is:

$$\Delta p * 4\pi r^2 * sin(\alpha) = 6\pi\mu r v \tag{7.21}$$

where Δp is the pressure difference between the two sheath flow channels, by substituting Equation 7.18 for the velocity, v, the relationship for Δp is given as:

$$\Delta p = \frac{3\mu}{2r} * \frac{sin^2(\alpha)}{sin(\alpha) - sin(\alpha)cos(\alpha)} * v_f \tag{7.22}$$

Equation 7.22 shows the general solution for the minimum required pressure difference between both sheath flows for a given flow velocity in the central channel. For the two geometries, type (a) and type (b) discussed in Section 7.3, the angle $\alpha = 45°$ and $90°$ respectively. The corresponding pressure difference required to sort a particle of radius $r = 1$ μm in water (viscosity $\mu = 10^{-3}$ Pa/s) can therefore be calculated for the type (a) and type (b) devices using, respectively:

$$\Delta p_a = 3.63 * 10^3 * v_f \tag{7.23}$$

and

$$\Delta p_b = 1.5 * 10^3 * v_f \tag{7.24}$$

Given that the maximum flow velocity generated by the SAW micropumps used here was $v_f = 5$ mm/s, then the resulting pressure differences for type a and type b devices are $\Delta p_a = 18.2$ Pa and $\Delta p_b = 7.5$ Pa. This suggests that the perpendicular channel design

is more efficient at particle sorting as a lower pressure difference between the two sheath flows is required in order to deflect the particles.

Fluid takes approximately 80 ms to change velocity in response to a change in applied power levels. However, in addition to this time, there is also the interaction time (Δt_{int}) required to physically move the particle from the LHS to the RHS outlet. Thus the maximum sorting rate for a SAW pump is given by:

$$\nu = \frac{1}{\Delta t_{pump} + \Delta t_{int}} \tag{7.25}$$

The interaction time as determined by Equation 7.13 shows reducing the channel width will decrease the interaction time, which will consequently increase the sorting rate of the on-chip system. For the perpendicular channel design used here, $\Delta t_{int} = 25\ ms$. Consequently, the maximum sorting rate achievable by the system is expected to be $\nu = 10\ particles/s$.

If the solution is made up of uneven numbers of cells to be sorted (i.e. the target cells are rare in the solution), then by adjusting the central position of the stream such that the majority of the cells without deflection go to the sorting chamber will increase the sorting rate. This is because to increase the sorting rate, the flow should be deflected as infrequently as possible, thus approaching the maximum sorting limit imposed by the fluid response time.

Finally, it must be considered that the examples described here are simplistic two-dimensional models for the purpose of evaluating the differences between channel designs. This example does not take into account the fact that the particle velocity is not only a function of the width but also a function of height within the channel. This simple analysis is therefore relevant for a particle which remains at a fixed height within the channel, and which has an x-position that is at least 50 μm away from any channel wall as seen in the flow profile shown in Figure 6.8. In the next section, the actual particle sorting rates will be evaluated through experimentation.
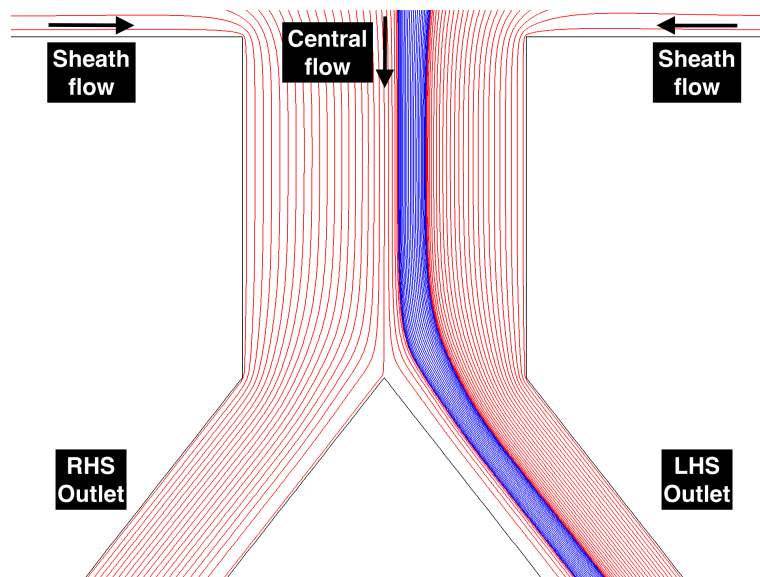
Figure 7.18: A schematic of the streamlines of the fluid with the focused stream of particles (in blue) being by default directed to the LHS channel with the stream being as close to the central of the channel as possible as to decrease the time needed to direct the particles. This figure was produced with help from *Dr Akshay Kale*.

7.4.3 Particle sorting results

Having derived a framework for the required interaction time between the sorting force and the particle, this section is concerned with evaluating the physical particle sorting capabilities with type (a) and type (b) devices. The first set of experiments were performed using type a (angled) microfluidic channels, with $\alpha = 45°$. It was calculated in the previous section that by applying a pressure difference of 18.2 Pa between the two side channels, the maximum particle sorting rate of 13 particles/s will be obtained. Figure 7.19 shows that it is possible to direct a stream of particles into the left hand or right hand outlet channel by applying a pressure difference of 12 Pa, which was the maximum pressure difference that could have be applied. It was not possible to apply the theoretical maximum of 18.2 Pa because of the high sheath flow rates necessary to focus the central flow during the experiments. The expected transition time between the two regimes is
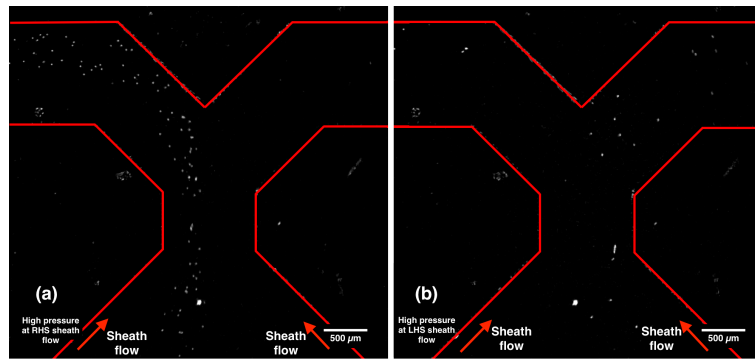
Figure 7.19: Micrographs of a type a device in which the particle stream has been directed into (a) the LHS outlet channel (as shown by the arrow), and (b) the RHS outlet channel, both by application of a 12 Pa pressure difference between the side channels.

on the order of 160 ms, as the fluid response time Δt_{fluid} = 75 ms and the expected interaction time therefore is 235 ms, however, the transition time between the regimes was measured to be on the order of a second - significantly longer than expected. This was found to be the case with even higher pressure differences, and it was therefore concluded that the angled design is not appropriate for the on-chip sorting system.

Therefore the next step was to utilise the perpendicular design for on-chip sorting experiments. Figure 7.20 shows time-lapse images of a pair of particles which were sorted sequentially into first the left hand, and then the right hand outlet channel.

By recording and analysing N = 108 particles sorted from the LHS to the RHS channel, it was possible to construct a contour plot depicting the force exerted on the particle as a function of its location within the channel, as shown in Figure 7.21.

The smallest force exerted on the particles was found to be ~3 pN (blue colour), which occurred in the regions, located furthermost from the high pressure regions. Conversely, the maximum force was recorded immediately adjacent to the high pressure inlet, and had a peak amplitude ~15 pN. Intuitively it is expected that the particle will experience the maximum sorting force when it is adjacent to the centre section of the side channel, due
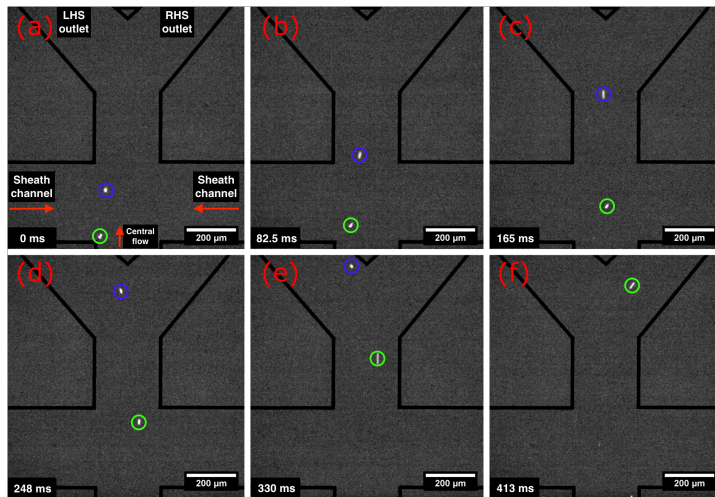
Figure 7.20: A time-lapse of two particles being sorted into two different sorting chambers recorded at (a) 0ms (defined when both particles are present in the interaction area with the side channels), (b) 82.5 ms, (c) 165 ms, (d) 248 ms, (e) 330 ms, (f) 413 ms. Particle sorting was achieved by setting the pressure difference between side-channels to 12 Pa, where the pressure drops from right to left to sort into the left outlet, and *vica versa*.

to the Poiseuille flow distribution (i.e. the higher velocity flow from the side channel will be at its centre).

The force map was constructed by first measuring the particle position as a function of time, and from this extracting the force acting on the particle. Briefly, by recording the particle's (x, y) coordinates in any given frame of the recording, the particle displacement between frames, and therefore the particle velocity, can be extracted. By assuming that the particle is at its terminal velocity in each frame, the force exerted can then be calculated using Equation 7.21, and subsequently the pressure difference between the two side flows can be obtained using Equation 7.22, in which the v_f is the measured velocity in x-direction. See Appendix B for a table of values for displacement as a function of the particles x and y coordinates.
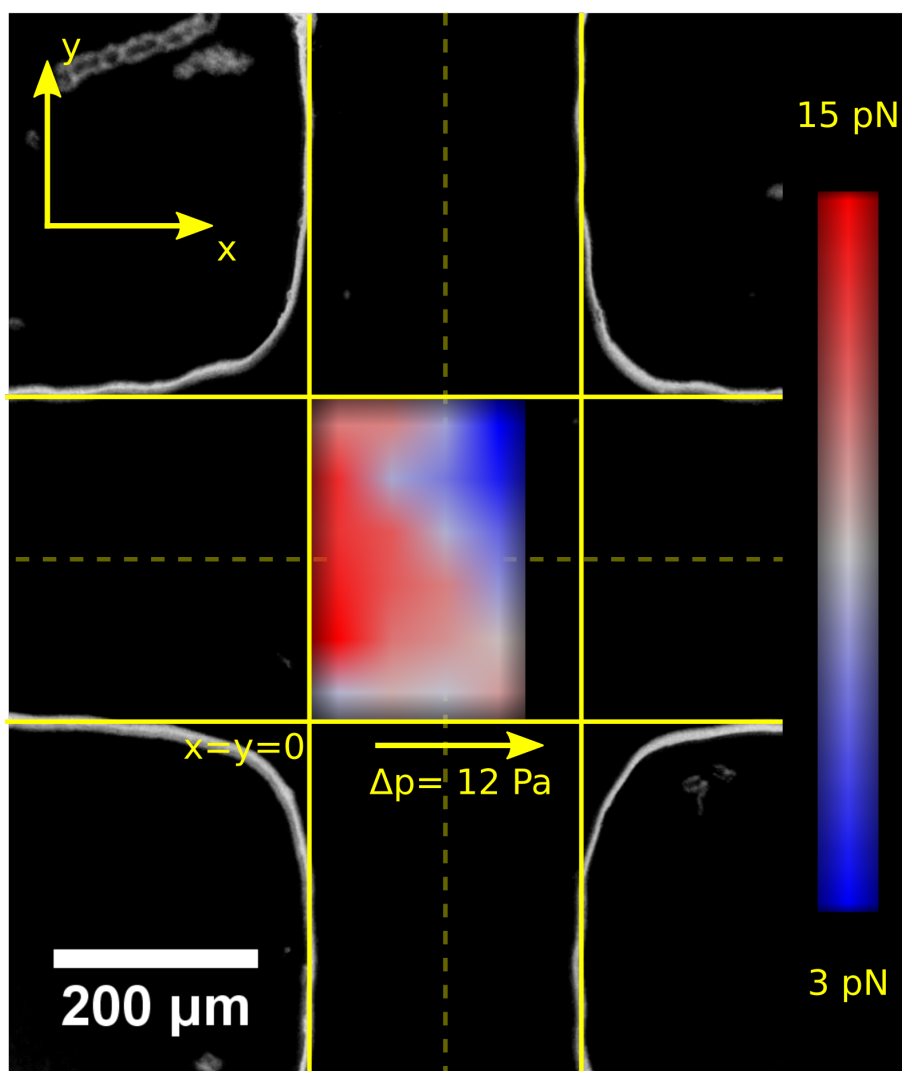
Figure 7.21: A map of the force exerted on a particle as a function of its x and y position. The distribution of the force across the side channel opening is likely a result of the Poiseuille-like fluid flow within the side channel, in which the maximum flow velocity is observed at the channel centre. The force ranges from 3.2 pN (blue regions) to 15.2 pN (red regions). The pressure difference across the sorting region is 12 Pa derived from the particle trajectory.

The previous discussion produced an effective pressure difference value from observations of the particle trajectory as a function of time (i.e. the pressure difference that drives the movement of particle along the x-axis if no other forces are present). For comparison, the actual applied pressure difference, derived from the flow rates generated by the micropumps, can be calculated using:

$$\Delta p = p_{rhs} - p_{lhs} \tag{7.26}$$

in which each pressure can be obtained by applying the Hagen-Poiseuille law [24]:

$$p = QR_H \tag{7.27}$$

where Q is the volume flow rate generated by the IDTs, and R_H is the hydraulic resistance of the microfluidic channel given by:

$$R_H = \frac{8\mu L}{AR^2} \tag{7.28}$$

In Equation 7.28 μ is the liquid viscosity, L is the distance between the two points across which the pressure is applied, A is the cross-sectional area of the channel, given by $A = \pi R^2$ and R is the hydraulic radius of the channels. Since all fluidic channels used in this project have a rectangular cross-section, the hydraulic radius is given by $R = \frac{w*h}{w+h}$, where w and h are channel width and height respectively.

This yields values of $p_{rhs} = 68.6$ Pa and $p_{lhs} = 58.4$ Pa and consequently the pressure difference applied across the particle is $\Delta p = 12.2$ Pa.

The discrepancy between the measured pressure difference and the applied pressure to each side channel is likely to arise from multiple sources. The main discrepancy is likely to result from the assumption used in Equation 7.27 that the PDMS channel is rigid. However, as discussed in Section 7.2 the microfluidic channel has a none-zero compliance due to the elasticity of the PDMS, which results in energy from the pump being lost in expansion/contraction of the channel. Secondly, due to changing channel dimensions, the

microfluidic channel resistance will also change, again, having negative effect on sorting efficiency.

It is possible to estimate the time required to move a particle trajectory from the LHS sorting channel to the RHS sorting channel by considering the particle's average velocity. If the particle is initially located at $x = 0$ (as labelled in Figure 7.21), then it must travel a distance $l = {}^w\!/_2 = 125$ μm. Thus the interaction time between particle and the sorting force whilst traversing this distance is 200 ms. Using Equation 7.25 it is possible to determine the *minimum* sorting rate for a given pressure difference, which for a pressure difference of 12.1 Pa is $\nu = 3.4$ particles/s.

Since not all particles will be located at $x = 0$ when entering the sorting region, the *mean* sorting rate at this pressure difference will be somewhat higher. Since the flow is initialised such that the particles travel towards the LHS outlet by default, the RMS particle x-displacement will be $x = 62.5$ μm, consequently the *mean* sorting rate of the type (b) operating with a pressure difference of 4.3 Pa is calculated to be $\nu = 5.2$ particles/s.

Having established a framework to calculate both the minimum and the mean sorting rates, the sorting force exerted on a particle, and the applied pressure, these characteristics were then calculated for different applied pressure differences as shown in Table 7.2

Table 7.2: Various characteristics of particle sorting at different applied pressure differences.

Applied pressure difference, Pa	Sorting force, pN	Measured pressure difference, Pa	Minimum sorting rate, s^{-1}	Mean sorting rate, s^{-1}
12.1	3.2 ... 15.2	0.3 ... 1.2	3.4	5.2
26.3	6.2... 28.3	0.5 ... 2.3	4.8	6.5
95.0	7.6 ... 34.5	0.6 ... 3.9	6.0	8.0
135	12.4 ... 52.3	1.0 ... 5.8	7.4	9.5

7.5   Conclusions

The aim for this Chapter was to demonstrate the use of the SAW micropumps for hydrodynamic flow switching, such as might be used in a micro FACS device, with the emphasis on demonstrating particle sorting. The flow manipulation capabilities were investigated using two device geometries compromised of three inlet channels and two outlet channels: type (a), in which the side inlet channels were arranged at $45°$ angle to the central channel, and type (b) devices, in which the side channels were perpendicular to the central channel. The first part of this Chapter was devoted to studying the transient characteristics of the pump, specifically the transition time required for the flow velocity to alter when the pump pressure was altered between two states. It was found that the response time of the pump is approximately constant for different pressure differences within the range measured, although it is expected that the response time would be shorter for smaller pressure differences.

This was followed by demonstration of hydrodynamic flow manipulation, including flow focussing and flow switching, which are required for on-chip particle sorting. It is possible to predict the width of the central stream during flow focusing by application of the Poiseuille-Hagen law. However, the experiments showed significant deviations from the predicted values, which again was attributed to the compliance of PDMS; the Poiseuille-Hagen law assumes infinitely rigid microfluidic channel sidewalls.

Finally, proof-of-principle particle sorting was demonstrated using both type (a) and type (b) devices. Experimentally, the sorting rates achieved using type a devices were significantly less than one particle per second. Therefore the perpendicular channel type (b) design was used for subsequent particle sorting experiments since it was predicted to require a significantly lower pressure difference to induce the same sorting force on the particles.

By applying pressure difference of 12 Pa between side channels in a type (b) device, a

sorting rate of 10 particles/s was expected. However, by tracking the velocity of particles within the channel, a real sorting rate of 5.2 particles/s was observed, which would correspond to a pressure difference experienced by the particle of only 1 Pa. Furthermore, by mapping the force experienced by a particle during sorting, it was found that the force is not constant throughout the sorting region. This has implications on the sorting algorithm; namely, the particle must be sorted into the correct streamline before travelling halfway through the sorting region.

Finally, the pump described has the a maximum sorting rate of 9.5 particles/s, achieved at 135 Pa, which is the maximum value achievable here. This is significantly lower than the previously reported maximum values which are around 1000 particles per second in systems that utilise external forces to actuate the particles, yet it is comparable to systems that utilise hydrodynamic fluid flow manipulations for particle sorting.

Again, the principle explanation for the low sorting rates is the non-zero compliance of PDMS, that increases the pump response time. Thus, to improve the sorting rate one of the first steps would be to use a different (more rigid) material for the microfluidic channels. Alongside changing the channel material, a higher sorting rate might be achieved through more complex channel designs that pre-focus the sample stream prior to entering the sorting region.

This page is intentionally left blank.

Chapter 8

Conclusions and Outlook

This thesis outlines the development of an efficient SAW micropump suitable for LOC applications including for example on-chip micro-FACS device. This chapter begins by outlining the key achievements made in the project, followed by a discussion of the target POC technologies suitable for integration with SAW micropump. The final three sections discuss possible avenues for the future work in this field.

8.1   Summary of key achievements in this thesis

Chapter 5 reviewed the fabrication of SAW-micropumps formed on $LiNbO_3$ substrates, alongside their integration with microfluidic channels and subsequent electrical characterisation of the devices. Further, the chapter described a framework for evaluating the coupling efficiency of the applied power into the SAW and its dependency on SAW wavelength. This was next expanded into developing a method by which the pump operating parameters from PIV data. Finally, these investigations culminated in fabrication of the first-generation SAW micropumps, which were based on the planar pumping principle in which only the forward motion of the SAW was utilised to pump an overlaid fluid flow within a microfluidic channel. The results, obtained using an enclosed

PDMS channel, were comparable to those previously published for devices using glass microfluidics, even though the latter is inherently better suited to SAW transmission.

Chapter 6 began with a discussion of how a SAW interacts with an overlaid liquid in three dimensions, which underpinned the need to develop three-dimensional microfluidic channels. The method used to fabricate three-dimensional microfluidic channels employed a combination of planar, 3D printed moulds combined with acetone-soluble beams positioned on top of vertical pillars. This technique allows preparation of closed three-dimensional microfluidic channels in a single PDMS cast, which removes issues in PIV analysis caused by interfacial scattering in multi-layer PDMS devices. These channels were then integrated with a SAW micropump, and used to demonstrate significantly improved pump performance. The best performing devices produced pressure gradients of over an order of magnitude higher than previously published devices whilst operating at significantly lower applied power levels. The results in this chapter formed the basis of a publication.[62]

Chapter 7 focused on using the SAW micropump described in Chapter 6 to demonstrate hydrodynamic fluid manipulation, including flow focusing and flow switching. Firstly, the response time of the pump was characterised in order to understand the maximum theoretical particle sorting rate of the pump. Finally, three SAW micropumps were combined to build an on-chip flow cytometer which was capable of sorting up to 10 particles per second (mean rate). This was achieved by focusing the fluid flow to impose single-file particle entry in the sorting region, where the flow shifting was then used to alter the particle trajectory between two outlet channels.

8.2 Suitability of the SAW pump in POC device applications

The main outcome from this thesis is a well characterised Rayleigh SAW-based micropump. The intended application for such pump throughout the work is in a POC device, for which the following criteria are the key:

- Small footprint for on-chip integration;

- Low-power operation;

- Sufficiently high performance in terms of volume flow rate and the pressure gradient;

- Low cost.

The SAW micropump described here has a small footprint, as active region of the pump is the IDT, which have a typical surface area a only few tens of mm^2 (as seen in Chapter 5). Secondly, Chapter 6 shows that these pumps can be actuated by applying a continuous, low power input (<0.5 W), and yet still deliver volume flow rates of tens of microliters per minute, which is an appropriate value for a range of POC devices. Furthermore, the SAW micropump described here are using a low-cost gain block and AC oscillator. It is easy to overlook the importance of the connection between the driving unit and a POC device cartridge: for example, any membrane-based pumps require a physical actuator, and the pumping performance will be dependent on the actuator head alignment with respect to the membrane centre. In the case of a SAW micropump, as long as there is an electrical connection between the IDTs and the driving circuit, the pump will perform as expected.

Currently, the single biggest drawback of the SAW micropump described here, as it was mentioned during the literature review, is the price. A standard 150 mm wafer of $LiNbO_3$

costs £200, and yields just over 500 devices used here[1].[234] When the cost of metal deposition required to make the fine IDTs is included, the pumping unit alone will cost >£1, which might be too expensive to be commercially sustainable for rapid and cheap diagnostic tests.

Throughout this work, PDMS was used as the material of choice for microfluidic channel fabrication. Although, PDMS has various useful qualities, it is generally regarded as unsuitable material for large scale manufacturing, which means that for SAW pump use in a setting where high volume of samples are required, a switch to a different material would be needed. Various thermoplastics, such as polypropylene, polycarbonate and others, usually are regarded as well suited for mass manufacturing owing to the fact that these materials are suited for injection moulding.[45] This brings the only other notable drawback of SAW micropump technology described here, it is the integration of the pump with the microfluidic channels formed in thermoplastics or other materials due to the piezoelectric and pyroelectric nature of $LiNbO_3$. This material property prevents use of thermal bonding which is conventionally employed for mass production of POC devices (which was one of the factors why PDMS was used here). An alternative technique would be to use UV adhesive to bond the $LiNbO_3$ chip to the microfluidic channels, for example, yet requires more processing steps.

8.3 Future work

8.3.1 Rapid on-chip PCR

The SAW micropump described in the Chapter 6 have three key characteristics that are required to produce an efficient on-chip PCR system - a high volume flow rate, the

---

[1]The calculation was done with the following assumptions: die dimensions $(w \times l)$ 5×5 mm, 0.2 mm saw thickness, 5 mm edge clearance, 10 mm wafer flat

capability to rapidly actuate a small volume of liquid and a short response time.[88, 235] An on-chip PCR also requires a heater system, which can be integrated in the form of resistive electrode heaters.[236, 115] The advantage of microfabricated heaters is their small footprint and the possibility of depositing both the SAW IDTs and the heaters in the same step. Physical realisation of an on-chip PCR device could be quite simple as the PCR will typically require either two or three different temperature zones, thus the same circular contour design as seen in Chapters 5 and 6 can be utilised, as described in Figure 8.1. The liquid can be actuated between the annealing and extension zones, and DNA amplification could be monitored using real-time fluorescence (since PDMS is optically transparent).[237, 238] This would effectively present an on-chip version of extreme PCR setup which was done on external set of heaters by Trauba and Wittwer.[239] The advantage of such an on-chip PCR device would be the reduced foot print compared to conventional setup where external heaters are necessary and increased throughput owing to reduced sample volumes, fast response time and the high flow rate of the SAW micropump.

8.3.2   Alternatives to PDMS

PDMS has a finite compliance, i.e. it can absorb and release energy from/to a coupled system. Sometimes the compliance can be useful, e.g. in membrane-based pumping, but in other circumstances (such as particle sorting) it can impede device performance as demonstrated in Chapter 7 by the low achievable particle sorting rates. Therefore, a logical investigation would explore alternative channel materials to replace PDMS. The earlier of potential applications for SAW micropumps included high-value POC devices, in which high device function density is required. High microfluidic channel density can only be achieved using surface micromachining techniques. Although it is possible to use photolithography, for example, on advanced thermoplastics[40], more common materials which are compatible with such processing are silicon and glass.[46]
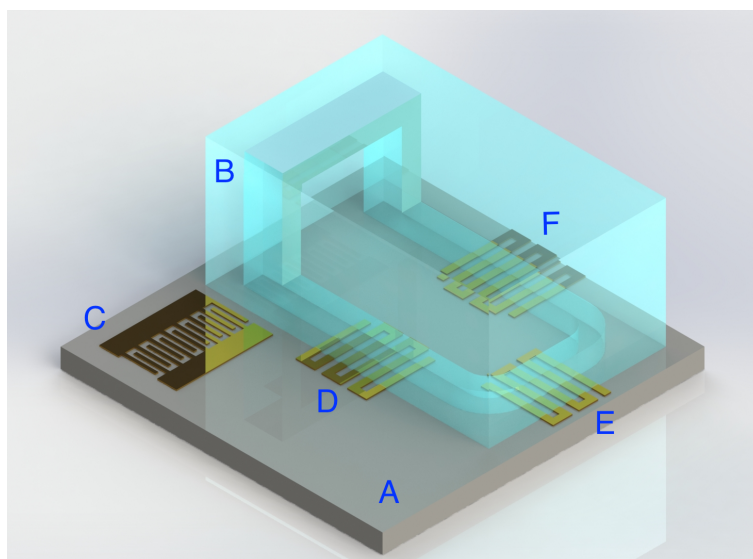
Figure 8.1: A schematic of an on-chip PCR device utilising SAW micropumps, where **A** is the LiNbO$_3$ substrate, **B** is the PDMS block containing microfluidic channels, **C** are the gold IDTs, **D, E** and **F** are three gold heater tracks that generate Joule heating.

Furthermore, as shown in Chapter 6 SAW energy is scattered upwards from the device surface, therefore the channel must be three dimensional. This is achieved commercially either by stacking and bonding multiple thin layers of material by laser ablation[240, 241] or by 3D printing[242, 243], the first two of which are compatible with processing both glass and silicon. Finally, any channel must be bonded to the LiNbO$_3$ chip, which is complicated by the pyroelectric nature of the LiNbO$_3$, which prevents high temperature bonding. However, there are examples of using laser-mediated bonding of LiNbO$_3$ to silicon[244], as well as examples of bonding quartz to LiNbO$_3$ via a thin film adhesion layers[245].

8.3.3 On-chip flow cytometer using alternative material

The primary reason for investigating alternative microfluidic channel materials, is to replace PDMS in the on-chip flow cytometer described in Chapter 7. Such devices would

require re-evaluation in terms of their pump response time, and correspondingly, particle sorting rates. Notably, previously published on-chip cytometers achieve sorting rates in the region of 1000 cells/s, but it is done using external actuating system.[56] Publications utilising hydrodynamic flow manipulation, typically report sorting values similar to those described here. To obtain the highest cell sorting rate possible, the cross-sectional geometry of the microfludic channels, as well as the overall channel contour, would have to be optimised. Furthermore, a suitable cell capture system must be developed to prevent recirculation of sorted cells in the closed, circular channel. An implementation of, for example, a filter[246, 247] or sedimentation based[248] cell capturing region.

8.4 Final remarks

The invention of integrated circuit and translation of electronic circuit elements into a single substrate components by Kilby and Noyce in the 1950s have allowed the very large scale integration of electronic components that can be observed nowadays. In a similar fashion, the use of microfluidic systems in various fields allows the potential to scale down sample sizes, reagents used and offers an unprecedented level of integration and parallelisation in the fields of diagnostics, biology, chemistry and others. However, the field of microfluidics has not yet seen a fully developed toolbox of the various components used in the 'circuits'. For example, although, there has been a large focus devoted to the microfluidic pumping, there is no one 'gold standard' approach that delivers high performance, small footprint, low cost and scalability. Surface acoustic wave based micropumps offer an exciting alternative to the currently used systems. However, to date presented SAW micropumps suffer from either poor performance or from the use of open channel systems which present contamination issues.

The goal of this thesis was to present a SAW-based micropump, which would attempt to deliver these requirements. Throughout this work, four key developments to the

field were presented. First of all was thorough analysis of SAW wavelength choice for SAW pumping alongside electrode design principles. Since SAWs interact with liquid in three dimensions, there was a need for a single-cast protocol that would allow three dimensional microfluidic channel fabrication. Such protocol was presented in Chapters 4 and 5, and as such is the second development. Further, combination of appropriate SAW wavelength choice and use of three-dimensional microfluidic channels, allowed to present a SAW micropump capable of delivering an order of magnitude higher power than to date published SAW micropumps. This work resulted in a publication.[62] Finally, using herein developed micropumps, an on-chip particle sorting system was presented capable of sorting up to 10 particles per second, which compares well to systems utilising similar working principles.

Appendices

A   Image of the in-house developed amplifiers utilised in Chapter 7.
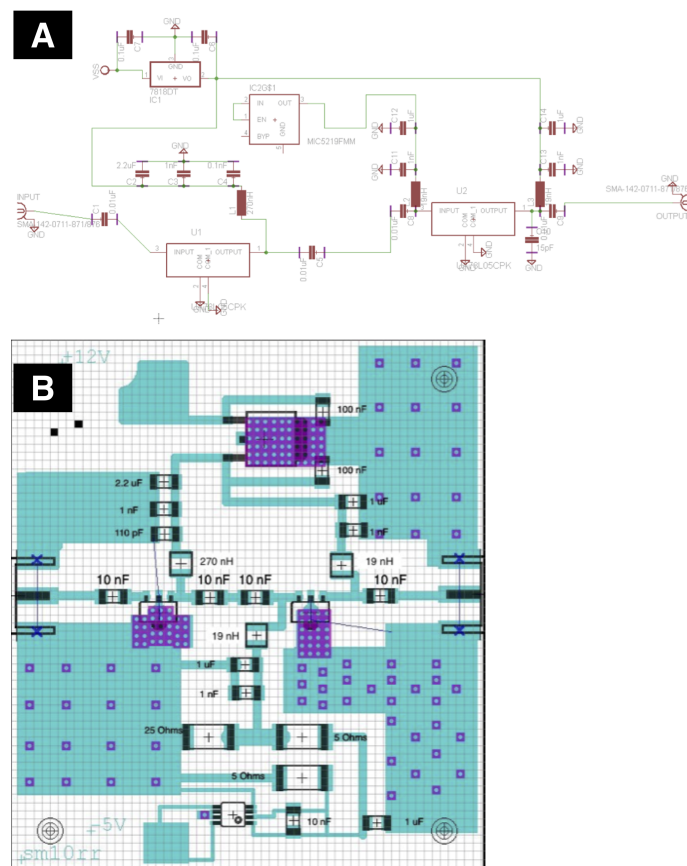
Figure A.2: A schematic (A) and the PCB (B) used for the custom-made RF amplifiers.

This page is intentionally left blank.

Appendices

A   Impedances and S_{11} values for devices fabricated throughout the work

Wavelength, μm	S11 peak, dB	Impedance, Ω
20	-27.0	42.5
20	-15.7	35.7
20	-15.1	44.2
20	-23.0	44.3
25	-21.2	70.3
25	-19.0	40.2
25	-15.6	40.0
25	-26.4	51.2
30	-18.9	46.0
30	-26.1	46.7
30	-23.0	54.6
30	-19.6	54.6
30	-16.4	46.8
30	-25.1	51.0
30	-17.0	47.0
40	-34.0	49.0

40	-30.0	54.1
40	-22.7	48.7
40	-28.4	46.7
40	-19.6	53.0
40	-28.1	53.1
40	-27.2	-53.2
40	-27.3	53.6
40	-26.0	49.9
40	-33.0	50.1
40	-25.5	54.1
40	-44.0	49.6
40	-25.4	49.7
40	-45.0	55.1
40	-30.0	51.0
40	-31.4	53.1
40	-27.3	50.1
40	-29.5	51.1
40	-28.6	52.4
40	-32.1	49.7
40	-30.2	50.5
40	-30.0	50.7
40	-29.8	53.6
50	-15.9	44.8
50	-23.7	49.1
50	-22.5	48.5
50	-21.5	55.0
50	-22.3	46.8
50	-24.0	51.4

50	-19.0	48.6
60	-24.4	48.0
60	-20.7	48.0
60	-19.1	45.0
60	-22.0	45.0
60	-23.3	48.0
60	-19.1	45.0
60	-19.4	46.2
60	-19.6	46.4
60	-18.0	50.5
60	-19.7	44.8
60	-22.9	46.1
60	-18.5	52.6
60	-20.1	55.1
60	-20.0	47.0
70	-15.3	46.0
70	-27.0	54.3
70	-21.0	49.7
70	-17.6	54.5
70	-17.9	44.7
70	-20.6	54.5
70	-19.2	50.6
80	-23.9	45.6
80	-19.8	52.0
80	-29.0	46.5
80	-22.4	47.2
80	-23.4	45.3
80	-21.1	47.1

80	-20.0	45.2
80	-22.7	48.0
80	-24.0	44.8
80	-22.5	45.3
80	-19.2	52.4
80	-17.7	52.9
80	-31.0	50.6
80	-28.7	50.8
80	-25.0	46.0
100	-22.0	47.2
100	-24.0	48.3
100	-22.4	54.4
100	-18.5	45.5
100	-17.0	45.4
100	-37.7	50.4
100	-29.5	47.2
100	-30.2	51.6
100	-27.2	53.4
100	-22.8	48.6
100	-22.3	48.3
100	-27.2	49.8
100	-29.0	49.4
100	-46.0	50.1
100	-23.2	47.2
125	-17.0	47.0
125	-19.0	45.4
125	-15.2	46.5
125	-17.2	47.0

| 125 | -15.7 | 52.2 |
| 125 | -17.0 | 49.0 |

This page is intentionally left blank.

Appendices

A   Data for fluid flow velocities as a function of applied power and SAW wavelength

Table 2: A table of average fluid flow velocities (with errors) for 125 μm wavelength SAW device as a function of position in the channel and applied power.

X position, μm	0.125 W	0.125 W error	0.25 W	0.25 W error	0.5 W	0.5 W error	0.75 W	0.75 W error	1 W	1 W error
-240	57.42	0.73	96.23	1.26	163.63	2.14	198.20	3.08	239.07	3.72
-220	84.92	1.49	175.60	2.33	389.97	5.18	456.30	4.38	562.17	5.39
-200	123.85	2.16	253.45	1.12	548.60	2.43	668.91	4.30	788.23	5.07
-180	140.11	2.29	290.20	1.13	637.27	2.47	784.74	3.55	921.46	4.16
-160	153.20	1.85	311.50	1.45	683.36	3.17	832.07	5.03	997.86	6.03
-140	155.89	0.86	314.51	0.62	696.61	1.37	863.09	6.97	1050.55	8.49
-120	161.18	2.71	323.01	1.83	708.14	4.01	879.68	4.30	1059.52	5.18
-100	162.35	1.84	338.06	0.35	718.55	0.74	901.08	4.85	1086.67	5.85
-80	161.73	1.93	334.48	0.55	729.42	1.21	901.14	5.08	1087.74	6.13
-60	163.00	6.68	336.28	0.28	724.22	0.61	886.72	6.84	1094.40	8.44
-40	162.10	0.59	326.81	1.49	731.42	3.33	890.57	9.45	1102.63	11.70
-20	161.73	1.08	331.86	1.67	730.44	3.67	894.88	5.44	1093.69	6.65
0	164.02	2.20	346.32	1.38	719.71	2.86	890.70	6.61	1084.03	8.05
20	161.11	2.44	339.17	1.49	722.16	3.16	895.05	5.64	1091.78	6.88
40	162.92	1.46	330.77	1.26	725.14	2.77	888.31	9.14	1073.28	11.05
60	160.08	0.68	331.91	1.71	714.44	3.68	892.33	6.41	1084.11	7.79
80	160.63	1.14	328.66	1.64	705.67	3.51	881.12	6.27	1067.07	7.60
100	159.44	1.52	339.09	0.41	709.31	0.86	867.49	8.21	1057.90	10.01
120	156.41	1.43	325.17	1.40	713.22	3.06	853.50	5.97	1038.07	7.26
140	157.77	1.44	324.41	1.39	685.85	2.94	870.40	6.09	1027.22	7.19
160	149.77	2.75	305.04	1.74	677.35	3.87	830.51	5.52	1016.94	6.76
180	144.56	1.08	295.42	0.80	650.39	1.76	800.24	6.80	982.10	8.34
200	132.02	4.40	274.63	1.01	592.13	2.17	751.45	4.98	875.91	5.81
220	111.72	1.73	233.96	1.34	503.97	2.88	608.54	3.97	719.71	4.70
240	69.93	1.72	148.25	0.47	326.74	1.03	368.34	4.92	429.30	5.73

Table 3: A table of average fluid flow velocities (with errors) for 100 µm wavelength SAW device as a function of position in the channel and applied power.

X position, µm	0.125 W	0.125 W error	0.25 W	0.25 error	0.5 W	0.5 W error	0.75 W	0.75 error	1 W	1 W error
-240	126.40	1.61	129.19	1.69	512.98	6.94	502.54	9.62	315.93	4.92
-220	194.28	3.41	311.21	4.13	684.40	7.35	750.14	11.22	598.43	5.74
-200	206.24	3.59	381.05	1.69	697.49	11.05	948.89	5.27	803.73	5.17
-180	201.66	3.30	432.54	1.68	772.35	7.13	943.16	12.54	912.73	4.12
-160	229.00	2.76	456.79	2.12	823.44	5.58	1029.83	10.40	1002.98	6.06
-140	242.74	1.33	478.02	0.94	817.82	8.03	1115.75	6.78	997.46	8.06
-120	231.24	3.89	496.15	2.81	894.38	4.80	1106.31	9.58	1055.01	5.16
-100	238.52	2.71	488.69	0.50	880.59	8.88	1082.51	8.93	1055.37	5.68
-80	248.64	2.97	494.17	0.82	876.90	5.66	1073.90	14.18	1055.88	5.95
-60	204.91	8.39	502.30	0.42	912.66	6.79	1120.48	6.51	1069.30	8.25
-40	259.76	0.94	517.22	2.35	892.17	8.36	1029.45	13.53	1025.42	10.88
-20	253.44	1.68	500.47	2.52	844.12	7.14	1073.63	13.12	1038.87	6.32
0	238.93	3.20	499.24	1.98	869.19	6.15	1076.56	12.19	1014.39	7.53
20	231.20	3.50	497.49	2.18	895.63	4.70	1102.81	7.88	1037.73	6.54
40	240.94	2.16	500.21	1.91	860.20	8.26	1092.42	10.13	1001.99	10.31
60	257.78	1.09	506.88	2.61	868.65	6.19	1039.46	10.76	1040.71	7.48
80	256.75	1.82	484.46	2.41	814.62	8.16	1073.03	9.30	1004.93	7.15
100	243.56	2.32	478.80	0.58	833.22	5.96	1119.58	7.01	972.90	9.21
120	245.68	2.25	481.92	2.07	816.14	5.16	1094.27	7.66	962.88	6.74
140	245.68	2.25	481.92	2.07	816.14	5.16	1093.96	7.64	962.88	6.74
160	209.00	3.84	482.15	2.75	788.26	6.85	1005.11	7.66	890.37	5.91
180	225.69	1.69	432.16	1.17	743.41	5.77	956.07	6.45	847.86	7.20
200	193.03	6.43	445.99	1.64	651.86	5.59	883.67	9.78	787.51	5.22
220	158.34	2.46	400.29	2.29	519.26	6.47	789.64	9.16	613.48	4.01
240	304.49	46.67	340.92	1.08	301.02	7.47	471.29	7.68	376.23	5.02

Table 4: A table of average fluid flow velocities (with errors) for 80 μm wavelength SAW device as a function of position in the channel and applied power.

X position, μm	0.125 W	0.125 W error	0.25 W	0.25 error	0.5 W	0.5 W error	0.75 W	0.75 error	1 W	1 W error
-240	169.15	5.15	263.13	7.62	763.50	12.56	825.36	12.22	836.49	18.74
-220	343.76	7.42	576.35	6.85	1084.83	4.95	1108.31	8.28	1236.96	14.15
-200	427.20	4.66	753.45	3.95	1272.51	5.15	1279.86	9.65	1448.12	12.08
-180	471.93	5.24	871.92	2.89	1364.22	8.27	1398.09	12.97	1580.91	12.83
-160	475.40	5.85	918.85	2.79	1387.07	7.29	1398.58	9.63	1630.44	15.22
-140	510.82	6.17	966.65	1.37	1436.60	6.81	1458.39	13.13	1663.11	13.40
-120	514.41	4.99	978.12	1.79	1424.80	8.49	1462.76	12.46	1705.60	19.49
-100	530.49	6.65	985.00	3.91	1427.83	9.33	1471.08	16.01	1734.73	10.80
-80	547.50	2.68	1001.60	1.74	1427.97	7.72	1477.22	10.91	1727.60	16.05
-60	568.29	3.04	991.60	3.43	1485.02	5.26	1497.10	10.24	1765.72	16.71
-40	507.91	6.02	992.79	3.70	1429.51	12.55	1510.01	14.24	1771.43	10.64
-20	506.73	5.62	986.17	3.85	1423.79	9.34	1478.73	13.04	1596.25	24.73
0	501.34	7.04	1011.12	3.26	1448.54	8.08	1485.88	14.43	1820.58	10.76
20	496.47	8.67	976.63	3.84	1454.76	8.12	1486.66	10.12	1728.34	11.65
40	548.64	4.24	967.86	5.03	1440.77	8.53	1488.97	12.09	1630.49	18.47
60	565.62	2.42	995.67	4.51	1433.49	8.21	1473.81	11.76	1647.55	17.83
80	534.12	4.40	986.64	3.59	1402.53	8.40	1417.35	13.98	1625.70	19.46
100	517.82	3.91	975.67	3.08	1406.18	7.07	1429.93	11.13	1619.30	22.68
120	540.47	4.81	963.04	4.09	1415.42	7.13	1458.55	17.48	1657.77	19.13
140	540.47	4.81	963.04	4.09	1415.42	7.13	1458.55	17.48	1657.77	19.13
160	464.95	5.18	934.81	2.98	1334.42	6.47	1304.87	5.41	1601.20	12.88
180	468.45	3.62	885.60	3.87	1236.21	7.92	1265.35	12.07	1532.18	10.87
200	405.29	5.19	812.33	3.84	1083.13	7.26	1155.46	10.49	1318.09	10.46
220	296.40	8.71	679.02	6.77	742.83	10.13	823.35	12.30	1011.66	11.25
240	120.69	1.52	369.22	12.92	270.66	1.53	383.87	8.47	486.08	14.09

Table 5: A table of average fluid flow velocities (with errors) for 70 µm wavelength SAW device as a function of position in the channel and applied power.

X position, µm	0.125 W	0.125 W error	0.25 W	0.25 error	0.5 W	0.5 W error	0.75 W	0.75 error	1 W	1 W error
-240	142.10	4.12	93.06	0.92	190.90	2.69	125.09	1.05	186.73	10.11
-220	158.03	8.74	252.77	2.72	337.49	6.75	432.36	9.22	636.65	7.43
-200	222.24	9.05	351.74	3.31	394.53	2.96	610.30	3.49	718.21	11.76
-180	273.42	2.63	399.56	2.49	436.04	7.21	653.32	4.02	781.76	5.51
-160	275.14	8.42	416.48	1.32	413.85	1.69	631.54	17.80	795.72	15.94
-140	289.33	5.81	437.52	2.52	454.72	4.14	642.42	12.48	787.23	13.96
-120	296.77	4.16	459.66	2.87	495.33	7.68	716.16	10.35	834.11	13.18
-100	300.91	3.95	463.12	3.58	439.11	2.59	660.14	15.43	839.94	11.78
-80	309.42	2.35	450.66	2.79	440.03	3.13	691.06	12.07	811.12	13.69
-60	298.27	12.14	455.91	1.67	456.21	3.61	652.26	12.62	876.39	12.16
-40	309.90	4.76	438.49	3.73	532.79	10.96	688.03	8.76	817.57	11.27
-20	297.31	3.55	428.77	3.06	474.41	5.31	680.55	11.30	872.61	15.92
0	303.38	2.62	444.24	1.27	432.85	3.62	690.62	16.84	826.27	15.31
20	305.33	3.93	447.16	3.63	535.62	14.37	703.57	10.13	834.12	10.65
40	301.75	6.21	449.59	3.91	588.57	20.00	703.10	18.15	842.05	10.03
60	297.80	10.10	451.24	1.71	495.80	8.97	741.27	13.59	834.07	11.48
80	305.53	3.47	454.03	2.65	485.70	8.80	773.20	8.11	849.85	14.43
100	302.56	2.51	457.09	2.97	486.03	12.52	692.74	14.25	816.91	7.61
120	301.90	2.33	454.93	2.08	538.94	9.50	705.38	11.33	814.95	9.40
140	301.90	2.33	454.93	2.08	538.94	9.50	705.38	11.33	814.95	9.40
160	288.26	2.74	416.98	1.97	453.03	0.87	665.10	4.54	840.88	12.30
180	254.71	11.01	406.74	2.63	398.33	1.76	667.92	15.90	761.86	7.39
200	233.05	10.49	370.12	3.19	409.02	7.53	709.99	2.85	723.22	7.07
220	168.11	3.34	296.96	3.32	350.35	5.05	684.35	6.59	674.23	6.22
240	126.30	4.46	114.79	0.98	171.14	5.49	485.83	10.60	499.49	18.87

Table 6: A table of average fluid flow velocities (with errors) for 60 μm wavelength SAW device as a function of position in the channel and applied power.

X position, μm	0.125 W	0.125 W error	0.25 W	0.25 error	0.5 W	0.5 W error
-240	183.75	7.75	305.79	20.89	429.93	2.19
-220	343.09	6.52	544.33	5.86	617.24	6.78
-200	454.56	3.28	656.30	3.69	763.79	22.16
-180	484.31	3.44	734.45	4.26	894.84	5.60
-160	516.92	4.78	756.50	6.14	902.00	16.96
-140	531.20	4.75	757.33	4.38	937.87	1.46
-120	540.14	6.72	781.76	4.91	925.22	17.95
-100	535.69	3.99	770.84	6.89	922.50	12.96
-80	539.27	3.79	770.87	5.21	977.02	8.71
-60	539.12	3.75	778.42	5.83	950.13	7.02
-40	563.78	2.67	768.34	3.18	983.27	2.67
-20	528.00	4.12	786.45	4.48	968.40	6.69
0	525.04	5.31	797.79	6.06	955.31	10.10
20	523.29	5.81	776.53	4.91	933.80	9.62
40	574.88	4.44	790.77	8.26	943.92	5.42
60	549.45	5.18	797.36	7.07	977.04	3.59
80	528.35	8.79	802.53	5.15	984.79	5.24
100	532.39	9.07	789.69	8.79	982.95	12.01
120	537.69	3.32	786.94	6.98	1001.98	7.35
140	537.69	3.32	786.94	6.98	1001.98	7.35
160	555.05	4.63	759.15	3.57	894.59	14.44
180	516.85	1.57	754.70	5.94	933.99	5.54
200	442.28	6.61	658.28	5.78	816.95	15.77
220	336.32	7.38	504.33	12.24	673.53	6.80
240	178.51	6.12	227.99	10.55	138.45	13.46

Table 7: A table of average fluid flow velocities (with errors) for 50 μm wavelength SAW device as a function of position in the channel and applied power.

X position, μm	0.125 W	0.125 W error	0.25 W	0.25 error	0.5 W	0.5 W error
-240	101.74	45.96	292.70	3.10	159.10	8.95
-220	291.32	6.14	499.39	5.08	681.48	5.56
-200	340.95	6.76	560.00	3.48	726.89	10.89
-180	376.23	11.41	664.20	1.00	795.51	6.44
-160	429.60	6.37	656.28	4.71	889.27	2.74
-140	390.72	13.59	675.75	5.14	804.90	15.87
-120	398.31	16.93	679.44	2.56	873.62	17.57
-100	463.12	7.61	690.95	2.94	877.88	16.35
-80	447.32	7.55	693.26	4.47	886.26	12.41
-60	456.14	2.13	679.57	3.35	937.49	5.56
-40	474.15	3.14	702.86	1.30	907.25	15.72
-20	462.73	4.28	696.85	7.23	905.06	14.27
0	449.66	3.85	694.52	4.35	855.89	18.79
20	452.76	3.43	694.04	3.39	857.48	14.24
40	444.03	8.35	686.04	2.77	844.85	15.54
60	437.86	6.27	671.53	1.54	842.89	13.44
80	458.83	1.44	674.77	7.04	893.24	7.91
100	457.42	0.95	680.08	5.08	836.14	11.22
120	436.16	2.56	662.35	1.06	851.53	7.27
140	436.16	2.56	662.35	1.06	851.53	7.27
160	404.70	4.92	660.35	2.56	833.54	9.17
180	409.40	1.03	646.97	2.75	770.25	7.49
200	336.24	2.15	558.52	8.95	712.94	6.66
220	266.44	2.98	402.61	13.07	680.55	5.04
240	82.18	37.47	178.78	12.15	356.41	22.67

Table 8: A table of average fluid flow velocities (with errors) for 40 μm wavelength SAW device as a function of position in the channel and applied power.

X position, μm	0.125 W	0.125 W error	0.25 W	0.25 W error	0.5 W	0.5 W error
-240	299.30	44.99649267	183.00	1.43	663.86	21.31
-220	425.89	3.856868568	766.27	5.67	1179.48	8.46
-200	545.48	2.136876699	995.53	3.78	1445.95	8.89
-180	599.06	3.270603897	1086.22	2.17	1602.41	7.07
-160	618.18	3.738628374	1152.66	3.77	1643.78	12.89
-140	630.47	4.867578733	1181.61	3.84	1754.41	9.06
-120	646.78	3.009810726	1214.09	2.36	1769.97	11.17
-100	649.80	3.867620989	1190.58	5.39	1725.21	13.20
-80	653.18	2.455866314	1238.20	0.57	1741.43	8.09
-60	661.67	5.661643017	1208.11	3.73	1735.46	12.96
-40	651.46	3.631500447	1219.58	4.40	1759.78	10.93
-20	642.18	2.842350324	1165.95	7.73	1822.54	6.89
0	656.96	2.205206552	1187.84	4.27	1774.37	11.41
20	660.73	1.698463983	1182.31	6.66	1767.53	10.43
40	656.30	2.385165336	1212.44	3.05	1800.13	10.73
60	649.77	3.839582386	1196.11	3.38	1764.20	8.95
80	646.89	3.642049688	1188.44	4.06	1743.20	12.70
100	638.12	3.739540191	1167.39	4.37	1728.43	12.89
120	638.38	4.403621533	1176.86	3.95	1699.77	9.33
140	638.38	4.403621533	1176.86	3.95	1699.77	9.33
160	665.24	1.25864448	1114.81	2.98	1612.90	11.20
180	584.58	3.157425019	1044.25	2.36	1532.19	11.44
200	528.06	2.449931206	908.57	4.13	1335.98	13.62
220	397.45	2.292845573	691.68	5.86	1061.35	14.06
240	341.77	1.120286602	273.71	17.52	119.52	2.46

Table 9: A table of average fluid flow velocities (with errors) for 30 μm wavelength SAW device as a function of position in the channel and applied power.

X position	0.125 W	0.125 W error	0.25 W	0.25 error	0.5 W	0.5 W error	0.75 W	0.75 error	1 W	1 W error
-240	55.00	0.23	114.97	0.25	155.00	14.29	191.26	14.21952027	461.80	32.87
-220	88.71	1.15	181.10	0.78	299.75	18.26	539.82	6.194411401	631.14	6.74
-200	132.45	0.08	196.10	0.55	585.00	1.15	686.29	2.875227992	823.61	7.10
-180	137.44	0.58	263.20	0.51	561.86	4.04	754.18	3.686128603	919.56	5.99
-160	151.96	0.38	266.33	0.67	602.41	2.51	800.78	2.162816934	979.50	4.98
-140	145.62	1.60	265.00	3.96	599.91	4.17	838.27	3.180099439	992.94	13.56
-120	159.30	0.26	273.01	2.79	630.51	14.80	841.85	1.476295301	1011.25	5.68
-100	161.72	1.78	275.23	1.03	631.65	3.79	862.79	1.277187336	1006.09	4.67
-80	163.45	0.37	282.33	2.45	618.31	1.41	835.75	2.854979413	1017.53	6.08
-60	161.71	0.50	266.77	2.14	598.06	3.69	856.77	1.785431605	1022.44	8.27
-40	163.16	0.20	270.11	0.92	616.33	2.16	869.91	0.914784714	1003.71	7.12
-20	161.68	0.58	283.15	2.91	620.34	1.90	841.66	2.731599095	1023.75	5.60
0	161.84	0.26	275.00	8.45	622.34	0.74	837.93	2.28377299	1024.50	6.40
20	161.35	0.28	271.13	0.86	611.57	3.30	840.26	1.623360844	1023.92	7.42
40	161.90	1.77	272.13	2.27	599.61	2.51	838.23	3.463641049	1002.40	6.98
60	161.68	0.26	273.57	0.57	622.65	3.03	805.97	3.822516851	1000.47	2.47
80	160.39	22.73	265.14	0.96	600.16	2.18	821.73	2.406335373	978.90	6.56
100	161.84	0.47	272.88	0.50	598.63	3.25	813.93	2.062543836	996.92	7.15
120	161.14	0.26	272.46	0.90	595.33	0.68	820.81	2.648014104	977.54	5.55
140	161.14	0.26	272.46	0.90	595.33	0.68	820.81	2.648014104	977.54	5.55
160	153.15	0.08	246.19	0.72	562.78	3.26	759.85	2.373428932	942.94	6.95
180	145.94	0.22	244.99	1.75	550.00	3.73	768.86	2.392368432	906.79	3.84
200	129.68	0.19	234.54	1.86	497.66	2.94	662.95	4.869839798	808.14	8.17
220	98.33	0.19	187.43	0.67	361.08	1.23	528.50	6.00568441	673.72	9.44
240	55.00	0.31	106.75	0.15	215.57	3.07	269.07	12.18423707	401.12	12.14

Appendices

A Particle velocity dependence on the x-y coordinates in sorting region of type-b devices seen in Chapter 7

Table 10: Particle velocity dependence on the x-y coordinates at 12.1 Pa pressure difference between side channels. Columns are the x-coordinates, and rows are the y-coordinates.

Y//X	50	100	150	200
50	449.5	521.3	471.2	551.4
100	798.7	619.1	558.1	501.3
150	753.3	663.7	531.4	403.0
200	715.8	660.0	443.6	327.5
250	726.9	431.1	360.9	215.6
300	421.1	591.5	421.1	167.1

Table 11: Particle velocity dependence on the x-y coordinates at 26.3 Pa pressure difference between side channels. Columns are the x-coordinates, and rows are the y-coordinates.

Y//X	50	100	150	200
50	1494.8	625.0	625.0	386.9
100	966.5	472.9	456.6	329.4
150	1140.2	927.5	646.9	467.9
200	1179.7	1038.6	776.8	390.6
250	1270.2	979.7	937.5	453.1
300	1129.5	989.6	834.5	471.0

Table 12: Particle velocity dependence on the x-y coordinates at 96 Pa pressure difference between side channels. Columns are the x-coordinates, and rows are the y-coordinates.

Y//X	50	100	150	200
50	1504.1	1161.4	1822.9	401.0
100	1331.3	936.7	1236.1	401.0
150	1653.0	1132.2	971.1	968.7
200	1694.1	1260.9	1236.1	1354.1
250	1659.9	1346.6	1295.5	1212.8
300	1440.2	1222.9	1284.7	1193.1

Table 13: Particle velocity dependence on the x-y coordinates at 135 Pa pressure difference between side channels. Columns are the x-coordinates, and rows are the y-coordinates.

Y//X	50	100	150	200
50	1441.3	2250.0	1156.2	656.2
100	1833.3	2333.3	1265.6	656.2
150	2189.6	1807.3	1441.3	1143.7
200	2333.3	2134.5	1991.2	1881.5
250	2434.9	2261.9	2324.4	2020.0
300	1935.3	2056.7	2386.2	2758.3

This page is intentionally left blank.

Bibliography

[1] Walter Isaacson. *The Innovators: How a Group of Hackers, Geniuses and Geeks Created the Digital Revolution*. Simon & Schuster Paperbacks, New York, NY, 2014.

[2] Gabriel Wildau and Leslie Hook. China mobile payments dwarf those in US as fintech booms. *Financial Times*, page 1, feb 2017.

[3] Gordon E Moore. Cramming more components onto integrated circuits. *Electronics*, 38(8):114–117, 1965.

[4] Min Cheng Chen, Hao Yu Chen, Chia Yi Lin, Chao Hsin Chien, Tsung Fan Hsieh, Jim Tong Horng, Jian Tai Qiu, Chien Chao Huang, Chia Hua Ho, and Fu Liang Yang. A CMOS-compatible poly-si nanowire device with hybrid sensor/memory characteristics for system-on-chip applications. *Sensors*, 12(4):3952–3963, 2012.

[5] Lin Li. *Post-CMOS microelectrode fabrication and packaging for on-CMOS electrochemical biosensor array By*. Msc, Michigan State University, 2012.

[6] Santosh Koppa, Youngjoong Joo, Meenakshi Venkataramasubramani, and Liang Tang. Nanoscale biosensor chip. *Midwest Symposium on Circuits and Systems*, pages 268–271, 2010.

[7] Sony DADC BioSciences and TSMC Receive AACC Industry Division Award. *Business Wire*, jul 2014.

[8] Paul C. Guest and Daniel Martins-de Souza. Enabling point-of-care testing and personalized medicine for schizophrenia. *npj Schizophrenia*, 3(1):1, 2017.

[9] Francesca L Guest and Paul C Guest. *Point-of-Care Testing and Personalized Medicine for Metabolic Disorders*, pages 105–114. Springer New York, New York, NY, 2018.

[10] Andrew J DeMello. Control and detection of chemical reactions in microfluidic systems. *Nature*, 442:394, jul 2006.

[11] David J Beebe, Glennys a Mensing, and Glenn M Walker. Physics and applications of microfluidics in biology. *Annual review of biomedical engineering*, 4:261–86, jan 2002.

[12] Kerstin Länge, Guido Blaess, Achim Voigt, Reiner Götzen, and Michael Rapp. Integration of a surface acoustic wave biosensor in a microfluidic polymer chip. *Biosensors & bioelectronics*, 22(2):227–32, aug 2006.

[13] Claudia Gärtner, Stefanie Kirsch, Birgit Anton, Holger Becker, Chipshop Gmbh, Carl-zeiss Promenade, and D Jena. Hybrid microfluidic systems combining a polymer microfluidic toolbox with biosensors. *Microfluidics, BioMEMS, and Medical Microsystems V*, pages 2–5, 2007.

[14] Brigitte Bruijns, Arian van Asten, Roald Tiggelaar, and Han Gardeniers. Microfluidic devices for forensic DNA analysis: A review. *Biosensors*, 6(3):1–35, 2016.

[15] Kang-Yi Lien, Wan-Chi Lee, Huan-Yao Lei, and Gwo-Bin Lee. Integrated reverse transcription polymerase chain reaction systems for virus detection. *Biosensors and Bioelectronics*, 22(8):1739–1748, 2007.

[16] Ken-ichi Ohno, Kaoru Tachikawa, and Andreas Manz. Microfluidics: Applications for analytical purposes in chemistry and biochemistry. *ELECTROPHORESIS*, 29(22):4443–4453, 2008.

[17] Francesca Costantini, Cristiana Sberna, Giulia Petrucci, Cesare Manetti, Giampiero de Cesare, Augusto Nascetti, and Domenico Caputo. Lab-on-chip system combining a microfluidic-ELISA with an array of amorphous silicon photosensors for the detection of celiac disease epitopes. *Sensing and Bio-Sensing Research*, 6:51–58, 2015.

[18] T. Thorsen, S. J. Maerkl, and Stephen R. Quake. Microfluidic Large-Scale Integration. *Science*, 298(5593):580–584, 2002.

[19] Sai Ma, Travis W. Murphy, and Chang Lu. Microfluidics for genome-wide studies involving next generation sequencing. *Biomicrofluidics*, 11(2):1–24, 2017.

[20] John M S Bartlett and David Stirling. A short history of the polymerase chain reaction. *Methods in molecular biology (Clifton, N.J.)*, 226:3–6, 2003.

[21] Takashi Yabuki, Yoko Motoda, Kazuharu Hanada, Emi Nunokawa, Miyuki Saito, Eiko Seki, Makoto Inoue, Takanori Kigawa, and Shigeyuki Yokoyama. A robust two-step PCR method of template DNA production for high-throughput cell-free protein synthesis. *Journal of Structural and Functional Genomics*, 8(4):173–191, 2007.

[22] Patrick Tabeling. *Introduction to Microfluidics*. Oxford University Press, Oxford, 2005.

[23] G K Batchelor. *An Introduction to Fluid Dynamics*. Cambridge University Press, Cambridge, 2000.

[24] B J Kirby. *Micro- and Nanoscale Fluid Mechanics: Transport in Microfluidic Devices*. Cambridge University Press, Cambridge, 1 edition, 2010.

[25] Luc Bissonnette and Michel G. Bergeron. Portable devices and mobile instruments for infectious diseases point-of-care testing. *Expert Review of Molecular Diagnostics*, 17(5):471–494, 2017.

[26] S. J. Lee and S. Y. Lee. Micro total analysis system (uTAS) in biotechnology. *Applied Microbiology and Biotechnology*, 64(3):289–299, 2004.

[27] Jay Kendall Taylor and Ben Arlett. Fluidic catridge and method for processing a liquid sample, 2016.

[28] S Hunter. Reader devices for manipulating multi-fluidic cartridges for sample analysis, 2014.

[29] Eric K Sackmann, Anna L Fulton, and David J Beebe. The present and future role of microfluidics in biomedical research. *Nature*, 507(7491):181–9, mar 2014.

[30] E. Bassous, H. H. Taub, and L. Kuhn. Ink jet printing nozzle arrays etched in silicon. *Applied Physics Letters*, 31(2):135–137, 1977.

[31] Jaime Castillo-León. Lab-on-a-Chip Devices and Micro-Total Analysis Systems. In Jaime Castillo-León and Winnie E. Svendsen, editors, *Lab-on-a-chip Devices and Micro-total Analysis Systems*, chapter 1, pages 17 – 26. Springer Switzerland, 2015.

[32] Andreas Manz, D. Jed Harrison, Elisabeth M J Verpoorte, James C. Fettinger, Aran Paulus, Hans L??di, and H. Michael Widmer. Planar chips technology for miniaturization and integration of separation techniques into monitoring systems. Capillary electrophoresis on a chip. *Journal of Chromatography A*, 593(1-2):253–258, 1992.

[33] D J Harrison, K Fluri, K Seiler, Z Fan, C S Effenhauser, and a Manz. Micromachining a miniaturized capillary electrophoresis-based chemical analysis system on a chip. *Science (New York, N.Y.)*, 261(SEPTEMBER):895–897, 1993.

[34] Theresa B. Taylor, Emily S. Winn-Deen, Enrico Picozza, Timothy M. Woudenberg, and Michael Albin. Optimization of the performance of the polymerase chain reaction in silicon-based microstructures. *Nucleic Acids Research*, 25(15):3164–3168, 1997.

[35] Mark A. Burns, Carlos H. Mastrangelo, Timothy S. Sammarco, Francis P. Man, James R. Webster, Brian N. Johnsons, Bradley Foerster, Darren Jones, Yakeitha Fields, Adam R. Kaiser, and David T. Burke. Microfabricated structures for integrated DNA analysis. *Proceedings of the National Academy of Sciences of the United States of America*, 93(11):5556–61, 1996.

[36] E. T. Lagally, I. Medintz, and R. A. Mathies. Single-molecule DNA amplification and analysis in an integrated microfluidic device. *Analytical Chemistry*, 73(3):565–570, 2001.

[37] The Academy of Medical Sciences. Stratified, personalised or P4 medicine: a new direction for placing the patient at the centre of healthcare and health education. *Summary of a joint FORUM meeting held on 12 May 2015*, (May):37, 2015.

[38] Marc Madou. *Fundamentals of microfabrication*. CRC Press, Boca Raton, Fla., 1997.

[39] Samuel K Sia and George M Whitesides. Microfluidic devices fabricated in poly(dimethylsiloxane) for biological studies. *Electrophoresis*, 24(21):3563–76, nov 2003.

[40] Xavi Illa, Olga Ordeig, Detlef Snakenborg, Albert Romano-Rodríguez, Richard G Compton, and Jörg P Kutter. A cyclo olefin polymer microfluidic chip with integrated gold microelectrodes for aqueous and non-aqueous electrochemistry. *Lab on a chip*, 10(10):1254–1261, 2010.

[41] David Erickson and Dongqing Li. Integrated microfluidic devices. *Analytica Chimica Acta*, 507(1):11–26, 2004.

[42] Holger Becker and Claudia Gärtner. Polymer microfabrication technologies for microfluidic systems. *Analytical and Bioanalytical Chemistry*, 390(1):89–111, 2008.

[43] Douglas B Weibel, Willow R Diluzio, and George M Whitesides. Microfabrication meets microbiology. *Nature reviews. Microbiology*, 5(3):209–18, 2007.

[44] AM Gracioso Martins and NR Glass. Toward Complete Miniaturisation of Flow Injection Analysis Systems: Microfluidic Enhancement of Chemiluminescent Detection. *Analytical chemistry*, 86:10812–10819, 2014.

[45] Paul Yager, Thayne Edwards, Elain Fu, Kristen Helton, Kjell Nelson, Milton R Tam, and Bernhard H Weigl. Microfluidic diagnostic technologies for global public health. *Nature*, 442(7101):412–8, jul 2006.

[46] Ciprian Iliescu, Hayden Taylor, Marioara Avram, and Jianmin Miao. A practical guide for the fabrication of microfluidic devices using glass and silicon. *Biomicrofluidics*, 016505:1–16, 2012.

[47] Sangeeta N Bhatia and Donald E Ingber. Microfluidic organs-on-chips. *Nat Biotech*, 32(8):760–772, 2014.

[48] Feng Guo, Peng Li, Jarrod B French, Zhangming Mao, Hong Zhao, Sixing Li, Nitesh Nama, and James R Fick. Controlling cell cell interactions using surface acoustic waves. *Proceedings of the National Academy of Sciences*, 112(1):43–48, 2015.

[49] Nupura S Bhise, Vijayan Manoharan, Solange Massa, Ali Tamayol, Masoumeh Ghaderi, Mario Miscuglio, Qi Lang, Yu Shrike Zhang, Su Ryon Shin, Giovanni

Calzone, Nasim Annabi, Thomas D Shupe, Colin E Bishop, Anthony Atala, Mehmet R Dokmeci, and Ali Khademhosseini. A liver-on-a-chip platform with bioprinted hepatic spheroids. *Biofabrication*, 8(1):014101, 2016.

[50] JR Anderson and DT Chiu. Fabrication of microfluidic systems in poly(dimethylsiloxane). *Electrophoresis*, 21(1):27–40, 2000.

[51] Wenfu Zheng, Zhuo Wang, Wei Zhang, and Xingyu Jiang. A simple PDMS-based microfluidic channel design that removes bubbles for long-term on-chip culture of mammalian cells. *Lab on a chip*, 10(21):2906–2910, 2010.

[52] Dongeun Huh, Hyun Jung Kim, Jacob P Fraser, Daniel E Shea, Mohammed Khan, Anthony Bahinski, Geraldine A Hamilton, and Donald E Ingber. Microfabrication of human organs-on-chips. *Nat. Protocols*, 8(11):2135–2157, nov 2013.

[53] Fang Qian, Chao Huang, Yi-Dong Lin, Anna Ivanovskaya, Ross Booth, Tom O'hara, Cameron Creek, Heather Ann Enright, David Soscia, Anna Belle, Ronglih Liao, Felice C. Lightstone, Kristen Kulp, and Elizabeth Wheeler. Simultaneous Electrical Recording of Cardiac Electrophysiology and Contraction on Chip. *Lab Chip*, 17(10):1732–1739, 2017.

[54] Li Wang, Tingting Tao, Wentao Su, Hao Yu, Yue Yu, and Jianhua Qin. A disease model of diabetic nephropathy in a glomerulus-on-a-chip microdevice. *Lab Chip*, 17:1749–1760, 2017.

[55] T Franke, S Braunmüller, L Schmid, A Wixforth, and D a Weitz. Surface acoustic wave actuated cell sorting (SAWACS). *Lab on a chip*, 10(6):789–94, mar 2010.

[56] Sung Hwan Cho. *Lab-on-a-chip flow cytometer and microfluidic fluorescence activated cell sorter (FACS) for biomedical applications*. PhD thesis, University of California, San Diego, 2010.

[57] Alban J. Smith, Richard D. O'Rorke, Akshay Kale, Roberts Rimsa, Matthew J. Tomlinson, Jennifer Kirkham, A. Giles Davies, Christoph Wälti, and Christopher D. Wood. Rapid cell separation with minimal manipulation for autologous cell therapies. *Scientific Reports*, 7(October 2016):41872, 2017.

[58] Younan Xia and GM Whitesides. Soft lithography. *Annual review of materials science*, 28:153–184, 1998.

[59] Miao Sun, Yanbo Xie, Jihong Zhu, Jun Li, and Jan C. T. Eijkel. Improving the Resolution of 3D-Printed Molds for Microfluidics by Iterative Casting-Shrinkage Cycles. *Analytical Chemistry*, 89(4):2227–2231, 2017.

[60] Anthony K. Au, Hoyin Lai, Ben R. Utela, and Albert Folch. Microvalves and micropumps for BioMEMS. *Micromachines*, 2:179–220, 2011.

[61] George M Whitesides. The origins and the future of microfluidics. *Nature*, 442(7101):368–73, jul 2006.

[62] R. Rimsa, A. J. Smith, C. Wälti, and C. D. Wood. A planar surface acoustic wave micropump for closed-loop microfluidics. *Applied Physics Letters*, 111(23):1–18, 2017.

[63] Zeno Guttenberg, Helena Muller, Heiko Habermüller, Andreas Geisbauer, Jürgen Pipper, Jana Felbel, Mark Kielpinski, Jürgen Scriba, and Achim Wixforth. Planar chip device for PCR and hybridization with surface acoustic wave pump. *Lab on a chip*, 5(3):308–17, mar 2005.

[64] Achim Wixforth. Acoustically driven planar microfluidics. *Superlattices and Microstructures*, 33(5-6):389–396, may 2003.

[65] B. Hadwen, G. R. Broder, D. Morganti, a. Jacobs, C. Brown, J. R. Hector, Y. Kubota, and H. Morgan. Programmable large area digital microfluidic array with integrated droplet sensing for bioassays. *Lab on a Chip*, 12(18):3305, 2012.

[66] Andrew J DeMello. Control and detection of chemical reactions in microfluidic systems. *Nature*, 442(7101):394–402, 2006.

[67] Venkatachalam Chokkalingam, Jurjen Tel, Florian Wimmers, Xin Liu, Sergey Semenov, Julian Thiele, Carl G Figdor, and Wilhelm T S Huck. Probing cellular heterogeneity in cytokine-secreting immune cells using droplet-based microfluidics. *Lab Chip*, 13(24):4740–4744, 2013.

[68] Milad Samie, Alinaghi Salari, and Mohammad Behshad Shafii. Breakup of microdroplets in asymmetric T junctions. *Phys. Rev. E*, 87(5):53003, may 2013.

[69] Venkatachalam Chokkalingam, Stephan Herminghaus, and Ralf Seemann. Self-synchronizing pairwise production of monodisperse droplets by microfluidic step emulsification. *Applied Physics Letters*, 93(25):254101, 2008.

[70] Victoria Mico, Antonia Charalambous, Sally A Peyman, Radwa H Abou-Saleh, Alexander F Markham, P Louise Coletta, and Stephen D Evans. Evaluation of lipid-stabilised tripropionin nanodroplets as a delivery route for combretastatin A4. *International Journal of Pharmaceutics*, 526(1):547–555, 2017.

[71] Daisuke Saeki, Shinji Sugiura, Toshiyuki Kanamori, Seigo Sato, and Sosaku Ichikawa. Microfluidic preparation of water-in-oil-in-water emulsions with an ultra-thin oil phase layer. *Lab Chip*, 10(3):357–362, 2010.

[72] Dirk Janasek, Joachim Franzke, and Andreas Manz. Scaling and the design of miniaturized chemical-analysis systems. *Nature*, 442(7101):374–80, jul 2006.

[73] Jamil El-Ali, Peter K Sorger, and Klavs F Jensen. Cells on chips. *Nature*, 442(7101):403–411, 2006.

[74] Katherine S Elvira, Xavier Casadevall i Solvas, Robert C R Wootton, and Andrew J DeMello. The past, present and potential for microfluidic reactor technology in chemical synthesis. *Nat Chem*, 5(11):905–915, nov 2013.

[75] Ying Zhu and Qun Fang. Analytical detection techniques for droplet microfluidicsA review. *Analytica Chimica Acta*, 787:24–35, 2013.

[76] Wei Lung Chou, Pee Yew Lee, Cing Long Yang, Wen Ying Huang, and Yung Sheng Lin. Recent advances in applications of droplet microfluidics. *Micromachines*, 6(9):1249–1271, 2015.

[77] Bas Wijnen, Emily J Hunt, Gerald C Anzalone, and Joshua M Pearce. Open-Source Syringe Pump Library. *PLOS ONE*, 9(9):1–8, 2014.

[78] M a Unger, H P Chou, T Thorsen, a Scherer, and S R Quake. Monolithic microfabricated valves and pumps by multilayer soft lithography. *Science (New York, N.Y.)*, 288(5463):113–116, 2000.

[79] Min Hsien Wu, Song Bin Huang, Zhanfeng Cui, Zheng Cui, and Gwo Bin Lee. Development of perfusion-based micro 3-D cell culture platform and its application for high throughput drug testing. *Sensors and Actuators, B: Chemical*, 129(1):231–240, 2008.

[80] Chuck Treutel. Peristaltic answer to caustic problems. *World Pumps*, page 1, 2009.

[81] Wikipedia Contributors. Peristaltic pump — Wikipedia, The Free Encyclopedia, 2018.

[82] T Boudot, N Petit, S Ritty, and C A Kieffer. Flow-rate calibration and control in a microfluidic device, 2014.

[83] S P Sutera and R Skalak. The History of Poiseuille Law. *Annual Review of Fluid Mechanics*, 25:1, 1993.

[84] Xiayan Wang, Chang Cheng, Shili Wang, and Shaorong Liu. Electroosmotic pumps and their applications in microfluidic systems. *Microfluidics and Nanofluidics*, 6(2):145–162, 2009.

[85] Shuhuai Yao and Juan G. Santiago. Porous glass electroosmotic pumps: Theory. *Journal of Colloid and Interface Science*, 268(1):133–142, 2003.

[86] Victor Pretorius, B. J. Hopkins, and J. D. Schieke. Electro-osmosis. A new concept for high-speed liquid chromatography. *Journal of Chromatography A*, 99(C):23–30, 1974.

[87] Felix Theeuwes. Elementary osmotic pump. *Journal of Pharmaceutical Sciences*, 64(12):1987–1991, 1975.

[88] Chunsun Zhang, Da Xing, and Yuyuan Li. Micropumps, microvalves, and micromixers within PCR microfluidic chips: Advances and trends. *Biotechnology Advances*, 25:483–514, 2007.

[89] P H Paul and D J Rakestraw. Electrokinetic high pressure hydraulic system, 2000.

[90] Jessica L Snyder, Jirachai Getpreecharsawas, David Z Fang, Thomas R Gaborski, Christopher C Striemer, Philippe M Fauchet, David a Borkholder, and James L McGrath. High-performance, low-voltage electroosmotic pumps with molecularly thin silicon nanomembranes. *Proceedings of the National Academy of Sciences of the United States of America*, 110(46):18425–30, 2013.

[91] Shuhuai Yao, Alan M. Myers, Jonathan D. Posner, Klint A. Rose, and Juan G. Santiago. Electroosmotic pumps fabricated from porous silicon membranes. *Journal of Microelectromechanical Systems*, 15(3):717–728, 2006.

[92] M. Morita, T. Ohmi, E. Hasegawa, M. Kawakami, and M. Ohwada. Growth of native oxide on a silicon surface. *Journal of Applied Physics*, 68(3):1272–1281, 1990.

[93] Saumitra K Vajandar, Dongyan Xu, and Dmitry A Markov. SiO2-coated porous anodic alumina membranes for high flow rate electroosmotic pumping. *Nanotechnology*, 18:275705–13, 2007.

[94] Ceming Wang, Lin Wang, Xiaorui Zhu, and Jianming Xue. Low-voltage electroosmotic pumps fabricated from track-etched polymer membranes. *Lab on a chip*, 12:1710–1716, 2012.

[95] Ji Wu, Karen Gerstandt, Mainak Majumder, Xin Zhan, and Bruce J Hinds. Highly efficient electroosmotic flow through functionalized carbon nanotube membranes. *Nanoscale*, 3(8):3321–8, 2011.

[96] a Ajdari. Pumping liquids using asymmetric electrode arrays. *Physical review. E, Statistical physics, plasmas, fluids, and related interdisciplinary topics*, 61(1):R45–8, 2000.

[97] A. B D Brown, C. G. Smith, and A. R. Rennie. Pumping of water with ac electric fields applied to asymmetric pairs of microelectrodes. *Physical Review E - Statistical, Nonlinear, and Soft Matter Physics*, 63(1 II):1–8, 2001.

[98] Vincent Studer, Anne Pépin, Yong Chen, and Armand Ajdari. An integrated AC electrokinetic pump in a microfluidic loop for fast and tunable flow control. *The Analyst*, 129(10):944–949, 2004.

[99] Michele D. Pysher and Mark A. Hayes. Electrophoretic and dielectrophoretic field gradient technique for separating bioparticles. *Analytical Chemistry*, 79(12):4552–4557, 2007.

[100] Akshay Kale, Saurin Patel, Guoqing Hu, and Xiangchun Xuan. Numerical modeling of Joule heating effects in insulator-based dielectrophoresis microdevices. *Electrophoresis*, 34(5):674–683, 2013.

[101] Mario A. Saucedo-Espinosa and Blanca H. Lapizco-Encinas. Experimental and theoretical study of dielectrophoretic particle trapping in arrays of insulating structures: Effect of particle size and shape. *Electrophoresis*, 36(9-10):1086–1097, 2015.

[102] Dmitri Lastochkin, Ronghui Zhou, Ping Wang, Yuxing Ben, and Hsueh Chia Chang. Electrokinetic micropump and micromixer design based on ac faradaic polarization. *Journal of Applied Physics*, 96(3):1730–1733, 2004.

[103] John H. Koschwanez, Robert H. Carlson, and Deirdre R. Meldrum. Thin PDMS films using long spin times or tert-butyl alcohol as a solvent. *PLoS ONE*, 4(2):2–6, 2009.

[104] AD Stroock and GM Whitesides. Components for integrated poly(dimethylsiloxane) microfluidic systems. *Electrophoresis*, 23(20):3461–3473, 2002.

[105] D. Baechi, R. Buser, and J. Dual. High-density microvalve arrays for sample processing in PCR chips. *Biomedical Microdevices*, 3(3):183–190, 2001.

[106] Vincent Studer, Giao Hang, Anna Pandolfi, Michael Ortiz, W. French Anderson, and Stephen R. Quake. Scaling properties of a low-actuation pressure microfluidic valve. *Journal of Applied Physics*, 95(1):393–398, 2004.

[107] Anna Pandolfi and Michael Ortiz. Improved design of low-pressure fluidic microvalves. *Journal of Micromechanics and Microengineering*, 17(8):1487–1493, 2007.

[108] Narayan Sundararajan, Dongshin Kim, and Andrew A. Berlin. Microfluidic operations using deformable polymer membranes fabricated by single layer soft lithography. *Lab on a Chip*, 5(3):350, 2005.

[109] William H. Grover, Alison M. Skelley, Chung N. Liu, Eric T. Lagally, and Richard A. Mathies. Monolithic membrane valves and diaphragm pumps for practical large-scale integration into glass microfluidic devices. *Sensors and Actuators, B: Chemical*, 89(3):315–323, 2003.

[110] Fu Chun Huang, Chia Sheng Liao, and Gwo Bin Lee. An integrated microfluidic chip for DNA/RNA amplification, electrophoresis separation and on-line optical detection. *Electrophoresis*, 27(16):3297–3305, 2006.

[111] 2. Design and dynamic characterization of "single-stroke" peristaltic PDMS micropumps. *Lab on a chip*, 11(2):336–342, 2011.

[112] J Dalton. "Essay II. On the force of steam or vapour from water and various other liquids, both in vacuum and in air" and Essay IV. "On the expansion of elastic fluids by heat". Technical report, Literary and Philosophical Society of Manchester, Manchester, 1802.

[113] F C M van de Pol, H T G van Lintel, M Elwenspoek, and J H J Fluitman. A thermopneumatic micropump based on micro-engineering techniques. *Sensors and Actuators A: Physical*, 23:198–202, 1990.

[114] D C Duffy, J C McDonald, O J Schueller, and G M Whitesides. Rapid Prototyping of Microfluidic Systems in Poly(dimethylsiloxane). *Analytical chemistry*, 70(23):4974–84, dec 1998.

[115] Yu Cheng Ou, Chih Sheng Yu, Chih Chung Yang, Chun Ming Chang, Yu Hsiang Tang, and Yu Hsin Lin. Biomimic PDMS valve applied in thermopneumatic micropump. *Journal of Applied Science and Engineering*, 15(4):317–322, 2012.

[116] W H Song and J Lichtenberg. Thermo-pneumatic, single-stroke micropump. *Journal of Micromechanics and Microengineering*, 15(8):1425, 2005.

[117] Minqiang Bu, Tracy Melvin, Graham Ensell, James S Wilkinson, and Alan G R Evans. Design and theoretical evaluation of a novel microfluidic device to be used for PCR. *Journal of Micromechanics and Microengineering*, 13(4):S125–S130, 2003.

[118] M C Tracey, I D Johnston, J B Davis, and C K L Tan. Dual independent displacement-amplified micropumps with a single actuator. *Journal of Micromechanics and Microengineering*, 16(8):1444–1452, 2006.

[119] I D Johnston, M C Tracey, J B Davis, and C K L Tan. Microfluidic solid phase suspension transport with an elastomer-based, single piezo-actuator, micro throttle pump. *Lab on a chip*, 5(3):318–325, 2005.

[120] M. Stehr, S. Messner, H. Sandmaier, and R. Zengerle. The VAMP - A new device for handling liquids or gases. *Sensors and Actuators, A: Physical*, 57(2):153–157, 1996.

[121] Supriyo Datta. *Surface Acoustic Wave Devices*. Prentice Hall, New Jersey, 1986.

[122] Leslie Y. Yeo and James R. Friend. Surface Acoustic Wave Microfluidics. *Annual Review of Fluid Mechanics*, 46(1):379–406, jan 2014.

[123] JW Strutt. On waves propagated along the plane surface of an elastic solid. *Proc. London Math. Soc*, s1-17(42):4–11, 1885.

[124] Sean M Langelier, Leslie Y Yeo, and James Friend. UV epoxy bonding for enhanced SAW transmission and microscale acoustofluidic integration. *Lab on a chip*, 12(16):2970–6, aug 2012.

[125] Myeong Chan Jo and Rasim Guldiken. Effects of polydimethylsiloxane (PDMS) microchannels on surface acoustic wave-based microfluidic devices. *Microelectronic Engineering*, 113:98–104, jan 2014.

[126] Richie J. Shilton, Sean M. Langelier, James R. Friend, and Leslie Y. Yeo. Surface acoustic wave solid-state rotational micromotor. *Applied Physics Letters*, 100(3):1–3, 2012.

[127] Ioana Voiculescu and Anis Nurashikin Nordin. Acoustic wave based MEMS devices for biosensing applications. *Biosensors & bioelectronics*, 33(1):1–9, mar 2012.

[128] Dustin J Kreft and Robert H Blick. Surface Acoustic Waves and Nano Electromechanical Systems. *cdn.intechweb.org*, 2008.

[129] T.W. Grudkowski, G.K. Montress, M. Gilden, and J.F. Black. GaAs Monolithic SAW Devices for Signal Processing and Frequency Control. *1980 Ultrasonics Symposium*, pages 88–97, 1980.

[130] G a Coquin and H F Tiersten. Surface Waves in Quartz by Means of Surface Electrodes X. *The Journal of the Acoustical Society of America*, 41(October):921–939, 1966.

[131] Goksen G. Yaralioglu, Ira O. Wygant, Theodore C. Marentis, and Butrus T. Khuri-Yakub. Ultrasonic mixing in microfluidic channels using integrated transducers. *Analytical Chemistry*, 76(13):3694–3698, 2004.

[132] P Ventura and JM Hode. Numerical Methods for SAW propagation characterization. *IEEE Ultrasonics Symposium*, pages 175–186, 1998.

[133] S.L. Peterie, R. D. Miller, and J. Ivanov. Seismology and Its Applications in Kansas. *Kansas Geological Survey*, 37(July):1–6, 2014.

[134] Kerstin Länge, Bastian E Rapp, and Michael Rapp. Surface acoustic wave biosensors: a review. *Analytical and bioanalytical chemistry*, 391(5):1509–19, jul 2008.

[135] Y. Q. Fu, J. K. Luo, X. Y. Du, A. J. Flewitt, Y. Li, G. H. Markx, A. J. Walton, and W. I. Milne. Recent developments on ZnO films for acoustic wave based bio-sensing and microfluidic applications: a review. *Sensors and Actuators, B: Chemical*, 143(2):606–619, 2010.

[136] Wiesław P. Jakubik. Surface acoustic wave-based gas sensors. *Thin Solid Films*, 520(3):986–993, 2011.

[137] Richie J. Shilton, Leslie Y. Yeo, and James R. Friend. Quantification of surface acoustic wave induced chaotic mixing-flows in microfluidic wells. *Sensors and Actuators B: Chemical*, 160(1):1565–1572, dec 2011.

[138] K. Sritharan, C. J. Strobl, M. F. Schneider, A. Wixforth, and Z. Guttenberg. Acoustic mixing at low Reynold's numbers. *Applied Physics Letters*, 88(5):054102, 2006.

[139] C. D. Wood, S. D. Evans, J. E. Cunningham, R. O'Rorke, C. Walti, and A. G. Davies. Alignment of particles in microfluidic systems using standing surface acoustic waves. *Applied Physics Letters*, 92(4):044104, 2008.

[140] C. D. Wood, J. E. Cunningham, R. O'Rorke, C. Walti, E. H. Linfield, a. G. Davies, and S. D. Evans. Formation and manipulation of two-dimensional arrays of micron-scale particles in microfluidic systems by surface acoustic waves. *Applied Physics Letters*, 94(5):054101, 2009.

[141] Xiaoyun Ding, Sz-Chin Steven Lin, Brian Kiraly, Hongjun Yue, Sixing Li, I-Kao Chiang, Jinjie Shi, Stephen J Benkovic, and Tony Jun Huang. On-chip manipulation of single microparticles, cells, and organisms using surface acoustic waves. *Proceedings of the National Academy of Sciences of the United States of America*, 109(28):11105–9, jul 2012.

[142] X. Ding, Z. Peng, S.-C. S. Lin, M. Geri, S. Li, P. Li, Y. Chen, M. Dao, S. Suresh, and T. J. Huang. Cell separation using tilted-angle standing surface acoustic waves. *Proceedings of the National Academy of Sciences*, 111:12992–12997, 2014.

[143] David J Collins, Adrian Neild, and Ye Ai. Highly focused high-frequency travelling surface acoustic waves (SAW) for rapid single-particle sorting. *Lab Chip*, 16(3):471–479, 2016.

[144] Linda Johansson, Johannes Enlund, Stefan Johansson, Ilia Katardjiev, and Ventsislav Yantchev. Surface acoustic wave induced particle manipulation in a PDMS channel–principle concepts for continuous flow applications. *Biomedical microdevices*, 14(2):279–89, apr 2012.

[145] L Johansson, J Enlund, S Johansson, I Katardjiev, M Wiklund, and V Yantchev. Surface acoustic wave-induced precise particle manipulation in a trapezoidal glass microfluidic channel. *Journal of Micromechanics and Microengineering*, 22(2):025018, feb 2012.

[146] Thach Vuong, Aisha Qi, Murat Muradoglu, Brandon Huey-Ping Cheong, Oi Wah Liew, Cui Xia Ang, Jing Fu, Leslie Yeo, James Friend, and Tuck Wah Ng. Precise drop dispensation on superhydrophobic surfaces using acoustic nebulization. *Soft Matter*, 9(13):3631, 2013.

[147] Layla Alhasan, Aisha Qi, Amgad R. Rezk, Leslie Y. Yeo, and Peggy P. Y. Chan. Assessment of the potential of a high frequency acoustomicrofluidic nebulisation platform for inhaled stem cell therapy. *Integr. Biol.*, 8(1):12–20, 2016.

[148] Lothar Schmid, Achim Wixforth, David A. Weitz, and Thomas Franke. Novel surface acoustic wave (SAW)-driven closed PDMS flow chamber. *Microfluidics and Nanofluidics*, 12(1-4):229–235, aug 2011.

[149] Michael B. Dentry, Leslie Y. Yeo, and James R. Friend. Frequency effects on the scale and behavior of acoustic streaming. *Physical Review E*, 89(1):013203, jan 2014.

[150] Salvatore Girardo, Marco Cecchini, Fabio Beltram, Roberto Cingolani, and Dario Pisignano. Polydimethylsiloxane-LiNbO3 surface acoustic wave micropump devices for fluid control into microchannels. *Lab on a chip*, 8(9):1557–63, sep 2008.

[151] Luca Masini, Marco Cecchini, Salvatore Girardo, Roberto Cingolani, Dario Pisignano, and Fabio Beltram. Surface-acoustic-wave counterflow micropumps for on-chip liquid motion control in two-dimensional microchannel arrays. *Lab on a chip*, 10(15):1997–2000, 2010.

[152] MK Tan, LY Yeo, and JR Friend. Rapid fluid flow and mixing induced in microchannels using surface acoustic waves. *EPL (Europhysics Letters)*, 87:47003, 2009.

[153] I D Johnston, D K McCluskey, C K L Tan, and M C Tracey. Mechanical characterization of bulk Sylgard 184 for microfluidics and microengineering. *Journal of Micromechanics and Microengineering*, 24(3):035017, 2014.

[154] Zhixin Wang, Alex A. Volinsky, and Nathan D. Gallant. Crosslinking effect on polydimethylsiloxane elastic modulus measured by custom-built compression instrument. *Journal of Applied Polymer Science*, 41050:1–4, 2014.

[155] S.A. Debiotech. DISPOSABLE PATCH PUMP FOR ACCURATE DELIVERY. Technical Report 44, 2013.

[156] Rashid O. Kadara, Norman Jenkinson, and Craig E. Banks. Characterization and fabrication of disposable screen printed microelectrodes. *Electrochemistry Communications*, 11(7):1377–1380, 2009.

[157] Shuqiang Huang, Chunyu Li, Bingcheng Lin, and Jianhua Qin. Microvalve and micropump controlled shuttle flow microfluidic device for rapid DNA hybridization. *Lab on a chip*, 10(21):2925–31, 2010.

[158] N. N. Barthakur and S. Bhartendu. Enhancement of evaporation rates from thin layers of liquids exposed to air ions. *International Journal of Biometeorology*, 32(3):163–167, 1988.

[159] Michael B Dentry, James R Friend, and Leslie Y Yeo. Continuous flow actuation between external reservoirs in small-scale devices driven by surface acoustic waves. *Lab on a chip*, 14(4):750–8, feb 2014.

[160] Food and Drug Administration. Reprocessing medical devices in Health care settings: validation methods and labeling guidance for industry and food and drug administration staff, 2015.

[161] Andrew St John and Christopher P. Price. Economic evidence and point-of-care testing. *Clinical Biochemist Reviews*, 34(2):61–74, 2013.

[162] Phillip Belgrader, Steve Young, Bob Yuan, Michael Primeau, Lee A Christel, Farzad Pourahmadi, and M Allen Northrup. Correction Cycler for Rapid Multiplex Real-Time PCR Analysis. *Analytical Chemistry*, 73(2):2001, 2001.

[163] Dino Di Carlo. Inertial microfluidics. *Lab Chip*, 9(21):3038–3046, 2009.

[164] Hermann Schlichting and Klaus Gersten. *Boundary-Layer Theory*. Springer-Verlag, Berlin, 9 edition, 2017.

[165] Michael J. Hargather and Gary S. Settles. Background-oriented schlieren visualization of heating and ventilation flows: HVAC-BOS. *HVAC and R Research*, 17(5):771–780, 2011.

[166] John P. Heller. An Unmixing Demonstration. *American Journal of Physics*, 28(4):348–353, 1960.

[167] Wikipedia Contributors. Stokes flow, 2018.

[168] Arman Molki, Lyes Khezzar, and Afshin Goharzadeh. Measurement of fluid velocity development in laminar pipe flow using laser Doppler velocimetry. *European Journal of Physics*, 34(5):1127–1134, 2013.

[169] J Paskauskas, R Rimeika, and D Ciplys. Velocity and attenuation of surface acoustic waves in proton-exchanged 128 degrees -rotated Y-cut LiNbO ₃. *Journal of Physics D: Applied Physics*, 28(7):1419–1423, 1995.

[170] N Jiménez, R Picó, F Camarena, J Redondo, and B Roig. Ultrasonic evaluation of the hydration degree of the orange peel. *Postharvest Biology and Technology*, 67:130–137, 2012.

[171] Daniel C Woods, J Stuart Bolton, and Jeffrey F Rhoads. Stress and Energy Transmission by Inhomogeneous Plane Waves into Dissipative Media Stress and Energy Transmission by Inhomogeneous Plane Waves into Dissipative Media. *Publications of the Ray W. Herrick Laboratories*, page 31, 2015.

[172] a.V. Mamishev, K. Sundara-Rajan, and M. Zahn. Interdigital sensors and transducers. *Proceedings of the IEEE*, 92(5):808–845, may 2004.

[173] Haekwan Oh, Keekeun Lee, Kyoungtae Eun, Sung Hoon Choa, and Sang Sik Yang. Development of a high-sensitivity strain measurement system based on a SH SAW sensor. *Journal of Micromechanics and Microengineering*, 22(2), 2012.

[174] James Friend and Leslie Y. Yeo. Microscale acoustofluidics: Microfluidics driven via acoustics and ultrasonics. *Reviews of Modern Physics*, 83(2):647–704, jun 2011.

[175] Richard O'Rorke. *The Spatial Control Of Particles In Microfluidic Systems Using Surface Acoustic Waves*. Phd thesis, University of Leeds, 2010.

[176] Thirumalai Kannan. *Finite Element Analysis of Surface Acoustic Wave Resonators*. PhD thesis, University of Saskatchewan, 2006.

[177] Z J Jiao, X Y Huang, and N-T Nguyen. Scattering and attenuation of surface acoustic waves in droplet actuation. *Journal of Physics A: Mathematical and Theoretical*, 41(35):355502, sep 2008.

[178] Ming K Tan, James R Friend, and Leslie Y Yeo. Microparticle collection and concentration via a miniature surface acoustic wave device. *Lab on a chip*, 7(5):618–25, may 2007.

[179] J. Vanneste and O. Buhler. Streaming by leaky surface acoustic waves. *Proceedings of the Royal Society A: Mathematical, Physical and Engineering Sciences*, 467(2130):1779–1800, 2011.

[180] S S Sadhal. Acoustofluidics 15: streaming with sound waves interacting with solid particles. *Lab on a chip*, 12(15):2600–11, aug 2012.

[181] Nam-Trung Nguyen, Audra H Meng, Justin Black, and Richard M White. Integrated flow sensor for in situ measurement and control of acoustic streaming in flexural plate wave micropumps. *Sensors and Actuators A: Physical*, 79(2):115–121, feb 2000.

[182] Leslie Y Yeo and James R Friend. Ultrafast microfluidics using surface acoustic waves. *Biomicrofluidics*, 3(1):12002, jan 2009.

[183] Trung-dung Luong and Nam-trung Nguyen. Surface Acoustic Wave Driven Microfluidics A Review. *Micro and Nanosystems*, 2(3):1–9, 2010.

[184] Marco Travagliati, Giorgio De Simoni, Carlo Maria Lazzarini, Vincenzo Piazza, Fabio Beltram, and Marco Cecchini. Interaction-free, automatic, on-chip fluid routing by surface acoustic waves. *Lab on a chip*, 12(15):2621–4, aug 2012.

[185] Ho Nam Chan, Yangfan Chen, Yiwei Shu, Yin Chen, Qian Tian, and Hongkai Wu. Direct, one-step molding of 3D-printed structures for convenient fabrication

of truly 3D PDMS microfluidic chips. *Microfluidics and Nanofluidics*, 19(9):1–10, 2015.

[186] Germán Comina, Anke Suska, and Daniel Filippini. PDMS lab-on-a-chip fabrication using 3D printed templates. *Lab on a chip*, 14(2):424–30, jan 2014.

[187] Vittorio Saggiomo and Aldrik H Velders. Simple 3D Printed Scaffold-Removal Method for the Fabrication of Intricate Microfluidic Devices. *Advanced Science*, 2:1500125, 2015.

[188] Jessamine Ng Lee, Cheolmin Park, and George M. Whitesides. Solvent Compatibility of Poly(dimethylsiloxane)-Based Microfluidic Devices. *Analytical Chemistry*, 75(23):6544–6554, 2003.

[189] Myeong Chan Jo and Rasim Guldiken. Dual surface acoustic wave-based active mixing in a microfluidic channel. *Sensors and Actuators, A: Physical*, 196:1–7, 2013.

[190] S. Talaei, O. Frey, P.D. van der Wal, N.F. de Rooij, and M. Koudelka-Hep. Hybrid microfluidic cartridge formed by irreversible bonding of SU-8 and PDMS for multi-layer flow applications. *Procedia Chemistry*, 1(1):381–384, sep 2009.

[191] Tongfan Sun and Amyn S Teja. Density, Viscosity, and Thermal Conductivity of Aqueous Ethylene, Diethylene, and Triethylene Glycol Mixtures between 290 K and 450 K. *Journal of Chemical & Engineering Data*, 48(1):198–202, jan 2003.

[192] Johannes Schindelin, Ignacio Arganda-Carreras, Erwin Frise, Verena Kaynig, Mark Longair, Tobias Pietzsch, Stephan Preibisch, Curtis Rueden, Stephan Saalfeld, Benjamin Schmid, Jean-Yves Tinevez, Daniel James White, Volker Hartenstein, Kevin Eliceiri, Pavel Tomancak, and Albert Cardona. Fiji: an open-source platform for biological-image analysis. *Nat Meth*, 9(7):676–682, jul 2012.

[193] Jean-Yves Tinevez, Nick Perry, Johannes Schindelin, Genevieve M Hoopes, Gregory D Reynolds, Emmanuel Laplantine, Sebastian Y Bednarek, Spencer L Shorte, and Kevin W Eliceiri. TrackMate: An open and extensible platform for single-particle tracking. *Methods*, 115:80–90, 2017.

[194] Sindy K Y Tang and George M Whitesides. Basic Microfluidic and Soft Lithographic Techniques. In Y. Fainman, editor, *Optofluidics: Fundamentals, Devices, and Applications*, chapter 2, pages 7–32. Mcgraw-Hill, 2009.

[195] Hong-bo Sun and Satoshi Kawata. Two-Photon Photopolymerization and 3D Lithographic Microfabrication. In *NMR 3D Analysis Photopolymerization*, pages 169–274. Springer Berlin Heidelberg, Berlin, Heidelberg, 2006.

[196] Skarphedinn Halldorsson, Edinson Lucumi, Rafael Gómez-Sjöberg, and Ronan M T Fleming. Advantages and challenges of microfluidic cell culture in polydimethylsiloxane devices. *Biosensors and Bioelectronics*, 63:218–231, 2015.

[197] Abhishek Jain, Amanda Graveline, Anna Waterhouse, Andyna Vernet, Robert Flaumenhaft, and Donald E. Ingber. A shear gradient-activated microfluidic device for automated monitoring of whole blood haemostasis and platelet function. *Nature communications*, 7:10176, 2016.

[198] Linzhi Tang and Nae Yoon Lee. A facile route for irreversible bonding of plastic-PDMS hybrid microdevices at room temperature. *Lab on a chip*, 10(10):1274–80, may 2010.

[199] K Dransfeld and E Salzmann. Excitation, Detection and Attenuation of High-Frequency Elastic Surface Waves. In Warren P. Mason and R. N. Thurston, editors, *Physical Acoustics: Principles and Methods vol 7*, chapter 4, page 395. Academic Press, New York, NY, 1970.

[200] Wc Wilson and Gm Atkinson. Rapid SAW Sensor Development Tools. *NASA Technical reports*, pages 1–7, 2007.

[201] Hirotsugu Ogi, Yasunori Kawasaki, Masahiko Hirao, Hassel Ledbetter, and I Introduction. Acoustic spectroscopy of lithium niobate: Elastic and piezoelectric coefficients. *Journal of Applied Physics*, 92(5):2451–2456, 2002.

[202] I D Johnston, D K McCluskey, C K L Tan, and M C Tracey. Mechanical characterization of bulk Sylgard 184 for microfluidics and microengineering. *Journal of Micromechanics and Microengineering*, 24:035017, 2014.

[203] R. D. O'Rorke, C. D. Wood, C. Walti, S. D. Evans, A. G. Davies, and J. E. Cunningham. Acousto-microfluidics: Transporting microbubble and microparticle arrays in acoustic traps using surface acoustic waves. *Journal of Applied Physics*, 111(9):094911, 2012.

[204] Y Li, B W Flynn, W Parkes, Y Liu, Y Feng, A D Ruthven, J G Terry, L I Haworth, A Bunting, S Smith, P Bobbili, Y Q Fut, and A J Walton. The Integration of EWOD and SAW Technologies for Improved Droplet Manipulation and Mixing. In *ESSDERC '09. Proceedings of the European Solid State Device Research Conference*, pages 371–374, 2009.

[205] Shen Jen and Romek Bobkowski. Black Lithium niobate SAW device fabrication and performance evaluation. *Ultrasonics Symposium, 2000 IEEE*, pages 269–273, 2000.

[206] Guigen Zhang. Nanostructure-Enhanced Surface Acoustic Waves Biosensor and Its Computational Modeling. *Journal of Sensors*, 2009:1–11, 2009.

[207] Wijaya Martanto, Jason S Moore, Osama Kashlan, Rachna Kamath, Ping M Wang, Jessica M O'Neal, and Mark R Prausnitz. Microinfusion Using Hollow Microneedles. *Pharmaceutical Research*, 23(1):104–113, 2006.

[208] Carl Eckart. Vortices and Streams caused by Sound waves. *Physical Review*, 73(1):68–76, 1948.

[209] Peter J Westervelt. The Theory of Steady Rotational Flow Generated by a Sound Field. *The Journal of the Acoustical Society of America*, 25(1):60–67, 1952.

[210] Kotaro Obata, Ayman El-Tamer, Lothar Koch, Ulf Hinze, and Boris N Chichkov. High-aspect 3D two-photon polymerization structuring with widened objective working range (WOW-2PP). *Light Sci Appl*, 2(August):1–4, 2013.

[211] Sima Rekštyt, Tomas Jonavičius, Darius Gailevičius, Mangirdas Malinauskas, Vygantas Mizeikis, Eugene G. Gamaly, and Saulius Juodkazis. Nanoscale Precision of 3D Polymerization via Polarization Control. *Advanced Optical Materials*, 4(8):1209–1214, aug 2016.

[212] B. Srinivasan and S. Tung. Development and Applications of Portable Biosensors. *Journal of Laboratory Automation*, 20(4):365–389, 2015.

[213] Arnold Chen and Tingrui Pan. Three-dimensional fit-to-flow microfluidic assembly. *Biomicrofluidics*, 5(4), 2011.

[214] Harris J. Hebert Jr. Sound Speed in Water-Ethylene Glycol Mixtures as a Function of Temperature and Pressure. *The Journal of the Acoustical Society of America*, 49(3):930–931, 2014.

[215] Horrace Lamb. *Hydrodynamics*. University Press, Cambridge, 4th edition, 1916.

[216] C Kunert and J Harting. Lattice Boltzmann simulations of liquid film drainage between smooth surfaces. *Ima Journal of Applied Mathematics*, 76(5):761–773, 2011.

[217] L M McDowall and R A Dampney. Calculation of threshold and saturation points of sigmoidal baroreflex function curves. *Am J Physiol Heart Circ Physiol*, 291(4):H2003–7, 2006.

[218] H Morgan and N G Green. *AC Electrokinetics: Colloids and Nanoparticles*. Microtechnologies and microsystems series. Research Studies Press, 2003.

[219] Pu Chen, Xiaojun Feng, Rui Hu, Jian Sun, Wei Du, and Bi Feng Liu. Hydrodynamic gating valve for microfluidic fluorescence-activated cell sorting. *Analytica Chimica Acta*, 663(1):1–6, 2010.

[220] Hirokazu Sugino, Kazuto Ozaki, Yoshitaka Shirasaki, Takahiro Arakawa, Shuichi Shoji, and Takashi Funatsu. On-chip microfluidic sorting with fluorescence spectrum detection and multiway separation. *Lab on a Chip*, 9(9):1254, 2009.

[221] Jean-Christophe Baret, Oliver J. Miller, Valerie Taly, Michaël Ryckelynck, Abdeslam El-Harrak, Lucas Frenz, Christian Rick, Michael L. Samuels, J. Brian Hutchison, Jeremy J. Agresti, Darren R. Link, David A. Weitz, and Andrew D. Griffiths. Fluorescence-activated droplet sorting (FADS): efficient microfluidic cell sorting based on enzymatic activity. *Lab on a Chip*, 9(13):1850, 2009.

[222] Lothar Schmid, David a. Weitz, and Thomas Franke. Sorting drops and cells with acoustics: acoustic microfluidic fluorescence-activated cell sorter. *Lab on a Chip*, 14(19):3710–3718, 2014.

[223] Yue Chen, Aram J. Chung, Ting Hsiang Wu, Michael A. Teitell, Dino Di Carlo, and Pei Yu Chiou. Pulsed laser activated cell sorting with three dimensional sheathless inertial focusing. *9th IEEE International Conference on Nano/Micro Engineered and Molecular Systems, IEEE-NEMS 2014*, pages 315–318, 2014.

[224] Ryan T Davies, Donghwan Kim, and Jaesung Park. Formation of liposomes using a 3D flow focusing microfluidic device with spatially patterned wettability by corona discharge. *Journal of Micromechanics and Microengineering*, 22(5):55003, 2012.

[225] James Knight, Ashvin Vishwanath, James Brody, and Robert Austin. Hydrodynamic Focusing on a Silicon Chip: Mixing Nanoliters in Microseconds. *Physical Review Letters*, 80(17):3863–3866, 1998.

[226] Jennifer L Osborn, Barry Lutz, Elain Fu, Peter Kauffman, Dean Y Stevens, and Paul Yager. Microfluidics without pumps: reinventing the T-sensor and H-filter in paper networks. *Lab Chip*, 10(20):2659–2665, 2010.

[227] Yu-jui Chiu, Sung Hwan Cho, Zhe Mei, Victor Lien, Tsung-feng Wu, and Yu-hwa Lo. Universally applicable three-dimensional hydrodynamic microfluidic flow focusing. *Lab on a chip*, 13(9):1803–9, 2013.

[228] Sara Abalde-Cela, Anna Gould, Xin Liu, Elena Kazamia, Alison G Smith, and Chris Abell. High-throughput detection of ethanol-producing cyanobacteria in a microdroplet platform. *Journal of the Royal Society, Interface / the Royal Society*, 12(106):20150216–, 2015.

[229] David Holmes, Joseph K She, Peter L Roach, and Hywel Morgan. Bead-based immunoassays using a micro-chip flow cytometer. *Lab on a chip*, 7(8):1048–56, aug 2007.

[230] Nico Westerhof, Nikos Stergiopulos, and Mark I.M. Noble. Law of Poiseuille. In *Snapshots of Hemodynamics*, chapter 2, page 192. Springer US, 2 edition, 2005.

[231] Aleksandra Radenovic. MICROFLUIDICS LAB ON CHIP. Technical report, LBEN, ÉCOLE POLYTECHNIQUE FÉDÉRALE DE LAUSANNE, Zurich, 2017.

[232] Jingrong Xiao, Weiqi He, Zhengtao Zhang, Weiying Zhang, Yiping Cao, Rongxiang He, and Yong Chen. PDMS micropillar-based microchip for efficient cancer cell capture. *RSC Adv.*, 5(64):52161–52166, 2015.

[233] Naga Siva Kumar Gunda, Jerry Joseph, Ali Tamayol, Mohsen Akbari, and Sushanta K. Mitra. Measurement of pressure drop and flow resistance in

microchannels with integrated micropillars. *Microfluidics and Nanofluidics*, 14(3-4):711–721, 2013.

[234] PM Optics. Lithium niobate wafer price list, 2017.

[235] Daniel Mark, Stefan Haeberle, Günter Roth, Felix von Stetten, and Roland Zengerle. Microfluidic lab-on-a-chip platforms: requirements, characteristics and applications. *Chemical Society reviews*, 39(3):1153–82, mar 2010.

[236] M. A. Burns, Brian N. Johnson, Sundaresh N. Brahmasandra, Kalyan Handique, James R. Webster, Madhavi Krishnan, Timothy S. Sammarco, Piu M. Man, Darren Jones, Dylan Heldsinger, Carlos H. Mastrangelo, and David T. Burke. An Integrated Nanoliter DNA Analysis Device. *Science*, 282(5388):484–487, 1998.

[237] Adam T. Woolley, Dean Hadley, Phoebe Landre, Andrew J. DeMello, Richard A. Mathies, and M. Allen Northrup. Functional integration of PCR amplification and capillary electrophoresis in a microfabricated DNA analysis device. *Analytical Chemistry*, 68(23):4081–4086, 1996.

[238] Emily A Oblath, W Hampton Henley, Jean Pierre Alarie, and J Michael Ramsey. A microfluidic chip integrating DNA extraction and real- time PCR for the detection of bacteria in saliva. *Lab on a Chip*, 13(7):1325–1332, 2013.

[239] James M. Trauba and Carl T. Wittwer. Microfluidic Extreme PCR: <1 Minute DNA Amplification in a Thin Film Disposable. *Journal of Biomedical Science and Engineering*, 10(05):219–231, 2017.

[240] Saulius Juodkazis, Mitsuru Watanabe, Masafumi Miwa, Shigeki Matsuo, Hiroaki Misawa, and Junji Nishii. Microfabrication in Silica. *Optics Letters*, 26(5):277–279, 2001.

[241] Changning Liu, Yang Liao, Fei He, Yinglong Shen, Danping Chen, Ya Cheng, Zhizhan Xu, Koji Sugioka, and Katsumi Midorikawa. Fabrication of three-

dimensional microfluidic channels inside glass using nanosecond laser direct writing. *Optics Express*, 20(4):4291, 2012.

[242] Frederik Kotz, Karl Arnold, Werner Bauer, Dieter Schild, Nico Keller, Kai Sachsenheimer, Tobias M. Nargang, Christiane Richter, Dorothea Helmer, and Bastian E. Rapp. Three-dimensional printing of transparent fused silica glass. *Nature*, 544(7650):337–339, 2017.

[243] Du T. Nguyen, Cameron Meyers, Timothy D. Yee, Nikola A. Dudukovic, Joel F. Destino, Cheng Zhu, Eric B. Duoss, Theodore F. Baumann, Tayyab Suratwala, James E. Smay, and Rebecca Dylla-Spears. 3D-Printed Transparent Glass. *Advanced Materials*, 1701181:1–5, 2017.

[244] Hiroki Kawano, Ryo Takigawa, Hiroshi Ikenoue, and Tanemasa Asano. Bonding of lithium niobate to silicon in ambient air using laser irradiation. *Japanese Journal of Applied Physics*, 55(8S3):08RB09, 2016.

[245] J Maniks and A Simanovskis. The Joining of LiNbO3, Quartz, TlBr-TlI and Other Optical Materials by the Use of Thin Metal Films as Bonding Agents BT - Defects and Surface-Induced Effects in Advanced Perovskites. In Gunnar Borstel, Andris Krumins, and Donats Millers, editors, *Defects and Surface-Induced Effects in Advanced Perovskites*, chapter 26, pages 267–272. Springer Netherlands, Dordrecht, 2000.

[246] Yadong Tang, Jian Shi, Sisi Li, Li Wang, Yvon E. Cayre, and Yong Chen. Microfluidic device with integrated microfilter of conical-shaped holes for high efficiency and high purity capture of circulating tumor cells. *Scientific Reports*, 4(1):6052, 2015.

[247] A Fatih Sarioglu, Nicola Aceto, Nikola Kojic, Maria C Donaldson, Mahnaz Zeinali, Bashar Hamza, Amanda Engstrom, Huili Zhu, Tilak K Sundaresan,

David T Miyamoto, Xi Luo, Aditya Bardia, Ben S Wittner, Sridhar Ramaswamy, Toshi Shioda, David T Ting, Shannon L Stott, Ravi Kapur, Shyamala Maheswaran, Daniel A Haber, and Mehmet Toner. A microfluidic device for label-free, physical capture of circulating tumor cell clusters. *Nat Meth*, 12(7):685–691, jul 2015.

[248] Kazunori Hoshino, Peng Chen, Yu Yen Huang, and Xiaojing Zhang. Computational analysis of microfluidic immunomagnetic rare cell separation from a particulate blood flow. *Analytical Chemistry*, 84(10):4292–4299, 2012.